

Force-matched interatomic potentials for tungsten and  
titanium-niobium

DISSERTATION

Presented in Partial Fulfillment of the Requirements for the Degree Doctor of  
Philosophy in the Graduate School of The Ohio State University

By

Robert Christopher Ehemann, M.S.  
Graduate Program in Physics

The Ohio State University

2017

Dissertation Committee:

Dr. John W. Wilkins, Advisor  
Dr. Maryam Ghazisaeidi  
Dr. Richard Kass  
Dr. Fengyuan Yang

©Copyright by

Robert Christopher Ehemann

2017

## Abstract

Classical interatomic potentials are an important bridge between nano-scale and meso-scale properties of materials, and facilitate an understanding of deformation and phase transitions at the atomistic level. This work presents the development of two semi-empirical interatomic potentials, one for the body-centered cubic metal tungsten and another for multi-phase titanium-niobium alloys. Accurate density functional theory calculations constitute large databases of forces, stresses and energies to which the empirical models are fit using an evolutionary algorithm. Accuracy of the potentials is verified by comparison with experiment and first-principles calculations for numerous structural, elastic and thermal properties. The models are used to investigate structural phase transitions under high pressure, in the case of tungsten, and chemical disorder, in the case of titanium-niobium. The presented models provide improved descriptions of these technologically important metals over existing classical potentials.

## **Acknowledgements**

I thank John Wilkins for his guidance, support, and friendship during the production of this work. I thank Jeremy Nicklas, Hyoungki Park, Michael Fellinger, Trisch Longbrake and Kristina Dunlap for their work, assistance and advice. I thank my family, both immediate and extended, for their support and faith. I thank my friends Jarred Hudson, Timothy McCormick and Ian Binnie for thoughtful discussion and humor in stressful times.

I was supported financially during the production of this work by The Ohio State University Department of Physics as a Fowler Fellow and Graduate Research Assistant, by The Ohio State University Graduate School as a University Fellow, and by the United States Department of Energy. Generous computational resources were provided by the Ohio Supercomputing Center.

Most of all I thank my loving partner Lacey Lubeley, without whose unyielding support this work may never have been completed.

Dedicated to my mentor and friend Dr. John Warren Wilkins.

As the last student of such a long and prolific line, I can only hope this work proves  
worthy.

## Vita

### EDUCATION

2007-2012 .....	B.S. Physics and Mathematics, Middle Tennessee State University, Murfreesboro, TN
2012-2015 .....	M.S. Physics, The Ohio State University, Columbus, OH
2015-present .....	Graduate Research Assistant, Department of Physics, The Ohio State University, Columbus, OH

### PUBLICATIONS

“Detection of hydrogen using graphene”

Robert C. Ehemann, Predrag S. Krstić, Jonny Dadras and Jacek Jakowski  
*Nanoscale Res. Lett.* **7**, 198 (2012)

“*Ab initio* based empirical potential applied to tungsten at high pressure”

Robert C. Ehemann, Jeremy W. Nicklas, Hyoungki Park and John W. Wilkins  
*Phys. Rev. B* **95**, 184101 (2017)

“Force-matched empirical potential for martensitic transitions and plastic deformation in Ti-Nb alloys”

Robert C. Ehemann and John W. Wilkins  
*Phys. Rev. B* **96**, 184105 (2017)

## **Field of Study**

Major Field: Physics

## Table of Contents

<b>Abstract</b> . . . . .	i
<b>Acknowledgements</b> . . . . .	ii
<b>Dedication</b> . . . . .	iii
<b>Table of Contents</b> . . . . .	vi
<b>List of Figures</b> . . . . .	ix
<b>List of Tables</b> . . . . .	xvii
<b>1 Essential Physics and Materials Science</b> . . . . .	1
1.1 Introduction and Motivation . . . . .	1
1.2 Crystallography . . . . .	4
1.2.1 Crystal lattices . . . . .	4
1.2.2 Reciprocal lattices . . . . .	8
1.2.3 Common notation . . . . .	8
1.3 Elasticity . . . . .	9
1.3.1 Voigt notation . . . . .	14
1.4 Phonons . . . . .	17
1.4.1 Thermal expansion . . . . .	20
1.4.2 Atomistic calculation of phonons . . . . .	21
1.5 Defects in Crystals . . . . .	21
1.5.1 Point defects . . . . .	21
1.5.2 Planar defects . . . . .	24
1.5.3 Generalized stacking faults . . . . .	25
1.5.4 Twin boundaries . . . . .	27
1.5.5 Dislocations . . . . .	27
1.6 Statistical Mechanics . . . . .	32
1.6.1 Microcanonical Ensemble . . . . .	34
1.6.2 Canonical Ensemble . . . . .	38
1.6.3 NPT Ensemble . . . . .	41
1.6.4 Other Ensembles . . . . .	42
1.7 Structural Phase Transitions . . . . .	43

1.7.1	bcc to hcp . . . . .	44
1.7.2	bcc to fcc . . . . .	45
1.7.3	bcc to $\omega$ -Ti . . . . .	47
<b>2</b>	<b>Density Functional Theory</b> . . . . .	<b>50</b>
2.1	The Schrödinger Equation in Condensed Matter . . . . .	51
2.2	The Kohn-Sham Method . . . . .	56
2.2.1	Exchange-Correlation Functionals . . . . .	61
2.3	Implementation . . . . .	63
2.3.1	Planewave Expansion . . . . .	63
2.3.2	Pseudopotentials . . . . .	64
2.3.3	Sampling the Brillouin Zone . . . . .	65
2.3.4	Smearing . . . . .	66
2.3.5	Convergence . . . . .	67
<b>3</b>	<b>Classical Molecular Dynamics</b> . . . . .	<b>69</b>
3.1	Fundamentals . . . . .	69
3.2	Ensemble Integration . . . . .	71
3.2.1	NVT . . . . .	71
3.2.2	NPT . . . . .	73
3.3	Interatomic Potentials . . . . .	76
3.3.1	Pair Potentials . . . . .	76
3.3.2	Pair Functionals . . . . .	78
3.3.3	Cluster Potentials . . . . .	81
3.3.4	Cluster Functionals: MEAM and Beyond . . . . .	82
<b>4</b>	<b>Optimization of Spline-Based Empirical Potentials</b> . . . . .	<b>85</b>
4.1	Spline-based parameterization . . . . .	86
4.1.1	Boundary conditions for spline-based interatomic potentials .	87
4.1.2	Non-invariance of splines under rescaling . . . . .	87
4.2	Global optimization via genetic algorithm . . . . .	90
4.3	Performing the right fit . . . . .	98
4.3.1	Under-fitting and over-fitting . . . . .	99
4.3.2	Saturating the spline functions . . . . .	100
4.3.3	Trends within a batch of potentials . . . . .	101
<b>5</b>	<b>Cluster Functional for Tungsten</b> . . . . .	<b>105</b>
5.1	DFT database and fitted parameters . . . . .	106
5.2	Accuracy of the fitted potential . . . . .	107
5.2.1	Energetics and elastic properties . . . . .	110
5.2.2	Point and planar defects . . . . .	113
5.3	Transferability of the fitted potential . . . . .	119
5.3.1	Dislocation core and deformation twinning . . . . .	119

5.3.2	Stabilization of fcc tungsten . . . . .	122
5.4	Summary . . . . .	126
<b>6</b>	<b>Cluster Functional for Titanium-Niobium . . . . .</b>	<b>128</b>
6.1	DFT Database and fitted parameters . . . . .	129
6.2	Accuracy of the fitted potential . . . . .	136
6.2.1	Structural, Elastic and Thermal Properties . . . . .	136
6.2.2	Planar and Point Defects . . . . .	142
6.3	Martensitic Transformations . . . . .	146
6.4	Dislocation Core Structures . . . . .	159
6.5	Summary . . . . .	162
<b>7</b>	<b>Conclusions and Future Directions . . . . .</b>	<b>164</b>
	<b>Bibliography . . . . .</b>	<b>167</b>

## List of Figures

1.1	Schematic showing stress tensor components $\sigma_{ij}$ in Cartesian coordinates. Cartesian unit vectors $\mathbf{e}_i$ are shown in red, and the action of an arbitrary stress vector $\mathbf{T}$ across their corresponding planes is shown in blue. Original image by Sanpaz for <a href="https://en.wikipedia.org/wiki/Cauchy_stress_tensor">https://en.wikipedia.org/wiki/Cauchy_stress_tensor</a> . . . . .	10
1.2	Anharmonic origins of thermal expansion. The Lennard-Jones (anharmonic) potential is shown in blue and a harmonic potential having the same curvature at the equilibrium bond length is imposed as a dashed line. Orange shaded regions represent the energetic filling at temperature $T$ . The harmonic potential is symmetric about the equilibrium bond length so the average position of an atom does not change with $T$ . The anharmonic potential softer at higher separation, so the average interatomic distance increases with $T$ . . . . .	20
1.3	Schematic of a free-surface slab calculation with periodic boundary conditions. . . . .	25
1.4	Schematic of the “tilt” method for computing the generalized stacking fault energy. The supercell vector $\mathbf{a}_3$ , initially normal to the stacking fault plane, is tilted in the direction of displacement ( $\mathbf{a}_1$ ) while cartesian positions of atoms are left unchanged. This produces a single stacking fault in the supercell, where the upper- and lower-most regions of the cell interact across the fault. . . . .	27
1.5	Geometries of low-index stacking faults considered in the present work. Body-centered cubic geometries shown for the (a) $\{110\}\langle111\rangle$ and (b) $\{112\}\langle111\rangle$ faults. The prismatic stacking fault of hcp is shown in (c) easy and (d) hard configurations, which correspond to a shift between different pairs of planes in the stacking sequence as shown in the inset of (d). . . . .	28
1.6	( $11\bar{2}$ )[111] twin in the bcc lattice. Base crystal atoms are shown in grey, twin atoms in blue and boundary atoms in orange. The formation of a twin corresponds to a reflection across the twin boundary ( $11\bar{2}$ ), which creates an effective shear in the [111] direction. . . . .	29

1.7	Schematic depiction of edge and screw dislocations in a single crystal. Large arrows represent the burgers vector $\mathbf{b}$ . Small arrows represent the burgers circuit used to calculate $\mathbf{b}$ . While the burgers vector for a particular dislocation is constant, the line sense vector $\xi$ is tangent to the dislocation at all points. Figure adapted from Passchier and Trouw [45] . . . . .	31
1.8	Schematic representation of the burgers transition mechanism in an orthorhombic unit cell. (Top) the standard bcc cell with bonds shown in orange inscribed in the orthorhombic (ort.) cell with $b/a = c/a = \sqrt{2}$ . (Center) transitioning to hcp involves a “shuffle” of atoms in a $\langle 1\bar{1}0 \rangle_\beta    \langle 1\bar{1}\bar{2}0 \rangle_\alpha    \langle 010 \rangle_{\text{ort}}$ . direction indicated by the blue arrows. Cones represent a change in the ort. box dimensions in the indicated direction. Atoms are treated in direct coordinates, so their cartesian positions change with “shear” in addition to “shuffle.” (Bottom) the standard hcp cell with bonds shown in orange inscribed in an ort. cell with $b/a = \sqrt{3}$ and $c/a = (c/a)_{\text{hcp}}$ . . . . .	46
1.9	Schematic relationship between face-centered cubic (blue) and body-centered tetragonal (bct) (orange). A two-atom bct cell can be used to describe fcc, and can be easily transformed to bcc by changing the axial ratio from $\sqrt{2}$ to unity. . . . .	47
1.10	Schematic representation of the hexagonal cell used to transform bcc into $\omega$ -Ti. (Top) a hexagonal representation of bcc with the standard cell inscribed with orange bonds. (Center) atoms in the $\{111\}$ planes at $c/3$ and $2c/3$ collapse toward $c/2$ to form the honeycomb layers of $\omega$ . (Bottom) the hexagonal $\omega$ -Ti structure is shown with bonds connecting to honeycomb atoms shown in orange. . . . .	49
2.1	Self-consistency loop of Kohn-Sham DFT. A Poisson equation is solved to obtain the Hartree potential, from which the effective potential can be formed. The single-particle Schrödinger equations are solved and the output density is calculated from the new single-particle orbitals. The new density is then fed back into the Poisson equation. The loop exits when some convergence criterion (e.g. a sufficiently small change in energy or density) is achieved. . . . .	60
2.2	“Jacob’s ladder” of exchange-correlation approximations for density functional theory. The bottom of the ladder (“earth”) represents the Hartree interaction energy, where exchange and correlation effects are ignored. The top of the ladder (“heaven”) represents the exact ground-state functional. Rungs are labeled according to the approximation, and the highest-order term included in the dependency of $v_{xc}(\rho(\mathbf{r}), \dots)$ is shown on the left-hand side. Climbing the ladder increases accuracy at the cost of computational efficiency as depicted by arrows to the right of the ladder. . . . .	62

2.3	Schematic of a pseudopotential and pseudo-wavefunction compared to the full potential and corresponding wavefunction. Rapid oscillations in the exact wavefunction near the origin, necessary to maintain orthogonality with the core states deep in the coulomb well, are replaced by a slowly decaying pseudo-wavefunction below the cutoff radius $r_c$ . Original image by Wolfram Quester for <a href="https://en.wikipedia.org/wiki/Pseudopotential">https://en.wikipedia.org/wiki/Pseudopotential</a>	65
3.1	Lennard-Jones potential for a single pair of atoms. Anharmonicity of the well is shown by comparison with a quadratic potential having the same curvature as the LJ potential at its minimum.	77
4.1	Demonstration of non-invariance of a linear spline under change of the domain. The original function is shown in blue, with knots represented as points. The rescaled function is shown similarly in red. Arrows indicate the minimum and maximum sampled values of the original domain. These values become the boundaries of the re-scaled spline and knots are distributed equally between them with $y$ -values computed from the original function. The two functions differ in regions where successive re-scaled knots do not lie between the same two original knots. Note that this is a view <i>before</i> the new function's boundaries are scaled toward $[-1, 1]$ .	89
4.2	Diagrammatic representation of the global optimization scheme. Ovals represent the beginning and end of the algorithm, with lists of input and output quantities respectively. Rectangles are functional steps in the algorithm and diamonds are “if” statements. The population is deemed “converged” if the change in total error for every member of the population is less than $10^{-3}$ . Partner selection and the breeding algorithm itself are discussed in more detail below.	92
4.3	Diagrammatic representation of the algorithm used to breed two parent potentials to form a member of the next generation. Flowchart shape meanings are as described above and symbols are defined in the key. Knots are taken from the current parent $P$ until a random number $q$ is generated to be less than the input crossover rate $c$ . The process ends when all child knots have been assigned $y$ values.	93

4.4	Crossover-breeding of two cubic spline functions. The first and second parents are shown in blue and orange, respectively, and the child is shown in black. A hypothetical post-downhill “relaxed” child function is shown in grey. Crossover points are depicted by vertical grey lines. When splines are significantly dissimilar (i.e. when their difference is much greater than their derivatives across successive knots), the child potential exhibits strong oscillations (and thus unphysically large forces) at and near the crossover. Powell optimization on the child potential will tend to smooth out the knots and reduce the oscillations in the splines while potentially evolving new features such as the hump shown the “relaxed” curve. . . . .	95
4.5	Diagrammatic representation of the algorithm used to determine breeding partners at each step in the evolutionary optimization. Rectangular panels represent algorithmic steps where commands are executed from top to bottom. Diamonds represent “if” statements and ovals represent the beginning and end. The two most-fit potentials are always copied into the next generation by breeding with itself. The first and second most fit potentials are also forced to breed. . . . .	96
4.6	Algorithmic flowchart for Powell’s conjugate direction optimizer. . . . .	97
4.7	Comparison of Powell optimization performance for two functions. Points and lines show iterations of the algorithm from different starting positions. Global minima are marked by a white asterisk. Powell’s algorithm finds the global minimum of the Rosenbrock function (left) within about 10 iterations, but quickly converges to local minima when they are near the starting position (right). . . . .	98
4.8	Simple examples of (a) under- (b) well- and (c) over-fit models. Red lines show model predictions while fitted points are shown in blue. The underlying data is a cubic polynomial with a sinusoidal random signal added. . . . .	100
4.9	Examples of (a) a properly fit spline model (b) an under-saturated spline model and (c) an over-fit spline model. Red lines show cubic spline interpolants, red points represent spline knots and data points are shown in blue. One cannot in general distinguish an under-saturated spline from an over-fit spline without examining the distribution of data. Note that the over-fit model uses twice the number of spline knots to fit the same data set. . . . .	101
4.10	Representation of the fitting error in a radial distribution format. (a) shows the error for a single potential, with labels on each radial ray and the error axis. (b) shows a batch of ten fits with unlabeled radial graphs side-by-side for easy comparison. . . . .	102

4.11	Splines functions from two GMEAM models: (a) A well-converged fit with smooth spline functions and sensible behavior at boundaries. (b) An overfit potential with too many parameters, where functions display frequent oscillation and non-physical behavior at the boundaries. . . . .	103
5.1	The seven quintic splines comprising the functions of our SWMEAM model. The embedding function here is given the symbol $F(n)$ . . . . .	107
5.2	(a) Comparison of energy-volume curves between SWMEAM and DFT for six crystal structures. Curves are ordered vertically according to the key. Our empirical potential reproduces the energies of each phase relative to that of the bcc ground state. (b) Pressure-volume relation for tungsten as computed by SWMEAM and DFT at 0 K compared with data from shock experiments[101] at room temperature. SWMEAM shows agreement with both experimental and <i>ab-initio</i> results, even at extreme pressures. (c) Thermal expansion of tungsten predicted by SWMEAM agrees with experimental data fit[102] up to the melting point of 3695 K. . . . .	109
5.3	Elastic constants versus pressure for bcc tungsten as computed with GGA-DFT and the fitted potential. SWMEAM produces elastic constants within 21% of the DFT values for all pressures shown. . . . .	112
5.4	Phonon dispersion for bcc W at zero pressure as calculated by DFT and SWMEAM, compared with inelastic neutron scattering data of Chen and Brockhouse[109]. . . . .	113
5.5	Vacancy migration pathway as calculated in GGA-DFT and SWMEAM at multiple pressures. The shallow local minimum at $\langle \frac{1}{2} \frac{1}{2} \frac{1}{2} \rangle$ is predicted by both DFT and SWMEAM to increase between 0 and 100 GPa, though this effect is non-monotonic in SWMEAM. . . . .	115
5.6	Unrelaxed low-index generalized stacking fault energies (GSFE) for bcc tungsten. SWMEAM accurately models the evolution of both {110} and {112} faults with pressure. Relaxed GSFE curves computed with SWMEAM are shown as dotted lines for 0 GPa. Relaxation lowers fault energy slightly but does not result in any metastable configurations. . .	116
5.7	Ideal shear energy (top) and stress (bottom) for a continuous deformation of a one-atom bcc unit cell corresponding to (112)[ $\bar{1}\bar{1}\bar{1}$ ] twinning system as described by Paxton <i>et al.</i> [121]. SWMEAM Accurately reproduces the energy barrier and shear stress of this deformation for pressures up to 100 GPa. Small discrepancies in shear stress are found at the inflection points of the energy barrier, which correspond to the two extrema of shear stress at $x = 0.25$ and $x = 0.75$ . . . . .	118
5.8	Differential displacement map of the $\frac{1}{2}\langle 111 \rangle$ screw dislocation. SWMEAM predicts a non-degenerate symmetric core structure consistent with previous bond-order[18] and GGA-DFT[122] calculations, whereas existing F-S potentials for tungsten predict a degenerate core[47]. . . . .	120

5.9 Deformation twinning and detwinning in a tungsten bicrystal nanowire under axial compression at room temperature. Compare to work of Wang <i>et al.</i> [5]. Structure identification was performed using adaptive common neighbor analysis as implemented in OVITO[43, 44]. Atoms are color-coded by structure: light (bcc) and dark (none). (a,b,c) Multiple deformation twins of the $\{112\}\langle 111 \rangle$ type grow and merge as the rod is compressed by 10%. (d,e,f) Detwinning occurs as the load is released, recovering the compressive strain. Different shades of gray appear in the bulk because of atomic-level shading in OVITO. . . . .	122
5.10 SWMEAM (solid) Phonon dispersions at various pressures compared with LDA-DFT (dashed) work of Einarsdotter <i>et al.</i> [57] (a) bcc: SWMEAM is consistent DFT even at the extreme pressure of 1200 GPa, but underestimates softening rate of the $L^{-\frac{2}{3}}[111]$ ( $\omega$ ) phonon and predicts an anomalous softening of the $T^{-\frac{1}{2}}[110]$ phonon with increasing pressure. (b) fcc: with the exception of the soft $T-[\xi\xi 0]$ and $T-[\xi\xi\xi]$ modes, SWMEAM dispersion at zero pressure diverges considerably from that of DFT. SWMEAM also underestimates the rate of stabilization of the soft modes with respect to DFT work. However at extreme pressures where fcc is thermodynamically stable, SWMEAM dispersion agrees closely with that of DFT. Displayed pressures are computed with SWMEAM. These dispersions were calculated using the small displacement method as implemented in the Atomic Simulation Environment[42]. As usual for phonons, negative values represent imaginary frequencies. . . . .	123
5.11 Stability of fcc tungsten at 0 K. (a) shows the elastic constants $C_{44}$ and $C'$ as functions of pressure, demonstrating the elastic stability of fcc tungsten for pressures above 455 GPa. (b) depicts the stabilization of the fcc- $T_{[1\bar{1}0]}[\xi\xi 0]$ phonon branch with pressure. SWMEAM predicts that fcc becomes dynamically stable around 543 GPa with the $\xi = 0.4$ mode being the last to stabilize. (c) depicts the enthalpy difference $H_{fcc}(P) - H_{bcc}(P)$ between fcc and bcc as a function of pressure, revealing that despite being dynamically stable, fcc tungsten is not energetically favorable until pressures above 762.5 GPa. (inset) The tetragonal Bain path at the determined transition pressure exhibits an energy barrier of 140 meV/atom, indicating that bcc will not spontaneously transform to fcc with the fitted potential. . . . .	125
6.1 Plots of the sixteen functions of the fitted potential. Points are spline knots and lines are cubic spline interpolants. Splines are clamped at the endpoints according to the derivatives listed in Table 6.1. . . . .	133

6.2 Energy versus volume curves for (a) Ti, (b) $\beta$ $Ti_3Nb$ , (c) $\alpha$ and $\omega$ $Ti_3Nb$ , and (d) Nb. GMEAM values are shown as solid curves, while DFT values are presented as points. Zero energy is defined for (a) as hcp Ti, for (b) and (c) as G1 $Ti_3Nb$ , and for (d) as bcc Nb. Values are given relative to these zeros for the two methods presented. For the $Ti_3Nb$ stoichiometry, fully relaxed solid-solution (S.S.) curves are shown for GMEAM. . . . .	135
6.3 Pressure-volume relations for hcp-Ti and bcc-Nb. DFT shows good agreement with room-temperature experimental data [101] obtained by shock measurements, but GMEAM under-estimates hcp-Ti pressure for compression below $V/V_0 = 0.7$ and over-estimates pressure at higher compression. . . . .	137
6.4 Elastic constants (in GPa) of bcc $Ti-x$ at.%Nb as a function of niobium concentration $x$ . Solid lines are from a 31,250-atom solid solution as calculated with the fitted GMEAM potential using a maximum strain of 0.5%. Open symbols are from DFT calculations of the present work and others, while filled symbols are experimental data. GMEAM shows good agreement with experiment across the range of niobium concentration, but in general overestimates $C_{12}$ compared to previous <i>ab initio</i> work (open symbols). This gives a smaller value for $C' = (C_{11} - C_{12})/2$ , meaning the potential is more elastically anisotropic as measured by the anisotropy ratio $A = C_{44}/C'$ . . . . .	140
6.5 Low-index stacking faults for (a) hcp Ti and (b) bcc Nb as predicted by GMEAM (solid curves) and the present DFT (points) calculations. Faults relaxed with GMEAM are shown as dashed curves. Relaxation of the easy prismatic ( $\{01\bar{1}0\}\langle11\bar{2}0\rangle$ ) fault in hcp titanium reveals a local minimum indicating the formation of partial dislocations consistent with Ghazisaeidi and Trinkle, and Tarrat <i>et al.</i> [152, 153]. No metastable fault structures are found for niobium. . . . .	145
6.6 Transition energy barriers for the $\omega$ to $\beta$ transition in G1- $Ti_3Nb$ and (inset) pure Ti via the planar collapse mechanism for GMEAM and DFT. The atomic motion during this transition corresponds to a longitudinal 2/3[111] phonon in the bcc lattice as shown schematically in the top left. The $c/a$ ratio is mapped with $\xi$ from the optimal value for $\omega$ to the ideal value in $\beta$ . The overall lattice constant $a$ is an average of the appropriate values in the endpoint phases. GMEAM accurately describes the transition in both systems, including the 5 meV/atom DFT barrier from G1- $\beta$ to $\omega$ first identified by Lai <i>et al.</i> [135]. . . . .	146

- 6.7 Evolution of the  $\omega \leftrightarrow \beta$  transition pathway at 0 K with niobium in solid solution. A six-atom orthorhombic  $\omega$  cell is repeated  $10 \times 10 \times 5$  (3,000 atoms in total) and atomic decoration is randomly assigned to match the niobium concentration shown on the right-hand side of the curves. The horizontal axis represents the displacement as the two 2D-sublattices of the bipartite honeycomb layers are shifted up and down along  $[0001]_{\omega}$ , as shown by upward-facing and down-ward facing triangles respectively, until they become different  $\langle 111 \rangle_{\beta}$  planes. At each point the cell dimensions are relaxed to zero pressure. The parameters of the lowest-energy structure for each concentration are plotted in the inset. Curves are colored according to the equilibrium structure, where black represents  $\omega$ -Ti and red represents bcc. The lack of any local minima indicates the potential will not form a trigonal  $\omega$  phase at equilibrium in any of the considered concentrations. The cell parameters remain relatively unchanged due to the inherent structural compatibility of the  $\beta$  and  $\omega$  phases. . . . . 148
- 6.8 Potential energy surfaces for the  $\alpha \leftrightarrow \beta$  transition by the Burgers mechanism as calculated with GMEAM (left) and DFT (right) for pure Ti (top) and  $Ti_3Nb$  (bottom). In all cases,  $\xi = \eta = 0$  is the location of the bcc  $\beta$  phase ( $L6_0$  structure for  $Ti_3Nb$ ) while  $\alpha$  or  $\alpha''$  is located at  $\xi = \eta = 1$ . Calculations were performed on a  $50 \times 50$  grid for which  $\eta$  and  $\xi$  each vary from -0.125 to 1.125. The energy surfaces are fitted to seventh-order polynomial functions for the purpose of drawing smooth contours. . . . . 150
- 6.9 Evolution of the 0 K equilibrium structure with niobium in solid solution as calculated with GMEAM. The four-atom orthorhombic hcp unit cell is repeated  $10 \times 10 \times 5$  (2,000 total atoms) and atomic decoration is randomly assigned to match the niobium concentration shown on the right-hand side of the curves. The horizontal axis represents displacement in angstroms as alternating basal planes are shifted along  $[1\bar{1}00]_{\alpha}$ . The displacement for the completed transformation to bcc is labeled on the right for pure Ti; because the lattice parameter  $b$  increases with Nb content, other curves slightly exceed this value. At each point the simulation cell parameters are relaxed to zero pressure. Curves are colored according to the lowest energy structure along the transition path where black is  $\alpha$  (hcp), purple is  $\alpha'$ , red is  $\alpha''$  and blue is  $\beta$  (bcc). Cell dimensions from this structure at 18 concentrations are plotted in the inset with phase boundaries. Only select stoichiometries are plotted in the main figure for clarity. Niobium induces a strain in the hexagonal structure, destabilizing it in favor of  $\alpha'$  by  $\sim 7.5$  at.% Nb,  $\alpha''$  between  $\sim 12.5$  and  $\sim 35$  at.% Nb, and bcc beyond 35 at.% Nb. 153



## List of Tables

1.1	Standard cells and Brillouin zones for body-centered cubic, body-centered tetragonal, hexagonally close-packed, orthorhombic, monoclinic and triclinic lattices. Symmetry groups are given in the standard notation. High-symmetry paths are shown in the irreducible wedge of each Brillouin zone; images are adapted from Setyawan and Curtarolo [39], who provide tables of special-point coordinates and other useful information.	7
1.2	Strains and corresponding stresses used to determine elastic constants following the method of Trinkle [40]. One volumetric and six volume-conserving strains yield an overdetermined linear system from which the elastic constants can be computed. The top half of the table gives volumetric and volume-conserving orthorhombic strains and the corresponding stress-strain relationships for compressive/tensile component $\sigma_{ii}$ . The bottom half gives volume-conserving shear strains and corresponding stress-strain relations for shear components of $\sigma_{ij}$ . . . . .	17
1.3	Self-interstitial defects for HCP. Direct coordinates are given for the acute (first-quadrant) hexagonal HCP cell and GGA-DFT formation energies are presented for titanium. Dumbell structures involve splitting an atom into two, displacing each by the coordinates given but in opposite directions. Atoms from the base crystal are shown in green and defect atoms in orange. . . . .	23
1.4	Self-interstitial defects for BCC. Direct coordinates are given for the standard cubic BCC cell and GGA-DFT formation energies are presented for niobium. Dumbell structures involve splitting an atom into two, displacing each by the coordinates given but in opposite directions. Atoms from the base crystal are shown in grey and defect atoms in red. . . . .	24
5.1	Parameters specifying the seven cubic splines of the SWMEAM tungsten potential. The first part of the table lists independent variables for each spline function, the bounds of such, and the number of spline knots $N$ . In the middle part, values of the spline functions are tabulated for each knot $i$ , where $t_i = t_{min} + (i - 1)(t_{max} - t_{min})/(N - 1)$ . Lastly, first derivatives are listed for each spline at its endpoint. . . . .	108
5.2	Zero-pressure elastic constants of bcc tungsten in GPa. . . . .	111

5.3	Table of vacancy and self-interstitial formation energies (in eV) for bcc tungsten. Entries with angle-brackets indicate that the defect in question relaxes to the dumbbell configuration shown. . . . .	114
5.4	Energy and structural relaxation of low-index free surfaces in bcc tungsten. Surface energies $E$ are given in meV/ $\text{\AA}^2$ and the changes $\Delta_{12}$ in inter-planar spacing between the first two planes of the surface, where available, are given in units of percent. . . . .	117
6.1	Structures, cell parameters and k-point meshes used in DFT calculations. Titanium atoms are shown in grey and niobium atoms in green.	130
6.2	Parameters specifying the sixteen cubic splines of the GMEAM alloy potential. The first part of the table lists independent variables for each spline function, the bounds of such, and the number of spline knots N. An alloy index is assigned for each unique combination of species for each function. In the middle part, values of the spline functions are tabulated for each knot $i$ , where $t_i = t_{min} + (i-1)(t_{max} - t_{min})/(N-1)$ . Last, first derivatives are listed for each spline at its endpoint. . . . .	134
6.3	Linear thermal expansion coefficients (TECs), in units of $10^{-6} \text{ K}^{-1}$ , calculated with GMEAM and compared with experiment. GMEAM overestimates the TEC at each considered concentration, but shows a decrease with niobium content consistent with experiment. . . . .	138
6.4	Single-crystal elastic constants of $\text{Ti}_3\text{Nb}$ phases by GMEAM and DFT compared with data from the literature. . . . .	141
6.5	Vacancy (Vac.) and self-interstitial formation energies in bcc Nb and hcp Ti. Interstitial configurations for bcc Nb are octahedral (O), tetrahedral (T), crowdion (C), and split (or “dumbbell”) structures indicated by angle brackets. Geometry of these defects can be found in Fellinger <i>et al.</i> [86]. In addition to O, T and C, basal octahedral (BO), basal tetrahedral (BT), basal crowdion (BC), basal split (BS) and $c$ -axis split (CS) configurations are presented for hcp Ti. These geometries can be found in Raji <i>et al.</i> [148]. Structures which relax to another interstitial configuration are shown by table entries containing the relaxed structure abbreviation. . . . .	142

# Chapter 1:

# Essential Physics and Materials

# Science

## 1.1 Introduction and Motivation

The development and improvement of materials is among the most important challenges in technological development. Models are a fundamental component of innovation in any field, nowhere more so than in materials science and condensed-matter physics. Modeling the real-world applicability of a material based on fundamental underlying physics requires connecting nano-scale properties to life-sized performance, and femtosecond-timescales to end-use lifespans. This is accomplished in small steps using a variety of techniques to link electronic structure to crystalline properties, crystalline properties to micron-scale structure, etc., with results of methods feeding one another in either direction. This approach is often called *multiscale modeling*.

The present work focuses on bridging the gap between quantum mechanics and mesoscopic physics. First-principles calculations of electronic structure are used to develop semi-empirical models known as classical interatomic potentials, which can

be used to model interactions of millions of atoms at a time. These models are used to describe defect structures, phase transformations, plastic deformation and more.

Classical interatomic potentials were traditionally developed by choosing analytic functional forms with a handful of free parameters determined by fitting directly to experimental bulk data such as cohesive energy, lattice, and elastic constants. The force-matching method of Ercolessi and Adams [1] has facilitated the development of interatomic potentials based on *ab initio* calculations of relaxed crystallographic defects, metastable structures, and other nonequilibrium configurations. Combined with spline-based parameterization of constituent functions first used by Lenosky *et al.* [2], this allows the development of empirical or semi-empirical interatomic potentials trained to large portions of the *ab initio* potential-energy landscape with minimal bias. The present work describes the development and application of two such potentials, one for elemental tungsten and another for titanium-niobium alloys.

Tungsten is an exceptional transition metal exhibiting the highest tensile strength, melting point, and elastic modulus of any pure metal and has important applications in aerospace, energy and armament industries. Much interest has been focused on  $\alpha$ -W (bcc) and  $\beta$ -W (A15) nanostructures including nanorods[3, 4, 5], nanoparticles[6, 7, 8, 9], and thin films[10, 11, 12]. Due to the technological importance of tungsten, classical interatomic potentials of various forms have been developed to study this metal [13, 14, 15, 16, 17, 18, 19, 20]. The present work provides a more robust potential consistent with previous classical and *ab initio* results across a range of conditions in tungsten.

Titanium is also an important material in many modern industries. When alloyed with bcc-stabilizing elements (so-called  $\beta$  alloys), the bcc  $\beta$  phase can be stabilized at room temperature. One class of  $\beta$  alloys which has garnered much attention is “gum metals,” which contain about 25 at.% of a primary  $\beta$  stabilizer and small

amounts of other elements, e.g. Ta, Zr and O. These alloys have exceptional yield strength, high ductility and low elastic modulus [21], and exhibit superelasticity [21, 22, 23, 24, 25], shape memory [26, 23] as well as martensitic [27, 28] and strain-glass [19] transitions. The plastic deformation behavior of gum metals has been explored with great interest in order to explain these mechanical properties. Proposed mechanisms include dislocation-free deformation [21, 29], stress-induced martensitic transitions [30, 31, 28], deformation twinning [30, 31] and conventional dislocation-driven plasticity [32, 33].

Niobium is commonly used as the major  $\beta$ -stabilizer in gum metals, and Ti-Nb alloys on their own show promise in biomedical [34, 35, 36] and orthodontic [37] applications, and are used as superconducting wires for electromagnets in MRI machines, synchrotrons and tokamaks. The present work provides a classical interatomic potential for Ti-Nb alloys with focus on properties of the gum metal approximant  $Ti_3Nb$ .

This work is organized into seven chapters: Chapter 1 contains the basic physics and materials science relevant to testing and using interatomic potentials in metals and alloys. Chapter 2 is dedicated to the fundamentals of density-functional theory and its implementation in periodic metallic systems. Chapter 3 describes molecular dynamics, its application to different statistical-mechanics ensembles, and some basic classes of interatomic potentials. Chapter 4 is devoted to the fitting algorithm employed in the present work, its use with spline-based potentials, and a roadmap for the trial-and-error process of developing flexible interatomic potentials. Chapter 5 contains an interatomic potential for high-pressure tungsten, an assessment of its accuracy through comparison with density-functional theory, and its application to deformation twinning and the stabilization of an fcc allotrope. Chapter 6 contains the main achievement of the present work, a novel empirical potential for the titanium-niobium system, and its application to the effect of alloying on structural

phase transitions. Chapter 7 contains concluding remarks and a brief discussion of the future direction of developing embedded-atom-like potentials for metals and alloys.

The remainder of this chapter describes the materials science and condensed-matter physics relevant to the development of force-models for crystalline metals. Crystallography, elasticity, crystalline defects, statistical mechanics and phase transitions are described in terms of interatomic forces and energies. Methods of atomistic calculation are discussed where necessary.

## 1.2 Crystallography

This section provides the basic definition of crystalline lattices and bases, symmetry groups, and the reciprocal lattice. An explanation of some common notation is provided at the end.

### 1.2.1 Crystal lattices

A *crystal* is mathematically defined in 3-dimensional space by a set of 3 linearly independent vectors, denoted  $\{\mathbf{a}\}$ , which we term the *primitive* lattice vectors. *Sites*  $\mathbf{R}_I$  in the lattice are then defined by the integers  $n_1, n_2, n_3$  such that

$$\mathbf{R}_I = n_1\mathbf{a}_1 + n_2\mathbf{a}_2 + n_3\mathbf{a}_3, \quad (1.1)$$

where the subscript  $I$  is shorthand for the integers  $\{n\}$ . This structure is referred to as a *Bravais lattice*. For any given point satisfying Eq. 1.1, the locus of points in real space which are closer to that point than all other lattice points is referred to as the *Wigner-Seitz cell* of the lattice.

Many crystalline materials have atomic positions which themselves do not form a

Bravais lattice. Such structures can be described by adding to the bravais lattice a set of *basis vectors* which describe the position of atoms relative to the lattice points.

Clearly every different lattice site set of integers describing its position, but for every crystal there exists a group, called the *space group* of the lattice, all operations  $\hat{O}$  from which satisfy

$$\hat{O}\mathbf{R}_I = n'_1\mathbf{a}_1 + n'_2\mathbf{a}_2 + n'_3\mathbf{a}_3 \quad (1.2)$$

for all lattice points  $\mathbf{R}$ , where  $\{n'\}$  are integers. These operations – called the *space group* of the crystal – leave the infinite perfect crystal unchanged and can be described by an orthonormal form to which we apply a shorthand notation following Madelung[38]:

$$\hat{O}\mathbf{r} = \hat{\alpha}\mathbf{r} + \mathbf{a} \equiv \{\alpha|\mathbf{a}\}\mathbf{r}. \quad (1.3)$$

In this notation,  $\alpha$  denotes the *point group* of the crystal, which is the set of all rotation, reflection and inversion operations about the origin (which we have assumed to be a lattice site) that leave the crystal unchanged while  $\mathbf{a}$  represents pure translation operations where  $\mathbf{a}$  is any integer combination of the primitive lattice vectors. The space group of the lattice translates directly to symmetries in the electronic structure and thus plays a major role in determining the properties of materials. The symmetries are also exploited within electronic structure methods such as DFT (Chapter 2) to increase computational efficiency.

The atomic arrangements of some crystal structures, e.g. hcp or  $\omega$ -Ti, cannot be described by lattice vectors alone. This is because their atomic positions do not satisfy the definition of a mathematical Bravais lattice. To describe these features we need so-called basis vectors which describe the position of each atom in a periodic cell relative to the lattice point of that cell. Crystals which require a basis of more than one atom often have a lower symmetry than their underlying Bravais lattice. The

widely used DFT packages like VASP automatically determine the full space group of an input crystal, so this effect of bases on symmetry need not be accounted for by the user.

Table 1.1: Standard cells and Brillouin zones for body-centered cubic, body-centered tetragonal, hexagonally close-packed, orthorhombic, monoclinic and triclinic lattices. Symmetry groups are given in the standard notation. High-symmetry paths are shown in the irreducible wedge of each Brillouin zone; images are adapted from Setyawan and Curtarolo [39], who provide tables of special-point coordinates and other useful information.

Structure	Standard Cell	Brillouin Zone
body-centered cubic		
hexagonally close-packed		
face-centered cubic		
body-centered tetragonal		
orthorhombic		
monoclinic		
triclinic		

### 1.2.2 Reciprocal lattices

Given the primitive lattice vectors  $\mathbf{a}_i$ , another mathematical lattice can be defined by the vectors  $\mathbf{b}_j$  defined by the dimensionless dot product

$$\mathbf{a}_i \cdot \mathbf{b}_j = 2\pi\delta_{ij}, \quad (1.4)$$

where  $\delta_{ij}$  is the usual Kronecker delta. Clearly the vectors  $\mathbf{b}_j$  have units of inverse length, so this new lattice is called the *reciprocal* lattice. Points  $\mathbf{K}_J$  in the reciprocal lattice are defined by an integer linear combination of the  $\mathbf{b}_j$ , just as the  $\mathbf{R}_I$  are defined in Eq. 1.1.

The Wigner-Seitz cell of the reciprocal lattice is known as the *Brillouin zone*. Momentum-space integration is done within the symmetrically irreducible wedge of this Brillouin zone (IBZ) determined by the symmetry group of the crystal. High-symmetry paths used to visualize phonon and electron bands are taken from special points in the IBZ. Standard unit cells, Brillouin zones and high-symmetry paths in the IBZ of crystal structures relevant to the present work are shown in Table 1.1.

### 1.2.3 Common notation

Directions in a crystal are typically given in the basis of lattice vectors and denoted by square brackets, with negative components written in “barred” form. For example, given a set of lattice vectors  $\mathbf{a}_i$ ,  $[1\bar{2}3]$  corresponds to the vector  $\mathbf{a}_1 - 2\mathbf{a}_2 + 3\mathbf{a}_3$ . Sets of symmetry-equivalent directions are denoted by angle brackets. For example in a simple cubic lattice the vectors  $[110]$ ,  $[1\bar{1}0]$  and  $[01\bar{1}]$  are all classified as  $\langle 110 \rangle$  vectors.

Planes in a lattice are described in a similar way by writing in parenthesis the reciprocals of the direct-coordinate *intercepts* of the plane in a unit cell. The plane

$(hkl)$  thus intercepts the boundary of the unit cell at  $\mathbf{a}_1/h$ ,  $\mathbf{a}_2/k$  and  $\mathbf{a}_3/l$ . One can see that  $(hkl)$  is actually a vector in the *reciprocal* lattice, representing the normal vector of the plane. The indices  $h$ ,  $k$  and  $l$  are known as *Miller indices*. Families of symmetry-equivalent planes are given in curly brackets  $\{hkl\}$ .

### Hexagonal crystals

Hexagonal crystals are often described in terms of an over-complete basis with three vectors in the basal plane having an angle  $2\pi/3$  between one-another. Four indices are thus used to describe planes and directions, given in general by  $[hkil]$ , where  $h+k+i = 0$  as a result of the over-completeness. This preserves a permutation symmetry in  $h$ ,  $k$  and  $i$  such that  $[11\bar{2}0]$ ,  $[2\bar{1}\bar{1}0]$  and  $[1\bar{2}10]$  are all in the set  $\langle 11\bar{2}0 \rangle$ . The same notation is utilized for lattice planes, where it is known as *Miller-Bravais* notation. It should be noted that Miller-Bravais notation does *not* represent planar normals in an overcomplete basis of the reciprocal lattice; it is an ad-hoc representation of the three-index reciprocal vector  $(hkl)$  (which *does* represent the planar normal) written  $(h, k, -h-k, l)$ , which preserves the intercept-interpretation and is thus more intuitive with respect to the direct lattice.

## 1.3 Elasticity

Elasticity is among the most important properties of materials, particularly those relevant to the present work. This section describes the continuum theory of elasticity, derives some important results and discusses the method of atomistic calculation used here.

Consider an infinite homogeneous material with density  $\rho$ . Let  $\mathbf{u}$  be the displacement field inside the material such that a vector  $\mathbf{r}_0$  in the *undeformed* material

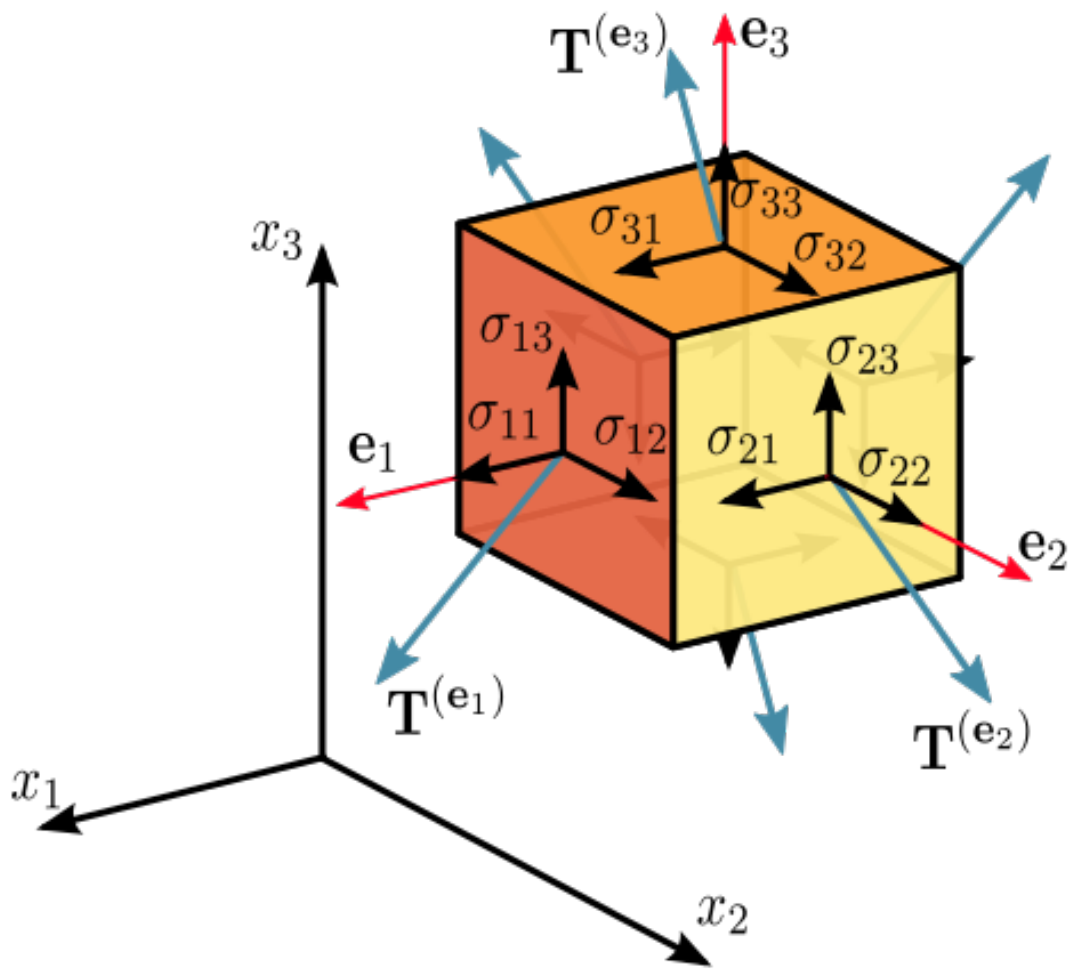


Figure 1.1: Schematic showing stress tensor components  $\sigma_{ij}$  in Cartesian coordinates. Cartesian unit vectors  $\mathbf{e}_i$  are shown in red, and the action of an arbitrary stress vector  $\mathbf{T}$  across their corresponding planes is shown in blue. Original image by Sanpaz for [https://en.wikipedia.org/wiki/Cauchy\\_stress\\_tensor](https://en.wikipedia.org/wiki/Cauchy_stress_tensor)

becomes at time  $t$  in the deformed material  $\mathbf{r}(t) = \mathbf{c}(t) + \mathbf{r}_0 + \mathbf{u}(\mathbf{r}, t)$ , where  $\mathbf{c}(t)$  is a time-dependence originating from center-of-mass motion and  $\mathbf{u}(\mathbf{r}, t)$  is the *displacement field*. Let the net force on the body as a whole to be zero and thus  $\mathbf{c}(t) = 0$ . The form of  $\mathbf{u}$  depends of course on the external force field  $\mathbf{f}$  and restorative force field  $\mathbf{f}_r$  caused by internal *stress*. Consider the net force experienced by volume element  $dV = dx dy dz$  at position  $\mathbf{r}$  and its resulting acceleration from newton's second law:

$$(\mathbf{f}_r + \mathbf{f})dV = \rho dV \frac{\partial^2 \mathbf{u}}{\partial t^2}. \quad (1.5)$$

Let  $\mathbf{n}$  be a unit vector specifying an arbitrary direction in the crystal. The *stress vector*  $\mathbf{T}^{(\mathbf{n})}$  is defined to be the force per unit area which produces a force  $\Delta \mathbf{f}_r$  on the volume element  $\Delta V$  at point  $\mathbf{r}$  according to  $\Delta \mathbf{f}_r = \mathbf{T}^{(\mathbf{n})} \Delta S$ , where  $\Delta S$  is the area of the plane defined by  $\mathbf{n}$  and  $\mathbf{r}$ . For an infinitesimal volume element

$$\mathbf{T}^{(\mathbf{n})} = \frac{d\mathbf{f}_r}{dS}. \quad (1.6)$$

To fully specify the state of stress in a crystal at time  $t$ , one must know the stress vector  $\mathbf{T}^{(\mathbf{n})}(\mathbf{r}, t)$  for *every*  $\mathbf{n}$  – of which there are infinitely many – at *every point*  $\mathbf{r}$  – of which there are also infinitely many. The *stress theorem* of Augustin-Louis Cauchy simplifies the situation by positing the existence of a second-order tensor field  $\bar{\sigma}(\mathbf{r}, t)$  from which the stress vector  $\mathbf{T}^{(\mathbf{n})}$  can be derived according to

$$\mathbf{T}^{(\mathbf{n})}(\mathbf{r}, t) = \mathbf{n} \cdot \bar{\sigma}(\mathbf{r}, t). \quad (1.7)$$

Clearly the components of  $\bar{\sigma}$  are given by the stress vectors along principal axes

$\mathbf{e}_i$ :

$$\bar{\sigma}(\mathbf{r}, t) = \begin{bmatrix} \mathbf{T}^{(\mathbf{e}_1)}(\mathbf{r}, t) \\ \mathbf{T}^{(\mathbf{e}_2)}(\mathbf{r}, t) \\ \mathbf{T}^{(\mathbf{e}_3)}(\mathbf{r}, t) \end{bmatrix}. \quad (1.8)$$

The net force on the volume element  $dV$  must be the difference

$[\mathbf{T}^{(\mathbf{e}_i)}(\mathbf{r} + dx_i \mathbf{e}_i, t) - \mathbf{T}^{(\mathbf{e}_i)}(\mathbf{r}, t)] dS_i$  of the action of stress vector  $\mathbf{T}^{(\mathbf{e}_i)}$  across the extent  $dx_i$  of  $dV$  in direction  $\mathbf{e}_i$ , summed over  $i$ :

$$\mathbf{f}_r dV = \sum_i [\mathbf{T}^{(\mathbf{e}_i)}(\mathbf{r} + dx_i \mathbf{e}_i, t) - \mathbf{T}^{(\mathbf{e}_i)}(\mathbf{r}, t)] dS_i, \quad (1.9)$$

which yields in the limit  $dx_i \rightarrow 0$

$$\mathbf{f}_r = \sum_i \frac{\partial \mathbf{T}^{(\mathbf{e}_i)}}{\partial x_i} = \sum_i \frac{\partial \bar{\sigma} \cdot \mathbf{e}_i}{\partial x_i} = \nabla \cdot \bar{\sigma}(\mathbf{r}, t). \quad (1.10)$$

Mechanical equilibrium thus produces “tensorized” Gauss’ law relationship wherein the external force (vector) field acts as a source for the internal stress (tensor) field. Mechanical equilibrium also requires the net torque on a volume element to be zero, which means that the stress tensor is symmetric:  $\sigma_{ij} = \sigma_{ji}$ .

It is useful for experimentalists and theorists alike to relate the stress to the deformation induced by the external force field, as opposed to the field itself. Within the limits of linear elasticity (in the limit of small distortions  $|\mathbf{u}| \ll 1$  and  $|\nabla \mathbf{u}| \ll 1$ ), the induced stresses take a Hooke’s law form generalized to three dimensions. The spring constant analogues are the familiar *elastic constants* as derived below.

Since a volume element can be simultaneously pushed, pulled and sheared in different directions, its “displacement” must take the form of a second rank tensor  $\bar{\epsilon}$  called the *strain*. If the displacement field is constant over the extent of a volume element, there is by definition no distortion and hence no induced stress within the

volume element. From this it can be seen that  $\epsilon_{ij}$  should depend on the gradient  $\nabla \mathbf{u}$  of the displacement across  $dV$ . In the absence of internal torques, however, the anti-symmetric part of  $\nabla \mathbf{u}$ ,  $\omega_{ij} = \frac{\partial u_i}{\partial x_j} - \frac{\partial u_j}{\partial x_i}$ , which represents rigid rotations of the body, also cannot produce stresses. The *strain tensor*  $\epsilon_{ij}$  is therefore defined to be the symmetric part of  $\nabla \mathbf{u}$  in the infinitesimal limit:

$$\epsilon_{ij} = \frac{1}{2} \left( \frac{\partial u_i}{\partial x_j} + \frac{\partial u_j}{\partial x_i} \right). \quad (1.11)$$

In general, a linear mapping between two second-rank tensors involves a fourth-rank tensor which in three dimensions has  $3^4 = 81$  independent components. Here  $C_{ijkl}$  is the *elastic stiffness tensor*, which maps the strain components  $\epsilon_{kl}$  to stress components  $\sigma_{ij}$ :

$$\sigma_{ij} = C_{ijkl}\epsilon_{kl}, \quad (1.12)$$

where repeated indices are summed. Properties of the stress and strain tensors can be used to determine symmetries of  $C_{ijkl}$  and reduce the number of independent components. From the symmetry of  $\bar{\sigma}$  and  $\bar{\epsilon}$  one can see

$$C_{ijkl} = C_{jikl} = C_{ijlk} = C_{jilk}, \quad (1.13)$$

which reduces the number of independent components to 36. Consider now the work done by an infinitesimal strain  $d\epsilon_{ij}$ :

$$dw = \sigma_{ij}d\epsilon_{ij} = C_{ijkl}\epsilon_{kl}d\epsilon_{ij}. \quad (1.14)$$

When determining elastic constants experimentally or through simulation, strains are very small and the system's temperature is held constant. For an isothermal deformation the work done by internal stress must be equal to the change in Helmholtz

free energy  $\mathcal{F}$ :

$$\left( \frac{\partial \mathcal{F}}{\partial \epsilon_{ij}} \right) d\epsilon_{ij} = d\mathcal{F} = \sigma_{ij} d\epsilon_{ij} = C_{ijkl} \epsilon_{kl} d\epsilon_{ij}. \quad (1.15)$$

Differentiating with respect to  $\epsilon_{kl}$ ,

$$\frac{\partial^2 \mathcal{F}}{\partial \epsilon_{ij} \partial \epsilon_{kl}} = C_{ijkl}, \quad (1.16)$$

and thus by the commutability of partial derivatives

$$C_{ijkl} = C_{klij}. \quad (1.17)$$

The above relation further reduces the number of independent components of  $C_{ijkl}$  to 21. The independent components of  $C_{ijkl}$  are known as *elastic constants*.

### 1.3.1 Voigt notation

Dealing with a full fourth-rank tensor is cumbersome, but the symmetries discussed above allow one to represent  $\bar{\sigma}$  and  $\bar{\epsilon}$  as 6-component vectors and  $C_{ijkl}$  as a  $6 \times 6$  symmetric matrix. This is known as *Voigt notation* and requires a mapping of pairs of indices to single indices according to the following equivalence:

$$\begin{pmatrix} \sigma_{11} & \sigma_{12} & \sigma_{13} \\ \sigma_{12} & \sigma_{22} & \sigma_{23} \\ \sigma_{13} & \sigma_{23} & \sigma_{33} \end{pmatrix} = \begin{pmatrix} \sigma_1 & \sigma_6 & \sigma_5 \\ \sigma_6 & \sigma_2 & \sigma_4 \\ \sigma_5 & \sigma_4 & \sigma_3 \end{pmatrix} \rightarrow \begin{pmatrix} \sigma_1 \\ \sigma_2 \\ \sigma_3 \\ \sigma_4 \\ \sigma_5 \\ \sigma_6 \end{pmatrix} \quad (1.18)$$

A slightly different form is taken for the strain vector. Consider the scalar quantity

$$\bar{\bar{\sigma}} \cdot \bar{\bar{\epsilon}} = \sigma_{ij} \epsilon_{ij}. \quad (1.19)$$

Momentarily dropping the summation convention, this can be split into diagonal and off-diagonal contributions

$$\bar{\bar{\sigma}} \cdot \bar{\bar{\epsilon}} = \sum_i \sigma_{ii} \epsilon_{ii} + \sum_i \sum_{j \neq i} \sigma_{ij} \epsilon_{ij}, \quad (1.20)$$

which by the symmetry of  $\sigma_{ij}$  and  $\epsilon_{ij}$  can be written

$$\bar{\bar{\sigma}} \cdot \bar{\bar{\epsilon}} = \sum_i \sigma_{ii} \epsilon_{ii} + 2 \sum_i \sum_{j < i} \sigma_{ij} \epsilon_{ij} = \sum_i \sigma_{ii} \epsilon_{ii} + \sum_i \sum_{j < i} \sigma_{ij} \gamma_{ij}, \quad (1.21)$$

where the *engineering shear strain* has been defined as  $\gamma_{ij} = 2\epsilon_{ij}$ . To preserve the invariance of  $\bar{\bar{\sigma}} \cdot \bar{\bar{\epsilon}}$  the Voight strain vector is written as follows:

$$\begin{pmatrix} \epsilon_{11} & \epsilon_{12} & \epsilon_{13} \\ \epsilon_{12} & \epsilon_{22} & \epsilon_{23} \\ \epsilon_{13} & \epsilon_{23} & \epsilon_{33} \end{pmatrix} = \begin{pmatrix} \epsilon_1 & \epsilon_6 & \epsilon_5 \\ \epsilon_6 & \epsilon_2 & \epsilon_4 \\ \epsilon_5 & \epsilon_4 & \epsilon_3 \end{pmatrix} \rightarrow \begin{pmatrix} \epsilon_1 \\ \epsilon_2 \\ \epsilon_3 \\ \gamma_4 \\ \gamma_5 \\ \gamma_6 \end{pmatrix}. \quad (1.22)$$

The same numbering scheme used here can be assigned to the sets of coordinate indices  $\{ij\}$  and  $\{kl\}$  to Voigt indices such that

$$\begin{aligned}
[C_{ijkl}] &= \begin{pmatrix} C_{1111} & C_{1122} & C_{1133} & C_{1123} & C_{1113} & C_{1112} \\ & C_{2222} & C_{2233} & C_{2223} & C_{2213} & C_{2212} \\ & & C_{3333} & C_{3323} & C_{3313} & C_{3312} \\ & & & C_{2323} & C_{2313} & C_{2312} \\ & & & & C_{1313} & C_{1112} \\ & & & & & C_{1312} \end{pmatrix} & (1.23) \\
&= \begin{pmatrix} C_{11} & C_{12} & C_{13} & C_{14} & C_{15} & C_{16} \\ & C_{22} & C_{23} & C_{24} & C_{25} & C_{26} \\ & & C_{33} & C_{34} & C_{35} & C_{36} \\ & & & C_{44} & C_{45} & C_{46} \\ & & & & C_{55} & C_{56} \\ & & & & & C_{66} \end{pmatrix}
\end{aligned}$$

In the work that follows, the  $3 \times 3$  tensor formulation of strain is employed because it can be used to distort a unit cell by simple matrix multiplication. All shear strains will represent the true strain  $\epsilon_i$  instead of the engineering strain  $\gamma_i$ . The elastic constants themselves will be represented in matrix form via Voigt notation as shown above. Equation 1.23 is the most general form of the elastic constant matrix, and fewer than 21 components will be independent in any material with greater symmetry than a general triclinic crystal.

### Atomistic calculation of elastic constants

In the work that follows, a general method for calculating the elastic constants of a crystal with monoclinic or higher symmetry is used. This method, first proposed by Trinkle [40], involves simple deformations of a crystal which yield stresses given by

Table 1.2: Strains and corresponding stresses used to determine elastic constants following the method of Trinkle [40]. One volumetric and six volume-conserving strains yield an overdetermined linear system from which the elastic constants can be computed. The top half of the table gives volumetric and volume-conserving orthorhombic strains and the corresponding stress-strain relationships for compressive/tensile component  $\sigma_{ii}$ . The bottom half gives volume-conserving shear strains and corresponding stress-strain relations for shear components of  $\sigma_{ij}$ .

$\epsilon_1$	$\epsilon_2$	$\epsilon_3$	$\sigma_1/\delta$	$\sigma_2/\delta$	$\sigma_3/\delta$
$\delta$	$\delta$	$\delta$	$C_{11} + C_{12} + C_{13}$	$C_{22} + C_{13} + C_{23}$	$C_{33} + C_{23} + C_{13}$
$\frac{\delta^2}{1-\delta^2}$	$-\delta$	$\frac{\delta^2}{1-\delta^2}$	$C_{11} - C_{12}$	$C_{12} - C_{22}$	$C_{13} - C_{23}$
$-\delta$	$\frac{\delta^2}{1-\delta^2}$	$\delta$	$C_{12} - C_{13}$	$C_{22} - C_{23}$	$C_{23} - C_{33}$
$\frac{\delta^2}{4-\delta^2}$	0	0	$\epsilon_4 = \delta$		$\sigma_4/\delta = C_{44}$
0	$\frac{\delta^2}{4-\delta^2}$	0	$\epsilon_5 = \delta$		$\sigma_5/\delta = C_{55}$
0	0	$\frac{\delta^2}{4-\delta^2}$	$\epsilon_6 = \delta$		$\sigma_6/\delta = C_{66}$

linear combinations of the  $C_{ijkl}$ . Strains and corresponding linear combinations of elastic constants are given in Table 1.2. Cell volumes are conserved for  $\delta \approx 0.001$ .

Using these strains with four or more values of  $\delta$ , distributed symmetrically about  $\delta = 0$ , stress-strain relations can be determined by a linear fit. The coefficient obtained in this fit corresponds to the entry on the right-hand side of Table 1.2. It is important to use more than two points and to verify that the stress-strain relationship is linear (visually or by examination of fitting error) for the considered values of  $\delta$ .

## 1.4 Phonons

Phonons govern the behavior of a crystal at finite temperature and are closely related to transformations between crystalline phases. This section describes the classical harmonic crystal and the dynamical matrix. An atomistic method for calculating phonon frequencies is described.

The hamiltonian function of a crystal is easily expressed through the momenta

$\mathbf{P}_I$  and positions  $\mathbf{R}_I$  of its  $N$  constituent atoms. At equilibrium all momenta in the center-of-mass frame must necessarily be zero, so the total energy is determined by the interaction of the atoms occupying the lattice sites of the crystal. Temporarily assuming a two-body form for the potential energy between atoms  $I$  and  $J$   $U_{IJ} = \varphi(\mathbf{R}_I - \mathbf{R}_J)$  the lattice potential can be written

$$U_{eq} = \frac{1}{2} \sum_{I=1}^N \sum_{J \neq I}^N \varphi(\mathbf{R}_I - \mathbf{R}_J), \quad (1.24)$$

which describes the total energy of the crystal at zero temperature. When the temperature is nonzero, the atoms of course begin to move. For small displacements from equilibrium (or more precisely, small displacements of the atoms  $I$  from their neighbors  $J$  for which  $U_{IJ} \sim k_B T$ ), the potential can be approximated by a harmonic well, and the motion of atoms described as an arrangement of balls and springs. This is known as the *harmonic approximation*.

In the harmonic approximation, each atom  $I$  in a crystal is described by a lattice vector  $\mathbf{R}$  and a displacement field  $\mathbf{u}(\mathbf{R}_I)$  such that its position is given by  $\mathbf{r}(\mathbf{R}_I) = \mathbf{R}_I + \mathbf{u}(\mathbf{R}_I)$ . This can be inserted into the potential energy  $U_{tot}$  and expanded in a Taylor series for each cartesian component. The expansion is centered around  $\mathbf{r}_{IJ} = \mathbf{R}_I - \mathbf{R}_J$  with small displacement  $\mathbf{u}(\mathbf{R}_I) - \mathbf{u}(\mathbf{R}_J)$ . The total potential energy is written

$$\begin{aligned} U_{tot} = & \frac{1}{2} \sum \varphi(\mathbf{r}_{IJ}) + \frac{1}{2} \sum (\mathbf{u}(\mathbf{R}_I) - \mathbf{u}(\mathbf{R}_J)) \cdot \nabla \varphi(\mathbf{r}_{IJ}) \\ & + \frac{1}{4} \sum ((\mathbf{u}(\mathbf{R}_I) - \mathbf{u}(\mathbf{R}_J)) \cdot \nabla)^2 \varphi(\mathbf{r}_{IJ}) + \dots, \end{aligned} \quad (1.25)$$

but the linear vanishes because net forces must be zero at lattice sites. Dropping

terms higher than second-order yields  $U_{tot} = U_{eq} + U_{harm}$  where

$$\begin{aligned} U_{harm} &= \frac{1}{4} \sum ((\mathbf{u}(\mathbf{R}_I) - \mathbf{u}(\mathbf{R}_J)) \cdot \nabla)^2 \varphi(\mathbf{r}_{IJ}) \\ &= \frac{1}{4} \sum (u_\mu(\mathbf{R}_I) - u_\mu(\mathbf{R}_J)) \left( \frac{\partial^2 \varphi(\mathbf{r}_{IJ})}{\partial r_\mu \partial r_\nu} \right) (u_\nu(\mathbf{R}_I) - u_\nu(\mathbf{R}_J)). \end{aligned} \quad (1.26)$$

The last line above was obtained by expanding the squared dot product and rearranging, bearing in mind that  $\mathbf{u}$  is independent of  $\mathbf{r}_{IJ}$ . This form inspires the definition

$$D_{\mu\nu}(\mathbf{r}_{IJ}) = \left( \frac{\partial^2 \varphi(\mathbf{r}_{IJ})}{\partial r_\mu \partial r_\nu} \right) \quad (1.27)$$

but relied on the assumption of a two-body interaction, a very limiting assumption when building empirical interatomic potentials. The harmonic energy can be written in a more general form capable of dealing with many-body interaction energies:

$$U_{harm} = \frac{1}{2} \sum u_\mu(\mathbf{R}_I) D_{\mu\nu}(\mathbf{R}_I - \mathbf{R}_J) u_\nu(\mathbf{R}_J). \quad (1.28)$$

Note that in this form  $D_{\mu\nu}(\mathbf{R}_I - \mathbf{R}_J)$  is no longer the matrix of second partials of the pair potential but rather of the exact interaction potential  $U$  (hence the prefactor of 1/2 instead of 1/4). It is often called the *force constant* matrix, as it plays the same role as a spring constant in Hooke's law.

Now consider the equation of motion for the atom  $I$ :

$$M_I \frac{\partial^2 u_\mu(\mathbf{R}_I, t)}{\partial t^2} = - \frac{\partial U_{harm}}{\partial u_\mu(\mathbf{R}_I, t)} = - \sum_{\mathbf{R}_{J,\nu}} D_{\mu\nu}(\mathbf{R}_I - \mathbf{R}_J) u_\nu(\mathbf{R}_J, t). \quad (1.29)$$

An oscillatory ansatz for the time-dependence of  $u$  is now taken:

$$u_\mu(\mathbf{R}_I, t) = \epsilon_\mu e^{i(\mathbf{k} \cdot \mathbf{R}_I - \omega t)} \quad (1.30)$$

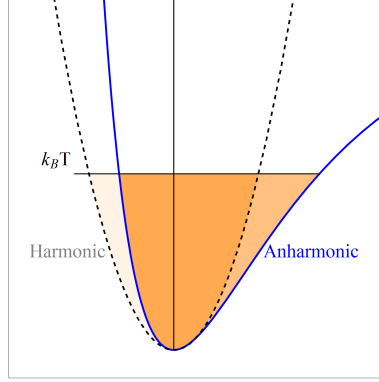


Figure 1.2: Anharmonic origins of thermal expansion. The Lennard-Jones (anharmonic) potential is shown in blue and a harmonic potential having the same curvature at the equilibrium bond length is imposed as a dashed line. Orange shaded regions represent the energetic filling at temperature  $T$ . The harmonic potential is symmetric about the equilibrium bond length so the average position of an atom does not change with  $T$ . The anharmonic potential softer at higher separation, so the average interatomic distance increases with  $T$ .

which yields, noting that  $D(-\mathbf{R}) = D(\mathbf{R})$ , the following eigenvalue equation:

$$M_I \omega(\mathbf{k})^2 \epsilon_\mu = \sum_{\mathbf{R}_J, \nu} D_{\mu\nu}(\mathbf{R}_J - \mathbf{R}_I) \epsilon_\nu e^{i\mathbf{k}\cdot(\mathbf{R}_J - \mathbf{R}_I)} = D_{\mu\nu}(\mathbf{k}) \epsilon_\nu. \quad (1.31)$$

The Fourier transform  $D_{\mu\nu}(\mathbf{k})$  of  $D_{\mu\nu}(\mathbf{R})$  is known as the *dynamical matrix*. Its eigenvalues are related to the phonon frequencies and the eigenvectors  $\epsilon_\mu$  are the corresponding normal modes. The wave-vector  $\mathbf{k}$  lives in reciprocal space, and the eigenvalue equation must be solved for every point in the Brillouin zone to fully describe the phonons. Nonetheless, the problem of describing crystalline excitations has been boiled down to an exercise in linear algebra.

### 1.4.1 Thermal expansion

The harmonic approximation is generally only valid at infinitesimal temperatures because inter-atomic forces are typically stronger at separations below the equilibrium

bond distance than above. Such an “anharmonic” potential means the atoms spend more time above the equilibrium separation than they do below it. This is manifest in the bulk material by *thermal expansion*. Figure 1.4.1 demonstrates the anharmonic origin of thermal expansion for the Lennard-Jones potential (see Section 3.3).

### 1.4.2 Atomistic calculation of phonons

Computing the  $\mathbf{k}$ -dependent eigen-frequencies  $\omega(\mathbf{k})$  with an atomistic method requires a full determination of the force-constant matrix  $D_{\mu\nu}(\mathbf{R}_I - \mathbf{R}_J) = \partial^2 U_{tot}/\partial r_\mu \partial r_\nu|_{\mathbf{r}_{IJ}}$ . This can be done using a finite-difference approximation to the derivatives as follows:

$$\frac{\partial^2 U_{tot}}{\partial r_\mu \partial r_\nu} \approx \frac{U_{tot}(\mathbf{r}_{IJ} + \mathbf{e}_\mu \Delta) + U_{tot}(\mathbf{r}_{IJ} + \mathbf{e}_\nu \Delta) - 2U_{tot}(\mathbf{r}_{IJ})}{\Delta^2}, \quad (1.32)$$

where  $\mathbf{e}_\mu$  is one of three cartesian unit vectors. A central-difference approximation is typically used in real applications for accuracy. Since calculating total energy can be costly (i.e. with first-principles methods), most codes implementing this so-called “small displacement” method, such as PHON [41] or the Atomic Simulation Environment (ASE) [42], will utilize the crystal symmetry to determine the minimal number of directional derivatives required to fully describe  $D_{\mu\nu}$ . The dynamical matrix is then calculated and diagonalized on a set of  $\mathbf{k}$ -points arranged in a grid or path in the Brillouin zone and  $\omega(\mathbf{k})$  is interpolated between these points.

## 1.5 Defects in Crystals

### 1.5.1 Point defects

Point defects considered in the present work come in two forms: self-interstitial atoms (SIAs) and vacancies. SIAs are atoms of the same chemical species as the host crystal

with positions in-between lattice sites. Many stable SIA configurations have nearest neighbor positions corresponding to a high-symmetry polygon; these sites are named according to the polyhedra. Another class of SIAs are the so-called “dumbbell” or “split” configurations where a lattice site is replaced by two atoms separated along a given direction. Dumbbell configurations are named according to the direction along which the lattice point is split. The formation energy of an SIA atom in a base crystal with  $N$  atoms and cohesive energy  $E_{coh}$  is given by

$$E_f^{SIA} = E_{tot}^{SIA} - (N + 1)E_{coh}. \quad (1.33)$$

SIA formation energies in metals tend to be on the order of a few eV. Geometries of SIAs in hcp and bcc crystals are shown in Table 1.3 and Table 1.4 respectively. Positions are given in direct coordinates.

Vacancies are lattice sites in a crystal without an occupying atom. Most basic crystals have only one type of vacancy, but phases with distinct sublattices (e.g.  $\omega$ -Ti) have more. The vacancy formation energy is calculated similarly to the SIA energy:

$$E_f^{Vac.} = E_{tot}^{Vac.} - (N - 1)E_{coh}. \quad (1.34)$$

Atomistic calculation of point-defect energies is a simple process of inserting or removing an atom at the appropriate location and relaxing the structure. Supercells must be used, and formation energies should be checked versus supercell size to ensure that the defects are not interacting with themselves across the periodic boundary.

Table 1.3: Self-interstitial defects for HCP. Direct coordinates are given for the acute (first-quadrant) hexagonal HCP cell and GGA-DFT formation energies are presented for titanium. Dumbell structures involve splitting an atom into two, displacing each by the coordinates given but in opposite directions. Atoms from the base crystal are shown in green and defect atoms in orange.

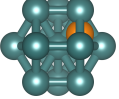
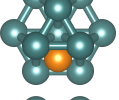
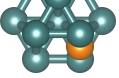
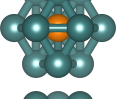
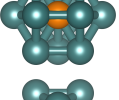
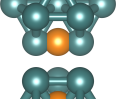
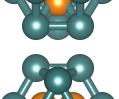
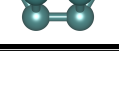
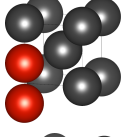
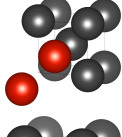
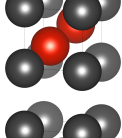
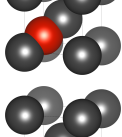
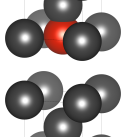
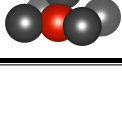
	$d_1$	$d_2$	$d_3$	
Tetrahedral	0	1/6	1/6	
Octahedral	1/2	1/3	1/4	
Crowdion	0	1/12	1/4	
Basal Tetrahedral	0	1/6	0	
Basal Octahedral	1/2	1/3	0	
Basal Crowdion	1/2	1/4	0	
[0001] Dumbell	0	0	1/6	
[11\bar{2}0] Dumbell	1/6	1/3	0	

Table 1.4: Self-interstitial defects for BCC. Direct coordinates are given for the standard cubic BCC cell and GGA-DFT formation energies are presented for niobium. Dumbell structures involve splitting an atom into two, displacing each by the coordinates given but in opposite directions. Atoms from the base crystal are shown in grey and defect atoms in red.

	$d_1$	$d_2$	$d_3$	
$\langle 001 \rangle$ Dumbell	1/3	0	0	
$\langle 011 \rangle$ Dumbell	1/3	1/3	0	
$\langle 111 \rangle$ Dumbell	1/3	1/3	1/3	
Crowdion	1/4	1/4	1/4	
Octahedral	1/2	1/2	0	
Tetrahedral	1/4	1/2	0	

### 1.5.2 Planar defects

Planar defects are disturbances to a local crystal structure across an entire lattice plane. In the present work, three types of planar defects are considered: free surfaces, generalized stacking faults and twin boundaries.

#### Free surfaces

Free surfaces are planes of a crystal exposed to vacuum. Atomistic determination of free surface energies typically involves what is known as a “slab” calculation, where

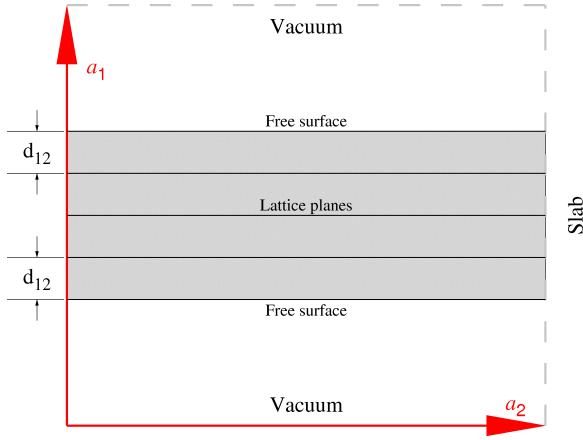


Figure 1.3: Schematic of a free-surface slab calculation with periodic boundary conditions.

a supercell containing a large region of vacuum is periodically repeated in three dimensions. Slab calculations contain *two* free surfaces which, if the cell is properly constructed, are identical.

Figure 1.5.2 provides a schematic for a slab calculation of a free surface. the quantity  $d_{12}$  represents the distance between the first two atomic layers. This distance often contracts upon relaxation. The energy of a free-surface is computed for a slab calculation as:

$$E^{surf} = \frac{E_{tot}^{surf} - NE_{coh}}{2A^{surf}}, \quad (1.35)$$

where  $A^{surf}$  is the area of the exposed surface and  $N$  is the number of atoms in the supercell.

### 1.5.3 Generalized stacking faults

Stacking faults in crystals are planes in which the equilibrium stacking order of atomic planes is disrupted. For example, if the equilibrium stacking is  $ABABAB$ , where the set  $AB$  can be thought of as a periodic unit in the stacking direction, then the sequence

$ABABCBCB$  contains a stacking fault in which two halves of the crystal have been displaced with respect to one another.

A generalized stacking fault (GSF) treats the relative displacement of two halves of a crystal as arbitrary. One typically computes the GSF energy  $\gamma(\xi)$  as a function of relative displacement  $\xi$ . Stable stacking faults are represented by local minima in  $\gamma(\xi)$  which lie higher than  $\gamma(\xi = 0)$ .

Atomistic calculation of stacking faults can proceed similarly to the free-surface calculation by using two slabs of a crystal displaced relative to one another. A more efficient method, however, involves “tilting” the supercell while leaving atomic positions unchanged. This is accomplished by changing the supercell vector that is initially normal to the stacking fault plane as follows:

$$\mathbf{a}_3(\xi) = \mathbf{a}_3^0 + \xi \mathbf{a}_1^0, \quad (1.36)$$

where it is assumed that  $\mathbf{a}_3^0$  is normal to the stacking fault plane and  $\mathbf{a}_1^0$  is the direction of displacement in the plane. A diagram of how the “tilt” method produces a GSF is shown in Figure 1.5.3.

The GSF energy  $\gamma$  is computed as a function of relative displacement  $\xi$  in the tilt method according to

$$\gamma(\xi) = \frac{E_{tot}^{GSF}(\xi) - NE_{coh}}{A^{GSF}}, \quad (1.37)$$

where  $A^{GSF}$  is the area of the stacking fault plane in the supercell and  $N$  is again the number of atoms. As such,  $\gamma(\xi)$  is periodic with unit period. Figure 1.5.3 shows low-index stacking faults geometries for (a) bcc and (b) hcp as considered in the present work. All structures correspond to  $\xi = 1/2$ . Atoms are color-coded according to local crystal structure by the method of adaptive common-neighbor analysis as implemented in OVITO[43, 44], where blue is bcc, red is hcp and white corresponds

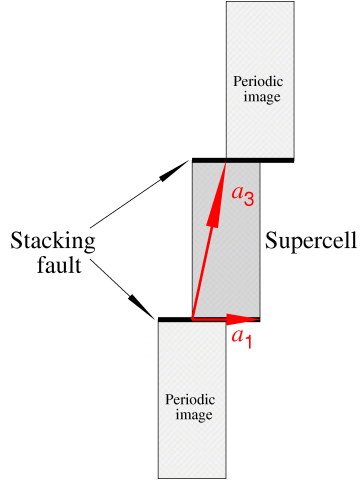


Figure 1.4: Schematic of the “tilt” method for computing the generalized stacking fault energy. The supercell vector  $\mathbf{a}_3$ , initially normal to the stacking fault plane, is tilted in the direction of displacement ( $\mathbf{a}_1$ ) while cartesian positions of atoms are left unchanged. This produces a single stacking fault in the supercell, where the upper- and lower-most regions of the cell interact across the fault.

to the atoms on the fault boundary.

#### 1.5.4 Twin boundaries

Twins are micro-structural regions of the same structure and sharing a lattice plane called the *twinning plane*, across which they are related by reflection. The direction of effective shear and the twinning plane define the twin. An example is shown in Fig. 1.5.4 for the bcc  $\{112\}\langle 111 \rangle$ -type twin. Twinning is one of the major modes of deformation exhibited by a crystal lattice; when twins are formed upon straining they are referred to as *deformation twins*.

#### 1.5.5 Dislocations

Dislocations are topological line-defects in crystals and are the primary mechanism of plastic deformation in solids. They can be uniquely specified with two vector quan-

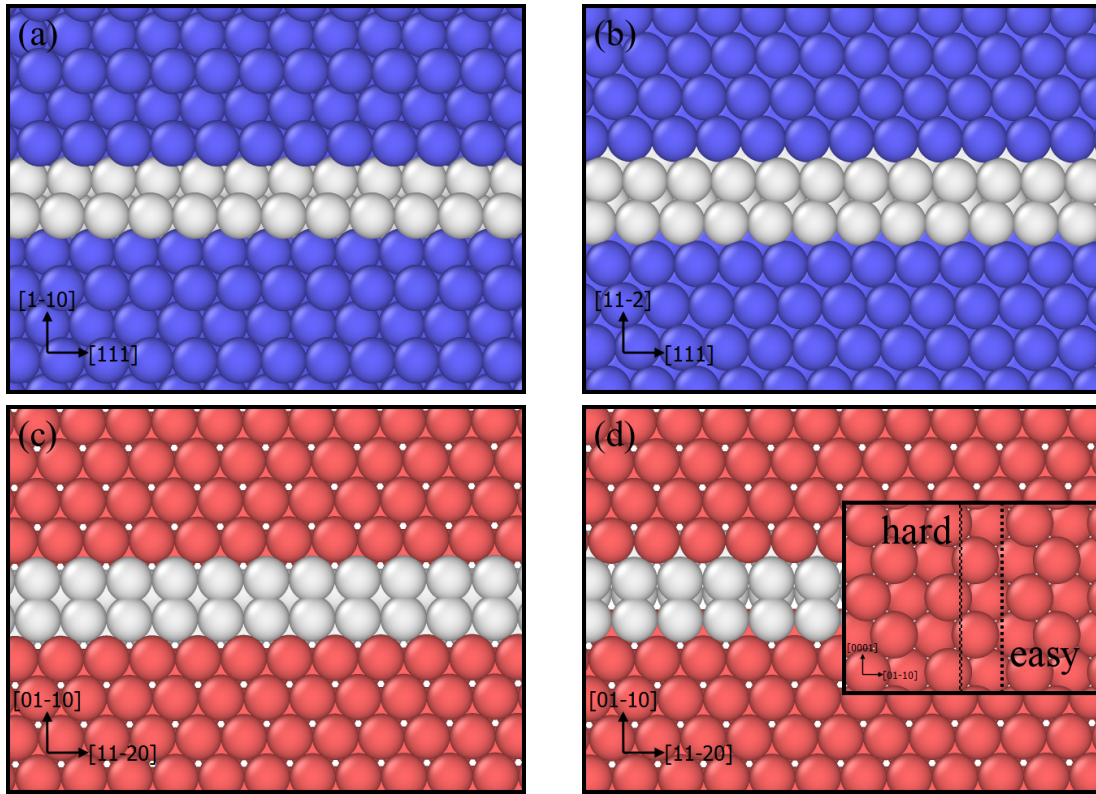


Figure 1.5: Geometries of low-index stacking faults considered in the present work. Body-centered cubic geometries shown for the (a)  $\{110\}\langle111\rangle$  and (b)  $\{112\}\langle111\rangle$  faults. The prismatic stacking fault of hcp is shown in (c) easy and (d) hard configurations, which correspond do a shift between different pairs of planes in the stacking sequence as shown in the inset of (d).

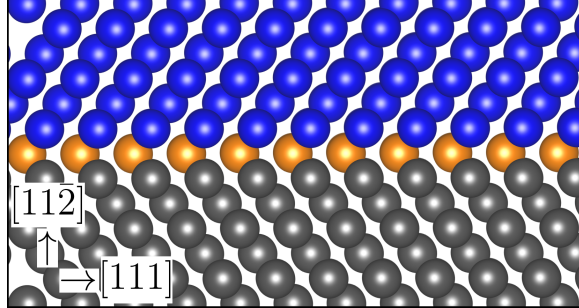


Figure 1.6:  $(11\bar{2})[111]$  twin in the bcc lattice. Base crystal atoms are shown in grey, twin atoms in blue and boundary atoms in orange. The formation of a twin corresponds to a reflection across the twin boundary  $(11\bar{2})$ , which creates an effective shear in the  $[111]$  direction.

tities: a *line-sense*  $\xi$  and a *burgers vector*  $\mathbf{b}$ . The line-sense specifies the direction in which the dislocation line points, while the burgers vector represents the direction and amount of distortion of the perfect crystal around the dislocation line.

The burgers vector is defined using the concept of a Burgers circuit, a sequence of primitive lattice vectors which defines closed circuit through a perfect crystal. Traversing the same path in a crystal which contains a dislocation *inside* the circuit will require one more displacement,  $\mathbf{b}$ , to return to the original lattice site. The Burgers circuit and Burgers vector are shown in Figure 1.5.5 by small and large arrows, respectively.

The orientation of unit vector  $\xi$  with respect to  $\mathbf{b}$  determines the *character* of the dislocation and thus the form of displacement caused by it. Figure 1.5.5 shows the two fundamental types of dislocation: edge (left), where  $\mathbf{b} \cdot \xi = 0$  and screw (right), where  $\mathbf{b} \times \xi = 0$ . Clearly, the displacement of the surrounding crystal is parallel to the burgers vector for screw dislocations and orthogonal to it for edge dislocations. Multiple burgers circuits around a screw dislocation will “spiral” up the lattice planes orthogonal to the line-sense. Contrarily, each successive Burgers circuit around an edge dislocation moves a sample point onto another lattice plane which is parallel

to the line-sense. In both cases this imagined motion is antiparallel to the Burgers vector.

Studying the structure of dislocations, both at the atomic level and microstructural level, is a major piece of materials science and metallurgy. Linear elasticity theory is used as a starting point for the understanding of this structure. For a screw dislocation, imagine a cylinder whose axis is aligned to the dislocation line sense and Burgers vector, taken to be along  $\hat{z}$ . Solving the continuum elasticity equations at equilibrium subject to the boundary conditions of discontinuity at the cut (placed on the positive  $x$ -axis):

$$\lim_{\epsilon \rightarrow 0} [u_z(x, \epsilon, t) - u_z(x, -\epsilon, t)] = b, \quad (1.38)$$

for  $x > 0$ , yields a displacement along the  $z$  direction given by

$$u_z^{screw}(x, y) = \frac{b}{2\pi} \tan^{-1} \left( \frac{y}{x} \right). \quad (1.39)$$

For an edge dislocation, leaving  $\xi$  along  $\hat{z}$  and placing  $\mathbf{b}$  along  $\hat{x}$ , the displacement components in the  $x - y$  plane can be shown to be:

$$\begin{aligned} u_x^{edge}(x, y) &= \frac{b}{2\pi} \left[ \tan^{-1} \left( \frac{y}{x} \right) + \frac{xy}{2(1-\nu)(x^2+y^2)} \right] \\ u_y^{edge}(x, y) &= -\frac{b}{2\pi} \left[ \frac{1-2\nu}{4(1-\nu)} \ln(x^2+y^2) + \frac{x^2-y^2}{4(1-\nu)(x^2+y^2)} \right], \end{aligned} \quad (1.40)$$

where  $\nu$  is the Poisson ratio and elastic isotropy has been assumed. Edge dislocations are clearly more complex, especially for anisotropic materials where these expressions are inaccurate even far from the core. These elasto-static solutions can be used as starting points for atomistic calculations of core structure, as will be discussed further in subsequent chapters where the issue of anisotropy will be avoided by considering only screw dislocations.

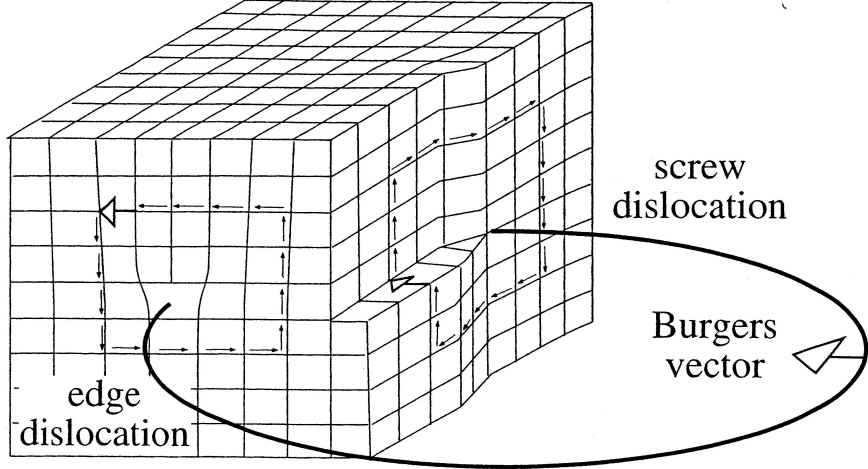


Figure 1.7: Schematic depiction of edge and screw dislocations in a single crystal. Large arrows represent the burgers vector  $\mathbf{b}$ . Small arrows represent the burgers circuit used to calculate  $\mathbf{b}$ . While the burgers vector for a particular dislocation is constant, the line sense vector  $\xi$  is tangent to the dislocation at all points. Figure adapted from Passchier and Trouw [45]

### Atomistic calculation of dislocation core structures

A variety of techniques exist for determining dislocation core structures from atomistic total-energy methods. In the present work such structures are only considered using classical molecular dynamics, enabling the use of large simulation cells. These cells are typically 100 lattice constants in dimension orthogonal to the burgers vector, with the dislocation running through the center. Periodic boundary conditions are only used parallel to the dislocation line. Atoms are displaced according to Equation 1.39 and a cylindrical region of  $\sim 40$  lattice parameters in radius, concentric with the dislocation, is relaxed to obtain the core structure.

### Differential displacement maps

Dislocation core structures are often visualized using so-called differential displacement maps of Vitek *et al.* [46]. Atoms are plotted in a plane whose normal vec-

tor is typically parallel to the dislocation line-sense and connected to neighbors by vectors. The magnitude and direction of vectors are determined by the *relative* displacement of atoms from their positions in the ideal crystal. Lengths are scaled such that the maximal relative displacement corresponds to a vector which touches both atoms. For ordinary dislocations, this maximal displacement occurs for those atoms nearest the core. A complete circuit of vectors arranged tail-to-tip must contain a total displacement of  $|\mathbf{b}|$  for ordinary dislocations or  $|\mathbf{b}/2|$  for partial dislocations in hcp. Differential displacement maps presented here were constructed using the utility DDPLT [47].

## 1.6 Statistical Mechanics

This section outlines the classical statistical mechanics as it relates to thermodynamics and molecular dynamics simulation.

Statistical mechanics connects the behavior of macroscopic systems with that of their atomic or molecular constituents by averaging over all possible combinations of microscopic states. The present development of statistical mechanics will follow the treatment of Tadmor and Miller[48].

Consider a general Hamiltonian which is dependent only on the positions  $q_i$  and momenta  $p_i$  of the constituent particles:

$$\mathcal{H} = \frac{1}{2} \sum_{i=1}^N \frac{p_i^2}{2m_i} + V(\{\mathbf{q}_i\}), \quad (1.41)$$

where  $V(\{\mathbf{q}_i\})$  is the total potential energy of the system. The set of positions and momenta, which instantaneous *microstate* of the system, are mutually coupled and time-dependent. In classical terms, the initial conditions determine the precise trajectory of the system in phase space. When one wants to measure some macroscopic

observable  $A$ , they generally cannot know the precise initial positions and momenta of every particle in the system. So, while in theory a value can be assigned to the macroscopic variable given the microscopic variables,  $A = A(\{\mathbf{q}_i\}, \{\mathbf{p}_i\})$ , a probabilistic approach must be taken to connect these values to an observation. The simplest approach is to take an average of  $A(\{\mathbf{q}_i\}, \{\mathbf{p}_i\})$  over all possible sets of positions and momenta. This is called the *phase average*, denoted by angle brackets (not to be confused with the expectation value from quantum mechanics). Henceforth a concatenated notation where  $(\{\mathbf{q}_i\}, \{\mathbf{p}_i\}) = (\mathbf{q}, \mathbf{p})$  is employed. If there are  $\Omega$  accessible microstates, the phase average of  $A$  is given by

$$\langle A \rangle = \frac{1}{\Omega} \sum_j^{\Omega} A(\mathbf{q}^j, \mathbf{p}^j). \quad (1.42)$$

Taking  $\Omega \rightarrow \infty$  will give us an integral in phase space, but one must be careful only to sample those microstates which are allowed by the externally applied constraints, e.g. finite temperature or volume. This is done through an integral kernel  $f(\mathbf{q}, \mathbf{p})$  which represents the probability density for the system to occupy the point in phase space at  $(\mathbf{q}, \mathbf{p})$ . Integrating over all of phase space must of course find every allowable initial condition. This produces the normalization condition for  $f$ :

$$\int f(\mathbf{q}, \mathbf{p}) d\mathbf{q} d\mathbf{p} = 1, \quad (1.43)$$

and the phase average is given by

$$\langle A \rangle = \int A(\mathbf{q}, \mathbf{p}) f(\mathbf{q}, \mathbf{p}) d\mathbf{q} d\mathbf{p}. \quad (1.44)$$

The form of the average (i.e. the distribution function) depends on the degrees of freedom of the system under consideration. There are three major averaging schemes,

or *ensembles*, that are discussed here: *microcanonical* (NVE), *canonical* (NVT) and *grand canonical* ( $\mu$ VT). The abbreviations refer to which macroscopic variables constrained to be constant and will be discussed further.

### 1.6.1 Microcanonical Ensemble

A system which in which the total energy  $E$ , volume  $V$  and number of particles  $N$  are fixed is referred to as a *microcanonical* or NVE ensemble. While the micro-state refers to the configuration of constituents (i.e. their instantaneous positions and momenta), the macro-state refers to the values of macroscopic thermodynamic quantities  $E$ ,  $V$  and  $N$ .

The microcanonical distribution function has a simple form that's manifest from the requirement of constant energy. If  $\mathcal{H}(\mathbf{q}, \mathbf{p})$  is the hamiltonian for a system of  $N$  particles, again where  $\mathbf{q} = \{\mathbf{q}_i\}$  and  $\mathbf{p} = \{\mathbf{p}_i\}$  are shorthand for all positions and momenta, integral kernel must pluck out those points in phase space where  $E = \mathcal{H}(\mathbf{q}, \mathbf{p})$ . By inspection,

$$f_{NVE}(\mathbf{q}, \mathbf{p}) = \frac{\delta(E - \mathcal{H}(\mathbf{q}, \mathbf{p}))}{\int \delta(E - \mathcal{H}(\mathbf{q}, \mathbf{p})) d\mathbf{q} d\mathbf{p}}, \quad (1.45)$$

where of course the denominator enforces the normalization condition. The most notable feature here is that all microstates are equally probable. Taking the energies  $E_i$  to be discrete, the average internal energy  $\mathcal{U} = \langle \mathcal{H} \rangle$  is given by

$$\mathcal{U} = \frac{1}{\mathcal{D}(E)} \int \mathcal{H}(\mathbf{q}, \mathbf{p}) \delta(E - \mathcal{H}(\mathbf{q}, \mathbf{p})) d\mathbf{q} d\mathbf{p}, \quad (1.46)$$

where the density of states  $\mathcal{D}(E)$  has been defined as the denominator of Equation 1.45, which has dimensions of  $(distance \times momentum)^{3N} / energy$ .  $\mathcal{D}(E)dE$  is a measure of the volume of accessible phase space for which  $\mathcal{H}(\mathbf{q}, \mathbf{p}) \in [E, E + dE]$ .

Both integrals can be easily performed; one finds  $\mathcal{D}(E) = \Omega$ , where  $\Omega$  is the number of discrete states, and

$$\mathcal{U} = \frac{1}{\Omega} \sum_i^{\Omega} E_i = \sum_i^{\Omega} p_i E_i. \quad (1.47)$$

The probability of a system occupying a particular micro-state  $i$  is given very simply for the NVE ensemble by  $p_i = 1/\Omega$ . This is an expression of the fundamental assumption of thermal physics: that a closed system is equally likely to be in any of the quantum states accessible to it.

Now consider an arbitrary division of a closed system into two subsystems,  $a$  and  $b$ , with number of particles  $N = N_a + N_b$  and internal energies related by  $E = E_a + E_b$ . If the systems cannot exchange particles, each will have a density of states given by its energy. The DOS of the entire system for a fixed value of  $E_a$  is given by the product  $\mathcal{D}_a(E_a)\mathcal{D}_b(E - E_a)$ . Since the value of  $E_a$  cannot be specified, all possible values must be summed over in order to obtain the complete DOS:

$$\mathcal{D}(E) = \int \mathcal{D}_a(E_a)\mathcal{D}_b(E - E_a)dE_a \quad (1.48)$$

Note that in general the DOS functions depend on the number of particles  $N_a$  and  $N_b$ , but this dependence won't be explicitly written. Since the total system is closed, there is one energy  $E_a$  (the equilibrium energy) which dominates the sum above. This energy can be located by maximizing the summand:

$$0 = \frac{\partial \mathcal{D}_a(E_a)}{\partial E_a} \mathcal{D}_b(E - E_a) + \mathcal{D}_a(E_a) \frac{\partial \mathcal{D}_b(E - E_a)}{\partial E_a}. \quad (1.49)$$

Noting that  $\frac{\partial \mathcal{D}_b(E - E_a)}{\partial E_a} = \frac{\partial \mathcal{D}_b(E - E_a)}{\partial(E - E_a)} \frac{\partial(E - E_a)}{\partial E_a} = -\frac{\partial \mathcal{D}_b(E_b)}{\partial E_b}$  and rearranging,

$$\frac{1}{\mathcal{D}_a(E_a)} \frac{\partial \mathcal{D}_a(E_a)}{\partial E_a} = \frac{1}{\mathcal{D}_b(E_b)} \frac{\partial \mathcal{D}_b(E_b)}{\partial E_b}. \quad (1.50)$$

Each side of this equilibrium condition has the form of a logarithmic derivative. This inspires the definition of “pure” entropy:  $\sigma = \ln \mathcal{D}(E)$ , so that

$$\left( \frac{\partial \sigma_a}{\partial E_a} \right) = \left( \frac{\partial \sigma_b}{\partial E_b} \right), \quad (1.51)$$

where the parenthesis indicate that other parameters ( $N$ ,  $V$ , etc.) are held constant.

The condition for equilibrium when two systems are allowed to exchange energy, but not particles, has been found. In common language, the systems have been placed in thermal contact. The equilibrium condition represents thermal equilibrium, where the temperatures must be equal. This gives us the definition of temperature:

$$\frac{1}{T} = k_B \left( \frac{\partial \sigma}{\partial E} \right). \quad (1.52)$$

The Boltzmann constant  $k_B$  is a historical artifact; temperature was measured in its own units before the foundational relationship of thermal physics and quantum mechanics was understood. In a pure sense, temperature has dimensions of energy and entropy is a dimensionless logarithmic measure of the number of accessible quantum states. Practically, temperature is given its own scale and entropy is given by  $S = k_B \ln \mathcal{D}(E)$ .

While the present approach is capable of dealing with the quantized nature of microscopic states, until now the real quantum nature of the particles themselves has been ignored. Indeed since  $\sigma = \ln \mathcal{D}(E)$  was defined based solely on the equality of *derivatives*, an integration constant has been tacitly ignored. This constant turns out to be related to the quantum nature of the particles considered here; a heuristic argument for its form is given below. A more detailed derivation can be found in

Penrose[49].

A many-body wavefunction for the  $N$  particles in our system are described at the quantum level by a wavefunction which, for indistinguishable particles, has some permutation symmetry. Permutations of these states yield identical (or exactly negated) quantum state with the same observable properties. There are  $N!$  permutations of  $N$  particles, and when every point  $(\mathbf{q}, \mathbf{p})$  in the many-particle phase space is summed over (again,  $\mathbf{q} = \{\mathbf{q}_i\}$ ), every state is counted  $N!$  times.

Furthermore, there is a fundamental unit of phase space prescribed by the Heisenberg uncertainty principle. This unit is commonly taken to be  $h^3$  for a single atom and  $h^{3N}$  for an  $N$ -particle system, where  $h$  is of course Planck's constant. Dividing this unit into the density of states ensures that states are counted per *quantum* unit volume. The correct form is thus given by

$$S = k_B \ln \frac{\mathcal{D}(E)}{N! h^{3N}}. \quad (1.53)$$

The quantity  $\sigma$  (and thus  $S$ ) has been derived by considering the equilibrium condition of two interacting systems in thermal equilibrium. A more general definition of entropy, accurate even far from thermal equilibrium, is called the Gibbs entropy:

$$\sigma = \sum_i p_i \ln p_i, \quad (1.54)$$

where  $p_i$  is the probability of state  $i$ .

Now, from the first law of thermodynamics

$$dU = TdS - PdV + \sum_j \mu_j dN_j, \quad (1.55)$$

which under the constraints of constant NVE becomes  $dU = -TdS$  so that the

internal energy of the system is directly determined by the number  $\Omega$  of microstates:

$$U = -k_B T \ln \Omega. \quad (1.56)$$

Expressions like this can be obtained for each ensemble, relating the logarithm of the partition function with a corresponding free energy. Each ensemble is based on our knowledge of the microcanonical ensemble. Systems are placed in contact (thermal, chemical, etc.) and the complete system, which is closed, is analyzed through the lens of the NVE. By assumption of relative size one can obtain the distribution functions satisfying our chosen external constraints, accurate when our system of interest is negligible in size (and thus all extensive variables) relative to the rest of the closed system, which is referred to as the *reservoir*. The most important ensembles to the present work are described in the sections that follow.

### 1.6.2 Canonical Ensemble

The so-called canonical ensemble treats a system at constant temperature, volume and particle count. This is commonly referred to in molecular dynamics literature as an NVT ensemble. The derivation for the canonical distribution function begins by considering two systems,  $a$  and  $b$ , which are in weak interaction with one another. Weak interaction here requires the total hamiltonian be approximately equal to the sum of hamiltonians for the constituent systems for all points in phase space:

$$\mathcal{H} \approx \mathcal{H}^a + \mathcal{H}^b. \quad (1.57)$$

If these systems only interacting with one another, the total hamiltonian  $\mathcal{H}$  must be conserved. Considering a phase function which depends only on *one* of the systems, say  $a$ , one can write the phase average of a quantity  $A$  as

$$\langle A \rangle = \int \frac{A(\mathbf{q}^a, \mathbf{p}^a) \delta(E - \mathcal{H}(\mathbf{q}^a, \mathbf{p}^a) - \mathcal{H}^b(\mathbf{q}^b, \mathbf{p}^b))}{\mathcal{D}^{a+b}(E)} d\mathbf{q} d\mathbf{p}, \quad (1.58)$$

where  $\mathcal{D}^{a+b}(E)$  is the total density of states:

$$\mathcal{D}^{a+b}(E) = \int \delta(E - \mathcal{H}(\mathbf{q}^a, \mathbf{p}^a) - \mathcal{H}^b(\mathbf{q}^b, \mathbf{p}^b)) d\mathbf{q}^a d\mathbf{p}^a d\mathbf{q}^b d\mathbf{p}^b. \quad (1.59)$$

Since  $A(\mathbf{q}^a, \mathbf{p}^a)$  is independent of  $\mathbf{q}^b$  and  $\mathbf{p}^b$ , the canonical distribution function can be defined as

$$\begin{aligned} f_{NVT}^a(\mathbf{q}^a, \mathbf{p}^a) &= \frac{1}{\mathcal{D}^{a+b}(E)} \int \delta(E - \mathcal{H}^a(\mathbf{q}^a, \mathbf{p}^a) - \mathcal{H}^b(\mathbf{q}^b, \mathbf{p}^b)) d\mathbf{q}^b d\mathbf{p}^b \\ &= \frac{1}{\mathcal{D}^{a+b}} \int \delta((E - E^a) - \mathcal{H}^b(\mathbf{q}^b, \mathbf{p}^b)) d\mathbf{q}^b d\mathbf{p}^b = \frac{\mathcal{D}^b(E - E^a)}{\mathcal{D}^{a+b}(E)} \end{aligned} \quad (1.60)$$

so that

$$\langle A \rangle = \int A(\mathbf{q}^a, \mathbf{p}^a) f_{NVT}^a(\mathbf{q}^a, \mathbf{p}^a) d\mathbf{q}^a d\mathbf{p}^a. \quad (1.61)$$

To obtain a functional form for  $f_{NVT}$ , system  $b$  is taken to be much, much larger than system  $a$  so that  $E \approx E^b \gg E^a$ . System  $b$  serves as a reservoir capable of exchanging an arbitrary amount of energy with system  $a$  in order to satisfy the constant-temperature constraint. In this case  $f_{NVT}^a$  can be simplified by expressing  $\mathcal{D}^b$  in terms of  $S^b$  through Equation 1.53 after multiplying and dividing by  $\mathcal{D}^b(E)$ . With a little foresight to convention the prefactor is defined  $(N!h^{3N}\mathcal{Z})^{-1} = \mathcal{D}^b(E)/\mathcal{D}^{a+b}(E)$ ,

which will be determined by the normalization condition. Now,

$$\begin{aligned} f_{NVT}^a(\mathbf{q}^a, \mathbf{p}^a) &= (N!h^{3N}\mathcal{Z})^{-1} \frac{\mathcal{D}^b(E - E_a)}{\mathcal{D}^b(E)} \\ &= (N!h^{3N}\mathcal{Z})^{-1} \exp \left[ (S^b(E - E^a) - S^b(E))/k_B \right], \end{aligned} \quad (1.62)$$

but since  $E^a \ll E$ ,  $S^b(E - E^a) - S^b(E) \approx \frac{\partial S^b(E^b)}{\partial E^b}|_{E^b=E} = 1/T^b$ , and  $E^a = \mathcal{H}^a(\mathbf{q}^a, \mathbf{p}^a)$  so that

$$f_{NVT}^a(\mathbf{q}^a, \mathbf{p}^a) = (N!h^{3N}\mathcal{Z})^{-1} \exp \left( -\frac{E^a}{k_B T^b} \right). \quad (1.63)$$

Dropping the subsystem labels and enforcing the normalization condition one finds an expression for the *canonical partition function*  $\mathcal{Z}$ :

$$\mathcal{Z} = \frac{1}{N!h^{3N}} \int \exp \left( -\frac{\mathcal{H}(\mathbf{q}, \mathbf{p})}{k_B T} \right) d\mathbf{q} d\mathbf{p}. \quad (1.64)$$

Finally, the NVT distribution function is given by

$$f_{NVT}(\mathbf{q}, \mathbf{p}) = \frac{1}{N!h^{3N}\mathcal{Z}} \int \exp \left( -\frac{\mathcal{H}(\mathbf{q}, \mathbf{p})}{k_B T} \right) d\mathbf{q} d\mathbf{p}. \quad (1.65)$$

If the energies  $E_i$  are taken to be discrete, the probability of a given state  $i$  being occupied is found to be

$$p_i = \frac{e^{-E_i/k_B T}}{\sum_j^\Omega e^{-E_j/k_B T}}. \quad (1.66)$$

The numerator here is known as the *Boltzmann factor* for the state  $i$ . Using the standard definition  $\beta = 1/k_B T$  and the Gibbs entropy one can obtain an expression

for the Helmholtz free energy  $\mathcal{F} = U - TS$  in terms of  $\mathcal{Z}$ :

$$\begin{aligned}
\mathcal{F} &= \sum_i^{\Omega} E_i p_i + k_B T \sum_i^{\Omega} p_i \ln(p_i) \\
&= \sum_i^{\Omega} \frac{1}{\beta} \frac{e^{-\beta E_i}}{\mathcal{Z}} \left( \beta E_i + \ln \frac{e^{-\beta E_i}}{\mathcal{Z}} \right) \\
&= -\frac{\ln \mathcal{Z}}{\beta \mathcal{Z}} \sum_i^{\Omega} e^{-\beta E_i} \\
&= -k_B T \ln \mathcal{Z}
\end{aligned} \tag{1.67}$$

### 1.6.3 NPT Ensemble

One of the most commonly used ensembles in MD simulations treats a system of constant temperature, particle number, and pressure. Such an ensemble is called *isothermal-isobaric* or NPT. The Boltzmann for a state being occupied must necessarily include the volume of the system in that state. The probability of a system occupying a state of energy  $E_i$  and volume  $V$  is given as

$$p_i = \frac{e^{-\beta(E_i+PV)}}{\Delta}, \tag{1.68}$$

where  $\Delta$  here is the thermodynamic partition function for the isothermal-isobaric ensemble, given by

$$\Delta = \sum_i^{\Omega} \int e^{-\beta(E_i+PV)} \delta_0 dV, \tag{1.69}$$

which is clearly related to the canonical partition function  $\mathcal{Z}$  by

$$\Delta = \int \mathcal{Z} e^{-\beta PV} \delta_0 dV. \tag{1.70}$$

Note that the normalization factor  $\delta_0$ , which is necessary to make  $\Delta$  dimensionless,

is not prescribed by theory and can be chosen to be any function of state variables that has units of inverse volume. While  $\Delta$  converges in the thermodynamic limit regardless of normalization, care should be taken when comparing NPT results between different MD software packages. This will be addressed more in the discussion of molecular dynamics.

#### 1.6.4 Other Ensembles

A more general ensemble treats a system with constant temperature and volume but variable particle number. In this case, the chemical potential  $\mu$  for each element is held constant. Such an ensemble is typically called a *grand canonical* or  $\mu$ VT ensemble. A term is introduced in the Boltzmann factor exponent which represents the chemical potential energy of a state  $i$ . The grand canonical partition function,  $\Xi$ , is given by the usual sum of Boltzmann exponentials:

$$\Xi = \sum_i^{\Omega} e^{-\beta(E_i - \mu N_i)} \quad (1.71)$$

It's easy to show, as was done for the canonical ensemble, that the partition function is related to the so-called *grand potential* or *Landau* free energy  $\mathcal{L}$ :

$$\mathcal{L} = \mathcal{F} - \mu N = -k_B T \ln \Xi. \quad (1.72)$$

As with the canonical ensemble, the grand canonical ensemble can be generalized to variable volume by instead fixing the pressure. This so-called  $\mu$ PT ensemble has partition function  $\Theta$ , given by

$$\Theta = \int \sum_i^{\Omega} e^{-\beta(E_i + PV - \mu N_i)} \theta_0 dV = \int \Xi e^{-\beta PV} \theta_0 dV, \quad (1.73)$$

a weighted average of the  $\mu$ VT partition function analogous to the relation between NVT and NPT ensembles. Like  $\delta_0$  in the canonical case,  $\theta_0$  is a normalization factor with units of inverse volume whose form is not uniquely prescribed by theory. One can easily show that the logarithm of  $\Theta$  is related to the Gibbs free energy  $G$ :

$$G = \mathcal{L} + PV = U - TS + PV - \mu N = -k_B T \ln \Theta. \quad (1.74)$$

While commonplace in simulations of chemical or biophysical reactions, neither the  $\mu$ VT nor  $\mu$ PT ensembles are used in any molecular dynamics simulations in the work presented here. More information on how the NVE, NVT and NPT statistical ensembles are used to perform simulations will be covered in Chapter 3.

## 1.7 Structural Phase Transitions

The nature of transitions from one crystal structure to another is of considerable interest in the present work. Pure titanium undergoes a transition from hexagonal close-packed to body-centered cubic at a temperature of 1155 K [50, 51, 52] and a transition from hcp to the  $\omega$ -Ti phase at high pressure [50, 53, 54, 55]. The hcp to bcc (or  $\alpha$  to  $\beta$ ) transition was measured by Petry *et al.*[56] to result from the entropy contribution of low-lying transverse phonon branches  $T_1[\xi\xi0]$  and  $T_1[\xi\xi2\xi]$  in the bcc lattice at high temperature. Furthermore, the stabilization of fcc tungsten has been proposed [57, 58, 20] and will be investigated further in the present work. This section describes the structures used to model the bcc $\leftrightarrow$ hcp, bcc $\leftrightarrow$  $\omega$ -Ti and bcc $\leftrightarrow$ fcc transformations.

### 1.7.1 bcc to hcp

The  $\alpha \leftrightarrow \beta$  transition is modeled in the present work using the Burgers [59] distortion. Two free parameters  $\lambda_1$  and  $\lambda_2$  control the motion of basis atoms and the shape of the unit cell. A structure in the Burgers path between hcp and bcc titanium is given by a four-atom orthorhombic cell with lattice vectors

$$A = (\mathbf{a}_1, \mathbf{a}_2, \mathbf{a}_3) = a \begin{bmatrix} \frac{1}{\alpha(\lambda_1)} & 0 & 0 \\ 0 & \sqrt{2}\alpha(\lambda_1) & 0 \\ 0 & 0 & \sqrt{2} \end{bmatrix} \quad (1.75)$$

and basis atoms in direct coordinates

$$\begin{aligned} \mathbf{B}_1 &= [0, 0, 0] \\ \mathbf{B}_2 &= \left[ \frac{1}{2}, \frac{1}{2}, 0 \right] \\ \mathbf{B}_3 &= \left[ \frac{1}{2}, \left(1 - \frac{3 + \lambda_2}{6}\right), 0 \right] \\ \mathbf{B}_4 &= \left[ 0, \left(\frac{1}{2} - \frac{3 + \lambda_2}{6}\right), \frac{1}{2} \right] \end{aligned} \quad (1.76)$$

where  $\alpha(\lambda_1) = 1 + \left[\left(\frac{3}{2}\right)^{(1/4)} - 1\right]\lambda_1$ . Here,  $\lambda_1 = \lambda_2 = 1$  corresponds to the hcp lattice while  $\lambda_1 = \lambda_2 = 0$  corresponds to bcc. The  $c/a$  ratio at  $\lambda_1 = 1$  is  $6^{(1/4)} = 1.565$ , very close to the experimental value of 1.586.

In titanium alloys containing niobium, the hcp  $\alpha$  phase is distorted into an orthorhombic phase named  $\alpha''$ . One can think of this distortion in terms of niobium “pulling” the  $\alpha$  phase along a Burgers-like transition toward the bcc phase. To de-

scribe  $\alpha''$  and its relation to bcc, the above equations are generalized as follows:

$$A = a \begin{bmatrix} 1 & 0 & 0 \\ 0 & b/a & 0 \\ 0 & 0 & c/a \end{bmatrix} \quad (1.77)$$

and

$$\begin{aligned} \mathbf{B}_1 &= [0, 0, 0] \\ \mathbf{B}_2 &= \left[ \frac{1}{2}, \frac{1}{2}, 0 \right] \\ \mathbf{B}_3 &= \left[ \frac{1}{2}, (1 - 2y), 0 \right] \\ \mathbf{B}_4 &= \left[ 0, \left( \frac{1}{2} - 2y \right), \frac{1}{2} \right] \end{aligned} \quad (1.78)$$

where clearly  $y = \frac{3+\lambda_2}{12}$ , which is the formulation given by Nishitani *et al.* [50], but the lattice ratios  $b/a$  and  $c/a$  can now be adjusted to fit any general orthorhombic cell. The bcc structure is obtained by setting  $b/a = c/a = \sqrt{2}$  and  $y = 1/4$  while hcp corresponds to  $b/a = \sqrt{3}$ ,  $c/a = (c/a)_{hcp}$  and  $y = 1/6$ . This structure is used to describe the  $\alpha \leftrightarrow \beta$  and  $\alpha'' \leftrightarrow \beta$  transitions in Ti and  $Ti_3Nb$ , respectively, in Chapter 6. A schematic representation of how the cell is used to map bcc to hcp is shown in Figure 1.7.1.

### 1.7.2 bcc to fcc

The body-centered cubic and face-centered cubic structures each contain a tetragonal modification of the other as illustrated in Figure 1.7.2. There are a number of methods to transform from bcc to fcc and vice versa but the present work employs the Bain [60] path, wherein the lattice parameter and axial ratio are changed in a linear fashion.

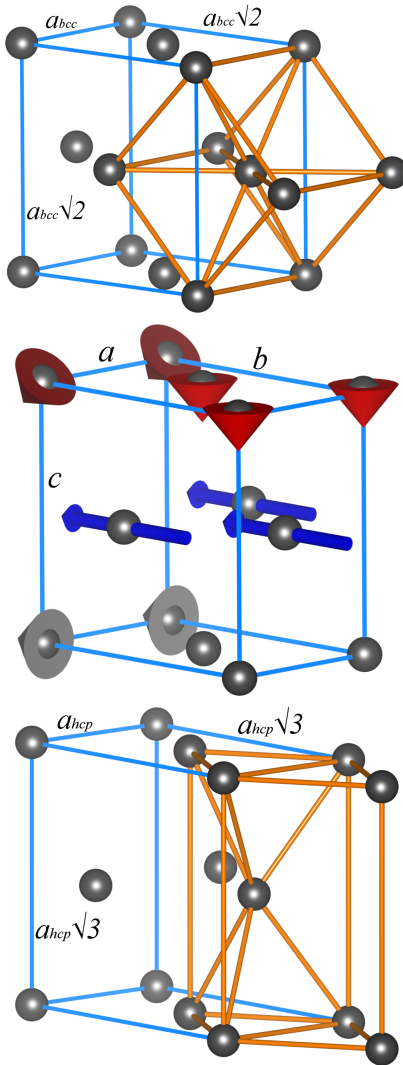


Figure 1.8: Schematic representation of the burgers transition mechanism in an orthorhombic unit cell. (Top) the standard bcc cell with bonds shown in orange inscribed in the orthorhombic (ort.) cell with  $b/a = c/a = \sqrt{2}$ . (Center) transitioning to hcp involves a “shuffle” of atoms in a  $\langle 1\bar{1}0 \rangle_\beta || \langle 11\bar{2}0 \rangle_\alpha || \langle 010 \rangle_{ort}$ . direction indicated by the blue arrows. Cones represent a change in the ort. box dimensions in the indicated direction. Atoms are treated in direct coordinates, so their cartesian positions change with “shear” in addition to “shuffle.” (Bottom) the standard hcp cell with bonds shown in orange inscribed in an ort. cell with  $b/a = \sqrt{3}$  and  $c/a = (c/a)_{hcp}$ .

At low pressure the two must be considered independent of one another, but at high pressure the minimum-energy transition path approximately collinear.

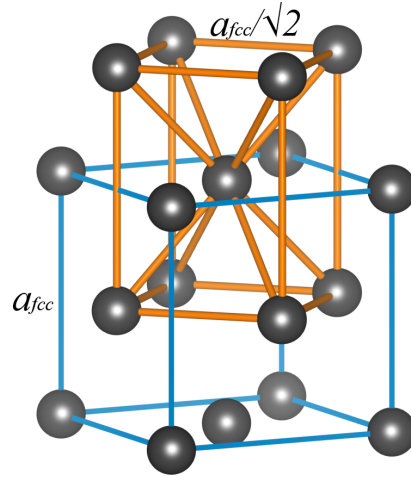


Figure 1.9: Schematic relationship between face-centered cubic (blue) and body-centered tetragonal (bct) (orange). A two-atom bct cell can be used to describe fcc, and can be easily transformed to bcc by changing the axial ratio from  $\sqrt{2}$  to unity.

A body-centered tetragonal cell is employed with variable  $c/a$  ratio:

$$A = (\mathbf{a}_1, \mathbf{a}_2, \mathbf{a}_3)$$

$$= a \begin{bmatrix} 1 & 0 & 0 \\ 0 & 1 & 0 \\ 0 & 0 & c/a \end{bmatrix} \quad (1.79)$$

with basis atoms at  $[0, 0, 0]$  and  $[\frac{1}{2}, \frac{1}{2}, \frac{1}{2}]$ . Here  $c/a = \sqrt{2}$  and  $a = a_{fcc}$  produces a face-centered cubic structure and  $c/a = 1$  with  $a = a_{bcc}$  of course produces bcc.

### 1.7.3 bcc to $\omega$ -Ti

Formation of the  $\omega$  phase of titanium has important ramifications for bulk material properties. The  $\omega$  phase is closely related to the bcc lattice and results from insta-

bilities [61] therein. In titanium and zirconium, where the bcc phase is not stable at room temperature, a calculation of phonon band structures reveals unstable eigenmodes for the longitudinal branch centered around the  $\frac{2}{3}[111]$  point in  $\mathbf{k}$ -space. Such a phonon corresponds precisely to a collapse of two adjacent  $\{111\}_{bcc}$  planes, leaving every third plane unchanged. These collapsed planes become the honeycomb layers of  $\omega$ -Ti, i.e.  $\{111\}_{bcc}||\{0001\}_\omega$ . A simple hexagonal cell can be used to model this transformation:

$$A = (\mathbf{a}_1, \mathbf{a}_2, \mathbf{a}_3) = a \begin{bmatrix} 1 & \frac{1}{2} & 0 \\ 0 & \frac{\sqrt{3}}{2} & 0 \\ 0 & 0 & c/a \end{bmatrix} \quad (1.80)$$

with three basis atoms given in direct coordinates by

$$\begin{aligned} \mathbf{B}_1 &= [0, 0, 0] \\ \mathbf{B}_2 &= \left[ \frac{1}{3}, \frac{1}{3}, \frac{1}{3} + \frac{\xi}{6} \right] \\ \mathbf{B}_3 &= \left[ \frac{2}{3}, \frac{2}{3}, \frac{2}{3} - \frac{\xi}{6} \right], \end{aligned} \quad (1.81)$$

where  $\xi = 0$  yields the bcc structure and  $\xi = 1$  produces  $\omega$ -Ti. The lattice parameters of the hexagonal structure in terms of the cubic bcc cell are  $a = a_\beta\sqrt{2}$ , and  $c = a_\beta\sqrt{3}/2$ , thus the axial ratio in the hexagonal representation has the ideal value  $c/a = \sqrt{3/8}$ .

The lattice parameters of  $\omega$ -Ti are commensurate as a result of the structural similarity of the two phases. In titanium  $a_\omega = 4.58$  Å and  $a_\beta\sqrt{2} = 4.60$  Å, however the equilibrium  $c/a$  ratio of  $\omega$  differs slightly from the ideal value. When calculating the transition energy, the overall lattice constant is taken as an average of the appropriate

values from the two phases and the axial ratio is mapped as a linear function of  $\xi$ . A schematic of this transformation is shown in Figure 1.7.3.

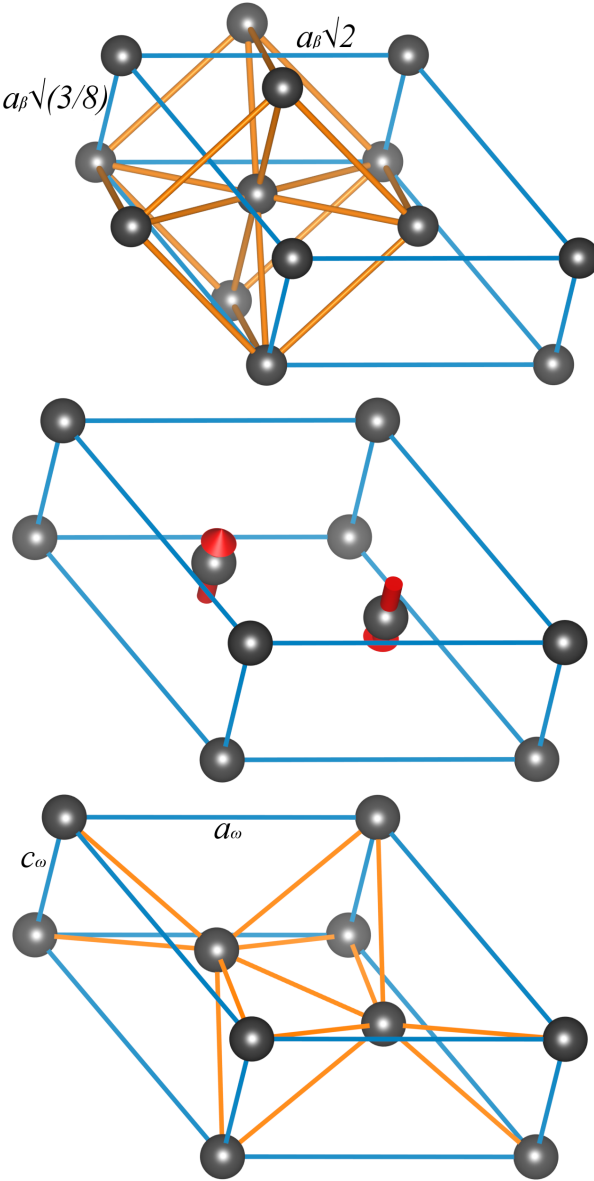


Figure 1.10: Schematic representation of the hexagonal cell used to transform bcc into  $\omega$ -Ti. (Top) a hexagonal representation of bcc with the standard cell inscribed with orange bonds. (Center) atoms in the  $\{111\}$  planes at  $c/3$  and  $2c/3$  collapse toward  $c/2$  to form the honeycomb layers of  $\omega$ . (Bottom) the hexagonal  $\omega$ -Ti structure is shown with bonds connecting to honeycomb atoms shown in orange.

# Chapter 2:

## Density Functional Theory

Density functional theory (DFT) calculates electronic structure in chemical and condensed-matter systems. While frequently referred to as “*ab initio*,” or “from first principles,” practical DFT necessarily involves an approximation to the so called *exchange-correlation energy*, a term in the hamiltonian which contains the quantum pieces of the electron-electron interaction. Despite this mis-characterization, or perhaps because of it, DFT is one of the most widely-used electronic structure methods and can be reliably used for calculations of transition metals and alloys if care is taken to ensure convergence with respect to input parameters.

In 2.1 the basic tenants of DFT as used in this work are reviewed. In 2.2.1 the various levels of approximation made to the energy functional are discussed. In 2.3 the implementation for planewave-DFT in metals is outlined and a procedure for ensuring convergence is presented.

## 2.1 The Schrödinger Equation in Condensed Matter

As with all electronic structure methods, the primary objective of DFT is to solve the  $N_Z$ -atom,  $N$ -electron Schrödinger equation, that is, to diagonalize the hamiltonian

$$H^{(N)} = T^{(N)} + V^{(N)}, \quad (2.1)$$

where  $T^{(N)}$  is the kinetic energy operator of the atoms and electrons:

$$T^{(N)} = \sum_{I=1}^{N_Z} \left( \frac{P_I^2}{2M_I} + \sum_{i=1}^{n_I} \frac{p_i^2}{2m} \right) = \sum_{I=1}^{N_Z} \frac{P_I^2}{2M_I} + \sum_{i=1}^N \frac{p_i^2}{2m}. \quad (2.2)$$

Here,  $M_I$  is the mass of atom  $I$ 's nucleus,  $m$  is the electron mass, and  $n_I$  is the number of electrons contributed by atom  $I$ . The system is assumed to be composed of neutral atoms such that  $n_I$  is also the atomic number of atom  $I$ . The potential energy necessarily includes the ion-ion ( $Z-Z$ ), ion-electron ( $Z-e$ ) and electron-electron ( $e-e$ ) interactions:

$$\begin{aligned} V^{(N)} &= V_{Z-Z}^{(N)} + V_{Z-e}^{(N)} + V_{e-e}^{(N)} \\ &= \frac{1}{2} \sum_{I=1}^{N_Z} \sum_{J \neq I}^{N_Z} \frac{n_I n_J}{|\mathbf{R}_J - \mathbf{R}_I|} - \sum_{I=1}^{N_Z} \sum_{i=1}^N \frac{n_I}{|\hat{\mathbf{r}}_i - \mathbf{R}_I|} + \frac{1}{2} \sum_{i=1}^N \sum_{j \neq i}^N \frac{1}{|\hat{\mathbf{r}}_i - \hat{\mathbf{r}}_j|}, \end{aligned} \quad (2.3)$$

where the Hartree units for which  $e = \hbar = m = 4\pi\epsilon_0 = 1$  are used.

Before solving Equation 2.1, first consider the motion of ions and electrons. The nuclear mass  $M_I$  is roughly 1,000 times greater than the electron mass  $m$ . This means given the same force, electrons are accelerated 1,000 times more than ions. Electrons are able to rapidly adjust to changes in ionic configuration while changes in electronic

structure are adjusted to very slowly by the ions. One can therefore assume that the ionic and electronic motions are dynamically decoupled and that the electrons remain in the ground state at all times for any reasonable (thermal or mechanical) ionic motion. This approximation is known as the *adiabatic*, or *Born-Oppenheimer*, approximation.

In the adiabatic approximation the ionic and electronic portions of the crystal hamiltonian can be separated; the electronic part, dubbed  $\mathcal{H}^{(N)}$ , is given in Hartree units by

$$\mathcal{H}^{(N)} = \sum_{i=1}^N \frac{\hat{p}_i^2}{2} - \sum_{I=1}^{N_Z} \sum_{i=1}^N \frac{n_I}{|\hat{\mathbf{r}}_i - \mathbf{R}_I|} + \frac{1}{2} \sum_{i=1}^N \sum_{j \neq i}^N \frac{1}{|\hat{\mathbf{r}}_i - \hat{\mathbf{r}}_j|}, \quad (2.4)$$

which in the  $\mathbf{r}$ -basis becomes

$$\mathcal{H}^{(N)} = -\frac{1}{2} \sum_{i=1}^N \nabla_i^2 - \sum_{I=1}^{N_Z} \sum_{i=1}^N \frac{n_I}{|\mathbf{r}_i - \mathbf{R}_I|} + \frac{1}{2} \sum_{i=1}^N \sum_{j \neq i}^N \frac{1}{|\mathbf{r}_i - \mathbf{r}_j|}, \quad (2.5)$$

where  $\nabla_i^2$  is the laplacian for the coordinates of electron  $i$ . Equation 2.5 contains all the complexity of the electronic structure in a crystal. There are many approaches to solving the electronic Schrödinger equation

$$\mathcal{H}^{(N)} |\Psi\rangle = E^{(N)} |\Psi\rangle, \quad (2.6)$$

with or without approximation. Here take the approach of DFT, which treats the charge density  $\rho(\mathbf{r})$  representing the many-body wavefunction  $\Psi(\{\mathbf{r}_i; \sigma_i\})$  as the fundamental quantity:

$$\rho(\mathbf{r}_1) = N \sum_{\sigma_i} \int |\Psi(\{\mathbf{r}_i; \sigma_i\})|^2 d\mathbf{r}_2 d\mathbf{r}_3 \cdots d\mathbf{r}_N. \quad (2.7)$$

Given the antisymmetry of any wavefunction for indistinguishable fermions, Equation

2.7 represents the density of electrons no matter which  $N - 1$  positions are integrated over.

Now examine the total energy of the (normalized) ground state:

$$\begin{aligned} E^{(N)} &= \langle \Psi | \mathcal{H}_N | \Psi \rangle \\ &= \langle \Psi | -\frac{1}{2} \sum_{i=1}^N \nabla_i^2 | \Psi \rangle + \langle \Psi | V_{Z-e}^{(N)} | \Psi \rangle + \langle \Psi | V_{e-e}^{(N)} | \Psi \rangle. \end{aligned} \quad (2.8)$$

The first term is the full kinetic energy operator  $\mathcal{T}^{(N)}$  of the  $N$  electrons. Without further assumptions on the form of the wavefunction, no simplifications can be done. The second term is the potential energy due to the lattice ions and takes a simple form:

$$\begin{aligned} \langle \Psi | V_{Z-e}^{(N)} | \Psi \rangle &= \langle \Psi | -\sum_{I=1}^{N_Z} \sum_{i=1}^N \frac{n_I}{|\hat{\mathbf{r}}_i - \mathbf{R}_I|} | \Psi \rangle \\ &= \sum_j \sum_{\sigma_j} \int \sum_{I=1}^{N_Z} \sum_{i=1}^N \frac{-n_I \langle \Psi | \{ \mathbf{r}_j; \sigma_j \} \rangle \langle \{ \mathbf{r}_j; \sigma_j \} | \Psi \rangle}{|\mathbf{r}_i - \mathbf{R}_I|} d\mathbf{r}_1 \cdots d\mathbf{r}_N, \end{aligned} \quad (2.9)$$

where a complete set of states  $|\{ \mathbf{r}_j; \sigma_j \}\rangle$  has been inserted. Notice that for each  $i$  in the summation, the  $N - 1$  integrals over  $\mathbf{r}_j$  for  $j \neq i$  can be performed. Thus from equation 2.7 the ion-electron potential can be written

$$\begin{aligned} \langle \Psi | V_{Z-e}^{(N)} | \Psi \rangle &= E_{Z-e}^{(N)} [\rho(\mathbf{r})] = \sum_{I=1}^{N_Z} \sum_{i=1}^N \int \frac{-n_I \rho(\mathbf{r}_i)/N}{|\mathbf{r}_i - \mathbf{R}_I|} d\mathbf{r}_i \\ &= - \int \sum_{I=1}^{N_Z} \frac{n_I \rho(\mathbf{r})}{|\mathbf{r} - \mathbf{R}_I|} d\mathbf{r}, \end{aligned} \quad (2.10)$$

which is exactly the form of the classical electrostatic potential energy between a negative charge distribution  $\rho(\mathbf{r})$  with discrete point charges  $n_I$  at positions  $\mathbf{R}_I$ . The kernel of this integral is a simple function of  $\mathbf{r}$  which is given the symbol  $v_{Z-e}(\mathbf{r})$ :

$$v_{Z-e}(\mathbf{r}) = - \sum_{I=1}^{N_Z} \frac{n_I}{|\mathbf{r} - \mathbf{R}_I|} \quad (2.11)$$

such that

$$E_{Z-e}^{(N)}[\rho(\mathbf{r})] = \int v_{Z-e}(\mathbf{r})\rho(\mathbf{r})d\mathbf{r}. \quad (2.12)$$

The periodicity of  $v_{Z-e}(\mathbf{r})$  has an important effect on the electronic wavefunctions known as Bloch's theorem, which states that the eigenstates of Equation 2.6 can be written as a linear combination of functions known as Bloch waves (BW). A Bloch wave is given by a planewave defined by wavevector  $\mathbf{k}$  and an envelope  $u(\mathbf{r})$ :

$$\chi_{\mathbf{k}}^{BW}(\mathbf{r}) = e^{i\mathbf{k}\cdot\mathbf{r}}u_n(\mathbf{r}) \quad (2.13)$$

where the envelope satisfies  $u(\mathbf{r} + \mathbf{R}) = u(\mathbf{r})$  for any lattice vector  $\mathbf{R}$ . This is our first sign that the eigenstates of a crystal are crucially described in reciprocal space. The lattice periodicity of  $u$  allows any point  $\mathbf{k}'$  in  $\mathbf{k}$ -space to be remapped into the first Brillouin zone by letting  $\mathbf{k}' = \mathbf{k} + \mathbf{K}_n$  where  $\mathbf{K}_n$  is the reciprocal lattice vector nearest to  $\mathbf{k}'$ . The planewave  $e^{i\mathbf{K}_n\cdot\mathbf{r}}$  thus has the same periodicity as  $u(\mathbf{r})$ , and the band index  $n$  is defined such that  $u_n(\mathbf{r}) = e^{i\mathbf{K}_n\cdot\mathbf{r}}u(\mathbf{r})$  or

$$\chi_{n\mathbf{k}}^{BW}(\mathbf{r}) = e^{i\mathbf{k}\cdot\mathbf{r}}u_n(\mathbf{r}). \quad (2.14)$$

Bloch waves are the cornerstone of band theory and elucidate the necessity of the reciprocal lattice in describing wavefunctions in crystals. The dependence of  $\Psi$  on  $\mathbf{k}$  will be suppressed for now, and returned to when discussing the practical implementation of DFT in Section 2.3.

The electron-electron interaction potential contains many of the significant quantum complexities owing to the two-body operator  $|\mathbf{r}_i - \mathbf{r}_j|$ .  $V_{e-e}^{(N)}$  cannot be simply

expressed in terms of the total density alone. This can be seen simply by enforcing anti-symmetry in the full wavefunction  $|\Psi\rangle$  through the ansatz

$$\langle\{\mathbf{r}_i; \sigma_i\}|\Psi\rangle = \Psi(\{\mathbf{r}_i; \sigma_i\}) = \frac{1}{\sqrt{N!}} \begin{vmatrix} \psi_1(\mathbf{r}_1; \sigma_1) & \psi_2(\mathbf{r}_1; \sigma_1) & \cdots & \psi_N(\mathbf{r}_1; \sigma_1) \\ \psi_1(\mathbf{r}_2; \sigma_2) & \psi_2(\mathbf{r}_2; \sigma_2) & \cdots & \psi_N(\mathbf{r}_2; \sigma_2) \\ \vdots & \vdots & \ddots & \vdots \\ \psi_1(\mathbf{r}_N; \sigma_N) & \psi_2(\mathbf{r}_N; \sigma_N) & \cdots & \psi_N(\mathbf{r}_N; \sigma_N) \end{vmatrix}, \quad (2.15)$$

where the  $\psi_i$  are mutually orthonormal single-particle states. Note that for now the notational complications arising from the electron spin states have been ignored. This form, called a *Slater determinant*, ensures mathematically that exchanging any two electrons will produce an over-all minus sign in the  $N$ -electron wavefunction  $|\Psi\rangle$  consistent with Fermi-Dirac statistics. The prefactor  $1/\sqrt{N!}$  ensures normalization of the full wavefunction:

$$\int |\Psi(\{\mathbf{r}_i; \sigma_i\})|^2 d\mathbf{r}_1 d\mathbf{r}_2 \cdots d\mathbf{r}_N = 1. \quad (2.16)$$

Using a Slater determinant wavefunction in Equation 2.6 and a single-particle form for the kinetic energy leads to the Hartree-Fock (HF) theory, which has two distinct terms in the interaction potential [62] (dropping the  $\sigma$ -dependence of  $\psi$  for clarity)

$$V_{e-e}^{HF} = \frac{1}{2} \sum_{i,j} \int \frac{\psi_i^*(\mathbf{r})\psi_j^*(\mathbf{r}')\psi_i(\mathbf{r})\psi_j(\mathbf{r}')}{|\mathbf{r} - \mathbf{r}'|} d\mathbf{r} d\mathbf{r}' - \frac{1}{2} \sum_{i,j} \delta_{\sigma_i \sigma_j} \int \frac{\psi_i^*(\mathbf{r})\psi_j^*(\mathbf{r}')\psi_j(\mathbf{r})\psi_i(\mathbf{r}')}{|\mathbf{r} - \mathbf{r}'|} d\mathbf{r} d\mathbf{r}'. \quad (2.17)$$

The first is called the *Hartree* energy, and can be interpreted as the electrostatic self-energy of the electron cloud. The second term, known as the *exchange* energy or *Fock* energy, represents the energetic effect of maintaining orthogonality of the

electron states as they interact through the coulomb potential. It serves to lower the total energy by keeping electrons of like spin spatially separated [63]. The *correlation energy* can be defined precisely as the difference between the exact energy and the Hartree-Fock energy.

Note that the Hartree energy can be expressed as a *local* operator and represented by an integral kernel  $v_H(\mathbf{r})$  called the Hartree potential:

$$E_H = \frac{1}{2} \sum_{i,j} \int \frac{\psi_i^*(\mathbf{r})\psi_j^*(\mathbf{r}')\psi_i(\mathbf{r})\psi_j(\mathbf{r}')}{|\mathbf{r} - \mathbf{r}'|} d\mathbf{r}d\mathbf{r}' = \frac{1}{2} \int \frac{\rho(\mathbf{r})\rho(\mathbf{r}')}{|\mathbf{r} - \mathbf{r}'|} d\mathbf{r}d\mathbf{r}' = \frac{1}{2} \int \rho(\mathbf{r})v_H(\mathbf{r})d\mathbf{r}, \quad (2.18)$$

but no such simplification can be performed for the exchange energy. An operator which cannot be represented as such a kernel integrated over the density is called a *non-local* operator, and complicates the typical self-consistency scheme of DFT for reasons addressed in the next section.

## 2.2 The Kohn-Sham Method

The Fock exchange is impractical for use in DFT, but one can still proceed with taking  $\Psi(\{\mathbf{r}_i; \sigma_i\})$  to be a Slater determinant of single-particle orbitals  $\psi_i(\mathbf{r}_i; \sigma_i)$ . Let the spatial component of the wavefunction be  $\phi_i(\mathbf{r}_j)$  and the spin component be  $\alpha_s(\sigma_j)$  such that  $\psi_{is}(\mathbf{r}_j; \sigma_j) = \alpha_s(\sigma_j)\phi_i(\mathbf{r}_j)$ . The subscript  $s$  here represents spin-up or spin-down, so for every spatial orbital  $\phi$  there are two single-particle states  $\psi$ ; one corresponding to  $s = \uparrow$  and one to  $s = \downarrow$ . The index  $i$  thus runs not to  $N$  but to  $N/2$  or  $(N + 1)/2$ , depending on whether  $N$  is even or odd. Henceforth the sum is be over the single-particle spatial orbitals and an occupation number  $f_\mu$  is used to do the spin-bookkeeping.

The total density is written in terms of the single-particle orbitals as

$$\begin{aligned}
\rho(\mathbf{r}) &= \rho(\mathbf{r}_1) = N \int \sum_{\sigma_i} |\Psi(\{\mathbf{r}_i; \sigma_i\})|^2 d\mathbf{r}_2 \cdots d\mathbf{r}_N \\
&= \sum_i \sum_{\sigma_i} |\psi_{is}(\mathbf{r}; \sigma_i)|^2 \\
&= \sum_i \sum_s \sum_{\sigma_i} |\alpha_s(\sigma_i)|^2 |\phi_i(\mathbf{r})|^2 \\
&\equiv \sum_{\mu} f_{\mu} |\phi_{\mu}(\mathbf{r})|^2.
\end{aligned} \tag{2.19}$$

The second line follows from the orthonormality of the spin and spatial components of the  $\psi_i$ . The sum over occupied orbitals is then changed to a sum over the entire set of single-particle orbitals by in the last line using the occupation numbers  $f_{\mu}$ . The index is changed from  $i$  to  $\mu$  to emphasize the change in summation from electrons to single-particle orbitals.

Note that  $|\alpha_s(\sigma_i)|^2 = 1$  for all  $\sigma_i = \pm 1$ , so one might expect  $f_{\mu}$  to take an integer value between 0 and 2. In practice, however, a “smearing” of the density of states is often used to speed up calculations as discussed later. In metals, since the fermi energy lies in the conduction band where the density of states is nonzero, a basis set containing more single-electron orbitals than  $N/2$  or  $(N+1)/2$  is required to accurately describe the highest-lying eigenstates. This is due to the partial occupancy of states above the chemical potential resulting from smearing.

The antisymmetry of the many-electron state has been guaranteed, and a useful description of the density has been obtained, but as of yet there is no way of computing the orbitals  $\phi_{\mu}$ . Kohn and Sham[64] addressed this by starting with the variational principle for the electronic hamiltonian

$$\min_{\Psi} \frac{\langle \Psi | \mathcal{T} + V_{e-e} + V_{Z-e} | \Psi \rangle}{\langle \Psi | \Psi \rangle} = E_0, \tag{2.20}$$

where minimization is respect to the full wavefunction  $\Psi$ .

Take the density  $\rho(\mathbf{r})$  to be continuous and non-negative such that it can be represented by an  $N$ -electron wavefunction through the first line of Equation 2.7. Then since  $V_{Z-e}$  is an exact local operator it is fixed by this choice and the determination of  $\mathcal{T}$  and  $V_{e-e}$  amounts to a minimization of their sum under the constraint of fixed density. This defines a functional

$$F[\rho(\mathbf{r})] = \min_{\Psi \rightarrow \rho(\mathbf{r})} \langle \Psi | \mathcal{T} + V_{e-e} | \Psi \rangle = \mathcal{T}[\rho(\mathbf{r})] + V_{e-e}[\rho(\mathbf{r})] \quad (2.21)$$

such that

$$E[\rho(\mathbf{r})] = F[\rho(\mathbf{r})] + V_{e-Z}[\rho(\mathbf{r})], \quad (2.22)$$

and if  $\rho_0(\mathbf{r})$  is the ground-state density then  $E_0 = E[\rho_0(\mathbf{r})]$ . The variational principle has been expressed as an optimization problem with respect to the density, but the difficult work has been swept into the problem of finding the wavefunction  $\Psi$  which actually determines  $F[\rho(\mathbf{r})]$ . Neither term in  $F$  can be simply expressed using the total density, so the quantities  $\mathcal{T}_s$  and  $E_{xc}$  are defined such that

$$F[\rho(\mathbf{r})] = \mathcal{T}_s[\rho(\mathbf{r})] + E_H[\rho(\mathbf{r})] + E_{xc}[\rho(\mathbf{r})], \quad (2.23)$$

where  $E_H[\rho(\mathbf{r})]$  is the Hartree energy for density  $\rho(\mathbf{r})$ .  $\mathcal{T}_s$  is interpreted as that portion of the kinetic energy which can expressed using our single-particle orbitals

$$\mathcal{T}_s = -\frac{1}{2} \sum_{\mu} f_{\mu} \int \phi_{\mu}^*(\mathbf{r}) \nabla^2 \phi_{\mu}(\mathbf{r}) d\mathbf{r}. \quad (2.24)$$

The difference  $\mathcal{T} - \mathcal{T}_s$  represents the *many-body* effects on the kinetic energy of the N-electron system. This is one source of electron correlations, the other being

the electron-electron potential. These correlations have been swept into the so-called exchange-correlation functional  $E_{xc}[\rho(\mathbf{r})]$ . No real progress has been made in finding a solution to the many-body Schrödinger equation, but no approximations either have been made either. It can be proven [64] that there exists a functional  $E_{xc}$  which produces the exact many-body ground state energy, but the proof provides no form and the evaluation of such a functional must be at least as difficult as a direct solution to the full Schrödinger equation. What has truly been accomplished is to collect the quantum complexity of the interacting system into a single quantity which can be approximated to various degrees.

Next the quantity  $v_{xc}(\mathbf{r})$  is defined as the functional derivative of the exchange-correlation energy with respect to the density,

$$v_{xc}(\mathbf{r}) = \frac{\delta E_{xc}[\rho(\mathbf{r})]}{\delta \rho(\mathbf{r})}, \quad (2.25)$$

and the optimization problem is written under the constraint of fixed number of electrons  $N$ . The Lagrange multiplier  $\mu$ , which is of course the chemical potential, represents the energy required to add an electron to the system. The variation of the constrained total energy with respect to the density must be zero:

$$\frac{\delta}{\delta \rho(\mathbf{r})} \left[ E[\rho(\mathbf{r})] - \mu \left( \int \rho(\mathbf{r}) d\mathbf{r} - N \right) \right] = 0. \quad (2.26)$$

This can be written as

$$\frac{\delta \mathcal{T}_s[\rho(\mathbf{r})]}{\delta \rho(\mathbf{r})} + v_H(\mathbf{r}) + v_{Z-e}(\mathbf{r}) + v_{xc}(\mathbf{r}) = \mu, \quad (2.27)$$

which the Euler-Lagrange equation for a system of non-interacting particles having kinetic energy  $\mathcal{T}_s$  and experiencing the effective potential  $v_{eff}(\mathbf{r}) = v_H(\mathbf{r}) + v_{Z-e}(\mathbf{r}) +$

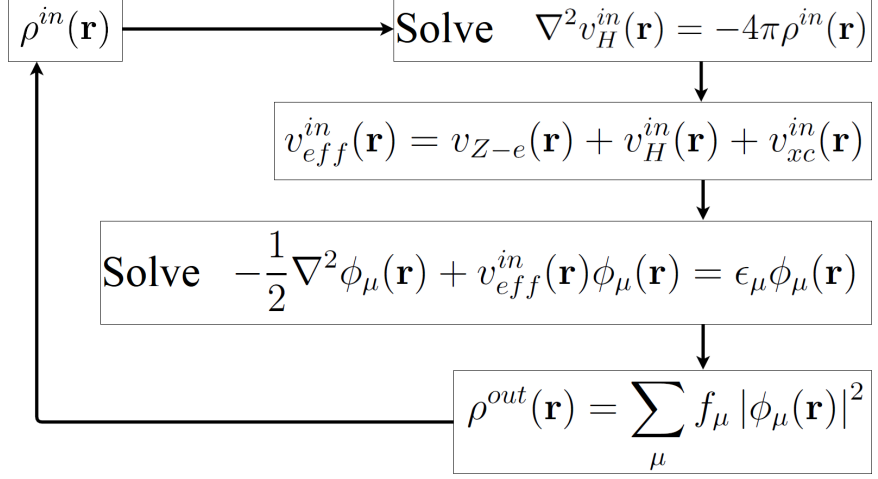


Figure 2.1: Self-consistency loop of Kohn-Sham DFT. A Poisson equation is solved to obtain the Hartree potential, from which the effective potential can be formed. The single-particle Schrödinger equations are solved and the output density is calculated from the new single-particle orbitals. The new density is then fed back into the Poisson equation. The loop exits when some convergence criterion (e.g. a sufficiently small change in energy or density) is achieved.

$v_{xc}(\mathbf{r})$ . This is equivalent to a set of single-particle Schrödinger equations

$$-\frac{1}{2}\nabla^2\phi_\mu(\mathbf{r}) + v_{eff}(\mathbf{r})\phi_\mu(\mathbf{r}) = \epsilon_\mu\phi_\mu(\mathbf{r}) \quad (2.28)$$

known as the Kohn-Sham equations. The solutions  $\phi_\mu(\mathbf{r})$  are called the Kohn-Sham (KS) orbitals and can be used to construct  $\rho(\mathbf{r})$  and  $\mathcal{T}_s$  through Equation 2.19 and Equation 2.24 respectively. The Hartree potential at each iteration is typically found by solving a Poisson equation. The self-consistency loop in Kohn-Sham DFT is shown diagrammatically Figure 2.1

While it looks like the problem has been simplified into a more easily-solved set of partial differential equations, the dependence of  $v_{eff}(\mathbf{r})$  on the KS orbitals through  $\rho(\mathbf{r})$  means an iterative process is required where the current  $\phi_\mu(\mathbf{r})$  determine the Hartree and exchange-correlation potentials used in computing the next generation

of orbitals.

Typically it is the exchange-correlation potential  $v_{xc}(\mathbf{r})$  that is tabulated, allowing the total energy to be written using local integral kernels as:

$$E[\rho(\mathbf{r})] = \mathcal{T}_s + \int v_{Z-e}(\mathbf{r})\rho(\mathbf{r})d\mathbf{r} + \int v_H(\mathbf{r})\rho(\mathbf{r})d\mathbf{r} + \int v_{xc}(\mathbf{r})\rho(\mathbf{r})d\mathbf{r}. \quad (2.29)$$

This inherent assumption of locality means that even the Fock exchange is necessarily approximated in such a formulation. There are many different approaches to approximating  $E_{xc}$ , and the development of better functionals is an ongoing area of research. In the next section the most commonly used exchange-correlation functionals are outlined.

### 2.2.1 Exchange-Correlation Functionals

The exchange-correlation energy functional  $E_{xc}[\rho(\mathbf{r})]$  can be expressed in integral form by defining the exchange-correlation energy density  $\epsilon_{xc}(\rho(\mathbf{r}), \dots) = v_{xc}(\mathbf{r})$ :

$$E_{xc}[\rho(\mathbf{r})] = \int \rho(\mathbf{r})v_{xc}(\rho(\mathbf{r}), \dots)d\mathbf{r}, \quad (2.30)$$

where  $\dots$  indicates the possibility of including more dependencies than just  $\rho(\mathbf{r})$ . Exchange-correlation functionals can be categorized according to the functional dependence of  $v_{xc}$ . The local-density approximation (LDA) depends, unsurprisingly, only on the local density of electrons. The generalized-gradient approximation (GGA) contains a typically nonlinear dependence on the gradient  $|\nabla\rho(\mathbf{r})|$ . Higher-order approximations can contain the single-particle kinetic energy density  $\sum f_\mu \phi_\mu^*(\mathbf{r}) \nabla_\mu^2 \phi_\mu(\mathbf{r})$ , higher-order derivatives like  $\nabla^2\rho(\mathbf{r})$ , or even a portion [65] of the Fock exchange (see Equation 2.17).

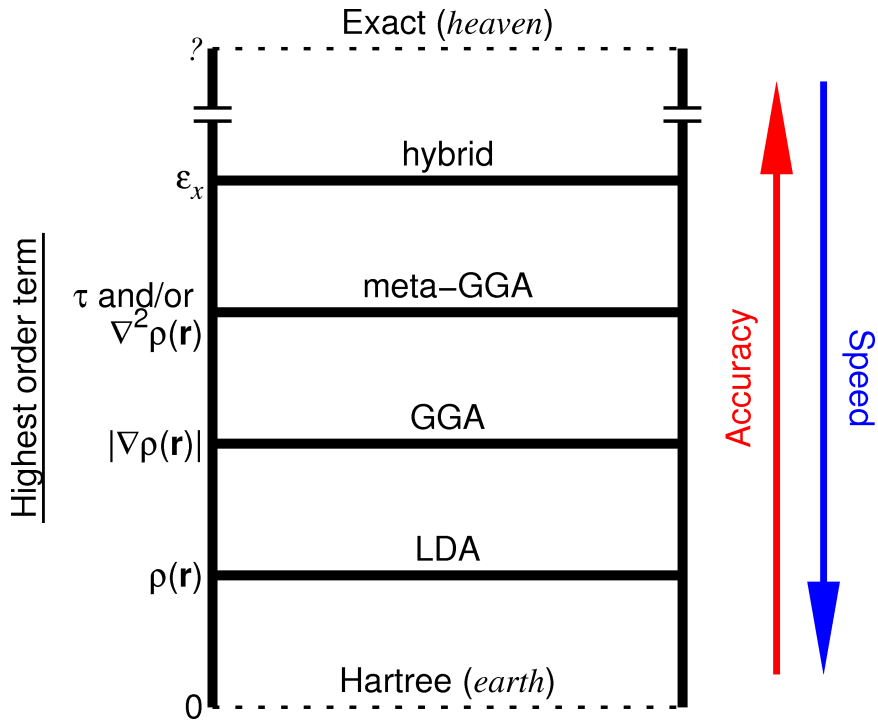


Figure 2.2: “Jacob’s ladder” of exchange-correlation approximations for density functional theory. The bottom of the ladder (“earth”) represents the Hartree interaction energy, where exchange and correlation effects are ignored. The top of the ladder (“heaven”) represents the exact ground-state functional. Rungs are labeled according to the approximation, and the highest-order term included in the dependency of  $v_{xc}(\rho(\mathbf{r}), \dots)$  is shown on the left-hand side. Climbing the ladder increases accuracy at the cost of computational efficiency as depicted by arrows to the right of the ladder.

The various classifications of exchange-correlation functionals are often assigned to the rungs of a ladder, blasphemously called “Jacob’s ladder,” as shown in Figure 2.2. In the theological analogy “heaven” represents the exact functional shown to exist by Kohn and Sham while our terrestrial realm represents the Hartree energy (i.e.  $\epsilon_{xc} = 0$ ). Climbing the ladder gets us closer to heaven (more accurate ground-state energies) but requires us to expend energy in the form of decreased computational efficiency.

## 2.3 Implementation

So far the theory of Kohn-Sham DFT has been developed without addressing details of its practical implementation. A great many software packages have been developed for doing this in different ways, but in most methods the Kohn-Sham orbitals are expanded in terms of some basis functions to cast the problem as one of linear algebra. In real-space these basis functions are typically the Wannier orbitals, which are the Fourier transforms of the Bloch waves seen earlier. In  $\mathbf{k}$ -space, planewaves are often used. Each implementation has its idiosyncrasies but in this section the basics employed by the Vienna Ab-initio Simulation Package (VASP) [66, 67, 68, 69], and how to ensure that calculations are properly converged, are discussed.

### 2.3.1 Planewave Expansion

VASP is a  $\mathbf{k}$ -space method which expands the Kohn-Sham orbitals in terms of planewaves:

$$\phi_{j\mathbf{k}}(\mathbf{r}) = \sum_{\mathbf{G}}^{|G| < G_{cut}} c_{j\mathbf{k},\mathbf{G}} e^{i(\mathbf{k}+\mathbf{G}) \cdot \mathbf{r}} \quad (2.31)$$

where  $\mathbf{G}$  is from a set of points in reciprocal space. The coefficients  $c_{j\mathbf{k},\mathbf{G}}$  form a vector representing the KS orbital  $\phi_{j\mathbf{k}}(\mathbf{r})$ , and matrix elements of the hamiltonian in this representation are straightforward to evaluate. In general an infinite number of planewaves are needed to represent a three-dimensional function to arbitrary precision, but in practice the basis set is truncated at some maximal  $\mathbf{G}$ -vector magnitude  $G_{cut}$ . This quantity is often related to an energy, called the *cutoff energy*, as if it were the momentum of a free electron in three dimensions:

$$E_{cut} = \frac{\hbar^2 G_{cut}^2}{2m}. \quad (2.32)$$

The cutoff energy has a strong effect on the accuracy and speed of planewave DFT calculations because it determines the size of the matrix that needs to be diagonalized. General diagonalization routines are typical of order  $\mathcal{O}(N^3)$ , and since  $N \sim G_{cut}^3$  the algorithms scale with  $E_{cut}$  on the order  $\mathcal{O}(E_{cut}^{9/2})$ . Too few planewaves, however, and the KS orbitals may be ill-represented near the ion cores where the coulomb potential is strong and the wavefunctions are rapidly-varying.

### 2.3.2 Pseudopotentials

The efficiency problem outlined above can be addressed by orthogonalizing the basis functions with the core states before expansion [62]. This can be re-cast as modifying the hamiltonian into a “pseudo” hamiltonian appyling only to the valence orbitals  $\phi_{\mathbf{k}}^v(\mathbf{r})$ :

$$H^{pseudo}\phi_{\mathbf{k}}^v(\mathbf{r}) = (T + V^{pseudo})\phi_{\mathbf{k}}^v(\mathbf{r}) = \epsilon_{\mathbf{k}}^v\phi_{\mathbf{k}}^v(\mathbf{r}), \quad (2.33)$$

where  $V^{pseudo}$  (the *pseudopotential*) is the original potential with a (positive) correction depending on the energies of the valence states above those of the core states. Since  $V^{pseudo}$  is smaller than  $V$ , fewer planewaves are needed to describe the valence states. Pseudopotentials are complicated and specific to the exchange-correlation functional being used, but the general logic is to ignore the inner-shell electrons (i.e. *not* use them in calculating the density or total energy) under the assumption that their energies will be unchanged in a crystal, but to account for their required orthogonality with the valence states through an added potential energy term. This is shown graphically in Figure 2.3. It is important to note that the number of valence electrons included in the calculation has a strong effect on the accuracy at low ionic separations. If one intends to do high-pressure DFT calculations, pseudopotentials which do not average out the high-lying core states (so-called semicore states) should

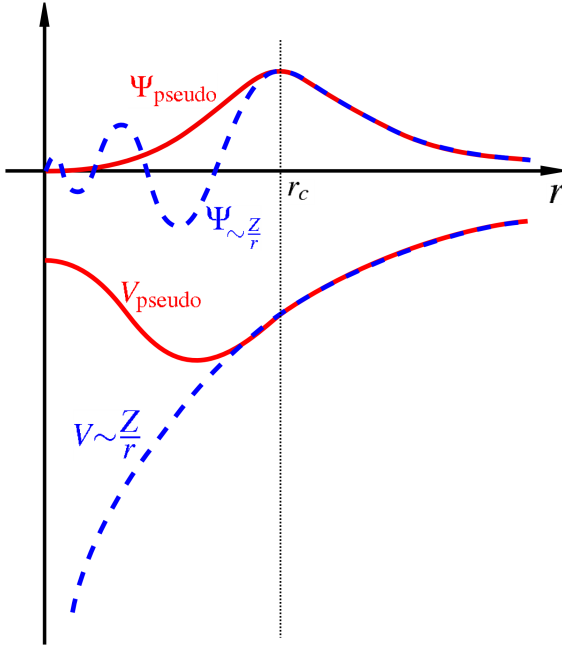


Figure 2.3: Schematic of a pseudopotential and pseudo-wavefunction compared to the full potential and corresponding wavefunction. Rapid oscillations in the exact wavefunction near the origin, necessary to maintain orthogonality with the core states deep in the coulomb well, are replaced by a slowly decaying pseudo-wavefunction below the cutoff radius  $r_c$ . Original image by Wolfram Quester for <https://en.wikipedia.org/wiki/Pseudopotential>

be used.

### 2.3.3 Sampling the Brillouin Zone

As suggested by Equation 2.31, diagonalization of the KS hamiltonian must be done for each KS orbital  $j$  at every  $\mathbf{k}$  in the Brillouin zone. The variation of  $\phi_{j\mathbf{k}}(\mathbf{r})$  throughout the Brillouin zone enters the total density as an integral:

$$\rho(\mathbf{r}) = \sum_{\mu} f_{\mu} \int_{BZ} d\mathbf{k} \phi_{\mu\mathbf{k}}^*(\mathbf{r}) \phi_{\mu\mathbf{k}}(\mathbf{r}), \quad (2.34)$$

but one can't well tabulate  $\phi$  at an infinite number of points. An evenly-spaced grid of  $\mathbf{k}$  points is thus used to sample the Brillouin zone. These grids must be compatible with the symmetry of the bravais lattice, so the points are given as multiples of the reciprocal lattice vectors. In the present work the scheme of Monkhorst and Pack [70], where a mesh size  $N_\alpha \times N_\beta \times N_\gamma$  is input and  $\mathbf{k}$  points are constructed according to

$$\begin{aligned}\mathbf{k}_{\alpha\beta\gamma} &= u_\alpha \mathbf{b}_1 + u_\beta \mathbf{b}_2 + u_\gamma \mathbf{b}_3 \\ u_\beta &= \frac{2\beta - N_\beta - 1}{2N_\beta}, \quad \beta = 1, 2, \dots, N_\beta \text{ etc,}\end{aligned}\tag{2.35}$$

is employed.

Sampling the BZ on a grid of course converts the integral in Equation 2.34 into a sum, but this is only accurate if the  $\phi_{j\mathbf{k}}$  are slowly varying compared to the spacing of the grid.

### 2.3.4 Smearing

In metals, the chemical potential (or Fermi energy, at zero temperature) lies inside the conduction band where the electronic density of states is nonzero. This produces a discontinuity in quantities which must be integrated in the BZ. Such a discontinuity requires a very large number of planewaves, and thus  $\mathbf{k}$ -points, to describe accurately. The solution is to “smear” the density of states around the Fermi level into a continuous function that is easier to integrate.

In the present work the method of Methfessel and Paxton (MP) [71] is used. The general idea is to smear the DOS into a function which quickly drops to zero in such a way as to approximately balance the error above and below the Fermi level. This is accomplished using a combination of the error function  $\text{erf}(x)$  and Hermite

polynomials of various degree. Here the 1<sup>st</sup> order MP smearing is employed. The smeared DOS ( $g_s$ ) is given by

$$g_s(E) = g(E) \left[ \frac{1}{2} \left( 1 - \text{erf} \left( \frac{E - E_F}{\sigma} \right) \right) - \frac{E - E_F}{2\sigma\sqrt{\pi}} e^{-\left(\frac{E-E_F}{\sigma}\right)^2} \right], \quad (2.36)$$

where  $\sigma$  is called the *smearing parameter* and is sometimes equated to  $k_B T$  to obtain the “smearing temperature” or “electronic temperature.”

### 2.3.5 Convergence

The cutoff energy, smearing parameter  $\mathbf{k}$ -point mesh size are the most important parameters determining the accuracy of a KS-DFT calculation in VASP. To optimally balance speed and accuracy, a careful check of convergence should be done before serious calculations are attempted. Presented below is a convergence-testing strategy employed for every phase considered in the present work:

- (i) Choose lattice constants based on experiment, previous calculations, rule of mixtures, or an estimate. Choose convergence criterion (i.e. desired precision of calculations), called  $\Delta E^{cvg}$ . In the present work,  $\Delta\varepsilon^{cvg} = 1$  meV/atom
- (ii) With a large  $\mathbf{k}$ -point mesh (e.g.  $40 \times 40 \times 40$  in a b.c.c. cell) and no smearing (Tetrahedron method with Blochl corrections) run a single self-consistent electron calculation (a.k.a. “single-point” calculation) for planewave cutoffs between 200 and 700 eV. At least one very large cutoff, between say 700 eV and 900 eV, should be used as the “converged” value ( $E_{cut}^{cvg}$ ) and the optimal planewave cutoff ( $E_{cut}$ ) chosen to be the smallest value such that  $\varepsilon(E_{cut}) - \varepsilon(E_{cut}^{cvg}) \leq \Delta\varepsilon^{cvg}$ , where  $\varepsilon(E_{cut})$  is the total energy per atom calculated with cutoff  $E_{cut}$ . A typical value for  $E_{cut}$  in the present work is 500 eV.
- (iii) Using the chosen  $E_{cut}$ , do single-point calculations for various sized  $\mathbf{k}$ -point

meshes from  $1 \times 1 \times 1$  up to mesh used in (ii).  $N_\alpha$ ,  $N_\beta$  and  $N_\gamma$  should be chosen according to Brillouin zone dimensions such that the mesh-spacing is approximately equal in all directions. If  $N_{kpt}$  is the number of k-points for a given calculation and  $N_{kpt}^{cvg}$  is the number used in step (ii), the mesh size should be the smallest value such that  $\varepsilon(N_{kpt}) - \varepsilon(N_{kpt}^{cvg}) \leq \Delta\varepsilon^{cvg}$ . For example, a grid of  $17 \times 17 \times 13$  k-points are used for hcp-Ti in the present work. As a rule of thumb, supercells require fewer k-points than unit cells because the Brillouin zone is smaller.

(iv) Using the previously determined values of  $E_{cut}$  and k-point mesh size, run single-point calculations for smearing parameters between roughly 0.01 and 2 eV. Since total energy generally increases with smearing, the parameter  $\sigma$  should be chosen to be the largest value such that  $\varepsilon(\sigma) - \varepsilon(\text{Blochl}) \leq \Delta\varepsilon^{cvg}$ . A value of  $\sigma = 0.1$  eV is used for all structures in the present work.

# Chapter 3:

## Classical Molecular Dynamics

Molecular dynamics (MD) is a field of computational physics involving the modeling of materials – (bio)molecular, crystalline or otherwise – at the atomic level. Atoms are typically treated as point-particles, though can be modeled as hard spheres or ellipsoids as well, and interatomic forces are used to update their configuration at each successive timestep. While forces can be derived directly from the multi-electron Schroedinger equation (so-called *ab-initio* MD) via the Hellman-Feynman theorem, it is far more common to approximate forces by deriving them from classical potential energy functions dependent only on the positions (and possibly orientations) of atoms in the simulated system. This latter method, referred to as classical MD (CMD), is the focus of the present work.

### 3.1 Fundamentals

In essence, a CMD simulation is a numerical integration of the classical equations of motion for each atom in a system with forces derived from the interatomic potential

$V(\{\mathbf{r}_i\})$ :

$$m_j \frac{d^2 \mathbf{r}_j}{dt^2} + \nabla_j V(\{\mathbf{r}_i\}) = 0, \quad j = 1, \dots, N \quad (3.1)$$

where  $m_j$  is the mass of atom  $j$ . Forces are typically evaluated at the present timestep and the position  $\mathbf{r}$  of each atom is updated simultaneously. While various numerical integrators exist, the most widely used – and the only one used in the present work – is the Velocity Verlet (VV) algorithm. Given a simulation at time  $t$  and a timestep  $\delta t$ , the position  $\mathbf{r}_j$  and velocity  $\mathbf{v}_j$  of each atom in a system is updated according to

$$\begin{aligned} \mathbf{f}_j(t) &\equiv \mathbf{f}_j(\mathbf{r}_j(t)) \\ \mathbf{r}_j(t + \delta t) &= \mathbf{r}_j(t) + \mathbf{v}_j(t)\delta t + \frac{1}{2m_j}\mathbf{f}_j(t)\delta t^2 \\ \mathbf{v}_j(t + \delta t/2) &= \mathbf{v}(t) + \frac{1}{m_j}\mathbf{f}(t)\frac{\delta t}{2} \\ \mathbf{f}_j(t + \delta t) &\equiv \mathbf{f}_j(\mathbf{r}(t + \delta t)) \\ \mathbf{v}_j(t + \delta t) &= \mathbf{v}(t + \delta t/2) + \frac{1}{m_j}\mathbf{f}(t + \delta t)\frac{\delta t}{2}, \end{aligned} \quad (3.2)$$

where the force is of course derived from the equation of motion as  $\mathbf{f}_j(\mathbf{r}(t)) = \nabla_j V(\{\mathbf{r}_i(t)\})$ . The VV integrator is a use case of the more general Leapfrog algorithm, as can be seen by the use of half-time steps in evaluating the velocity, which can be shown to be of order  $\mathcal{O}(\delta t^4)$  and is superior compared to simpler approaches such as the Euler method. Furthermore, only one copy of each array ( $\{\mathbf{r}\}$ ,  $\{\mathbf{v}\}$  and  $\{\mathbf{f}\}$ ) is necessary to hold in memory at a time.

The ordinary VV algorithm conserves the hamiltonian  $H = T + V$  for small  $\delta t$  (typically on the order of a femtosecond for metallic systems), clearly has no steps which can vary the total volume of a system – a quantity defined by simulation inputs – and also has no mechanism for adding or removing particles. Hence it is a numerical integration of the NVE ensemble discussed in Chapter 1. Integrating the equations

of motion under different constraints, such as NVT or NPT, require modifications to the VV discussed in the next section.

## 3.2 Ensemble Integration

Evolving the system of atoms in accordance with more general statistical mechanics ensembles (see Section 1.6) requires additional terms in the hamiltonian function, leading to time-integration equations distinct from Equation 3.2. This section describes the ensemble integration techniques employed in the present work for the NVT and NPT ensembles.

### 3.2.1 NVT

Integrating the equations of motion in such a way as to keep the temperature fixed in a simulation requires the use of a *thermostat*. Choices include the Langevin[72] or Berendsen[73] thermostats, but the present work employs the Nosé-Hoover[74, 75] (NH) method. A description of the NH thermostat following that of Tadmor and Miller[48] is provided below, with a slight re-definition of the free parameter consistent with the implementation in LAMMPS.

The NH method begins by adding to the  $N$ -particle hamiltonian the energy of a fictitious particle at position  $Q$  and with momentum  $P$  and mass  $M$  such that

$$H_{NVT} = H_{NH} = H + \frac{P^2}{2M} + 3Nk_B T \ln Q, \quad (3.3)$$

where  $T$  is the target temperature for the simulation. With clever application of

Hamilton's equations the time-evolution can be written

$$m_j \frac{d^2 \mathbf{r}_j}{dt^2} = \mathbf{f}_j - \gamma m_j \frac{d\mathbf{r}_j}{dt}, \quad (3.4)$$

where  $\gamma = P/M$  satisfies

$$\frac{d\gamma}{dt} = \frac{1}{M} \left( \sum_j \frac{p_j^2}{m_j} - 3Nk_B T \right). \quad (3.5)$$

This is equivalent to

$$\frac{d\gamma}{dt} = \frac{1}{M^*} (T_{inst} - T) \quad (3.6)$$

with  $M^* = 3k_B M/N$ . Since  $\gamma m \mathbf{v}$  has units of force, it follows that  $\gamma$  has units of frequency, hence Equation 3.6 can be written as

$$\dot{\gamma} = \frac{1}{\tau_T^2} \left( \frac{T_{inst}}{T} - 1 \right), \quad (3.7)$$

where  $\tau_T$  is a characteristic time determining the rate at which the system is thermostatted. A typical value for  $\tau_T$  in simulations of metals is  $\sim 1$  ps.

Integrating Equations 3.3 and 3.6 together will cause the instantaneous temperature  $T_{inst}$  to tend toward (while oscillating around) the target temperature  $T$  at a rate dependent on the input parameter  $\tau_T$ . Not all values of  $\tau_T$  are viable, and the appropriate value depends on the system under study.

A modification of the VV algorithm for use with the NH thermostat is given below. The physical force from Equation 3.2 is replaced by the Nosé-Hoover force  $\mathbf{f}_j^{NH}(\mathbf{r}_j, \mathbf{v}_j) = \mathbf{f}_j(\mathbf{r}_j) - \gamma m_j \mathbf{v}_j$  and  $\gamma$  is evolved using the half-step time:

$$\begin{aligned}
\mathbf{f}_j^{NH}(t) &\equiv \mathbf{f}_j^{NH}(\mathbf{r}_j(t), \mathbf{v}_j(t), \gamma(t)) \\
\mathbf{r}_j(t + \delta t) &= \mathbf{r}_j(t) + \mathbf{v}_j(t)\delta t + \frac{1}{2m_j}\mathbf{f}_j^{NH}(t)\delta t^2 \\
\mathbf{v}_j(t + \delta t/2) &= \mathbf{v}(t) + \frac{1}{m_j}\mathbf{f}^{NH}(t)\frac{\delta t}{2} \\
\gamma(t + \delta t) &= \gamma(t) + \left[ \frac{T_{inst}(\mathbf{v}(t + \delta t/2))}{T} - 1 \right] \frac{\delta t}{\tau_T^2} \\
\mathbf{f}_j^{NH}(t + \delta t) &\equiv \mathbf{f}_j^{NH}(\mathbf{r}(t + \delta t), \mathbf{v}(t + \delta t/2), \gamma(t)) \\
\mathbf{v}_j(t + \delta t) &= \mathbf{v}(t + \delta t/2) + \frac{1}{m_j}\mathbf{f}_j^{NH}(t + \delta t)\frac{\delta t}{2},
\end{aligned} \tag{3.8}$$

where the instantaneous temperature as a function of velocity is given by Equations 3.5 and 3.6. The half-step velocity  $\mathbf{v}_j(t + \delta t/2)$  is used to evaluate  $\gamma(t + \delta t)$  and  $\mathbf{f}_j^{NH}(t + \delta t)$  in order to avoid a situation where  $\mathbf{v}_j(t + \delta t)$  depends on itself, requiring a self-consistency loop much like the Kohn-Sham equations of Chapter 2. Given the right choice of  $\tau_T$ , self-consistency of the velocity will emerge from this algorithm after a few iterations. Early timesteps of a simulation are thus un-physical, so an “equilibration” time is necessary before the output is reliable.

### 3.2.2 NPT

In order to integrate the atomic equations of motion consistent with the NVT ensemble, simulation cell dimensions must be allowed to change in response to internal and external stresses. This requires an equation of motion for the cell parameters, the nature of which depends heavily on the form of stresses to be considered. The present approach, described in detail by Melchionna *et al.* [76], is analogous to the NH thermostat but where the variable is a tensor  $\bar{\eta}(t)$ .

The stress tensor  $\bar{\sigma}$  in this case is analogous to  $T_{inst}$  in the NH method, and can

be computed from the atomic positions and momenta in a cell of volume  $\Omega$  as follows:

$$\sigma_{\mu\nu} = \frac{1}{\Omega} \left[ \sum_i^N \frac{p_i^\mu p_i^\nu}{m_i} + \frac{1}{2} \sum_{i \neq j}^N \frac{\partial V}{\partial r_{ij}} \frac{r_i^\mu r_j^\nu}{r_{ij}} \right]. \quad (3.9)$$

This expression for the stress tensor is known as the Cauchy stress or virial stress. Note that it is a function of the momenta (i.e. velocity) and position of each atom as well as the cell volume.

As with the NH (NVT) method, the present NPT approach starts by adding auxiliary terms to the hamiltonian, from which equations of motion are derived from Hamilton's equations. Let  $\bar{\bar{\Omega}}(t)$  be the matrix containing the cell vectors (column-wise) such that  $\Omega(t) = \det[\bar{\bar{\Omega}}(t)]$  is the volume. The NPT hamiltonian is given by

$$H_{NPT} = H_{NVT} + P\Omega(t) + \frac{1}{2}Nk_B T \text{tr}[\bar{\bar{\eta}}(t)^T \bar{\bar{\eta}}(t)]\tau_P^2, \quad (3.10)$$

and leads to time-evolution equations for  $\bar{\bar{\eta}}$  and  $\Omega(t)$ :

$$\begin{aligned} \frac{d\bar{\bar{\eta}}(t)}{dt} &= \frac{\Omega(t)}{Nk_B T \tau_P^2} \left( \bar{\bar{\sigma}} - \bar{\bar{I}}P \right) \\ \frac{d\bar{\bar{\Omega}}(t)}{dt} &= \bar{\bar{\eta}}(t)\bar{\bar{\Omega}}(t). \end{aligned} \quad (3.11)$$

Here the parameter  $\tau_P$  is a characteristic time for stress evolution analogous to  $\tau_T$  and  $\bar{\bar{I}}$  is the identity tensor. A typical value of  $\tau_P$  in NPT simulation of metals is  $\sim 10 \tau_T$ . Integration of these equations can be done simultaneously with those of the NH thermostat as they are independent of one another. The time-evolution of the box tensor can be solved by inspection:

$$\bar{\bar{\Omega}}(t) = \exp \left( \int_0^t dt' \bar{\bar{\eta}}(t') \right) \quad (3.12)$$

The volume at time  $t$  is thus

$$\begin{aligned}\Omega(t) &= \det \left[ \exp \left( \int^t dt' \bar{\bar{\eta}}(t') \right) \right] \\ &= \exp \left( \text{tr} \left[ \int^t dt' \bar{\bar{\eta}}(t') \right] \right) = \exp \left( \int^t dt' \text{tr}[\bar{\bar{\eta}}(t')] \right).\end{aligned}\tag{3.13}$$

An exponential function of a tensor is necessarily treated as a truncated power series, and the volume is treated similarly so the two remain commensurate. The VV algorithm is implemented within the NPT ensemble by replacing the physical force with  $\mathbf{f}_j^{NPT} = \mathbf{f}_j - (m_j \gamma(t) \bar{\bar{I}} - \bar{\bar{\eta}}(t)) \mathbf{v}_j(t)$  and performing the following steps:

$$\begin{aligned}\mathbf{f}_j^{NVT}(t) &\equiv \mathbf{f}_j^{NVT}(\mathbf{r}_j(t), \mathbf{v}_j(t), \gamma(t), \bar{\bar{\eta}}(t)) \\ \mathbf{r}_j(t + \delta t) &= \mathbf{r}_j(t) + \mathbf{v}_j(t) \delta t + \frac{1}{2m_j} \mathbf{f}_j^{NH}(t) \delta t^2 \\ \mathbf{v}_j(t + \delta t/2) &= \mathbf{v}(t) + \frac{1}{m_j} \mathbf{f}^{NH}(t) \frac{\delta t}{2} \\ \gamma(t + \delta t) &= \gamma(t) + \left[ \frac{T_{inst}(\mathbf{v}(t + \delta t/2))}{T} - 1 \right] \frac{\delta t}{\tau_T^2} \\ \bar{\bar{\eta}}(t + \delta t) &= \frac{\Omega(t)}{Nk_B T \tau_P} \left( \bar{\bar{\sigma}}(\mathbf{r}(t + \delta t), \mathbf{v}(t + \delta t/2), \Omega(t)) - \bar{\bar{I}} P \right) \delta t \\ \mathbf{f}_j^{NVT}(t + \delta t) &\equiv \mathbf{f}_j^{NPT}(\mathbf{r}(t + \delta t), \mathbf{v}(t + \delta t/2), \gamma(t + \delta t), \bar{\bar{\eta}}(t + \delta t)) \\ \mathbf{v}_j(t + \delta t) &= \mathbf{v}(t + \delta t/2) + \frac{1}{m_j} \mathbf{f}_j^{NH}(t + \delta t) \frac{\delta t}{2} \\ \Omega(t + \delta t) &= \Omega(t) \exp(\text{tr}[\bar{\bar{\eta}}(t)] \delta t) \\ \bar{\bar{\Omega}}(t + \delta t) &= \bar{\bar{\Omega}}(t) \exp(\bar{\bar{\eta}}(t) \delta t)\end{aligned}\tag{3.14}$$

### 3.3 Interatomic Potentials

The accuracy of a molecular dynamics simulation depends mostly on algorithm inputs and the behavior of the interatomic potential, the appropriate form of which depends on the materials and physics of interest. This chapter describes some common forms found in the literature and other possible routes of empirical expansion.

The total potential energy of a system of  $N$  atoms can be formally [48] written as a sum of  $n$ -body contributions for  $n = 0, \dots, N$ :

$$V^{(N)} = V_0 + \sum_{i=1}^N V_1(\mathbf{r}_i) + \frac{1}{2} \sum_{i \neq j}^N V_2(\mathbf{r}_i, \mathbf{r}_j) + \frac{1}{6} \sum_{i \neq j \neq k} V_3(\mathbf{r}_i, \mathbf{r}_j, \mathbf{r}_k) + \dots + V_N(\mathbf{r}_1, \dots, \mathbf{r}_N) \quad (3.15)$$

where the  $V_n$  are simple functions of  $n$  atomic coordinates. Henceforth any model which can be written in the form of Equation 3.15 is referred to as a “potential,” while forms which cannot be obtained by simply specifying the functions  $V_n$  is referred to as a “functional.”

#### 3.3.1 Pair Potentials

Pair potentials are the simplest approximation one can make for molecular dynamics. They necessarily depend only on the magnitude  $r_{ij}$  of the distance between pair  $i, j$  of atoms. They must take into account the strong repulsion at low interatomic separation, which originates from the orthogonalization between core electrons from the different atoms, as well as the bonding and electrostatic energies of valence electrons. The most common form, which is semi-empirical in nature, is the Lennard-Jones potential[77]

$$V_{LJ} = \frac{1}{2} \sum_i \sum_{j \neq i} 4\epsilon \left[ \left( \frac{\sigma}{r_{ij}} \right)^{12} - \left( \frac{\sigma}{r_{ij}} \right)^6 \right]. \quad (3.16)$$

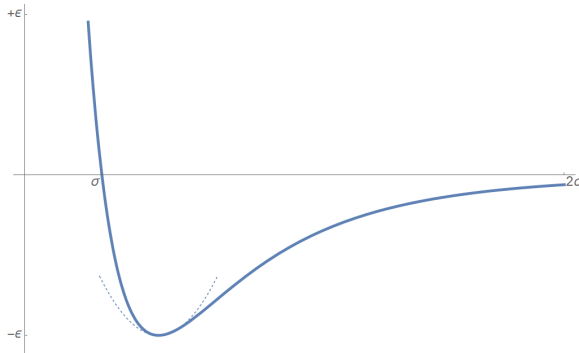


Figure 3.1: Lennard-Jones potential for a single pair of atoms. Anharmonicity of the well is shown by comparison with a quadratic potential having the same curvature as the LJ potential at its minimum.

The  $r^{-1/6}$  term is due to instantaneous dipole-dipole forces between (non-bonding) electron clouds, while the  $r^{-1/12}$  term is chosen for computational convenience (squaring of the previous term) to represent the strong repulsion from the Pauli principle. This form is easily extended to multicomponent systems since each distinct pair  $I, J$  of species simply gets its own parameters  $\epsilon_{IJ}, \sigma_{IJ}$ . A plot of the Lennard Jones potential for a single pair of atoms with parameters  $\epsilon = 0.25$  and  $\sigma = 3.0$  is shown in Figure 3.3.1. A quadratic well with the same curvature is superimposed for comparison.

Such potentials can replicate basic properties of simple close-packed metals and noble gases, but fail even to replicate the stability of the bcc lattice because the optimal structure is necessarily close-packed with primitive lattice constant defined by  $a_0 = \underset{r_{ij}}{\operatorname{argmin}}[V_{LJ}(r_{ij})]$ . LJ potentials are also incapable of reproducing elastic anisotropy in cubic metals. Despite these limitations LJ potentials have been widely used for atomistic modeling. However, for transition metals and alloys more sophisticated models, generally referred to as *pair functionals*, have been far more successful.

### 3.3.2 Pair Functionals

A class of interatomic potentials termed *pair functionals* includes the most widely-used empirical and semi-empirical potentials for metals and alloys. They are named as such because all pair functionals have a form which involves a mapping of some combination of two-body functions into an energy. It is crucial for this mapping to be nonlinear, else the form reduces to that of a simple pair interaction. Pair functionals frequently include a simple pair potential in the total energy, ostensibly to describe the internuclear energy, but certain invariances of these models destroy any unique interpretation of the terms. The two most common pair functionals, the Embedded Atom Method (EAM) and Finnis-Sinclair (FS) potentials, are described and different generalizations to multicomponent systems, owing to the distinct theoretical foundations of each model, are discussed.

#### Embedded Atom Method potentials

The EAM, developed by Baskes and Daw[78], has the following form:

$$V_{EAM} = \frac{1}{2} \sum_i^N \sum_{j \neq i}^N \phi(r_{ij}) + \sum_i^N U(n_i) \quad (3.17)$$

where

$$n_i = \sum_{j \neq i}^N \rho(r_{ij}), \quad (3.18)$$

where  $\phi(r)$  is interpreted as an internuclear pair potential,  $U(n)$  is known as the “embedding function,” and  $\rho(r)$  is a pair contribution to the “electronic density”  $n$ . This model originates with the pseudo-atom formalism of Stott and Zaremba[79], who considered the energy of an impurity atom in a host material and found a corollary to DFT, written (in simplified form) as follows:

$$E_{impurity} = \mathcal{F}[n_{host}], \quad (3.19)$$

meaning the energy required to add an impurity into the host is a functional of the host's electron density *only*, with the functional  $\mathcal{F}$  being determined by calculations of the impurity energy in a uniform electron gas. This approximation was thus referred to as the "uniform density approximation" (UDA), and was also used by Nørskov and Lang[80] to develop the so-called effective medium theory (EMT).

As written, the forms of the pair potential  $\phi(r)$ , embedding function  $U(n)$  and density  $\rho(r)$  can be parameterized analytical forms or splines.

Note that the so-called "density"  $n_i$  in EAM does not strictly represent the electronic density as it does in the Stott-Zaremba corollary. This is because there exists an invariant transformation that mixes the functions, meaning there is no unique interpretation of each. Using a shorthand notation where  $\phi(r_{ij}) \equiv \phi_{ij}$  etc., this gauge transformation can be written with arbitrary real constants  $c_i$  as:

$$\begin{aligned} \phi_{ij} &\rightarrow \phi_{ij} - c_j \rho_i - c_i \rho_j \\ U_i &\rightarrow U_i + c_i n_i. \end{aligned} \quad (3.20)$$

It is easy to prove the invariance of  $V_{EAM}$  with respect to this transformation given the symmetry of the pair functions, e.g.  $\phi_{ij} = \phi_{ji}$ .

### Finnis-Sinclair potentials

In the language of EAM, the FS model is obtained simply by specifying  $U(n) = -\sqrt{n}$ :

$$V_{FS} = \frac{1}{2} \sum_i^N \sum_{j \neq i}^N \phi(r_{ij}) - \sum_i^N \sqrt{n_i} \quad (3.21)$$

with  $n_i$  still specified by Eq. 3.18. The similarity of the two forms is due to their being two approaches to what is essentially the same problem. EAM ultimately originates from DFT, which of course is an approach to solving the Schrödinger equation using the electronic density as the fundamental quantity. Stott and Zaremba found the energy of an atom to be a functional of the electronic density of the rest of the solid to which Baskes and Daw applied a local approximation and parameterization. The FS model was derived by starting with a local approximation within a tight-binding formalism, then expanding the density of states into its moments defined by

$$\mu_I^{(n)} = \int_{-\infty}^{\infty} \epsilon^n \mathcal{D}_I(\epsilon) d\epsilon, \quad (3.22)$$

where  $\mathcal{D}_I(\epsilon)$  is the density of states at site  $I$ . Using a gaussian form for  $\mathcal{D}_I$  and keeping terms up to the second (the so-called second-moment approximation) results in a  $-\sqrt{n_i}$  energy term. Here the density  $n_i$  is actually a sum of overlap integrals  $S_{I\alpha J\beta} = \langle \Psi_{I\alpha} | \Psi_{J\beta} \rangle$  of the atomic electron wavefunctions  $\Psi_{I\alpha}$ , where  $I, J$  are atomic indices and  $\alpha, \beta$  are orbital indices. Instead of a local approximation to DFT, the FS model is an approximation to tight-binding theory.

This difference in interpretation of the density function leads to different generalizations to multi-species systems. Since the EAM model by construction treats each atom as an impurity, the embedding energy of which is a functional of the density of the electrons from *other* atoms, one considers each atomic type  $J$  to have its own density  $\rho_J(r_{ij})$  which it contributes to its neighbors. On the other hand, since  $S_{I\alpha J\beta}$  depends on the host *and* “impurity” atom, one expresses  $n$  as a sum of doubly-indexed functions  $\rho_{IJ}(r_{ij})$ . An advantage to this is that it allows one to fit an alloy potential using *fixed* single-element potentials, because there are gauge transformations which leave the one-species terms invariant while changing the mixed pair potential and

density functions.

### 3.3.3 Cluster Potentials

Both EAM and FS models were derived and intended for use in metals, but exhibit limitations with partially-filled  $d$ -band transition metals and covalent materials. For such systems three-body terms in the total energy play an important role from an empirical modeling perspective. There are a number of interatomic potentials which include terms involving more than two atoms. Here the most renown of such models, the Stillinger-Weber potential, is described. A more general cluster potential formalism is the Model Generalized Pseudopotential Theory (MGPT) [81, 82], which includes terms depending on up to four atoms.

#### Stillinger-Weber

The original Stillinger-Weber model was constructed with the intent of reproducing the cubic-diamond ground state of solid silicon. The internal angles between nearest neighbors in cubic diamond can be easily shown to be  $\theta_0 = \cos^{-1}(-1/3)$ . By including a three-body term which is minimized at  $\theta_0$ , the potential is forced to predict tetrahedral packing. In addition to the angle-dependent term the usual pair potential is added to describe the internuclear energy. The potential is given by

$$V_{SW} = \frac{1}{2} \sum_i^N \sum_{j \neq i}^N \phi(r_{ij}) + \frac{1}{2} \sum_i^N \sum_{j \neq i}^N \sum_{k \neq i,j}^N f(r_{ij})f(r_{ik}) \left( \cos \theta_{jik} + \frac{1}{3} \right)^2, \quad (3.23)$$

where  $\theta_{jik}$  is the angle of the triplet centered on atom  $i$ , typically evaluated as

$$\cos \theta_{jik} = \frac{\mathbf{r}_{ij} \cdot \mathbf{r}_{ik}}{|\mathbf{r}_{ij}| |\mathbf{r}_{ik}|}. \quad (3.24)$$

The function  $f$  is taken to be a decaying exponential, while  $\phi$  is taken to have Lennard-Jones form with an exponentially decaying prefactor. This model has been successful in the description of silicon and germanium as well as semi-conducting compounds like GaN [83] and InGaN [84].

### 3.3.4 Cluster Functionals: MEAM and Beyond

The value of interatomic potentials traditionally lay in their ability to study trends in material behavior with relative computational efficiency. Molecular dynamics was used as a tool to understand basic behavior on scales impractical for first-principles calculations. Progress in computing power has since expanded the reach of ab-initio methods and the development of high-tech alloys exhibiting complex microstructural properties and deformation behavior, often very sensitive to slight changes in alloying elements, has opened a new door for empirical potentials to be used in a targeted fashion to study these phenomena. Until significant breakthroughs occur in the efficiency of ab-initio methods or the practicality of quantum computing, first-principles calculations of alloy properties on large spatial or temporal scales will remain impractically cumbersome and molecular dynamics simulations will be needed to study the atomistic behavior at this level.

With greater material complexity comes the need for improved model flexibility, necessarily meaning more parameters and degrees of freedom. Empirical extensions of existing models, such as the modified embedded atom method (MEAM) proposed by Baskes [85], have proven valuable in studying transition metals [14, 55, 86, 87, 88] and alloys [89]. The total potential energy in a MEAM model is given by

$$V_{MEAM} = \frac{1}{2} \sum_i^N \sum_{j \neq i}^N \phi(r_{ij}) + \sum_i^N U(n_i), \quad (3.25)$$

where

$$n_i = \sum_{j \neq i}^N \rho(r_{ij}) + \frac{1}{2} \sum_{j \neq i}^N \sum_{k \neq i,j}^N f(r_{ij})f(r_{ik})g(\cos \theta_{jik}), \quad (3.26)$$

and  $\theta_{jik}$  is the triplet angle as defined for Stillinger-Weber potentials above.

In this work two empirical extensions of MEAM are presented. The first is a combination of a Stillinger-Weber potential with the embedding energy of MEAM:

$$\begin{aligned} V_{SW+MEAM} = & \frac{1}{2} \sum_i^N \sum_{j \neq i}^N \phi(r_{ij}) + \sum_i^N U(n_i) \\ & + \frac{1}{2} \sum_i^N \sum_{j \neq i}^N \sum_{k \neq i,j}^N p(r_{ij})p(r_{ik})q(\cos \theta_{jik}) \end{aligned} \quad (3.27)$$

where again

$$n_i = \sum_{j \neq i}^N \rho(r_{ij}) + \frac{1}{2} \sum_{j \neq i}^N \sum_{k \neq i,j}^N f(r_{ij})f(r_{ik})g(\cos \theta_{jik}). \quad (3.28)$$

This is the simplest three-body extension of MEAM which cannot be gauge-transformed back to the original potential because the sum  $p(r)p(r)q(x)+f(r)f(r)g(x)$  cannot in general be expressed as a function of the same form,  $s(r)s(r)t(x)$ , as was seen with two-body terms in ordinary EAM potentials. This method is used to model tungsten in Chapter 5.

The second extension is specific to alloys; the labels  $I, J, K$  are used to indicate the species of atoms  $i, j$  and  $k$ . This form is referred to as “GMEAM” in the present work due to the number of angular functions. The total potential energy is given by

$$V_{GMEAM} = \frac{1}{2} \sum_i^N \sum_{j \neq i}^N \phi_{IJ}(r_{ij}) + \sum_i^N U_I(n_i), \quad (3.29)$$

where

$$n_i = \sum_{j \neq i}^N \rho_J(r_{ij}) + \frac{1}{2} \sum_{j \neq i}^N \sum_{k \neq i,j}^N f_{IJ}(r_{ij})f_{IK}(r_{ik})g_{JIK}(\cos \theta_{jik}). \quad (3.30)$$

At first glance this looks like an ordinary MEAM potential, but further examination reveals that the density  $n_i$  depends on the species of atom  $i$ . It is thus more akin to a three-body extension of Finnis-Sinclair potentials where the “density” is interpreted as a wavefunction overlap integral, which of course depends on the species of each atom involved. Moreover, optimal corrections to the Effective Medium and Embedded Atom approximations have been shown to depend on the electrostatic potential[90] or electron density[91, 92, 93], of the “impurity” atom. Application of the GMEAM form, chosen for the versatility of the sixteen functions to be fit, to titanium-niobium alloys is the main achievement of the present work and is described in Chapter 6.

# Chapter 4:

## Optimization of Spline-Based Empirical Potentials

Due to the complexity of the large *ab initio* databases and the flexibility of spline-based potentials with many knots employed here, fitting is the most time-consuming and computationally demanding part of the development process. It is not a straightforward one-time application of an optimization routine to a single fitting database. Rather, an iterative process is required wherein about ten fits are performed simultaneously (referred to as a “batch”), the resultant potentials are tested and compared, and algorithm inputs and database contents are adjusted in response to the results.

First described in this chapter are the parameterizations of functions through cubic and quintic splines. The algorithms employed during optimization are then presented. In the end, the testing procedure and appropriate response to particular results such as under- or over-fitting and certain characteristics of the splines themselves, are discussed.

## 4.1 Spline-based parameterization

Spline functions take many forms but the most common are cubic splines, which are piecewise polynomial functions of degree three. A spline function of degree  $d$  consists of a set of  $N$  points called *knots* which are sequential along the independent axis, and a set of  $N - 1$  polynomials of degree  $d$  connected in a piecewise fashion at the knots. In order to evaluate the spline function, one must determine the  $d + 1$  coefficients for all  $N - 1$  polynomials.

The  $(N - 1)(d + 1)$  unknowns require a commensurate number of equations to determine. Each polynomial is fixed to the value of the knots which flank it, providing  $2(N - 1)$  equations. At each interior knot (i.e. not end-points) the splines on either side are required to be continuous up to their derivative of order  $d - 1$ , giving an additional  $(d - 1)(N - 2)$  equations. The remaining  $d - 1$  unknowns are determined by boundary conditions specifying some derivatives at each end-point. The user has some freedom in choosing which derivatives should be specified based on intended application.

Since cubic splines have discontinuous third derivatives, there are intrinsic limitations to how well they can model certain properties. For example, a cubic spline function will exhibit kinks in any quantity depending on second derivatives of the potential (e.g.  $C_{ij}$ - $P$  curves). If more accuracy for such properties is required, splines of higher degree can be used. In the present work, a potential parameterized by quintic (degree 5) splines is applied to high-pressure properties of tungsten. A cubic parameterization is sufficient to model Ti-Nb alloys at ambient pressure.

### 4.1.1 Boundary conditions for spline-based interatomic potentials

As discussed in Section 3.3, radial cutoffs defining the range of interaction are necessary in any interatomic potential. When parameterized by spline functions, boundary conditions consistent with the physical system must be supplied at these cutoffs. In all cases the first derivative at the outer cutoff should be “clamped” to zero such that forces vanish smoothly with interatomic separation. No such argument can be provided for the inner radial cutoff, so a “natural” spline is typically used. For  $d = 3$  a natural spline amounts to setting the second derivative be zero at the endpoint.

Cluster functional potentials, such as those which are the topic of the present work, require boundary conditions for angular and embedding functions as well. In general the embedding function boundaries should be natural, as this is the least restrictive BC and the embedding term is the most important part of the potential in terms of fitting error. A user has the most freedom in dealing with the angular functions. In the present work the angular functions are given natural boundary conditions. During the course of fitting, however, some success has been found in clamping the knot and first derivative to zero at  $\cos(\theta) = -1$ . It is worth experimenting with different conditions, as the best may vary from system to system.

### 4.1.2 Non-invariance of splines under rescaling

It is sometimes advantageous to re-scale the domain the embedding function during the course of fitting. This can help keep the embedding function constrained to a given range, but does not conserve forces, stresses or energies upon transformation. Let  $U(\rho)$  be a spline function and  $\alpha$  a real-valued scalar. The domain of the function

$U$  can be re-scaled by performing the following transformations:

$$\begin{aligned} U(\rho) &\rightarrow U(\rho/\alpha) \\ \rho &\rightarrow \alpha\rho. \end{aligned} \tag{4.1}$$

If  $U(\rho)$  were an analytic function, this gauge transformation would preserve the total energy for arbitrary  $\alpha$ . For spline functions the process of rescaling requires a redefinition of the knot boundaries, and maintaining an even spacing between knots necessitates sampling interpolated values for use as new knot values. The process of re-scaling is outlined algorithmically below. Let  $U(\rho)$  be the original embedding function with  $N$  spline knots  $\{x_i, y_i\}$  and  $\bar{U}(\bar{\rho})$  be the new spline with knots  $\{\bar{x}_i, \bar{y}_i\}$ :

- Compute the set  $\{\rho\}$  of  $\rho$  values in the fitting database
- Determine  $\rho_{min}$  and  $\rho_{max}$  from  $\{\rho\}$
- Set boundaries of new embedding function  $\bar{U}$  to be  $\rho_{min}$  and  $\rho_{max}$ :

$$\bar{x}_1 = \rho_{min}, \bar{y}_1 = U(\rho_{min})$$

$$\bar{x}_N = \rho_{max}, \bar{y}_N = U(\rho_{max})$$

- Determine remaining  $N - 2$  evenly spaced (by  $\Delta\rho$ ) knots for  $\bar{U}$  and take  $y$ -values from  $U(\rho)$ :

$$\bar{x}_i = \rho_{min} + i\Delta\rho, \bar{y}_i = U(\bar{x}_i)$$

- Determine scaling factor to keep the domain of  $\bar{U}$  in  $[-1, 1]$ :

$$\rho_{bound} = \max(-\rho_{min}, \rho_{max})$$

$$\alpha = 1/\rho_{bound}$$

- Rescale new knots and densities

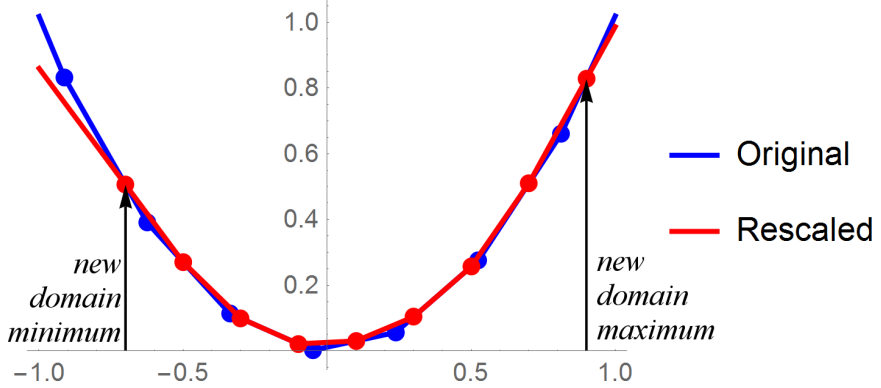


Figure 4.1: Demonstration of non-invariance of a linear spline under change of the domain. The original function is shown in blue, with knots represented as points. The rescaled function is shown similarly in red. Arrows indicate the minimum and maximum sampled values of the original domain. These values become the boundaries of the re-scaled spline and knots are distributed equally between them with  $y$ -values computed from the original function. The two functions differ in regions where successive re-scaled knots do not lie between the same two original knots. Note that this is a view *before* the new function’s boundaries are scaled toward  $[-1, 1]$ .

$$\bar{x}_i = \alpha \bar{x}_i$$

$$\bar{\rho} = \alpha \bar{\rho}$$

Figure 4.1 demonstrates the invariance of linear splines under the described re-scaling procedure. Changing the distribution of spline knots across the function provides a new spline which is not identical from the first, since the  $y$  values of the new knots are taken as *interpolated* values from the old function. Rescaling the embedding function of a pair functional does not conserve forces, stresses or energies and thus serves as a “mutation” in the language of evolutionary optimization.

Triplet terms in the potential are re-scaled along with the embedding function and total density in such a way as to keep the maximal value of radial prefactors fixed at unity. This is done e.g. for the “GMEAM” potential by simple multiplication and

division of the functions:

$$\begin{aligned} f_{IJ}(r_{ij}) &\rightarrow f_{IJ}(r_{ij})/f_{IJ}^{\max} \\ f_{IK}(r_{ik}) &\rightarrow f_{IK}(r_{ik})/f_{IK}^{\max} \\ g_{JIK}(\cos \theta_{jik}) &\rightarrow f_{IJ}^{\max} f_{IK}^{\max} g_{JIK}(\cos \theta_{jik}). \end{aligned} \tag{4.2}$$

Rescaling of the three-body terms does not require a changing of spline boundaries and so does not serve as a genetic mutation to the potential.

## 4.2 Global optimization via genetic algorithm

In the present work, the objective function for optimization is a weighted mean-squared error following the force-matching method of Ercolessi and Adams[1].

$$\mathcal{Z}(\mathbf{y}) = \sum_i^C W_i^2 (Q_i(\mathbf{y}) - Q_i^{DFT})^2, \tag{4.3}$$

where  $\mathbf{y}$  is the vector of spline-knot free parameters and  $C$  is the number of configuration properties  $Q_i$  (stresses, forces, energies) in the database. For the high-flexibility empirical potentials employed here,  $\mathbf{y}$  has around 200 components and  $C$  is on the order of  $10^4$ . The objective function  $\mathcal{Z}(\mathbf{y})$  is in general non-convex and potentially littered with local minima. The regions of  $\mathbf{y}$ -space for which  $\mathcal{Z}(\mathbf{y})$  is convex around some minimum are known as “basins,” and will trap any local optimization algorithm to their corresponding minimum.

Genetic (or “evolutionary”) algorithms (GA) have found wide success as versatile global optimization methods. The idea is based on treating variables as traits or genes, with points in the  $n$ -dimensional space being thought of as members of a population (here typically  $\sim 10\text{-}20$ ) which “breed” with one another at each iteration.

The generality of this idea is a major contributor to its success in both discrete and continuous optimization problems. Practitioners have a large degree of flexibility in defining the manner and order in which members of the population are bred.

Basin-hopping is an inherent property of genetic algorithms provided a population is properly initialized such that all of the members do not lie in the same local basin. Including mutations, or random perturbations to a member's genes inspired by biological evolution, can provide an effective means of basin hopping even for a population confined to a single local basin.

This section details the evolutionary optimization scheme used to produce empirical potentials presented in Chapters 5 and 6. The program was written by Dr. Jeremy Nicklas, and further details are described in his Ph.D. thesis [94].

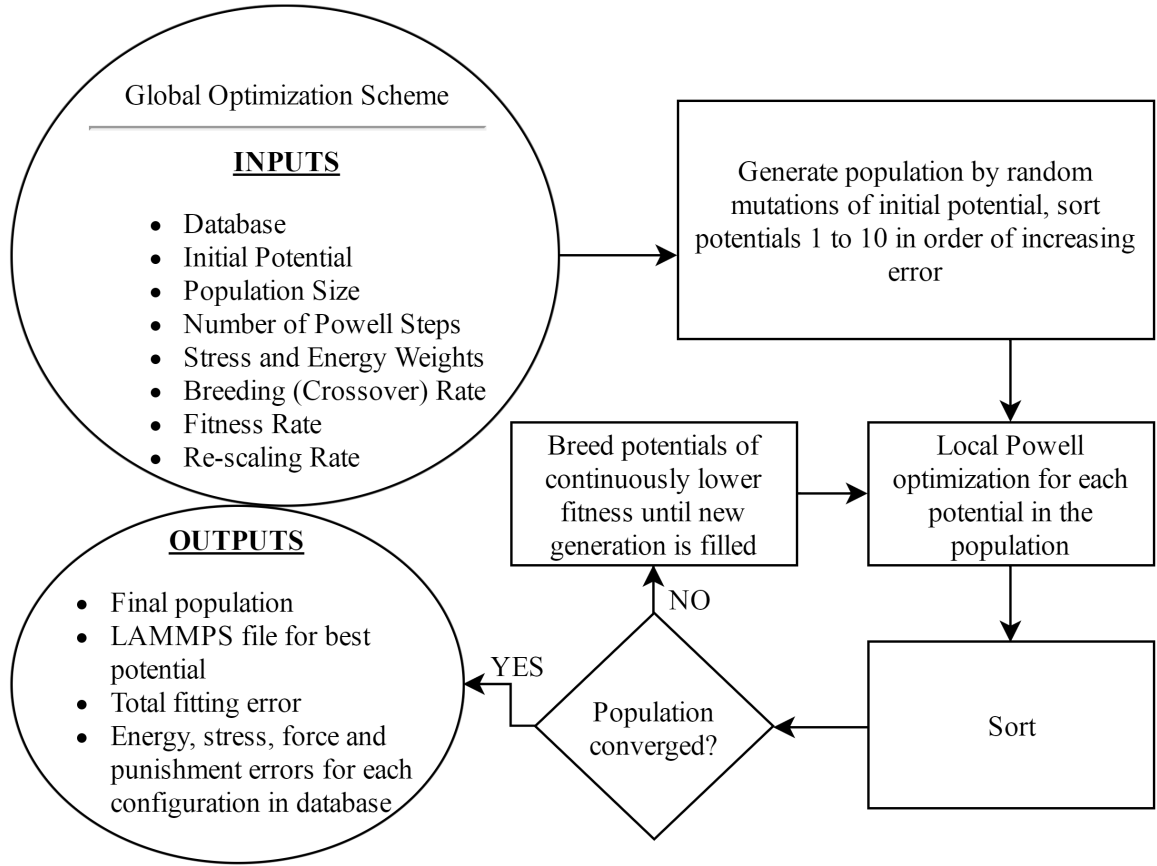


Figure 4.2: Diagrammatic representation of the global optimization scheme. Ovals represent the beginning and end of the algorithm, with lists of input and output quantities respectively. Rectangles are functional steps in the algorithm and diamonds are “if” statements. The population is deemed “converged” if the change in total error for every member of the population is less than  $10^{-3}$ . Partner selection and the breeding algorithm itself are discussed in more detail below.

Figure 4.2 describes the global optimization algorithm from inputs to outputs. The user provides a database of *ab-initio* forces, stresses and energies, an initial potential from which the rest of the population is seeded, the size of said population, the number of local conjugate-direction steps taken for each generation between breeding iterations, weights for quantities in the database, breeding, fitting and re-scaling rates. Outputs include the final population, a LAMMPS-format file for the best fit potential, and error information for the entire database.

A hybrid method is used wherein each new generation of potentials undergoes local optimization via Powell's method [95] for a fixed number of steps provided as input. The reason for this is due to the spline parameterization. If two members of a population are dissimilar (e.g. qualitatively different behavior of an angular function), breeding may result in a child potential with much higher error than either of the parents. This is due to the piece-wise nature of spline functions, the long-range effects of strong derivatives at knots, and the “crossover” manner of breeding employed here.

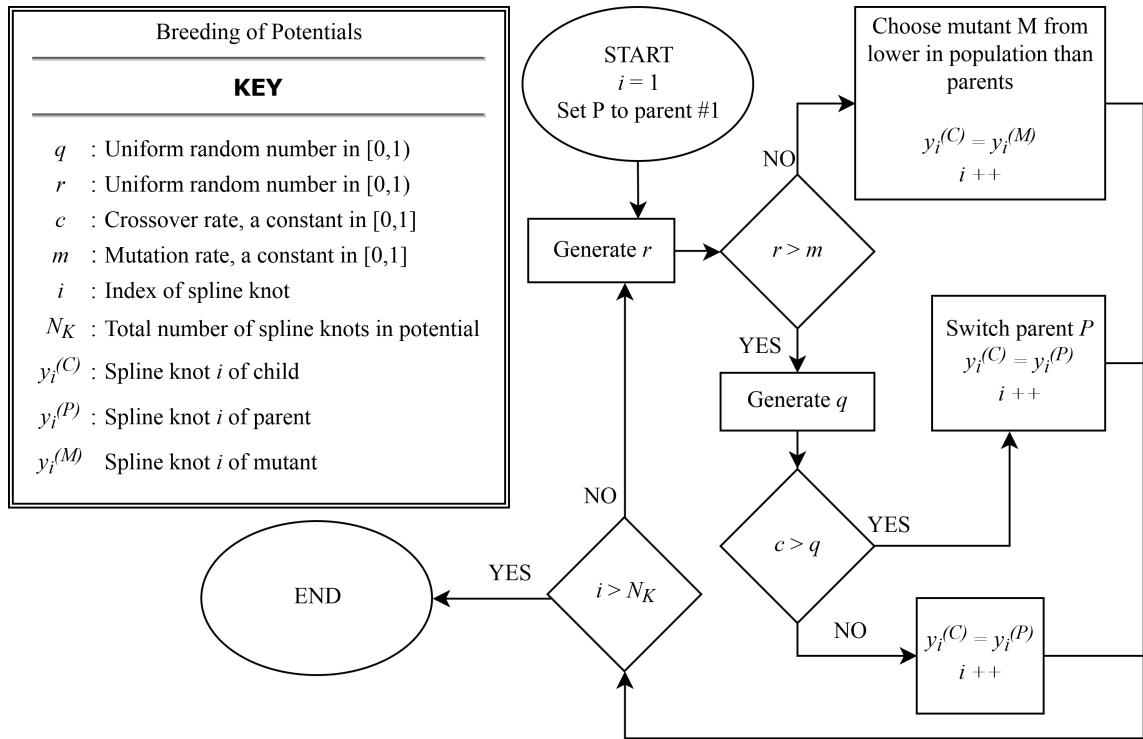


Figure 4.3: Diagrammatic representation of the algorithm used to breed two parent potentials to form a member of the next generation. Flowchart shape meanings are as described above and symbols are defined in the key. Knots are taken from the current parent  $P$  until a random number  $q$  is generated to be less than the input crossover rate  $c$ . The process ends when all child knots have been assigned  $y$  values.

Figure 4.2 describes the breeding of spline-based potentials within the evolutionary algorithm. Mutations are implemented by generating a uniform random number  $r$  and

checking it against the mutation rate  $m$ . If  $m < r$ , the knot is taken from a randomly chosen member of the population with lower fitness than the parents. Otherwise another uniform random number  $q$  is generated and compared to the “crossover” rate  $c$ . If  $q > c$ , the active parent  $P$  is switched and a knot is taken from it. If  $q < c$  a knot is taken from  $P$  without switching the active parent. A typical crossover rate for the present work is 20%, while mutation rates are typically  $\sim 0 - 5\%$ . Crossover breeding allows important features of the parent potentials to be mixed, but can result in long-range oscillations of the splines.

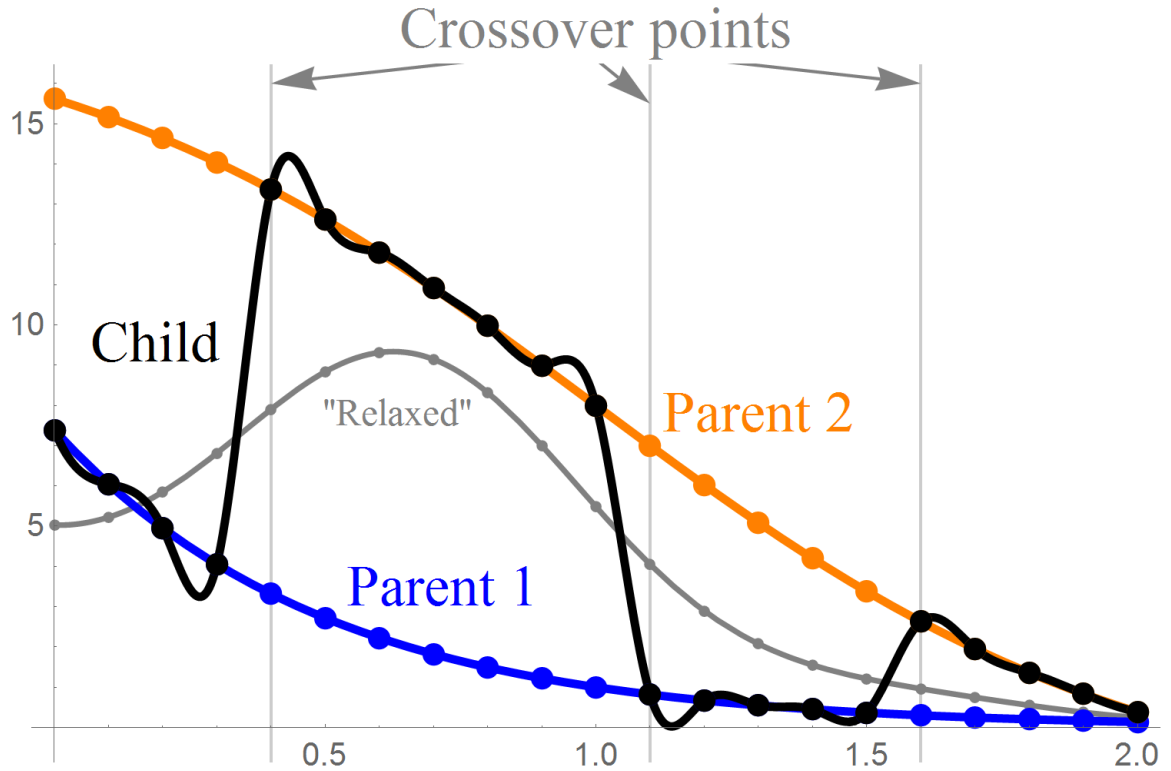


Figure 4.4: Crossover-breeding of two cubic spline functions. The first and second parents are shown in blue and orange, respectively, and the child is shown in black. A hypothetical post-downhill “relaxed” child function is shown in grey. Crossover points are depicted by vertical grey lines. When splines are significantly dissimilar (i.e. when their difference is much greater than their derivatives across successive knots), the child potential exhibits strong oscillations (and thus unphysically large forces) at and near the crossover points. Powell optimization on the child potential will tend to smooth out the knots and reduce the oscillations in the splines while potentially evolving new features such as the hump shown the “relaxed” curve.

Figure 4.2 shows the “crossover” breeding of two dissimilar cubic spline functions. The child potential takes knots from the first parent (blue) until  $q < c$  is satisfied (see Figure 4.2), whence knots are taken from the second parent (orange). Strong derivatives are exhibited by the child function (black) at and near the crossover points. Since the splines are forced to have continuous derivatives at the knots, nearby splines exhibit oscillation as a result of the large difference between parent functions at the

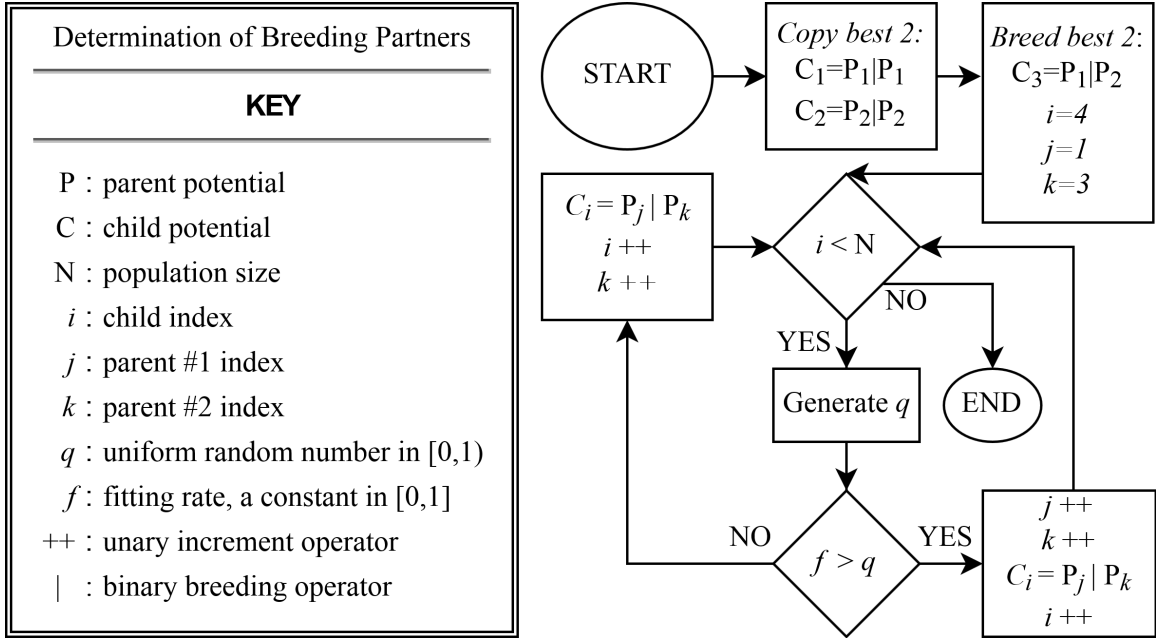


Figure 4.5: Diagrammatic representation of the algorithm used to determine breeding partners at each step in the evolutionary optimization. Rectangular panels represent algorithmic steps where commands are executed from top to bottom. Diamonds represent “if” statements and ovals represent the beginning and end. The two most-fit potentials are always copied into the next generation by breeding with itself. The first and second most fit potentials are also forced to breed.

crossover points. This effect is less pronounced when the difference between parent functions is small. A “relaxed” spline is shown in grey, representing the hypothetical child function after undergoing local minima. Breeding dissimilar splines can produce new genetic features, represented here by the hump in the relaxed function.

Figure 4.2 shows the method used for determining breeding partners in a sorted fashion. In all cases the best and second-best potentials are cloned to form the first two members of the next generation. The third member of the next generation is formed by breeding these top two and subsequent partners are chosen based on a uniformly generated random number  $q$  and a user-supplied “fitting rate”  $f$ . The use of hierarchical breeding in this fashion decreases the chances that a bad potential’s

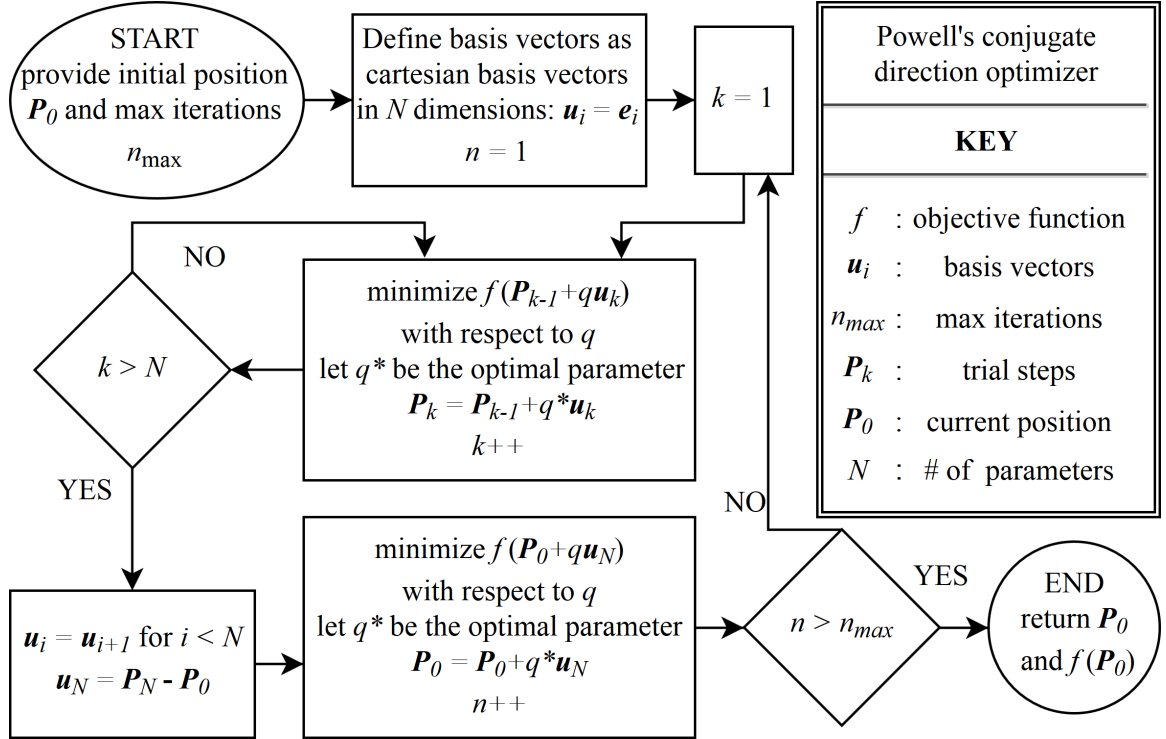


Figure 4.6: Algorithmic flowchart for Powell’s conjugate direction optimizer.

genes are passed on to the next generation, but the gene pool tends to be dominated by the top two potentials after a few generations. Saturation of the gene pool can be balanced by increasing the mutation and fitting rates.

The Powell[95] conjugate direction algorithm used in local optimization is useful for functions without a pre-defined mathematical form because no derivatives are necessary. The idea is to have a set of basis vectors, typically initialized as unit vectors in the multivariate space, and to perform a line-search optimization using linear combinations of these basis vectors. An algorithmic flowchart is shown in Figure 4.2. Since the local optimization is performed for every potential in a population, increasing the number of steps  $n_{max}$  can be computationally costly. In the present work, 20 to 60 steps was found to be effective.

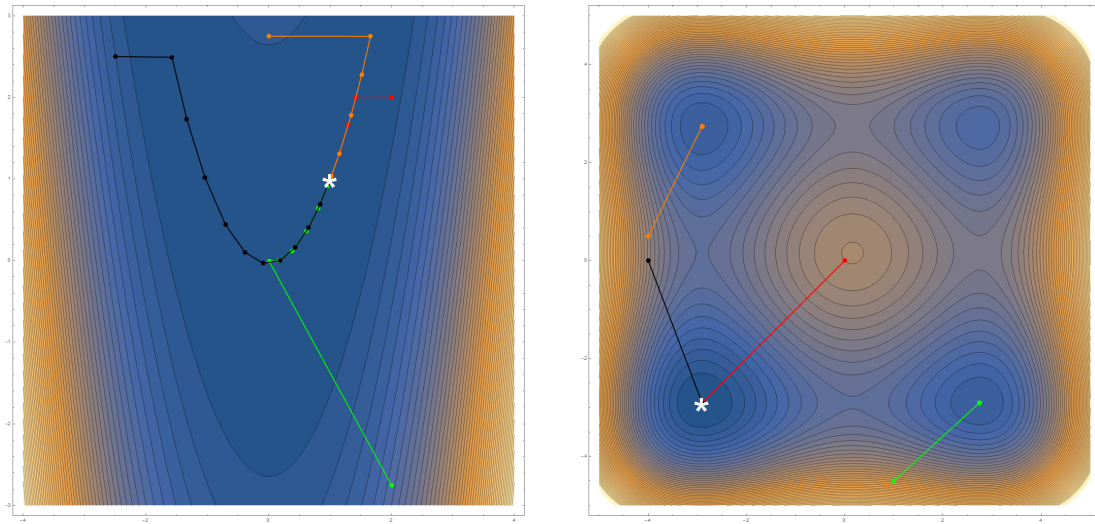


Figure 4.7: Comparison of Powell optimization performance for two functions. Points and lines show iterations of the algorithm from different starting positions. Global minima are marked by a white asterisk. Powell’s algorithm finds the global minimum of the Rosenbrock function (left) within about 10 iterations, but quickly converges to local minima when they are near the starting position (right).

### 4.3 Performing the right fit

It is not uncommon for simple potentials (e.g. Lennard-Jones or Finnis-Sinclair) to be fit to a small amount of very particular data, for example vacancy formation and migration, then employed for that purpose and rarely used again. Such models are said to have low *transferability* if their predictive power outside of the intended application is low.

Potentials with low transferability can be useful for extrapolating first principles data to system sizes impractical for  $\mathcal{O}(N^3)$  algorithms. However, practitioners must be careful when choosing a model, and the safe region of study is limited by the potential of choice.

It is thus desirable to produce an interatomic potential which can safely be used to study all — or at least most — of the interesting physical properties of a given system.

This necessarily means a larger fitting database, more free parameters in models, and thus a more complicated optimization procedure. Most advanced optimization algorithms (other than those intended specifically for convex spaces) involve some stochastic element, meaning they can give very different results when run twice on the same database. In general no optimization scheme can give a precise guarantee that the global minimum has been located without fully sampling the entire parameter space.

Such a large amount of variability typically means a large number of fits will be performed when searching for the “optimal” model. Mathematical optimization aside, the question of *which database* should be fit to in the first place is one which depends on the goals and time (in CPU- and man-hours) of the practitioner, but is not a simple “a-la carte” decision due to correlations between fitting data.

There is no clear prescription for navigating this complex problem of “choosing the right fit,” and intuition plays a significant role, but there are some rules of thumb which can typically be followed to at least get close to the right potential.

The general process is an iterative one where one fits a “batch” of ten to twenty potentials, tests them for a variety of properties compared to DFT and experiment, and analyzes the results. This section discusses some common situations encountered during the development process and appropriate responses to them, particularly for spline-based MEAM and MEAM-like models.

### 4.3.1 Under-fitting and over-fitting

One of the most important steps in fitting any model is obtaining a balance of free parameters and data to be fit. The precise ratio in general depends on the complexity of the model and data as well as the manner of parameterization, but the consequences of imbalance are commonly referred to as “under-fitting” and “over-fitting.”

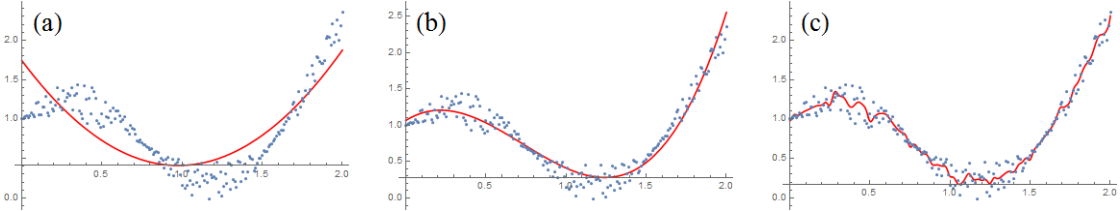


Figure 4.8: Simple examples of (a) under- (b) well- and (c) over-fit models. Red lines show model predictions while fitted points are shown in blue. The underlying data is a cubic polynomial with a sinusoidal random signal added.

When a model has too much flexibility, it can often match precisely every data point to which it's fit while destroying all predictive power. An over-fit interatomic potential is one with too many free parameters, where fitting error is very low but transferability is negligible. Such potentials will often incorrectly interpolate between widely spaced data points, so even simple properties like energy-volume curves could be wildly unphysical. As a result, over-fit potentials are easy to identify.

In contrast, a model with too little flexibility to match the fitting database is said to be “under-fit.” Such potentials will often be more realistic than over-fit ones, but will nonetheless exhibit significant fitting and testing errors. Examples of under-fit, well-fit and over-fit models are shown in Figure 4.3.1 (a), (b) and (c), respectively.

### 4.3.2 Saturating the spline functions

While spline parameterizations are useful for their implicit flexibility, care must be taken to ensure that the domains of each function are saturated with data such that each knot contributes to the fitting error. Since the first and second derivatives are forced to match at each knot, the forces derived from one knot are affected by the value of its neighbors. However, this is not in general sufficient to prevent a function from exhibiting unphysical oscillations in regions (i.e. angles, radii or total densities) which are not sampled in the database.

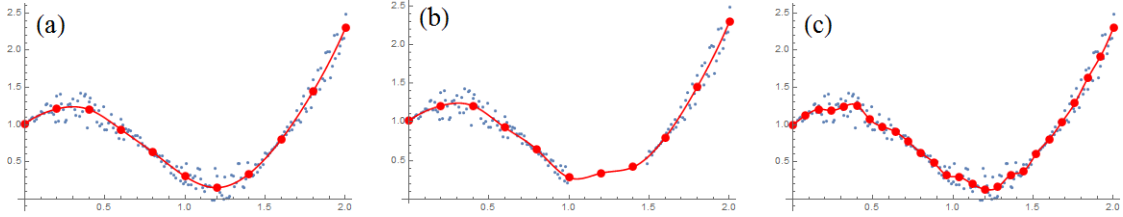


Figure 4.9: Examples of (a) a properly fit spline model (b) an under-saturated spline model and (c) an over-fit spline model. Red lines show cubic spline interpolants, red points represent spline knots and data points are shown in blue. One cannot in general distinguish an under-saturated spline from an over-fit spline without examining the distribution of data. Note that the over-fit model uses twice the number of spline knots to fit the same data set.

There is no clear way to discern an over-fit function from one whose domain has not been saturated aside from viewing the distribution of sampled angles, radii and total densities in comparison to the distribution of spline knots. Database contents, radial cutoffs and numbers of knots for each function should be chosen to ensure saturation before fitting in order to avoid mistaking an under-saturated potential from an over-fit one. Useful configurations for filling gaps include generalized stacking faults, ideal shear curves and high-temperature snapshots, the latter being the most effective at sampling many radii and triplet angles. Figure 4.3.2 provides examples of (a) a properly fit spline function, (b) an under-saturated spline and (c) an over-fit spline.

### 4.3.3 Trends within a batch of potentials

When performing ten or more fits simultaneously it is most efficient to present test results in a graphical fashion so as to quickly locate good models and spot patterns between fits in a batch. For this purpose a radial %-error presentation is employed wherein the radius  $r = 1$  is defined as zero error, the origin is -100% and  $r = 2$  is +100%. Batches are presented using a simplified version of these plots in an HTML

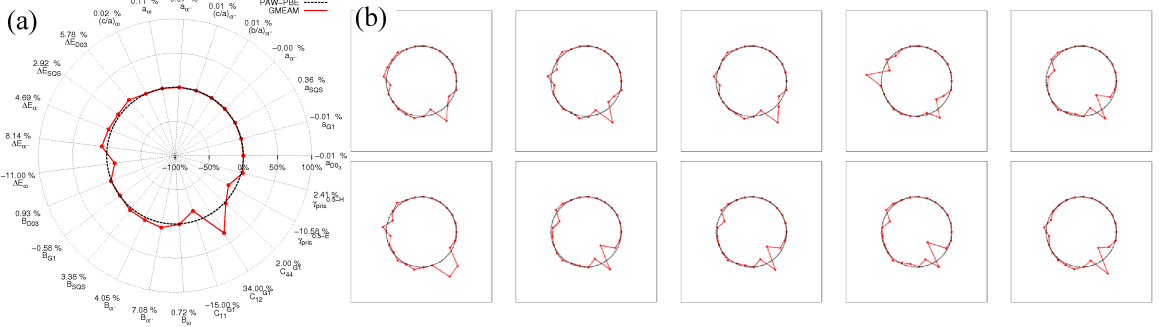


Figure 4.10: Representation of the fitting error in a radial distribution format. (a) shows the error for a single potential, with labels on each radial ray and the error axis. (b) shows a batch of ten fits with unlabeled radial graphs side-by-side for easy comparison.

table for easy access. An example presentation of (a) a single potential and (b) a batch is given in Figure 4.10.

Test results are a strong indicator of the quality of a fitted potential, but it is difficult to identify overfitting without examining the spline functions themselves. Figure 4.11 compares functions of (a) a well-balanced fit where model functions are smooth and (b) an over-fit potential where the number of parameters was too large for the size of the data set. Smooth functions do not guarantee a well-balanced fit, since “underfitting” (more data than the parameters can handle) will always produce smooth potentials with high fitting error.

Assuming the DFT calculations comprising the fitting database are well-converged, a number of conclusions can be drawn just by comparing potentials in a batch:

(1) If the distribution of errors is not consistent between most of the fitted potentials, the algorithm is not producing a reliable estimate of the global minimum with the provided parameters. Changes should be considered depending on the behavior of the splines:

- i. If the spline functions (radial ones in particular) oscillate wildly, increasing

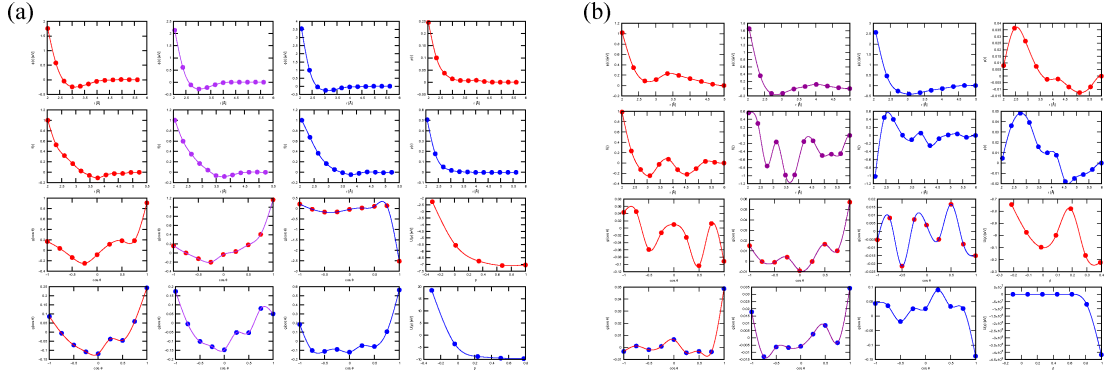


Figure 4.11: Splines functions from two GMEAM models: (a) A well-converged fit with smooth spline functions and sensible behavior at boundaries. (b) An overfit potential with too many parameters, where functions display frequent oscillation and non-physical behavior at the boundaries.

the number of local optimization steps can be useful. If a large number of Powell steps is already being used or increasing the number has little effect, the potential is probably being over-fit and fewer knots and/or more data are needed.

- ii. If the spline functions are smooth, underfitting is likely and more parameters are needed.
- (2) If the total fitting and testing errors are consistently high across the batch and:
- i. splines are smooth and similar, under-fitting is the problem and more knots and/or fewer data are needed.
  - ii. splines are oscillatory and dissimilar, more downhill steps are needed.
  - iii. splines are dissimilar but not wildly oscillatory, more “genetic diversity” is needed by increasing the breeding, rescaling or mutation rates.
- (3) If the fitting error is consistently low but testing error is high, the fitting database needs to be refined depending on the behavior of the splines:

- i. If the splines are smooth and consistent, a good balance of data to parameters has been found. In this case, related configurations in the database (e.g. close points on an E-V curve or a transition pathway) should be removed and replaced with data for which the potentials performed poorly in testing.
  - ii. If the splines are highly oscillatory, over-fitting is likely and the database should be expanded with configurations where tests were unsatisfactory.
- (4) If the fitting and testing errors are consistently low, a global minimum has likely been found. At this point, fine-tuning the potential by adjusting weights of energies, stresses, or individual configurations can be done. Data can be added, but a practitioner should be careful not to upset the balance of parameters and database size.

## Chapter 5:

# Cluster Functional for Tungsten

In this chapter we develop a unique semi-empirical potential based on a robust database of *ab initio* calculations that samples much of the potential-energy landscape. Our model combines the Stillinger-Weber (SW)[96] form with the modified embedded atom method[97] (MEAM) form with functions parameterized by quintic splines. The potential was fit by Dr. Jeremy Nicklas [94] and applied to high-pressure phase transitions by the present author [98]. Section 5.1 describes the density-functional theory (DFT) calculations comprising the large fitting database. Accuracy of the fitted potential is demonstrated in Section 5.2 by comparing SWMEAM to DFT for the various structural and elastic properties to which it was fit. Given that the potential is fit directly to important crystallographic defects, structural properties and elastic constants, transferability is demonstrated in Section 5.3 by examining SWMEAM predictions for  $\frac{1}{2}\langle 111 \rangle$  screw dislocation core structure, deformation twinning and detwinning of a nanorod, and dynamics of bcc and fcc tungsten at high pressure. Conclusions are given in Section 5.4.

## 5.1 DFT database and fitted parameters

The *ab-initio* fitting database contains 596 configurations with a total of 16,860 atoms and thus 54,752 force components, stress components and energies to be fit. Configurations in the database include volumetric strains of bcc, fcc, hcp,  $\beta$ -W (A15),  $\beta$ -Ta ( $\beta$ -U) and  $\omega$ -Ti. Tetragonal strains are included for hcp and  $\omega$ -Ti structures to ensure accurate  $c/a$  values. The database also contains elastic constants of the bcc phase at pressures between 0 and 100 GPa, in increments of 25 GPa, using volume-conserving orthorhombic and monoclinic strains of 0.5 % for  $C' = \frac{1}{2}(C_{11} - C_{12})$  and  $C_{44}$ , respectively. At zero pressure, configurations with orthorhombic strains up to 10 % and monoclinic strains up to 40 % are added. Unrelaxed symmetry-inequivalent configurations of  $\langle 110 \rangle$  and  $\langle 112 \rangle$   $\gamma$ -surfaces, ideal shear strain and vacancy migration are included at five equally spaced pressures between 0 and 100 GPa. Relaxed zero-pressure structures containing a vacancy at the lattice site and halfway along the  $\langle 111 \rangle$  migration path are also added. A  $7 \times 7 \times 7$  bcc supercell with a single atom displaced by 0.006 Å ensures accurate force-constants and phonons via the small-displacement method[99, 41]. Using a supercell of this size reduces the interaction of the displaced atom with its images across periodic boundaries and thus improves the accuracy of calculated force-constants and phonon dispersions. Relaxed low-index free surfaces as well as crowdion, octahedral,  $\langle 111 \rangle$ -split and  $\langle 110 \rangle$ -split self-interstitial configurations are included. *Ab-initio* MD snapshots of 125-atom bcc supercells at 1620 K, 2960 K and a liquid tungsten at 6730 K are added to improve performance for simulations at high temperature. A 36-atom hcp supercell at 100 K is also included. Lastly, a mesh of 36 points on the Bain[60] (bcc-fcc) and Burgers[59] (bcc-hcp) energy surfaces at pressures of 0 GPa and 700 GPa in addition to 600 GPa for the Bain path and 800 GPa for the Burgers path are included to ensure that the potential can be used

to explore properties of these close-packed phases at extreme pressures.

Parameters for the fitted potential and plots of the final splines are given in Table 5.1 and Figure 5.1 respectively.

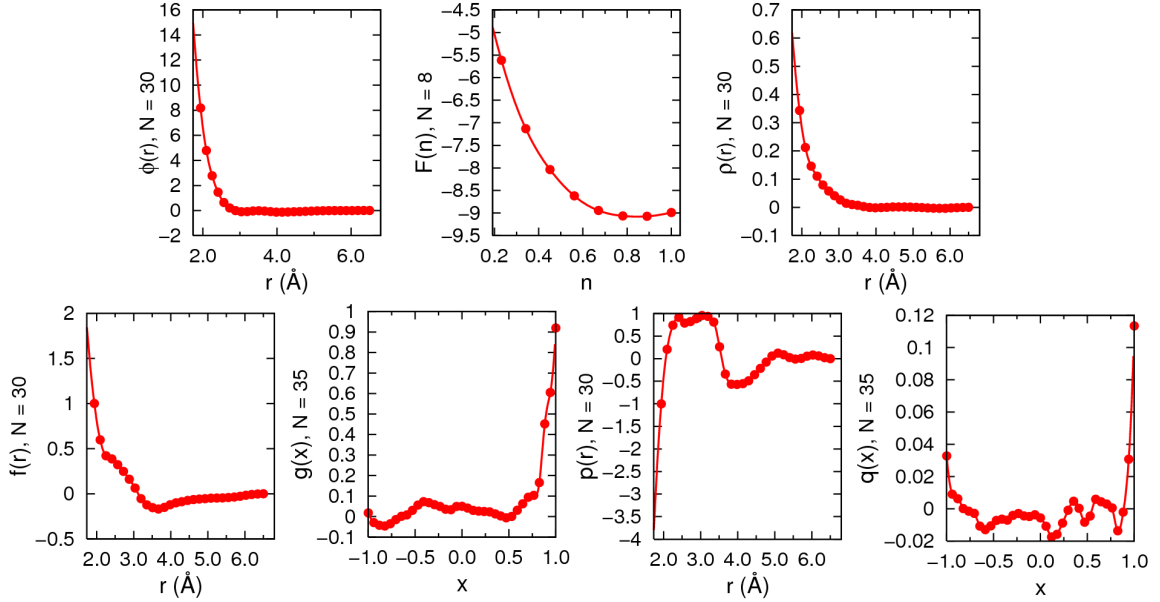


Figure 5.1: The seven quintic splines comprising the functions of our SWMEAM model. The embedding function here is given the symbol  $F(n)$ .

## 5.2 Accuracy of the fitted potential

We demonstrate the accuracy of the fitted SWMEAM potential through the energetics of non-equilibrium structures, crystallographic defects, thermodynamic properties and phonon dispersion. All SWMEAM calculations in this work (other than those necessary for fitting) are performed in the Large-scale Atomic/Molecular Massively Parallel Simulator (LAMMPS)[100]. Compatibility of the module has been verified for LAMMPS versions as recent as 17 November, 2016. If at any step during an MD run the density seen by an atom exceeds the embedding function domain, the embedding energy is linearly extrapolated from the nearest endpoint.

Table 5.1: Parameters specifying the seven cubic splines of the SWMEAM tungsten potential. The first part of the table lists independent variables for each spline function, the bounds of such, and the number of spline knots  $N$ . In the middle part, values of the spline functions are tabulated for each knot  $i$ , where  $t_i = t_{\min} + (i - 1)(t_{\max} - t_{\min})/(N - 1)$ . Lastly, first derivatives are listed for each spline at its endpoint.

	$\phi$	$\rho$	$U$	$f$	$g$	$p$	$q$
$t$	$r$ [Å]	$r$ [Å]	$n$	$r$ [Å]	$\cos(\theta)$	$r$ [Å]	$\cos(\theta)$
$t_{\min}$	1.936	1.936	0.231451	1.936	-1.00	1.936	-1.00
$t_{\max}$	6.50	6.50	1.00	6.50	1.00	6.50	1.00
$N$	30	30	8	30	35	30	35
$i$	$\phi(r_i)$ [eV]	$\rho(r_i)$	$U(n)$ [eV]	$f(r_i)$	$g(x_i)$	$p(r_i)$	$q(x_i)$ [eV]
1	8.17754794	0.34354505	-5.61454815	1.00000451	0.01826953	-1.00355858	0.03275867
2	4.78088386	0.21248938	-7.13213530	0.59803251	-0.02895637	0.20528502	0.00908138
3	2.76877268	0.14610410	-8.03756015	0.42174644	-0.04189862	0.74087499	0.00625761
4	1.46070080	0.11067492	-8.61953525	0.38588088	-0.04592673	0.91254496	0.00010593
5	0.64017812	0.07925502	-8.94487218	0.32281049	-0.03450663	0.78648214	-0.00154648
6	0.20082462	0.05773259	-9.06465740	0.24776621	-0.01456063	0.82030055	-0.00285253
7	-0.00765327	0.04145698	-9.07252007	0.16176067	0.00164664	0.88605788	-0.01075190
8	-0.10152106	0.02676237	-8.98725594	0.06295668	0.00808308	0.95485119	-0.01295875
9	-0.09072809	0.01461594	-	-0.05352359	0.03015642	0.93639061	-0.01060539
10	-0.03360000	0.01025421	-	-0.12298181	0.05630755	0.80917294	-0.00725918
11	-0.01263542	0.00743289	-	-0.15336078	0.07257101	0.26181009	-0.00644182
12	-0.04609033	0.00312525	-	-0.16835342	0.06806116	-0.34277179	-0.00705714
13	-0.09178435	-0.00007454	-	-0.15045670	0.05831171	-0.56718711	-0.00411671
14	-0.12451900	-0.00144470	-	-0.12148391	0.04964783	-0.57293020	-0.00294010
15	-0.13252729	-0.00080199	-	-0.10079003	0.03568623	-0.55459986	-0.00439403
16	-0.11926969	0.00044550	-	-0.08713686	0.03376337	-0.49005332	-0.00484268
17	-0.10168872	0.00142523	-	-0.07416516	0.04927750	-0.35497080	-0.00374903
18	-0.08543444	0.00170742	-	-0.06395072	0.04988678	-0.21733041	-0.00567228
19	-0.06753495	0.00143689	-	-0.05841828	0.04155554	-0.07601496	-0.01087031
20	-0.04517064	0.00096186	-	-0.05333600	0.03071994	0.05621734	-0.01747516
21	-0.02724563	0.00011312	-	-0.04830354	0.02661144	0.12120550	-0.01587746
22	-0.01558261	-0.00083410	-	-0.04680635	0.02515616	0.08589555	-0.00888091
23	-0.00722958	-0.00184725	-	-0.04563719	0.02305014	0.02426416	-0.00090735
24	-0.00526288	-0.00288883	-	-0.04204248	0.01333036	-0.00950960	0.00463563
25	-0.00738615	-0.00349420	-	-0.03559011	0.00344994	0.00582449	0.00027324
26	-0.00672710	-0.00318169	-	-0.02703034	-0.00616400	0.05373423	-0.00829522
27	-0.00345596	-0.00211846	-	-0.01676385	0.00075618	0.08057652	-0.00451289
28	-0.00067225	-0.00098092	-	-0.00801562	0.03134535	0.06074919	0.00590844
29	0.00018443	-0.00028357	-	-0.00238667	0.06236685	0.02015950	0.00434745
30	0.00000000	-0.00000000	-	0.00000000	0.09427033	0.00000000	0.00293599
31	-	-	-	-	0.10348664	-	0.00052140
32	-	-	-	-	0.16594669	-	-0.01363307
33	-	-	-	-	0.45196039	-	-0.00205961
34	-	-	-	-	0.60528155	-	0.03072894
35	-	-	-	-	0.91946180	-	0.11345596
$i$	$\phi'(r_i)$ [eV/Å]	$\rho'(r_i)$ [Å $^{-1}$ ]	$U'(n)$ [eV]	$f'(r_i)$ [Å $^{-1}$ ]	$g'(x_i)$	$p'(r_i)$ [Å $^{-1}$ ]	$q'(x_i)$ [eV]
1	-26.28469957	-1.06808883	-17.15418928	-3.28496099	-1.20699864	10.36595022	-0.68561309
N	0.00000000	0.00000000	1.22019954	0.00000000	8.53609196	0.00000000	1.97868195

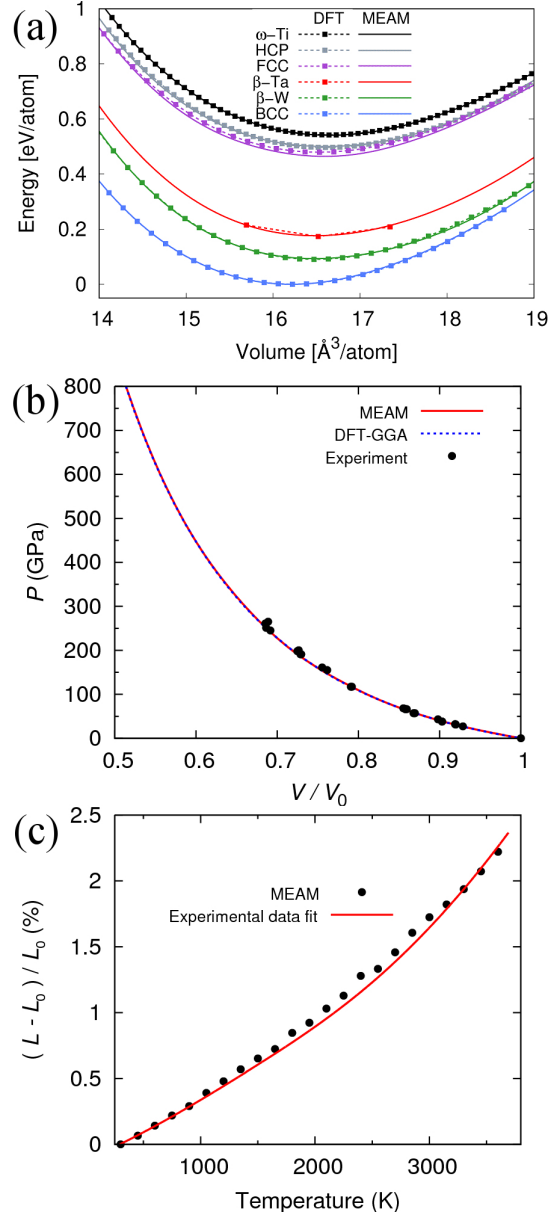


Figure 5.2: (a) Comparison of energy-volume curves between SWMEAM and DFT for six crystal structures. Curves are ordered vertically according to the key. Our empirical potential reproduces the energies of each phase relative to that of the bcc ground state. (b) Pressure-volume relation for tungsten as computed by SWMEAM and DFT at 0 K compared with data from shock experiments[101] at room temperature. SWMEAM shows agreement with both experimental and *ab-initio* results, even at extreme pressures. (c) Thermal expansion of tungsten predicted by SWMEAM agrees with experimental data fit[102] up to the melting point of 3695 K.

### 5.2.1 Energetics and elastic properties

Figure 5.2(a) shows the GGA-DFT and SWMEAM energy-volume relations for six distinct phases including A15  $\beta$ -W and high-energy close-packed structures. SWMEAM accurately predicts energies of all six phases relative to the ground state. An equilibrium bcc lattice constant of 3.189 Å is predicted by both GGA-DFT and SWMEAM, compared to the published experimental values between 3.15 and 3.165 Å[103, 104, 105]. It is well known now that GGA tends to overestimate the lattice constant of metals; the reason for this is discussed in Wang *et al.*[106] as well as Favot and Dal Corso[107] and references therein.

Figure 5.2(b) compares bcc tungsten pressure-volume relations as computed with SWMEAM, GGA-DFT, and measured through shock experiments[101]. SWMEAM and GGA-DFT curves, obtained by static calculations of volumetric strain, are indistinguishable for pressures through 800 GPa and in excellent agreement with experimental results up to 300 GPa, indicating applicability of the fitted SWMEAM potential to high-pressure physics in tungsten.

Figure 5.2(c) compares linear thermal expansion predictions by SWMEAM to experimental results[102] for temperatures between 300 K and the experimental melting point of 3695 K. Constant N-P-T MD simulations of 2000 atoms at  $P = 1$  atm yield the thermal-expansion curve. Each MD simulation runs for 50,000 steps with a 1 fs timestep and the lattice constant for each temperature is determined by averaging over the last 5,000 simulation steps. SWMEAM shows excellent agreement with experiment up to 1,000 K and remains within 1 % of the experimental fit for all temperatures considered, indicating that the potential interpolates between temperatures included in the fitting database.

Table 5.2 shows the zero-pressure bcc elastic constants of the present SWMEAM

Table 5.2: Zero-pressure elastic constants of bcc tungsten in GPa.

	B	C <sub>11</sub>	C <sub>12</sub>	C <sub>44</sub>
SWMEAM <sup>a</sup>	319	550	204	147
GGA <sup>a</sup>	304	513	199	142
F-S <sup>b</sup>	309	520	204	161
LDA <sup>c</sup>	320	552	204	149
F-S <sup>d</sup>	310	525	203	159
F-S <sup>e</sup>	310	522	204	161
EAM <sup>f</sup>	308	520	202	159
BOP <sup>g</sup>	310	522	204	161
Expt. <sup>h</sup>	308–314	501–521	199–207	151–160

<sup>a</sup>SWMEAM and GGA-DFT results of this work.<sup>b</sup>Finnis-Sinclair results of Wang *et al.*[19]<sup>c</sup>LDA-DFT results of Einarsdotter *et al.*[57]<sup>d</sup>Finnis-Sinclair results of Derlet *et al.*[17]<sup>e</sup>Finnis-Sinclair results of Ackland *et al.*[13]<sup>f</sup>EAM results of Zhou *et al.*[16]<sup>g</sup>Bond-order potential results of Mrovec *et al.*[18]<sup>h</sup>Expt. results of Bolef *et al.* from 77 to 500 K[108]

and GGA-DFT results, compared to previous *ab initio* calculations and other interatomic potentials. The bulk modulus B and C<sub>11</sub> predicted by SWMEAM are higher than experimental and GGA results but consistent with the LDA work of Einarsdotter *et al.*[57]. The pressure-dependence of bcc elastic constants is shown in Figure 5.3; SWMEAM does not predict a monotonic increase of C<sub>ij</sub> but remains within 21 % of the GGA-DFT values.

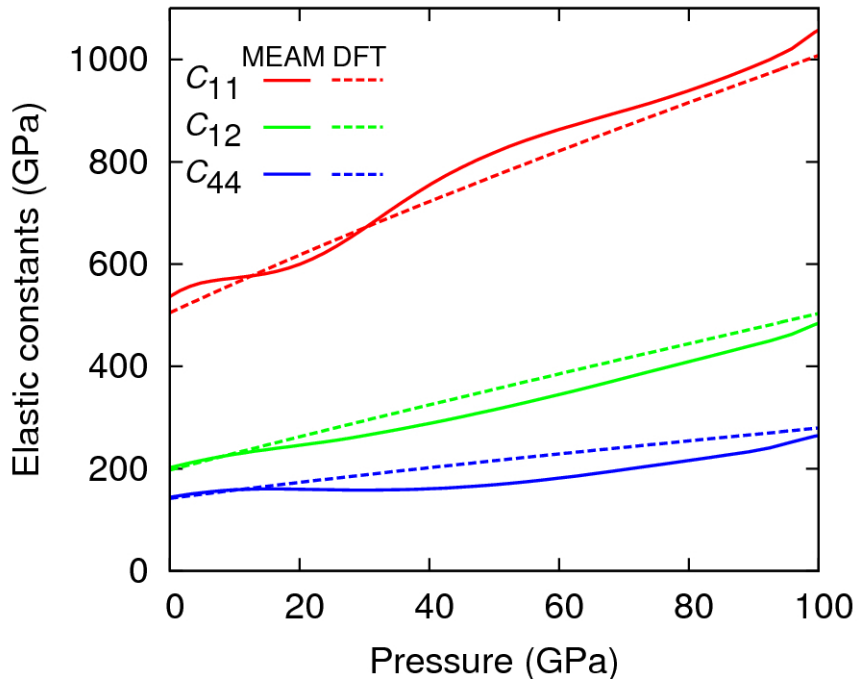


Figure 5.3: Elastic constants versus pressure for bcc tungsten as computed with GGA-DFT and the fitted potential. SWMEAM produces elastic constants within 21% of the DFT values for all pressures shown.

Figure 5.4 shows phonon dispersion of equilibrium bcc tungsten as computed with SWMEAM and DFT, compared to inelastic neutron scattering results of Chen and Brockhouse[109]. Dispersions are calculated using the finite-displacement method in a  $7 \times 7 \times 7$  primitive bcc supercell. DFT dispersion agrees well with experiment but exhibits oscillations in the longitudinal (low-lying) branch near the  $H$ -point, a feature also found in density-functional perturbation theory results within LDA-DFT[57]. Overall SWMEAM tracks both DFT and experiment but underestimates the frequency along the  $L[\xi\xi\xi]$  branch, particularly near the  $\omega$  mode at  $\xi = \frac{2}{3}$ .

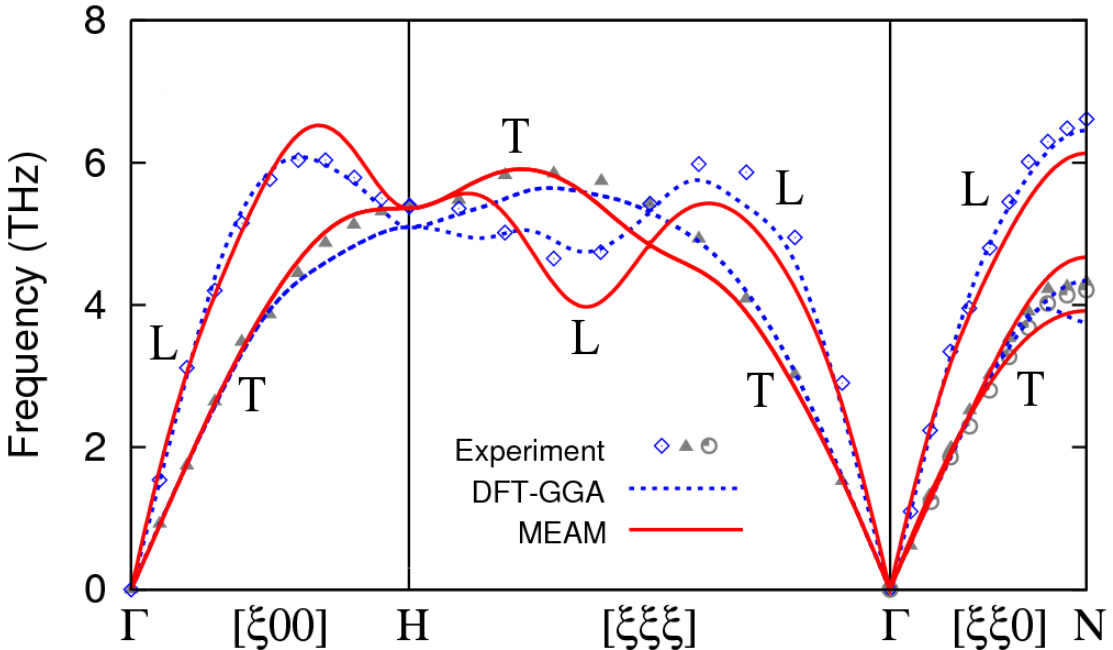


Figure 5.4: Phonon dispersion for bcc W at zero pressure as calculated by DFT and SWMEAM, compared with inelastic neutron scattering data of Chen and Brockhouse[109].

### 5.2.2 Point and planar defects

Table 5.3 lists the energies of vacancies and self-interstitial atoms (SIAs) in bcc tungsten, essential quantities for the accurate modeling of plasticity. Present SWMEAM and DFT calculations use a  $5 \times 5 \times 5$  cubic supercell. Atomic positions are relaxed to 0.01 eV. Geometric details of bcc SIA calculations can be found in Xu and Moriarty[112]. GGA-DFT calculations of Becquart *et al.*[110] and the present work indicate the  $\langle 111 \rangle$ -dumbbell to be the most energetically-favorable self-interstitial, as do the present SWMEAM potential and F-S potentials of Derlet[17] and Ackland[13]. Experiments[113, 114] and previous MD studies[16] found the  $\langle 011 \rangle$ -dumbbell to be the favored self-interstitial structure in tungsten, but recent work[115] combining the ob-

Table 5.3: Table of vacancy and self-interstitial formation energies (in eV) for bcc tungsten. Entries with angle-brackets indicate that the defect in question relaxes to the dumbbell configuration shown.

Defect	SWMEAM <sup>a</sup>	GGA <sup>a</sup>	F-S <sup>b</sup>	GGA <sup>c</sup>	F-S <sup>d</sup>	F-S <sup>e</sup>	EAM <sup>f</sup>	GGA <sup>g</sup>
Vac. Formation	2.99	3.17	3.58	3.11	3.56	3.63	3.57	3.56
Vac. Migration	1.73 <sup>†</sup>	1.70 <sup>†</sup>	1.43	1.66	2.07	1.44	2.98 <sup>†</sup>	1.78
Vac. Activation	4.72 <sup>†</sup>	4.87 <sup>†</sup>	5.01	4.77	5.63	5.07	6.55 <sup>†</sup>	5.34
$\langle 001 \rangle$ Dumbell	11.15	$\langle 111 \rangle$	11.53	11.74	11.51	9.82	12.20	11.49
$\langle 011 \rangle$ Dumbell	9.98	10.64	9.86	10.10	9.84	9.64	9.704	9.84
$\langle 111 \rangle$ Dumbell	9.73	10.31	9.58	9.82	9.55	9.82	10.56	9.55
Octahedral	11.76	12.42	11.72	11.99	11.71	10.02	12.03	11.68
Tetrahedral	10.54	$\langle 111 \rangle$	10.93	11.64	11.00	10.00	$\langle 011 \rangle$	11.05

<sup>†</sup>Unrelaxed calculation by present authors.

<sup>a</sup>SWMEAM and GGA-DFT results of this work.

<sup>b</sup>Finnis-Sinclair results of Wang *et al.*[19]

<sup>c</sup>GGA-DFT results of Becquart *et al.*[110]

<sup>d</sup>Finnis-Sinclair results of Derlet *et al.*[17]

<sup>e</sup>Finnis-Sinclair results of Ackland *et al.*[13]

<sup>f</sup>EAM results of Zhou *et al.*[16]

<sup>g</sup>GGA-DFT results of Nguyen-Manh *et al.*[111]

ject kinetic monte carlo (OKMC) method with dislocation loop measurements found OKMC simulations of  $\langle 111 \rangle$  interstitials and 1D migration best match experiment. Vacancy formation and migration energies predicted by SWMEAM compare favorably with present *ab-initio* results and those of Becquart and Domain[110] while existing F-S and EAM tungsten potentials are in closer agreement with GGA results of Nguyen-Manh *et al.*[111].

Figure 5.5 presents unrelaxed vacancy migration pathways at five equally-spaced pressures between 0 and 100 GPa. Calculations are performed using a 127-atom  $4 \times 4 \times 4$  cubic bcc supercell with migration in the  $\langle 111 \rangle$  direction. Overall SWMEAM tracks well with the DFT results; minor discrepancies are found when the vacancy lies near the lattice site and halfway between two lattice sites.

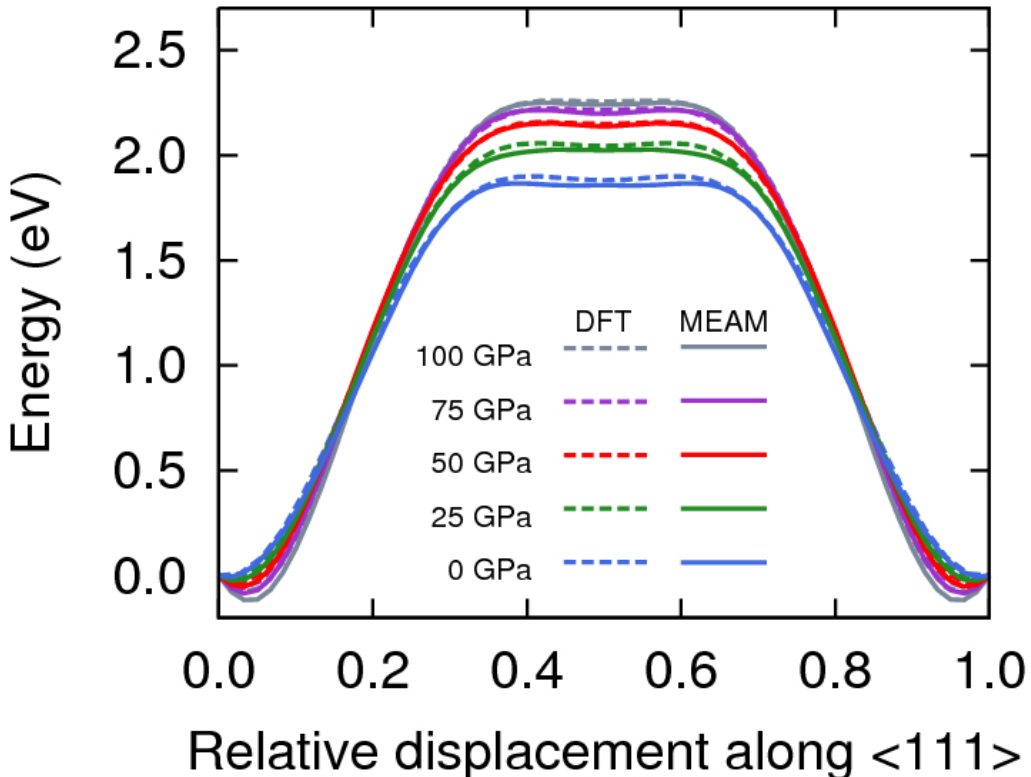


Figure 5.5: Vacancy migration pathway as calculated in GGA-DFT and SWMEAM at multiple pressures. The shallow local minimum at  $\langle \frac{1}{2} \frac{1}{2} \frac{1}{2} \rangle$  is predicted by both DFT and SWMEAM to increase between 0 and 100 GPa, though this effect is non-monotonic in SWMEAM.

Figure 5.6 shows unrelaxed generalized stacking fault energies (GSFEs) at five pressures on the  $\{112\}$  and  $\{110\}$  planes as a function of relative displacement along  $\langle 111 \rangle$  for SWMEAM and DFT. While bcc metals are less prone to stacking-fault formation than their close-packed counterparts, they have been observed in Fe, Nb, W and Mo-35%Re to exist on  $\{112\}$  and  $\{110\}$  planes, formed by the dissociation of  $\frac{1}{2}\langle 111 \rangle$  dislocations[116]. Relaxed GSFE curves, computed with SWMEAM at zero pressure, do not predict the presence of any metastable stacking fault configurations. At all pressures, SWMEAM agrees with DFT to within a few meV/ $\text{\AA}^2$ , and thus should be suitable for studying the effect pressure on  $\{112\}\langle 111 \rangle$  and  $\{110\}\langle 111 \rangle$  slip

systems.

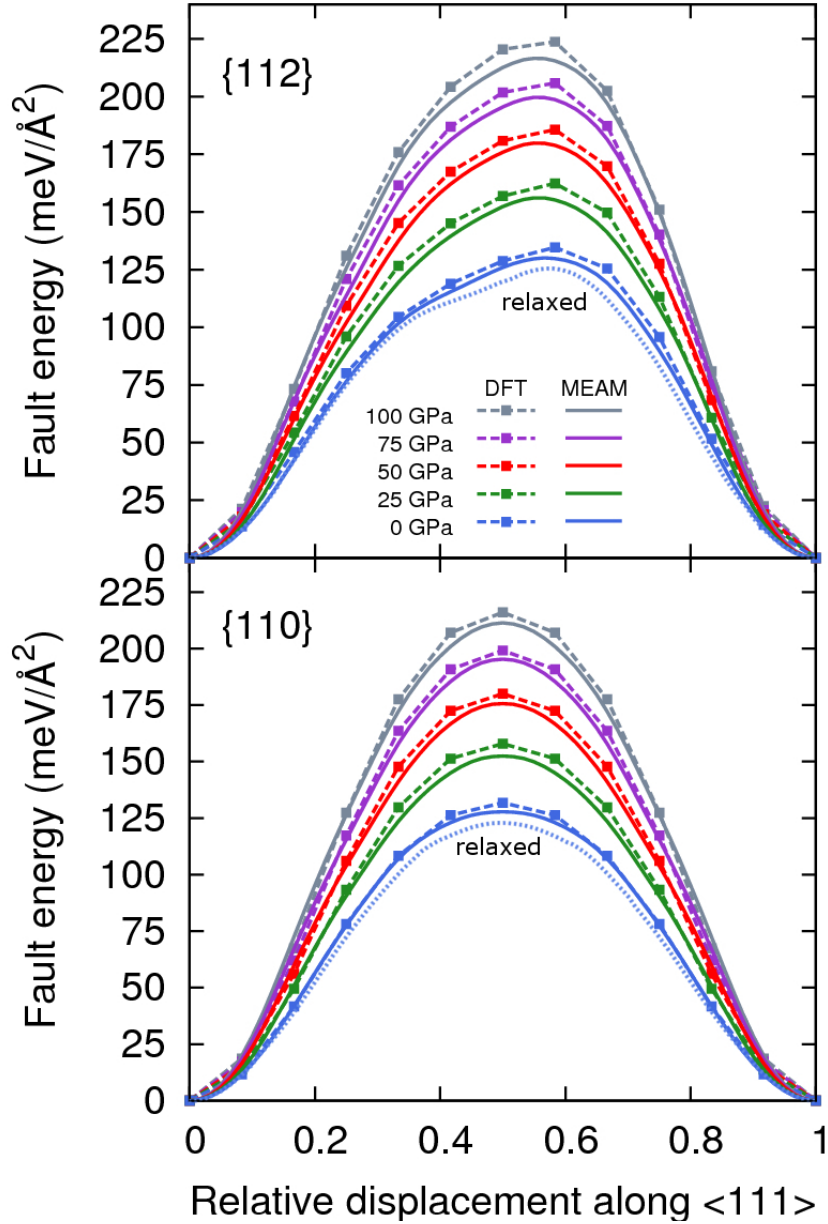


Figure 5.6: Unrelaxed low-index generalized stacking fault energies (GSFE) for bcc tungsten. SWMEAM accurately models the evolution of both {110} and {112} faults with pressure. Relaxed GSFE curves computed with SWMEAM are shown as dotted lines for 0 GPa. Relaxation lowers fault energy slightly but does not result in any metastable configurations.

Table 5.4: Energy and structural relaxation of low-index free surfaces in bcc tungsten. Surface energies  $E$  are given in meV/ $\text{\AA}^2$  and the changes  $\Delta_{12}$  in inter-planar spacing between the first two planes of the surface, where available, are given in units of percent.

	SWMEAM <sup>a</sup>	GGA <sup>a</sup>	F-S <sup>b</sup>	GGA <sup>c</sup>	F-S <sup>e</sup>	GGA <sup>f</sup>	AMEAM <sup>b</sup>	BOP <sup>g</sup>	MEAM <sup>h</sup>	Expt. <sup>i,j</sup>
$E_{001}$	233	245	186	289	183	487	373	237	243	—
$\Delta_{12}^{001}$	-5.7	-11.5	-0.9	—	-0.7	—	—	-2.5	-3.2	—
$E_{011}$	198	200	159	249	161	398	353	163	214	—
$\Delta_{12}^{011}$	-3.8	-3.8	-1.1	—	-0.5	—	—	-1.0	-3.0	—
$E_{111}$	204	216	—	278	—	449	314	—	271	—
$\Delta_{12}^{111}$	-18.9	-21.6	—	—	—	—	—	—	-13.2	—
$E_{poly}$	—	—	—	—	—	—	—	—	—	187 <sup>i</sup> , 216 <sup>j</sup>

<sup>a</sup>SWMEAM and GGA-DFT results of this work.

<sup>b</sup>Finnis-Sinclair results of Wang *et al.*[19]

<sup>c</sup>GGA-DFT results of Vitos *et al.*[117]

<sup>d</sup>Finnis-Sinclair results of Derlet *et al.*[17]

<sup>e</sup>Finnis-Sinclair results of Ackland *et al.*[13]

<sup>f</sup>GGA-DFT and AMEAM results of Moitra *et al.*[118]

<sup>g</sup>Bond-order potential results of Mrovec *et al.*[18]

<sup>h</sup>2NN-MEAM results of Lee *et al.*[15]

<sup>i</sup>Estimation by liquid-surface tension at 0 K, Tyson *et al.*[119]

<sup>j</sup>Estimation by atomization enthalpy at RT, Mezey *et al.*[120]

Table 5.4 shows energies and interplanar relaxations of low-index free surfaces. Present calculations employ 48-atom supercells, replicated along the surface normal with an equally-sized vacuum region and periodic boundary conditions. All results presented here predict the  $\langle 011 \rangle$  surface to have the lowest energy, followed by  $\langle 111 \rangle$ . Finnis-Sinclair potentials[13, 19] tend to underestimate the surface energy with respect to GGA-DFT. The present SWMEAM potential compares favorably with present *ab-initio* results and those of Vitos *et al.*[117] but underestimates the inter-planar relaxation of the high-energy  $\langle 100 \rangle$  surface by 50%. The origin of the discrepancy between GGA-DFT results of Moitra *et al.* and the others is unclear.

Figure 5.7 presents the unrelaxed ideal shear stresses and energy barriers for pressures up to 100 GPa. Ideal shear defines the upper limit of stress required to deform a perfect crystal and is fundamental to our current understanding of the strength of ma-

terials. Calculations are performed following the methodology of Paxton *et al.*[121], which uses a bcc primitive cell. SWMEAM accurately reproduces the GGA-DFT results for all pressures, with small discrepancies in shear stress around the extrema.

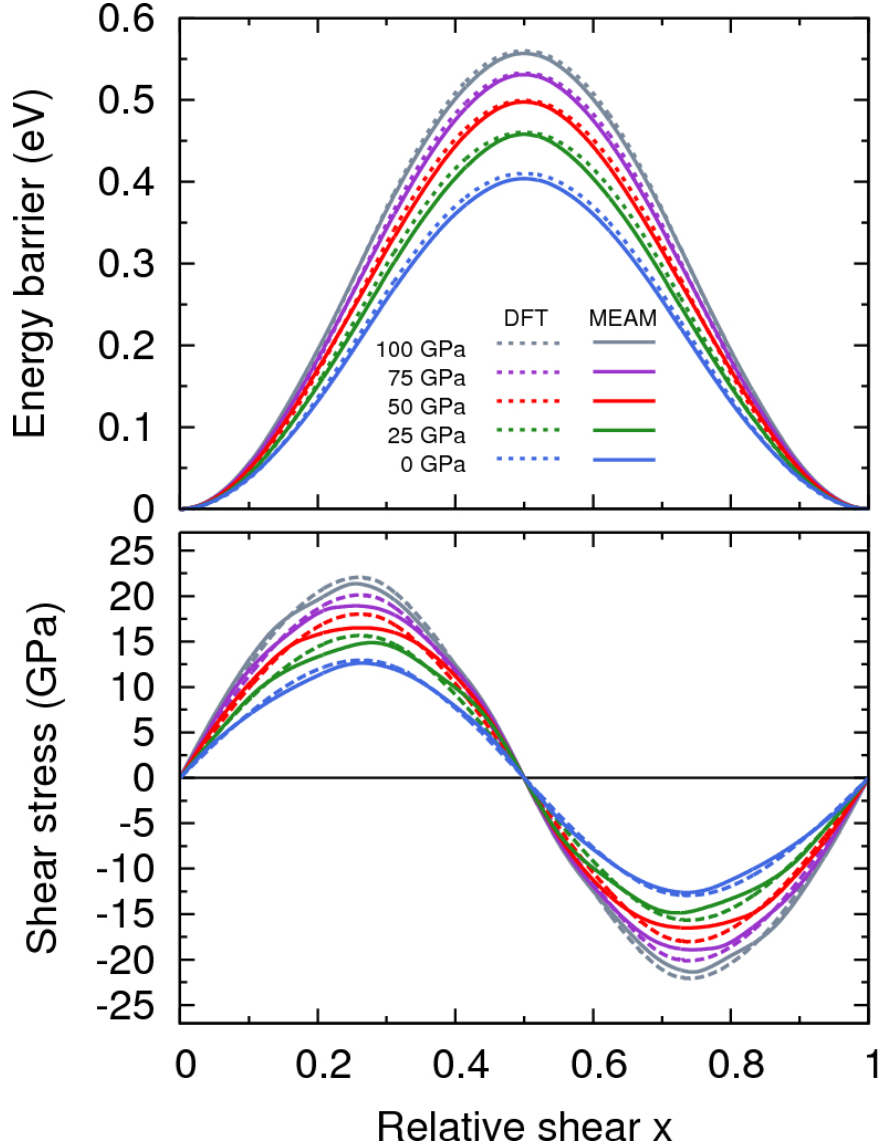


Figure 5.7: Ideal shear energy (top) and stress (bottom) for a continuous deformation of a one-atom bcc unit cell corresponding to  $(112)[\bar{1}\bar{1}1]$  twinning system as described by Paxton *et al.*[121]. SWMEAM Accurately reproduces the energy barrier and shear stress of this deformation for pressures up to 100 GPa. Small discrepancies in shear stress are found at the inflection points of the energy barrier, which correspond to the two extrema of shear stress at  $x = 0.25$  and  $x = 0.75$ .

## 5.3 Transferability of the fitted potential

Transferability of the fitted potential is demonstrated by application to screw dislocation core structure, deformation twinning in a bicrystal nanorod, and the high-pressure bcc-to-fcc phase transformation.

### 5.3.1 Dislocation core and deformation twinning

Core structure of the  $\frac{1}{2}\langle 111 \rangle$  screw dislocation is determined using a cell with lattice directions [1 $\bar{2}$ 1], [ $\bar{1}$ 01], [111] and periodic boundary conditions along the dislocation line. The first two lattice vectors are repeated to form a large cell containing 92,277 atoms which are displaced according to the appropriate elastic strain field. The core structure is then determined by relaxing a central region containing 54,396 atoms while the remaining atoms are fixed, ensuring that the correct boundary conditions are satisfied by the long-range anisotropic solution. This methodology is further explained in this group's previous work on Nb[86] and Mo[88].

Figure 5.8 shows a non-degenerate symmetric core structure predicted by SWMEAM, presented as a differential displacement map[46], is in agreement with results from an existing bond-order potential[18] and DFT-GGA[122] calculation for tungsten. Existing F-S potentials predict an asymmetric core[123, 47]. Our potential is also consistent with the criterion of Duesbery and Vitek[124], which is based on F-S calculations and states that the  $\frac{1}{2}\langle 111 \rangle$  screw dislocation in bcc metals will have a symmetric core structure if  $\gamma_{\{110\}}(b/3) > 2\gamma_{\{110\}}(b/6)$ , where  $\gamma_{\{110\}}$  is the relaxed {110}  $\gamma$ -surface and  $b = a\sqrt{3}/2$  is the burgers vector magnitude. Relaxed values taken from Figure 5.6 for SWMEAM are  $\gamma_{\{110\}}(b/3) = 100$  meV/ $\text{\AA}^2$  and  $\gamma_{\{110\}}(b/6) = 39$  meV/ $\text{\AA}^2$ .

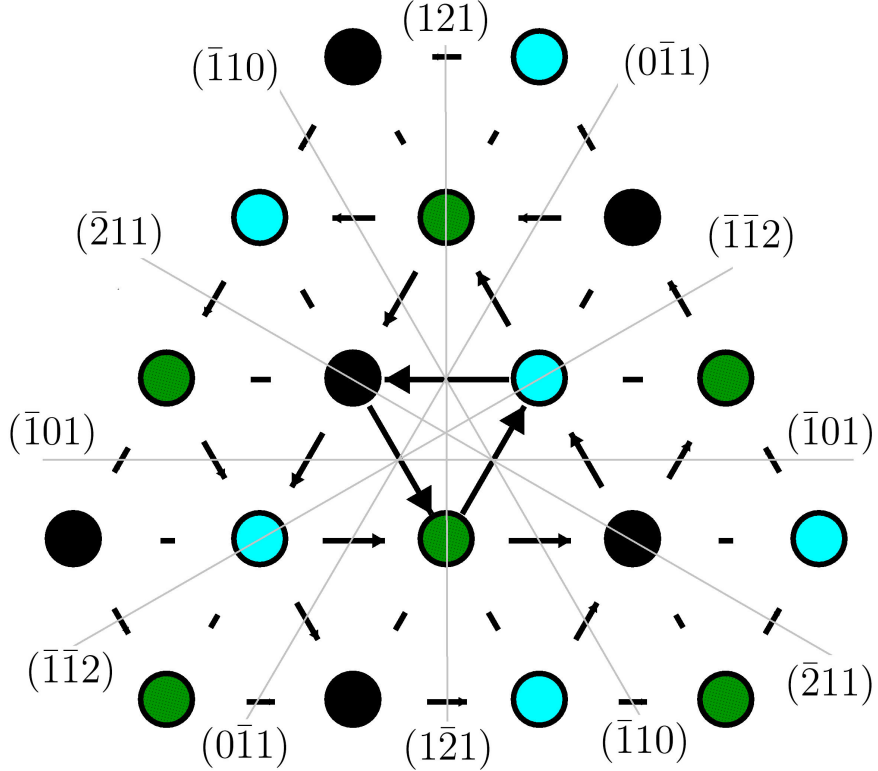


Figure 5.8: Differential displacement map of the  $\frac{1}{2}\langle 111 \rangle$  screw dislocation. SWMEAM predicts a non-degenerate symmetric core structure consistent with previous bond-order[18] and GGA-DFT[122] calculations, whereas existing F-S potentials for tungsten predict a degenerate core[47].

While dislocation slip is fundamental to plastic deformation of bulk transition metals, twinning has been found to dominate deformation in nanocrystalline Mo, Ta and Fe[125]. A recent study[5] observed deformation twinning and detwinning during uniaxial loading and unloading of a bicrystal nanorod. The Finnis-Sinclair potential of Ackland and Thetford[13] was used to model this twinning and detwinning in good agreement with experiment. We simulate this deformation as a challenge for our fitted SWMEAM potential and to demonstrate transferability to non-equilibrium conditions and consistency with existing models.

Figure 5.9 displays cross-sections of a bicrystal tungsten nanorod under uniaxial

stress at 300 K. The nanorod is 128 Å in diameter and 510 Å in length, with periodic boundary conditions parallel to the rod axis. A compressive strain of 10 % is applied from the top of the rod over 20 ps while atomic positions are updated using the Velocity Verlet[126] integrator and canonical ensemble with 1 fs timestep. The strain is then unloaded over an additional 20 ps. Multiple  $\{112\}\langle 111 \rangle$  deformation twins can be seen in Figure 5.9(a) through (c) to nucleate at the grain boundary and grow with increasing stress. At full loading, strain is accommodated primarily by a single large deformation twin extending from the grain boundary to the rod surface. During unloading the accumulated strain is released by detwinning as can be seen in panels (d) through (f). This deformation behavior is nearly identical to the results of Wang *et al.*[5], indicating the transferability of the fitted SWMEAM potential to modelling tungsten nanostructures and consistency with the successes of previously published potentials[13, 5]. Given that the F-S potential of Ackland and Thetford predicts an asymmetric core structure but accurately describes nanorod deformation[5], our current SWMEAM potential is well suited to study the interplay of deformation twinning and dislocation-induced plasticity in tungsten.

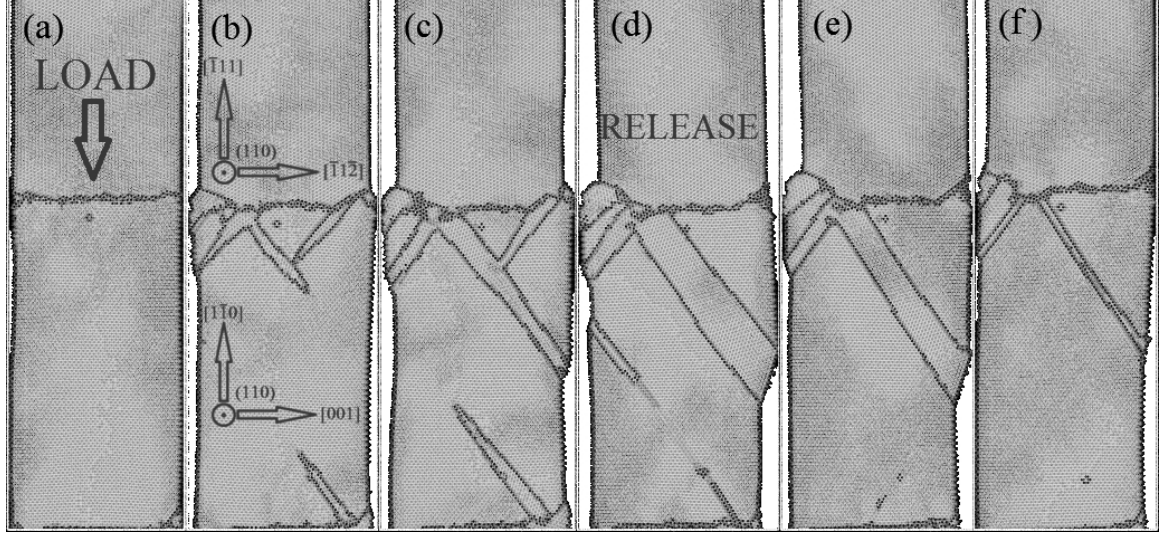


Figure 5.9: Deformation twinning and detwinning in a tungsten bicrystal nanowire under axial compression at room temperature. Compare to work of Wang *et al.*[5]. Structure identification was performed using adaptive common neighbor analysis as implemented in OVITO[43, 44]. Atoms are color-coded by structure: light (bcc) and dark (none). (a,b,c) Multiple deformation twins of the  $\{112\}\langle111\rangle$  type grow and merge as the rod is compressed by 10%. (d,e,f) Detwinning occurs as the load is released, recovering the compressive strain. Different shades of gray appear in the bulk because of atomic-level shading in OVITO.

### 5.3.2 Stabilization of fcc tungsten

Finally, the stabilization of fcc tungsten at high pressure is investigated. Theoretical studies have predicted that bcc tungsten becomes thermodynamically unstable with respect to close-packed fcc and hcp phases at extreme pressures[57] and under the conditions of strong electronic excitation during laser irradiation[58], for which a  $T_e$ -dependent interatomic potential was developed to study the transition[20]. To the authors' knowledge, fcc tungsten has only been observed in thin films formed by sputter deposition between 200 and 400 °C on glass, mica and rock-salt substrates[10]. The predicted zero-pressure lattice constants of fcc tungsten for SWMEAM and DFT are 4.049 Å and 4.044 Å, respectively, while Chopra *et al.*[10] found an fcc lattice

constant of 4.13 Å in the aforementioned tungsten films. This section considers the stabilization of fcc at high pressures, some accessible via diamond-anvil experiments.

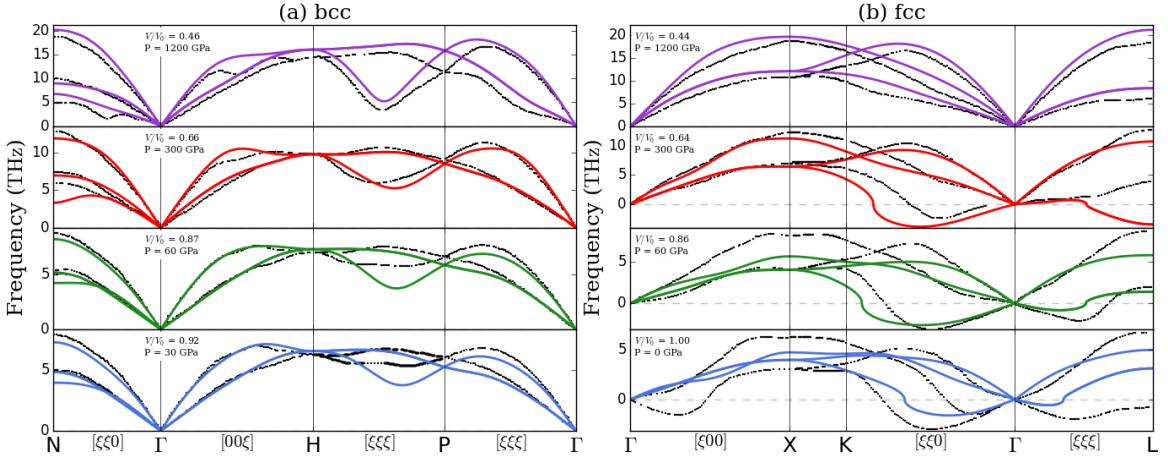


Figure 5.10: SWMEAM (solid) Phonon dispersions at various pressures compared with LDA-DFT (dashed) work of Einarsdotter *et al.*[57] (a) bcc: SWMEAM is consistent DFT even at the extreme pressure of 1200 GPa, but underestimates softening rate of the  $L-\frac{2}{3}[111]$  ( $\omega$ ) phonon and predicts an anomalous softening of the  $T-\frac{1}{2}[110]$  phonon with increasing pressure. (b) fcc: with the exception of the soft  $T-[\xi\xi 0]$  and  $T-[\xi\xi\xi]$  modes, SWMEAM dispersion at zero pressure diverges considerably from that of DFT. SWMEAM also underestimates the rate of stabilization of the soft modes with respect to DFT work. However at extreme pressures where fcc is thermodynamically stable, SWMEAM dispersion agrees closely with that of DFT. Displayed pressures are computed with SWMEAM. These dispersions were calculated using the small displacement method as implemented in the Atomic Simulation Environment[42]. As usual for phonons, negative values represent imaginary frequencies.

Figure 5.10(a) compares SWMEAM phonon dispersions for bcc W at pressures of 30 to 1200 GPa with LDA-DFT results of Einarsdotter *et al.*[57]. SWMEAM force constants are computed using the small-displacement method, implemented in the Atomic Simulation Environment[42], on a  $10 \times 10 \times 10$  supercell with  $\delta = a(P)/100$  where  $a(P)$  is the cubic lattice constant at pressure  $P$ . LDA-DFT results employed the density-functional linear response method, norm-conserving pseudopotentials, and  $5s5p5d6s6p$  valence. As seen in Figure 5.4, SWMEAM predicts the  $L-\frac{2}{3}[111]$  ( $\omega$ ) phonon to have lower frequency compared with DFT and experiment. This mode

softens with increasing pressure, albeit at a lower rate than predicted by LDA calculations. Otherwise SWMEAM accurately captures the other important features of bcc dispersion up to 1200 GPa. Low-pressure results (30-60 GPa) also compare favorably with the AMEAM results of Zhang and Chen[127].

Figure 5.10(b) compares the fcc phonon dispersion predicted by SWMEAM and LDA-DFT at pressures from 0 to 1200 GPa. At low pressure, where fcc is a highly unfavorable structure, SWMEAM does not compare well to *ab initio* results but correctly predicts unstable soft modes in the  $T[\xi\xi 0]$  and  $T[\xi\xi\xi]$  branches. However, the stabilization of these modes with increasing pressure is non-monotonic and particularly anomalous on the  $T[\xi\xi\xi]$  branch at intermediate pressures. By 1200 GPa, MEAM predicts fcc tungsten to be dynamically stable and shows excellent agreement with the LDA-DFT dispersion.

Figure 5.11(a) shows the elastic moduli  $C_{44}$  and  $C'$  between 400 and 500 GPa, where all  $C_{ij}$  are positive definite. It can be seen that  $C' = \frac{1}{2}(C_{11} - C_{12})$  is negative for pressures below 455 GPa, reflecting the slope of the  $T_{[1\bar{1}0]}[\xi\xi 0]$  branch arbitrarily close to the  $\Gamma$ -point. Figure 5.11(b) shows this mode for pressures around 540 GPa, where long-wavelength modes are stable but the  $\xi = 0.40$  mode remains unstable. According to SWMEAM, this mode is the last unstable phonon in any of the considered high-symmetry lines in the Brillouin zone and stabilizes at 543 GPa. However Figure 5.11(c), which displays the enthalpy difference  $\Delta H = H_{fcc} - H_{bcc}$  versus pressure, shows that the bcc phase remains energetically favorable until about 762 GPa. The inset in figure 5.11(c) shows the isobaric tetragonal Bain path at the determined pressure, displaying a barrier for the  $bcc \rightarrow fcc$  transition of 140 meV/atom. This barrier persists even above 2 TPa, but accuracy of the fitted potential in this pressure range has not been verified and any further investigation should be carefully checked with first-principles methods.

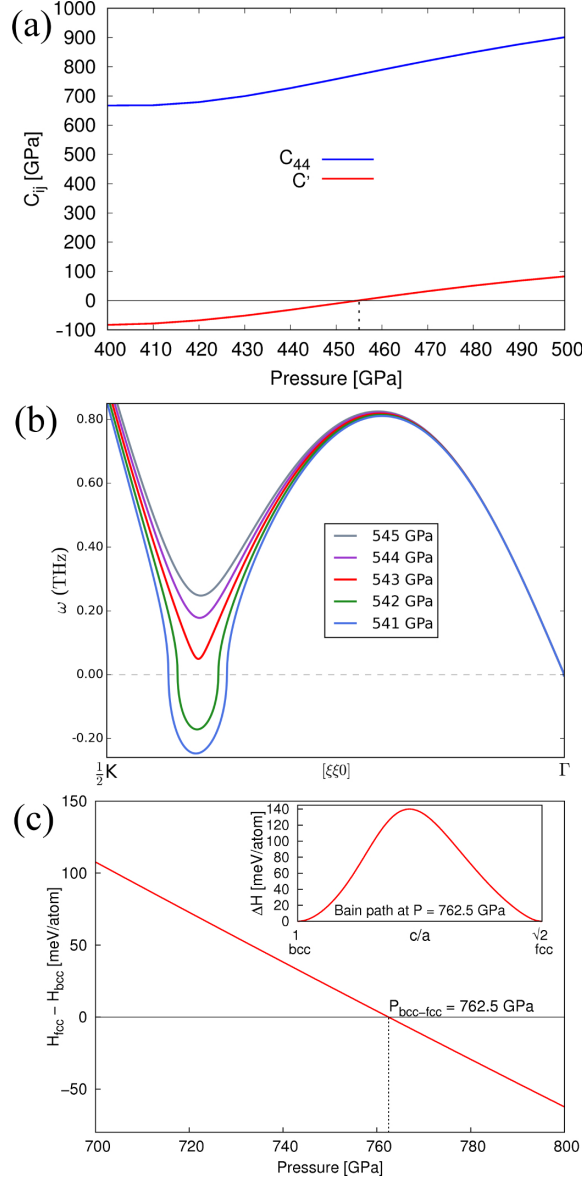


Figure 5.11: Stability of fcc tungsten at 0 K. (a) shows the elastic constants  $C_{44}$  and  $C'$  as functions of pressure, demonstrating the elastic stability of fcc tungsten for pressures above 455 GPa. (b) depicts the stabilization of the fcc-T<sub>[1̄10]</sub> [ξξ0] phonon branch with pressure. SWMEAM predicts that fcc becomes dynamically stable around 543 GPa with the  $\xi = 0.4$  mode being the last to stabilize. (c) depicts the enthalpy difference  $H_{fcc}(P) - H_{bcc}(P)$  between fcc and bcc as a function of pressure, revealing that despite being dynamically stable, fcc tungsten is not energetically favorable until pressures above 762.5 GPa. (inset) The tetragonal Bain path at the determined transition pressure exhibits an energy barrier of 140 meV/atom, indicating that bcc will not spontaneously transform to fcc with the fitted potential.

To summarize, present SWMEAM results are consistent with LDA-DFT predictions of Einarsdotter *et al.*[57] in that for fcc  $C_{44}$  is stable at relatively low pressures,  $C'$  stabilizes before fcc is thermodynamically favorable, the last phonon mode to become real is the  $T_{[1\bar{1}0]}[\xi\xi0]$  mode at  $\xi \approx 0.4$ , and that bcc remains energetically favorable until about 726 GPa. Even above this pressure there exists an energy barrier on the tetragonal bain path from bcc to fcc, again consistent with Einarsdotter *et al.*, which persists at all pressures considered here. The fitted potential should be suitable for further study of high-pressure fcc tungsten and its possible transition from the bcc phase, but predictions in the multi-TPa range should be checked with first-principles.

## 5.4 Summary

We have developed and applied a novel semi-empirical interatomic potential for tungsten, based on the MEAM and SW formalisms, parameterized using bias-free quintic splines and force-matched to a large database of highly-converged DFT data using an evolutionary global optimization scheme. We have demonstrated accuracy of the fit by reproducing phonon frequencies, compression and thermal-expansion curves, formation energies of unfavorable crystal structures, self-interstitial defects, free surfaces, vacancies, stacking faults and ideal shear at multiple pressures. Transferability of the fitted potential has been demonstrated by description of the high-pressure bcc to fcc phase transformation, dislocation core structure and deformation twinning and detwinning of a tungsten nanorod. Given the accurate description of both deformation twinning and dislocation structure this potential is more suitable than previous models for studying their interplay. Accuracy of elastic and vibrational properties at high pressures will enable quality shock simulations, and the combination of ac-

curate free-surfaces and non-equilibrium crystal structures should produce reliable descriptions of tungsten nanostructures.

# Chapter 6:

## Cluster Functional for Titanium-Niobium

This chapter presents the foremost achievement of the present work, an empirical potential force-matched to a large database of *ab initio* forces, stresses and energies with an optimization scheme combining the Powell conjugate-direction[95] and genetic algorithms. Our model is an empirical extension of the modified embedded-atom method (MEAM)[97, 78, 85, 14, 128] for alloys, referred to as “GMEAM” in Chapter 3.3, with functions parameterized by cubic splines. Section 6.1 describes the formulation of the model, the density functional theory (DFT) database, and the optimization scheme. Section 5.2 contains calculations of structural, elastic and thermal properties to demonstrate accuracy of the fit and consistency with existing data. Section 6.3 examines behavior of the fitted potential for martensitic transitions in pure titanium and Ti-rich alloys. Section 6.4 contains differential displacement maps of screw dislocation cores in hcp Ti and bcc Nb and examines the effect of alloying therein. Conclusions are given in Section 6.5.

## 6.1 DFT Database and fitted parameters

Highly converged DFT calculations performed with VASP [66, 67, 68, 69] using a projector-augmented planewave basis [129] and Perdew-Burke-Erzenhof (PAW-PBE) [130, 131] generalized-gradient exchange correlation approximation (GGA) comprise a database of forces, stresses and energies for fitting via the force-matching method of Ercolessi and Adams [1]. Valence configurations are  $3p4s3d$  and  $4p5s4d$  for Ti and Nb pseudopotentials, respectively. Convergence with respect to planewave basis size, number of k-points for Brillouin zone integration, and 1<sup>st</sup> order Methfessel-Paxton [71] smearing parameter is achieved to within 1 meV/atom for all structures in the fitting database. Planewave cutoffs and smearing parameters are 550 eV and 0.1 eV, respectively, for all phases. Table 6.1 contains the number of atoms and k-point meshes used for Ti,  $Ti_3Nb$ ,  $TiNb$  and  $TiNb_3$  structures. DFT results for pure niobium structures in the database were performed by Fellinger *et al.*[86] with additional details available in Fellinger [132]. All electronic self-consistency loops are converged to  $10^{-6}$ . Ionic relaxations are converged to  $10^{-5}$ .

The fitting database contains 411 configurations with a total of 9,079 unique force components, stress components and energies to be fit. The potential contains 200 fitted parameters. Optimization is done through the hybrid genetic algorithm described in Chapter 4

The remainder of this section describes the contents of the DFT database. The first paragraph that follows lists structures for which points on the energy-volume curve at 50%, 97.5%, 100%, 102.5% and 120% equilibrium are included in the fitting database. The second paragraph lists the structures for which elastic constants, calculated following the method of Trinkle [40], are included. The third paragraph, given the importance of martensitic transitions of this system, describes structures

Table 6.1: Structures, cell parameters and k-point meshes used in DFT calculations. Titanium atoms are shown in grey and niobium atoms in green.

Structure	Atoms	$a$ [Å]	$b/a$	$c/a$	k-point mesh	
– Ti –						
hcp	2	2.939	1	1.582	$17 \times 17 \times 13$	
bcc	1	3.254	1	1	$23 \times 23 \times 23$	
$\omega$	3	4.580	1	0.618	$11 \times 11 \times 18$	
A15	8	5.182	1	1	$11 \times 11 \times 11$	
fcc	1	4.110	1	1	$19 \times 19 \times 19$	
– $Ti_3Nb$ –						
D0 <sub>3</sub>	16	6.522	1	1	$11 \times 11 \times 11$	
D0 <sub>19</sub>	8	5.845	1	0.815	$9 \times 9 \times 13$	
L6 <sub>0</sub>	4	3.276	1.404	1.404	$20 \times 15 \times 15$	
G1	16	6.529	1	1	$11 \times 11 \times 11$	
A15	8	5.193	1	1	$11 \times 11 \times 11$	
SQS	16	7.354	1	2.831	$11 \times 11 \times 9$	
$\alpha''$	4	3.330	1.434	1.324	$20 \times 15 \times 16$	
$\alpha'$	16	5.976	1	1.582	$11 \times 13 \times 9$	
$\omega$	12	9.313	0.866	0.300	$8 \times 8 \times 27$	
– TiNb –						
B2	2	3.266	1	1	$13 \times 13 \times 13$	
A3	2	2.917	1	1	$13 \times 13 \times 9$	
Pmmm	4	3.276	1.414	1.414	$13 \times 9 \times 9$	
– $TiNb_3$ –						
A15	8	5.254	1	1	$11 \times 11 \times 11$	
SQS	16	7.363	1	2.828	$11 \times 11 \times 9$	

along the transition pathways. The fourth paragraph lists the various point and planar defect structures to which the potential is fit. The last two paragraphs in this subsection describe *ab initio* MD snapshots at finite temperature, each of which is run with a 1 fs timestep, and miscellaneous configurations which were added to correct for spurious results obtained with previous iterations of the potential. More detail on the iterative process of fitting, testing, and database refinement is provided Section 6.1.

The fitting database contains energy-volume relations for multiple phases at each considered stoichiometry, including those that are dynamically or elastically unstable, in order to broadly sample the configuration space and train the potential to non-equilibrium configurations. For pure titanium the database includes the hcp  $\alpha$ , bcc  $\beta$ , hexagonal  $\omega$ , fcc and A15 phases while for niobium it includes bcc, hcp,  $\omega$ -Ti, A15 (also known as  $\beta$ -W) and  $\beta$ -Ta phases. Since the solid-solution nature of alloys is impractical to account for within DFT, representative supercells for each phase must be used. Structure candidates for  $Ti_3Nb$  hexagonal  $\alpha'$ , orthorhombic  $\alpha''$ , bcc ( $\beta$ ) “G1” and hexagonal  $\omega$  phases are taken from Lazar *et al.* [133], who performed a thorough analysis of their stability. Additionally, a 16-atom bcc special quasi-random structure (SQS) [134], the bcc  $D0_3$  and  $L6_0$  structures, the hcp  $D0_{19}$  and the A15 structure are included for this stoichiometry. For TiNb, a [110]-layered bcc supercell (where [110] alternate between Ti and Nb, space group  $Pmmm$ ), bcc B2 and hcp A3 structures are included. Finally a bcc SQS and an A15  $TiNb_3$  phase, which is predicted by DFT to be elastically and dynamically stable, are included in the database.

The fitting database contains elastic constants for hcp, bcc and  $\omega$  phases of titanium;  $D0_3$ ,  $G1$ ,  $\omega$  and  $\alpha''$  phases of  $Ti_3Nb$ ; the  $B2$  phase of TiNb and bcc niobium; each at  $\pm 0.8$  and  $\pm 0.4\%$  strains at zero pressure.

Three evenly-spaced points on the  $\omega \leftrightarrow \beta$  pathway (via splitting of the honeycomb

layers into alternate  $\langle 111 \rangle$  bcc planes) are included for pure titanium. For  $Ti_3Nb$ , where the fully transformed  $\omega$  phase corresponds to  $G1-\beta$  as described in Lazar *et al.* [133], three additional points on the energetic barrier identified by Lai *et al.* [135] are included. A mesh of nine evenly-spaced points on the Burgers [59] energy surface of the  $\alpha \leftrightarrow \beta$  transition in pure Ti and  $\alpha'' \leftrightarrow \beta-L6_0$  in  $Ti_3Nb$  are included.

For defect structures, two points on the easy and hard prismatic stacking faults in hcp-Ti are included. Three points on  $\{112\}\langle 111 \rangle$  and one point on  $\{110\}\langle 111 \rangle$  faults of bcc-Nb, as well as an unrelaxed vacancy and (100), (110) and (111) free surfaces are included.

Finite temperature structures are included in the database to ensure accuracy in dynamics simulations, including: a 127-atom ab-initio MD snapshot of bcc-Ti containing a vacancy at 1300 K; 432-atom snapshots of  $Ti_3Nb$  at (bcc) 300 K, 1000 K and (liquid) 3000 K; a 256-atom snapshot of  $\alpha''$  at 300 K; and snapshots of bcc-Nb at 1200 K, 2200 K and (liquid) 5000 K.

Miscellaneous structures added through the course of fitting and testing for the purpose of improving specific behaviors include  $\alpha''$   $Ti_3Nb$  with  $b$  and  $c$  scaled by 0.95 and 1.05, lattice constants of bcc-Nb at 50 and 100 GPa, and large-strain (20% and 40%) configurations for  $C_{44}$  in niobium. Also included are peaks of the ideal shear curve of bcc Nb at 0 and 100 GPa. Last, configurations of bcc-Ti with a single atom displaced by  $\pm 0.003$  Å are included to improve accuracy of force constants in this system.

Fitting is performed using the hybrid genetic algorithm described in Chapter 4. Plots of the final splines are shown in Figure 6.1 and numerical values of the parameters are given in Table 6.1.

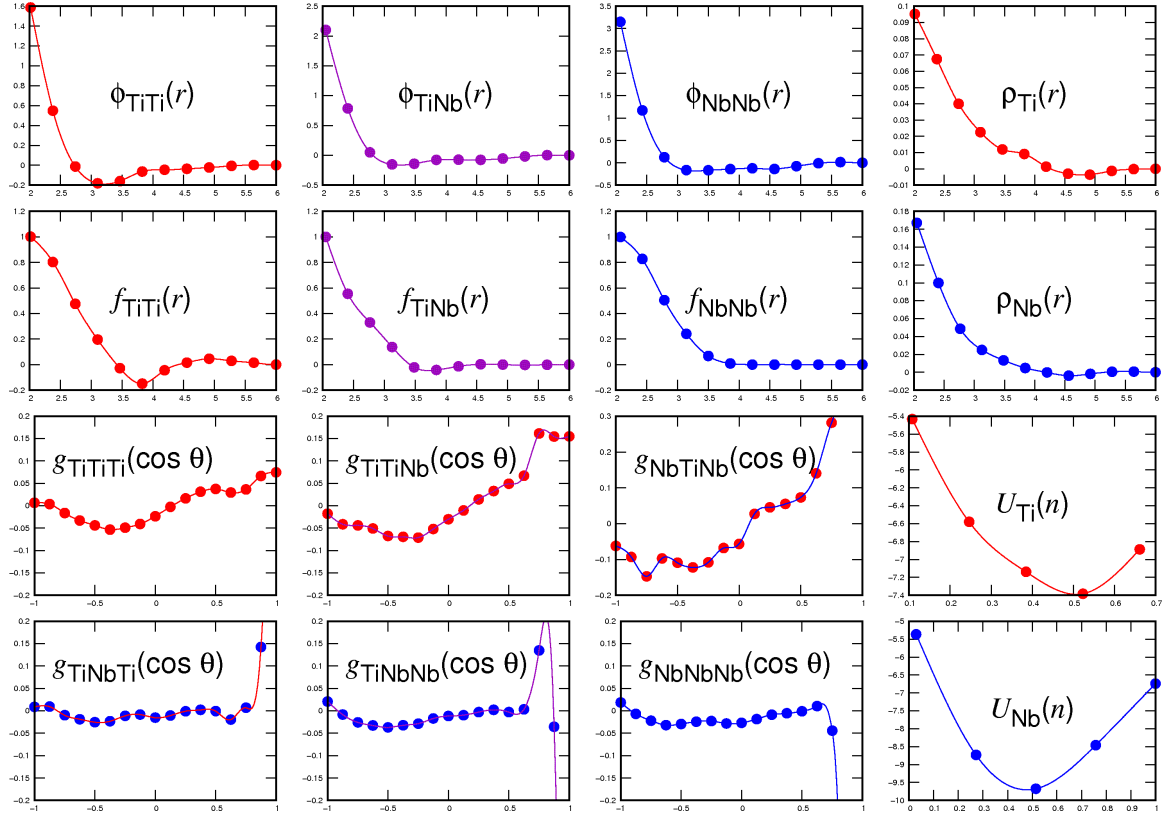


Figure 6.1: Plots of the sixteen functions of the fitted potential. Points are spline knots and lines are cubic spline interpolants. Splines are clamped at the endpoints according to the derivatives listed in Table 6.1.

Table 6.2: Parameters specifying the sixteen cubic splines of the GMEAM alloy potential. The first part of the table lists independent variables for each spline function, the bounds of such, and the number of spline knots  $N$ . An alloy index is assigned for each unique combination of species for each function. In the middle part, values of the spline functions are tabulated for each knot  $i$ , where  $t_i = t_{min} + (i - 1)(t_{max} - t_{min})/(N - 1)$ . Last, first derivatives are listed for each spline at its endpoint.

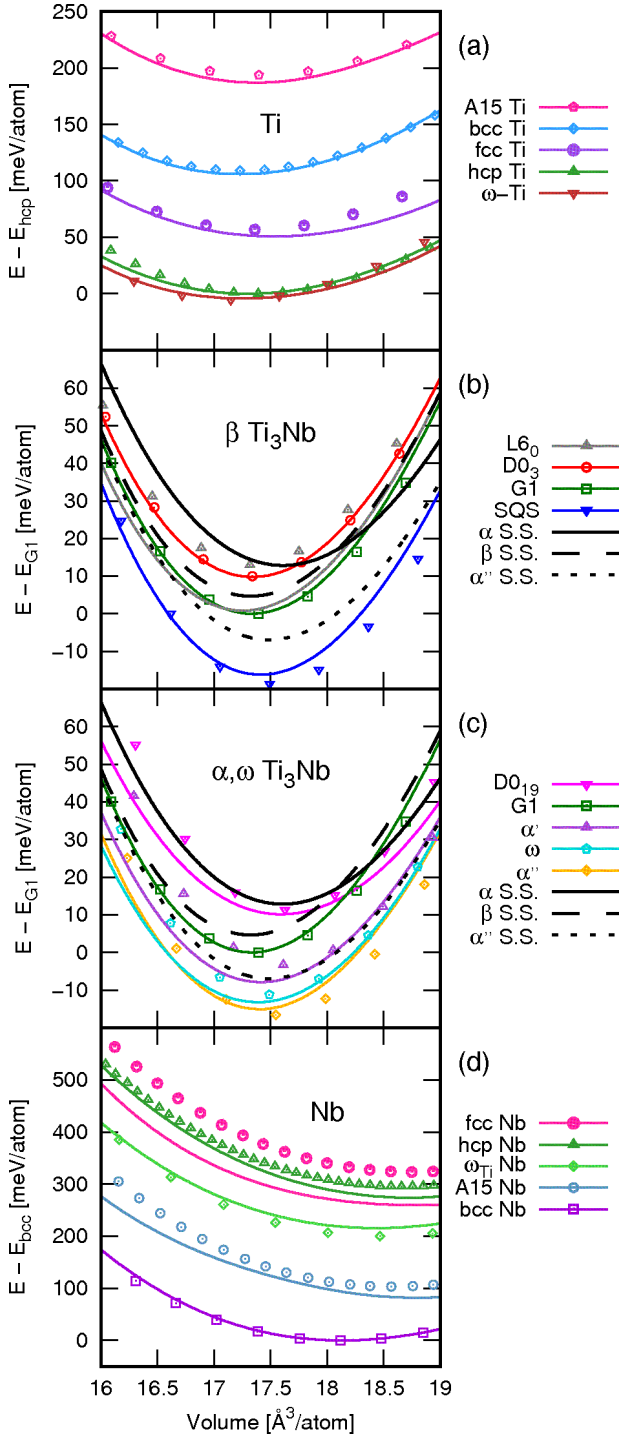


Figure 6.2: Energy versus volume curves for (a) Ti, (b)  $\beta$   $Ti_3Nb$ , (c)  $\alpha$  and  $\omega$   $Ti_3Nb$ , and (d) Nb. GMEAM values are shown as solid curves, while DFT values are presented as points. Zero energy is defined for (a) as hcp Ti, for (b) and (c) as G1  $Ti_3Nb$ , and for (d) as bcc Nb. Values are given relative to these zeros for the two methods presented. For the  $Ti_3Nb$  stoichiometry, fully relaxed solid-solution (S.S.) curves are shown for GMEAM.

## 6.2 Accuracy of the fitted potential

We demonstrate the accuracy and transferability of the fitted GMEAM potential through the energetics and elastic moduli, crystallographic defects and thermodynamic properties for phases throughout the Ti-Nb phase diagram. All molecular dynamics calculated presented here were performed with the Large-scale Atomic/Molecular Massively Parallel Simulator (LAMMPS) [100] version dated 31 March, 2017. If at any step during an MD run the density seen by an atom exceeds its embedding function domain, the embedding energy is linearly extrapolated from the nearest end point.

### 6.2.1 Structural, Elastic and Thermal Properties

In this section structural, thermal and elastic properties of various Ti-Nb phases are examined with the fitted GMEAM potential.

Figure 6.2 shows energy-volume curves volumetric scaling with fixed lattice ratios, where GMEAM energies are shown as curves and DFT energies are points. Figure 6.2(a) contains energies of pure titanium structures, where GMEAM shows excellent agreement with the *ab initio* data, including the nearly degenerate spacing of hcp ( $\alpha$ ) and  $\omega$ -Ti. Figures 6.2(b) and (c) contain structures for bcc ( $\beta$ ) and non-bcc  $Ti_3Nb$ , respectively. Common bcc intermetallic structures such as  $D0_3$  and  $L6_0$  are considered, as well as the  $G1$  structure proposed by Lazar *et al.*, which contains a chain of niobium atoms along the body diagonal. A fully-relaxed special quasi-random structure (SQS) for the 3:1 ratio in bcc [134] has the lowest energy of all bcc structures, and is slightly lower even than the  $\alpha''$  structure proposed by Sun *et al.* [136]. Solid solution predictions by GMEAM are presented as dashed curves. GMEAM agrees with DFT predictions of bcc structures with the notable exception of  $L6_0$ , which can be transformed into  $\alpha''$  by the Burgers [59] mechanism as described in Section 6.3.

In part (c), GMEAM shows good agreement with DFT, slightly underestimating the energy of  $\alpha'$  and the difference between  $\alpha''$  and  $\omega$ . Lastly, GMEAM again shows good agreement with DFT for pure niobium structures in part (d), except for the energetic ordering of high-lying hcp and fcc Nb.

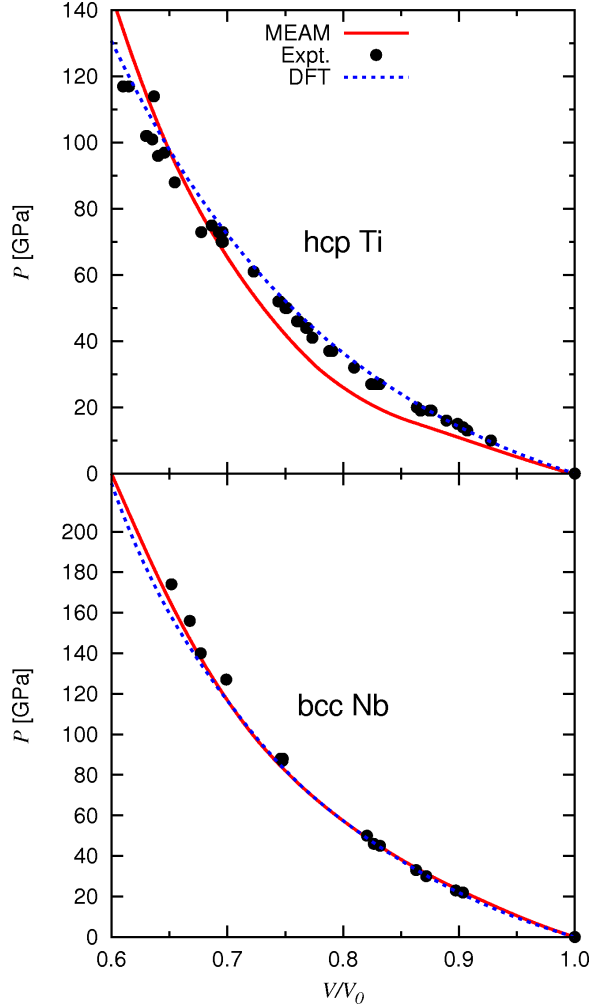


Figure 6.3: Pressure-volume relations for hcp-Ti and bcc-Nb. DFT shows good agreement with room-temperature experimental data [101] obtained by shock measurements, but GMEAM under-estimates hcp-Ti pressure for compression below  $V/V_0 = 0.7$  and over-estimates pressure at higher compression.

Figure 6.3 shows pressure-volume curves for hcp Ti (top) and bcc Nb (bottom) as computed with GMEAM and DFT at 0 K, compared with experimental shock

Table 6.3: Linear thermal expansion coefficients (TECs), in units of  $10^{-6} K^{-1}$ , calculated with GMEAM and compared with experiment. GMEAM overestimates the TEC at each considered concentration, but shows a decrease with niobium content consistent with experiment.

at. % Nb	GMEAM	Expt.
0	11.7	$9.50^a, 9.90^b$
2.64	10.9	$9.35^a$
11.41	10.8	$9.37^a$
100	7.87	$7.0^c$

<sup>a</sup>Experimental data for Ti and Ti-Nb from Han *et al.* [137].

<sup>b</sup>Experimental data for Ti from Zinelis *et al.* [138].

<sup>c</sup>Experimental data for Nb from Argent *et al.* [139].

data taken from Kinslow [101] at room temperature. GMEAM tracks DFT and experiment for bcc Nb, but underestimates hcp-Ti pressure by about 10 GPa at 80% equilibrium volume. The origin of this discrepancy is unclear since DFT agrees well with experiment. Given this anomaly, one must take care when applying the fitted potential to high-pressure phenomena in titanium-rich systems. Below 10 GPa, however, the difference between GMEAM and DFT is negligible.

Table 6.3 displays linear thermal expansion coefficients (TECs) predicted by the fitted GMEAM potential and compared with limited experimental data for Ti, Nb, and two alloy stoichiometries. Calculation of the TECs is done using 8,788-atom NPT ensemble simulations with a timestep of 1 fs, where the pressure is kept at zero and the temperature ramped up, starting at RT, over one nanosecond. Every 100 ps, the average temperature and volume over the last 10 ps are computed. The TEC is determined by fitting these to a linear function in the temperature range considered in experiment. GMEAM results are consistently higher than experimental fits, but the difference shrinks as niobium content increases. Notably, experimental data show a slight increase in TEC between 2.64 and 11.41 at.% Nb, but GMEAM values monotonically decrease across the range of niobium content.

Table 6.4 contains elastic constants of Ti, Nb, and  $\text{Ti}_3\text{Nb}$  computed in the present work and compared with other *ab initio* and EAM results. Moduli in the present work are calculated using the methodology described by Trinkle [40] using strains of  $\pm 0.2\%$ ,  $\pm 0.4\%$ ,  $\pm 0.6\%$ ,  $\pm 0.8\%$ . GMEAM matches present DFT calculations to within 20 GPa for most phases, the most notable exceptions being a much softer  $C_{11}$  and  $C_{33}$  for  $\omega$ - $\text{Ti}_3\text{Nb}$  and a negative  $C' = (C_{11} - C_{12})/2$  predicted for the  $\text{D}0_3$  structure. Since the elastic constants of pure  $\omega$ -Ti are generally softer than those computed for the alloy, it is possible the discrepancy for  $\omega$ - $\text{Ti}_3\text{Nb}$  is due to the lack of any strained  $\omega$ -Ti niobium configurations in the fitting database. Given the solid-solution nature of alloys, however, elastic constants of intermetallic structures do not necessarily give reliable predictions of bulk elasticity.

Figure 6.4 shows elastic constants of solid-solution bcc Ti-Nb as a function of niobium concentration at 0 K, compared with experiment and previous calculations. Solid lines are GMEAM predictions from a 31,250-atom solid solution. To prevent martensite formation and breaking of cubic symmetry, internal relaxations are not allowed. GMEAM results are compared with DFT calculations (open symbols) and experimental data for Ti-Nb alloys (filled symbols) as well as gum metals (half-filled symbols). GMEAM predicts elastic instability ( $C_{12} > C_{11}$ ) for  $x_{Nb} < 10\%$  because the bcc phase is only stable at high temperatures (experimental results for pure Ti from Ledbetter *et al.* are at 1000 °C). The majority of experimental elasticity data for Ti-Nb alloys is between 20 and 40 at.% niobium, where GMEAM predictions are accurate. Existing DFT data obtained from various intermetallic structures is also accurate compared to experiment. DFT calculations by Nikonov *et al.* [140] using the effective muffin-tin orbital (EMTO) basis within the coherent potential approximation (CPA) tends to over-estimate  $C_{44}$  relative to experiment, particularly in the Ti-rich region.

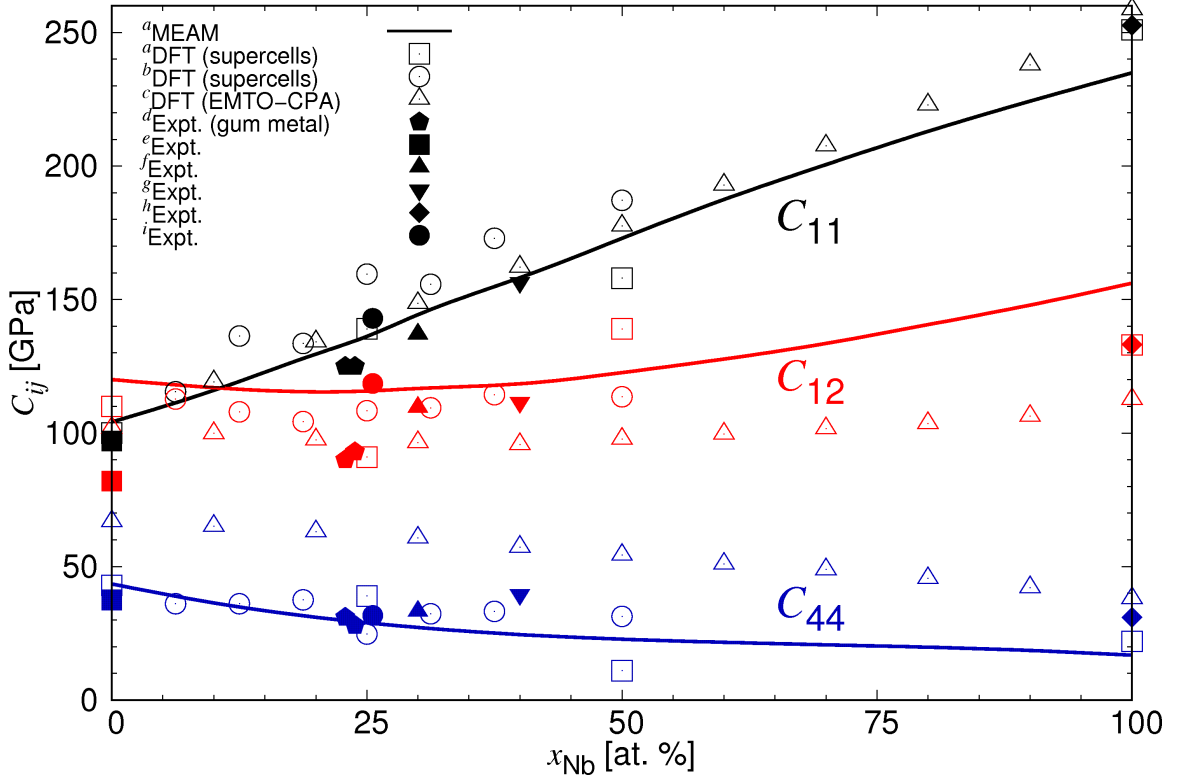


Figure 6.4: Elastic constants (in GPa) of bcc Ti- $x$  at.%Nb as a function of niobium concentration  $x$ . Solid lines are from a 31,250-atom solid solution as calculated with the fitted GMEAM potential using a maximum strain of 0.5%. Open symbols are from DFT calculations of the present work and others, while filled symbols are experimental data. GMEAM shows good agreement with experiment across the range of niobium concentration, but in general overestimates  $C_{12}$  compared to previous *ab initio* work (open symbols). This gives a smaller value for  $C' = (C_{11} - C_{12})/2$ , meaning the potential is more elastically anisotropic as measured by the anisotropy ratio  $A = C_{44}/C'$ .

<sup>a</sup>GMEAM and GGA-DFT results of this work.

<sup>b</sup>GGA-DFT results of Karre *et al.* [133].

<sup>c</sup>EMTO-CPA results of Nikonov *et al.* [136].

<sup>d</sup>Two gum metal results of Talling *et al.* [141].

<sup>e</sup>Experimental results of Ledbetter *et al.* [142].

<sup>f</sup>Experimental results of Hermann *et al.* [143].

<sup>g</sup>Experimental results of Reid *et al.* [144].

<sup>h</sup>Experimental results of Carroll [145].

<sup>i</sup>Experimental results of Jeong *et al.* [146].

Table 6.4: Single-crystal elastic constants of  $\text{Ti}_3\text{Nb}$  phases by GMEAM and DFT compared with data from the literature.

Phase	$C_{ij}$	GMEAM <sup>a</sup>	DFT <sup>a</sup>	DFT <sup>b</sup>	DFT <sup>c</sup>	EAM <sup>d</sup>
hcp Ti	$C_{11}$	162	172			189
	$C_{12}$	61	84			74
	$C_{13}$	68	74			68
	$C_{33}$	197	190			192
	$C_{44}$	62	44			50
$\beta$ -G1	$C_{11}$	147	142	149		176
	$C_{12}$	121	112	111		153
	$C_{44}$	34	34	37		66
$\beta$ -D0 <sub>3</sub>	$C_{11}$	115	122	131	117	106
	$C_{12}$	122	121	119	105	59
	$C_{44}$	20	19	-8	20	15
$\omega$ -G1	$C_{11}$	169	204	226	162	226
	$C_{12}$	82	102	117	125	-97
	$C_{13}$	72	67	81	85	28
	$C_{33}$	173	250	276	212	212
	$C_{44}$	30	30	39	19	39
	$C_{66}$	43	51	55	22	52
$\alpha''$	$C_{11}$	122	146	148	130	105
	$C_{12}$	103	92	93	91	142
	$C_{13}$	103	124	124	127	115
	$C_{22}$	183	182	171	148	212
	$C_{23}$	78	84	80	69	140
	$C_{33}$	200	176	175	136	149
	$C_{44}$	53	51	65	28	67
	$C_{55}$	49	34	45	23	48
	$C_{66}$	53	69	32	40	62
bcc Nb	$C_{11}$	235	251			243
	$C_{12}$	156	133			130
	$C_{44}$	17	22			28

<sup>a</sup>GMEAM and GGA-DFT results of this work.

<sup>b</sup>GGA-DFT results of Lazar *et al.* [133].

<sup>c</sup>GGA-DFT results of Sun *et al.* [136].

<sup>d</sup>Results from EAM Nb-Ti-Al potential of Farkas *et al.* [147].  
(calculations by present authors)

Table 6.5: Vacancy (Vac.) and self-interstitial formation energies in bcc Nb and hcp Ti. Interstitial configurations for bcc Nb are octahedral (O), tetrahedral (T), crowdion (C), and split (or “dumbbell”) structures indicated by angle brackets. Geometry of these defects can be found in Fellinger *et al.* [86]. In addition to O, T and C, basal octahedral (BO), basal tetrahedral (BT), basal crowdion (BC), basal split (BS) and *c*-axis split (CS) configurations are presented for hcp Ti. These geometries can be found in Raji *et al.* [148]. Structures which relax to another interstitial configuration are shown by table entries containing the relaxed structure abbreviation.

	GMEAM <sup>a</sup>	DFT <sup>a</sup>	EAM <sup>b</sup>	DFT <sup>c,d</sup>	MEAM <sup>e,f</sup>
— bcc Nb —					
Vac.	2.74	2.72	2.77	2.67	2.91
O	$\langle 001 \rangle$	4.89	2.17	5.08	5.27
T	$\langle 011 \rangle$	4.56	$\langle 011 \rangle$	4.90	5.38
C	4.73	3.99	$\langle 111 \rangle$	4.35	4.17
$\langle 001 \rangle$	5.80	4.76	2.31	5.02	5.27
$\langle 011 \rangle$	4.88	4.31	2.21	4.65	5.10
$\langle 111 \rangle$	C	3.95	2.30	4.34	4.16
— hcp Ti —					
Vac.	2.26	1.38	1.53	1.970	2.26
O	BO	1.57	C	2.13	2.00
T	CS	CS	BS	CS	CS
C	BO	2.16	2.24	2.53	2.30
BO	2.41	1.51	BS	2.25	2.02
BT	BO	3.01	BS	BO	3.69
BC	BO	BO	2.19	BO	BO
BS	2.85	1.87	2.19	2.45	2.22
CS	2.88	1.91	2.78	2.48	2.21

<sup>a</sup>GMEAM and GGA-DFT results of this work.

<sup>b</sup>Results from EAM Nb-Ti-Al potential of Farkas *et al.* [147].

(calculations by present authors)

<sup>c</sup>GGA-DFT results for bcc Nb of Cerdeira *et al.* [149].

<sup>d</sup>GGA-DFT results for hcp Ti of Raji *et al.* [148].

<sup>e</sup>Nb MEAM potential of Fellinger [132].

<sup>f</sup>Ti MEAM potential of Hennig *et al.* [55].

(calculations by present authors)

## 6.2.2 Planar and Point Defects

In this section, behavior of the fitted GMEAM potential for point defects and stacking faults in hcp-Ti and bcc-Nb is investigated

Table 6.5 contains vacancy and interstitial point defect formation energies for bcc Nb and hcp Ti as calculated in the present work and compared with an existing EAM potential and DFT work from the literature. Present DFT calculations employ 250( $\pm 1$ )-atom supercells while MD calculations use 1,024( $\pm 1$ ) atoms. Only vacancy structures are included in the fitting database of the present potential.

Vacancy formation energies of bcc Nb are very consistent between the methods considered here, but the EAM potential of Farkas *et al.* tends to underestimate all interstitial formation energies. We also found that the crowdion configuration collapses with this potential if neighboring atoms are not artificially shifted away from the interstitial atom before relaxation. The present GMEAM prediction that octahedral interstitials relax to  $\langle 001 \rangle$  dumbbells is consistent with the degenerate energies predicted by Fellinger [132]. GMEAM predicts the bcc crowdion to be the energetically favorable contrary to the DFT results, which find  $\langle 111 \rangle$  dumbbells to have the lowest energy. However, the *ab initio* energies of these two defects differ by 40 meV in the present work and only 10 meV according to Cerdeira *et al.* [149]. This is unsurprising, given their structural similarity. Indeed, the GMEAM prediction of crowdion stability is compatible with the known high mobility of interstitials in non-ferromagnetic bcc metals,[150, 151] recently found to result from migration of  $\langle 111 \rangle$  defects in tungsten [115].

The fitted GMEAM potential tends to overestimate interstitial formation energies in hcp Ti compared to the present DFT calculations, but correctly predicts the BO configuration to have the lowest energy. T and BC configurations are unstable with respect to CS and BO, respectively, in both methods. We find that the EAM potential of Farkas relaxes many of the interstitials to the BS configuration, which is energetically degenerate with BC despite being structurally distinct after relaxation. We find the present GMEAM potential to be consistent with that of Hennig *et al.*

[55] for the vacancy formation energy and the instability of T with respect to CS. We note that the formation energies calculated in the present work using the MEAM potential of Hennig *et al.* differ from their published results by as much as 0.64 eV. We suspect this is due to a difference in defect concentrations; their published values correspond to a concentration of about 1% while the present values are for roughly 0.1%.

Figure 6.5 shows low-index generalized stacking-fault energy (GSFE) curves for (a) hcp-Ti and (b) bcc-Nb. Unrelaxed DFT values are shown as points while GMEAM results are shown as solid lines (unrelaxed) and dashed lines (relaxed). For hcp-Ti (a), the  $\langle 11\bar{2}0 \rangle \{0001\}$  prismatic stacking fault relevant to partial dislocation formation is shown in easy (red) and hard (black) configurations. GMEAM predicts a stable partial dislocation as a result of the local minimum at 0.5. Part (b) shows  $\{110\}\langle 111 \rangle$  (red) and  $\{112\}\langle 111 \rangle$  (black) GSFE curves for bcc Nb. GMEAM predicts a much broader curve for the  $\{112\}$  fault than DFT, and reduces energy by about 5 meV/ $\text{\AA}^2$  upon relaxation. For the  $\{110\}$  fault, GMEAM tracks DFT quite well and shows a similar reduction in energy of about 5 meV/ $\text{\AA}^2$  upon relaxation.

In summary, the fitted GMEAM potential shows good agreement with existing data on elastic and defect structures near zero pressure. The pressure-volume relation of hcp-Ti (Fig. 6.3) does not track experiment as well as DFT, but the difference below 10 GPa is negligible. Linear thermal expansion coefficients (Table 6.3) are generally over-estimated but decrease with niobium content in agreement with experiment.

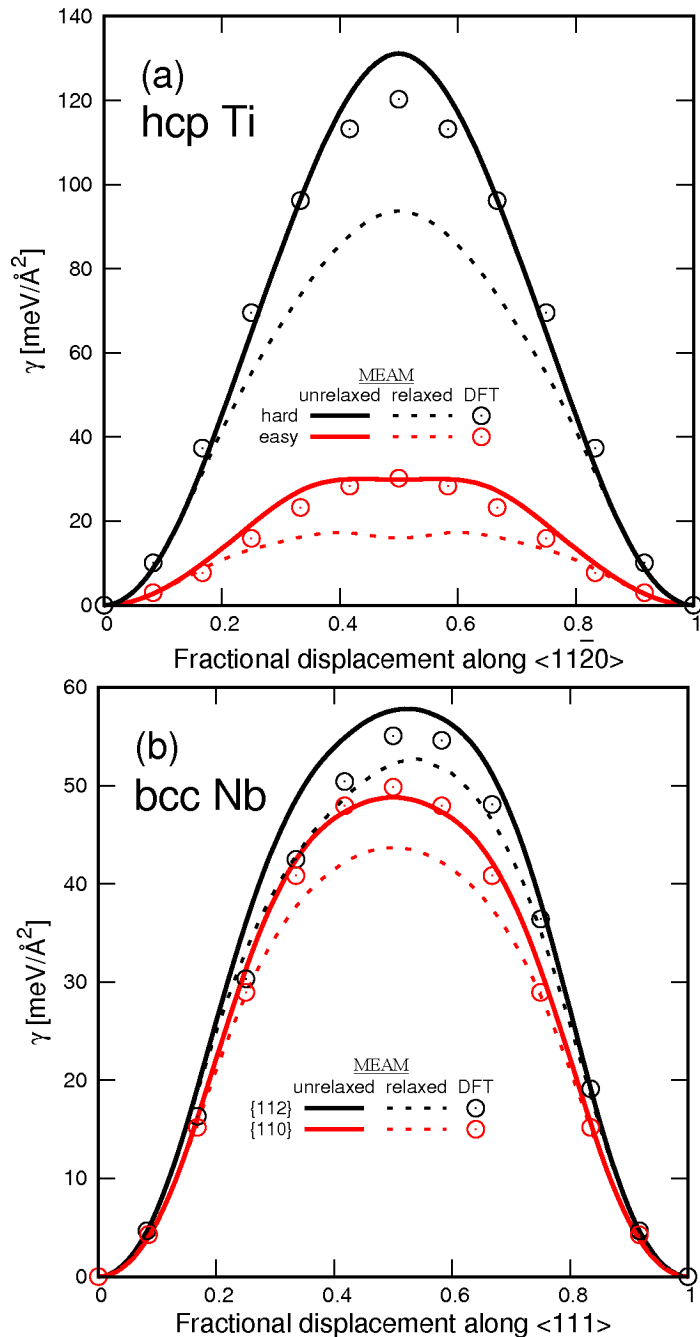


Figure 6.5: Low-index stacking faults for (a) hcp Ti and (b) bcc Nb as predicted by GMEAM (solid curves) and the present DFT (points) calculations. Faults relaxed with GMEAM are shown as dashed curves. Relaxation of the easy prismatic ( $\{01\bar{1}0\}\langle11\bar{2}0\rangle$ ) fault in hcp titanium reveals a local minimum indicating the formation of partial dislocations consistent with Ghazisaeidi and Trinkle, and Tarrat *et al.* [152, 153]. No metastable fault structures are found for niobium.

### 6.3 Martensitic Transformations

Much of the interest in Ti-Nb alloys near the 3:1 stoichiometry comes from their multi-phase nature and martensitic transformations. This section examines the energetics of these transitions for intermetallic structures and solid solutions. In the end, an NPT simulation of the shape-memory effect in Ti-25 at.%Nb is performed with the fitted potential.

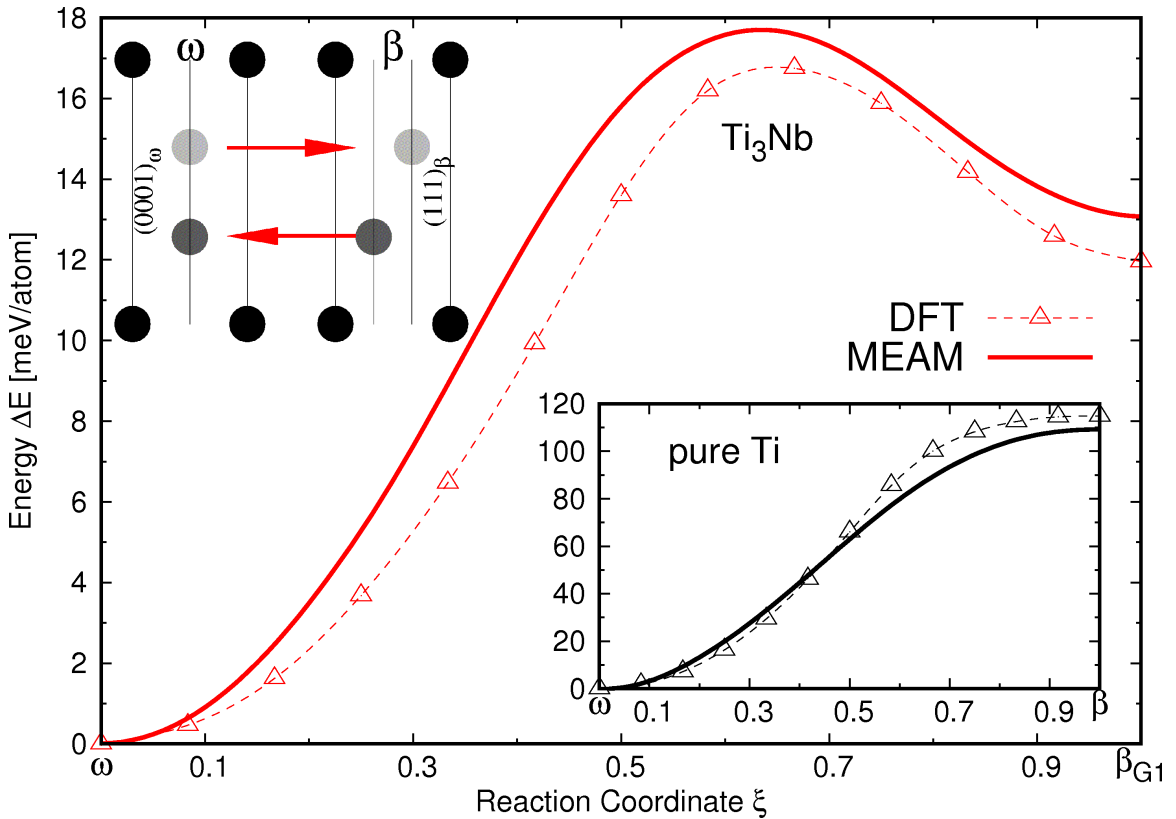


Figure 6.6: Transition energy barriers for the  $\omega$  to  $\beta$  transition in  $G1-\text{Ti}_3\text{Nb}$  and (inset) pure Ti via the planar collapse mechanism for GMEAM and DFT. The atomic motion during this transition corresponds to a longitudinal  $2/3[111]$  phonon in the bcc lattice as shown schematically in the top left. The  $c/a$  ratio is mapped with  $\xi$  from the optimal value for  $\omega$  to the ideal value in  $\beta$ . The overall lattice constant  $a$  is an average of the appropriate values in the endpoint phases. GMEAM accurately describes the transition in both systems, including the 5 meV/atom DFT barrier from  $G1-\beta$  to  $\omega$  first identified by Lai *et al.* [135].

Figure 6.6 shows the  $\omega \leftrightarrow \beta$  transition pathway for the G1 structure in  $\text{Ti}_3\text{Nb}$  and (inset) pure titanium. The reaction coordinate  $\xi$  represents a splitting of the sublattices of  $\omega$  honeycomb planes into bcc  $\langle 111 \rangle$  planes. The axial ratio  $c/a$  is mapped with  $\xi$  from the optimal value in  $\omega$  to the required value in  $\beta$ . The overall lattice constant  $a$  is an average of the corresponding values in the endpoint phases. While GMEAM overestimates the energetic spacing between  $\omega$  and  $\beta$ -G1 by 1 eV compared to DFT, a barrier height of about 5 meV/atom from  $\beta$  to  $\omega$  is predicted by both methods. This is consistent with the work of Lai *et al.* [135], who investigated the energetics of this transformation and the presence of  $\omega$  at  $\beta$  twin boundaries and  $\beta - \alpha''$  interfaces with DFT. The fitted potential also agrees well with present DFT calculations for pure titanium, where the energetic spacing between  $\beta$  and  $\omega$  is an order of magnitude higher than in the  $\text{Ti}_3\text{Nb}$  system. Since the G1 supercell is but one of many possible chemical decorations of the  $\omega$ -Ti lattice, the effect of alloying is considered next.

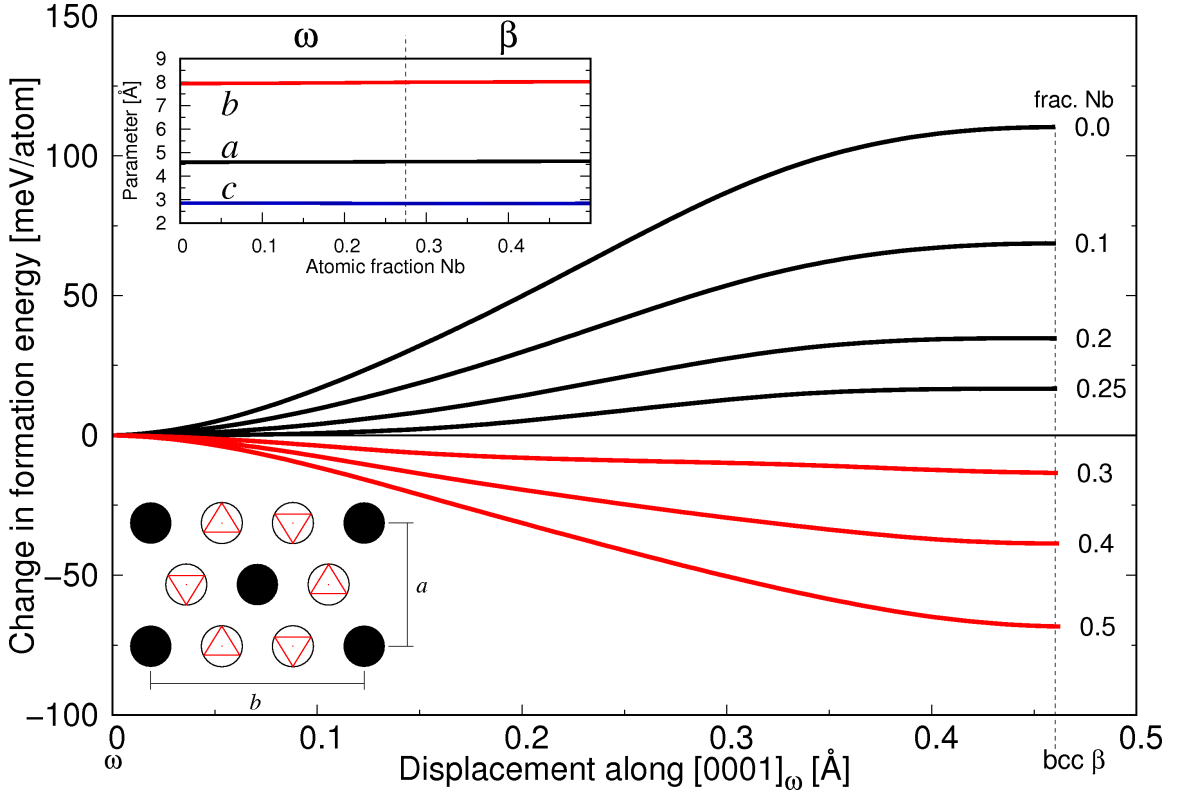


Figure 6.7: Evolution of the  $\omega \leftrightarrow \beta$  transition pathway at 0 K with niobium in solid solution. A six-atom orthorhombic  $\omega$  cell is repeated  $10 \times 10 \times 5$  (3,000 atoms in total) and atomic decoration is randomly assigned to match the niobium concentration shown on the right-hand side of the curves. The horizontal axis represents the displacement as the two 2D-sublattices of the bipartite honeycomb layers are shifted up and down along  $[0001]_{\omega}$ , as shown by upward-facing and down-ward facing triangles respectively, until they become different  $\langle 111 \rangle_{\beta}$  planes. At each point the cell dimensions are relaxed to zero pressure. The parameters of the lowest-energy structure for each concentration are plotted in the inset. Curves are colored according to the equilibrium structure, where black represents  $\omega$ -Ti and red represents bcc. The lack of any local minima indicates the potential will not form a trigonal  $\omega$  phase at equilibrium in any of the considered concentrations. The cell parameters remain relatively unchanged due to the inherent structural compatibility of the  $\beta$  and  $\omega$  phases.

Figure 6.7 shows the GMEAM  $\omega \leftrightarrow \beta$  transition at 0 K for multiple niobium concentrations in solid solution, labeled on the curves. The energy of  $\omega$  is taken as zero, and the right-hand side of the curve represents a complete transition to bcc. This is accomplished by splitting the honeycomb layers of an orthorhombic  $\omega$  supercell

into  $\langle 111 \rangle_\beta$  planes. At each step, the supercell lattice parameters are relaxed to zero-pressure. The equivalent six-atom orthorhombic cell parameters (shown in bottom left) for the lowest-energy structure are plotted in the inset, and curves in the main figure are colored according to the equilibrium structure for that stoichiometry. The fitted GMEAM potential does not display a transition barrier from  $\beta$  to  $\omega$  at any of the considered concentrations, unlike the  $G1$  intermetallic transition shown in Figure 6.6 and that computed by Lai *et al.* [135]. By 30 at.% Nb, the bcc phase is energetically favorable at 0 K. Despite the shift in energy, lattice parameters remain nearly constant due to the inherent structural compatibility between bcc and  $\omega$ -Ti. No stable configurations are found at partial transformations, indicating that the trigonal  $\omega$  phase will not exist in bulk at 0 K with the present GMEAM potential. It is worth noting that solutes in beta titanium alloys have been observed to be ejected from the isothermal  $\omega$  phase into the  $\beta$  matrix upon aging [154, 155] but not in quenched  $\omega$  precipitates where the planar collapse is incomplete [154], so the composition and structure of the  $\omega$  phase depends heavily on thermal history. The fitted potential should provide a useful tool for atomistic investigation of these effects.

Crystal structure of the  $\alpha$  martensite in  $\beta$ -titanium alloys varies with  $\beta$ -stabilizer content. A four-atom orthorhombic cell with space group  $Cmcm$  and Wyckoff positions  $(0, 0, 0)$ ,  $(1/2, 1/2, 0)$ ,  $(0, 1 - 2y, 1/2)$  and  $(1/2, 1/2 - 2y, 1/2)$  can be used to describe  $\beta$  and all variants of the  $\alpha$  martensite by changing  $y$  and the axial ratios. More detail about this cell is provided in Lazar *et al.* [133]. The Burgers [59] mechanism describing the  $\alpha \leftrightarrow \beta$  transition has two independent variables: one which changes the parameter  $y$  and another which changes axial ratios. As such, one can obtain potential energy surfaces for  $\alpha \leftrightarrow \beta$  and  $\alpha'' \leftrightarrow \beta$ -L<sub>6</sub><sub>0</sub> transitions via the Burgers mechanism by tuning this four-atom unit cell.

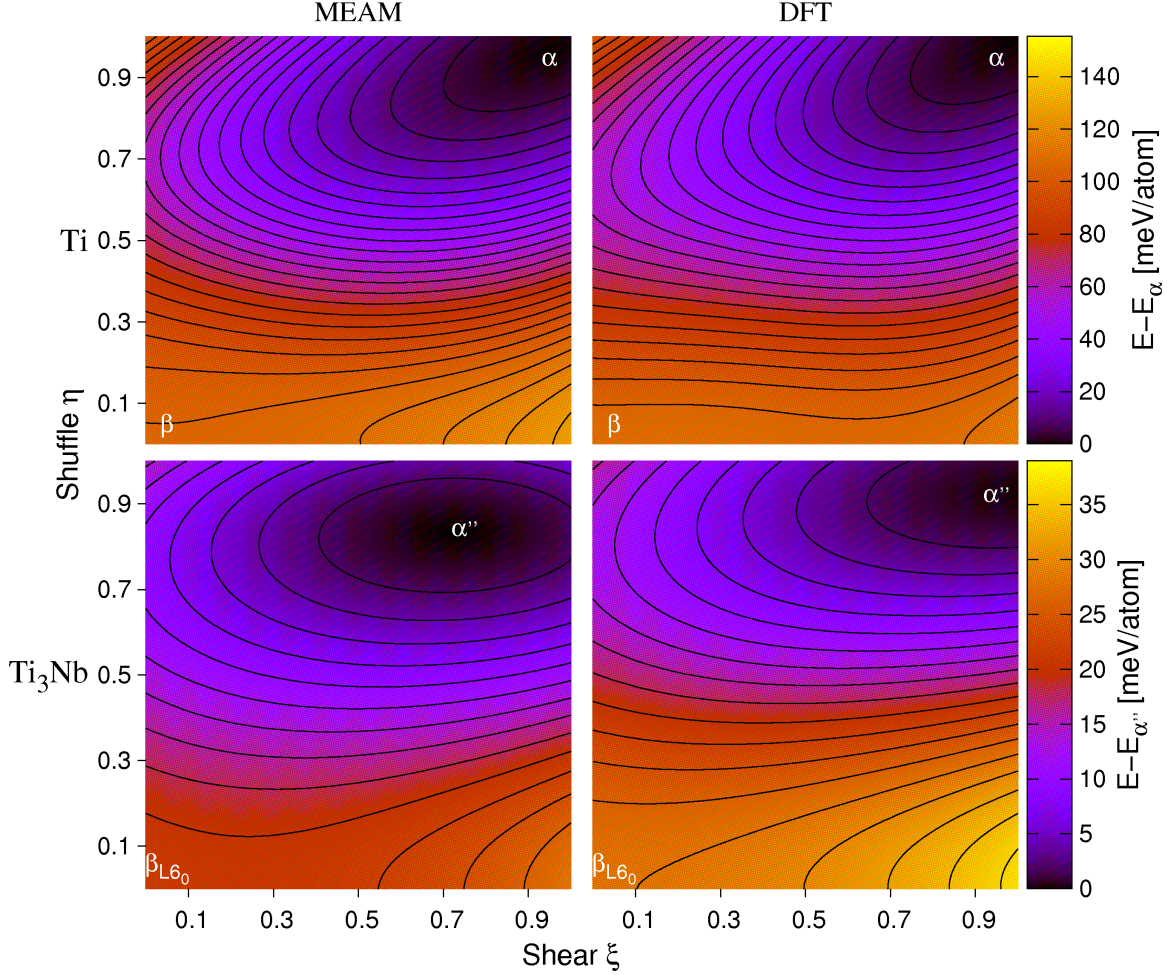


Figure 6.8: Potential energy surfaces for the  $\alpha \leftrightarrow \beta$  transition by the Burgers mechanism as calculated with GMEAM (left) and DFT (right) for pure Ti (top) and  $Ti_3Nb$  (bottom). In all cases,  $\xi = \eta = 0$  is the location of the bcc  $\beta$  phase ( $L6_0$  structure for  $Ti_3Nb$ ) while  $\alpha$  or  $\alpha''$  is located at  $\xi = \eta = 1$ . Calculations were performed on a  $50 \times 50$  grid for which  $\eta$  and  $\xi$  each vary from -0.125 to 1.125. The energy surfaces are fitted to seventh-order polynomial functions for the purpose of drawing smooth contours.

Figure 6.8 shows contour plots of energetic surfaces for the  $\alpha \leftrightarrow \beta$  transition via the Burgers mechanism. GMEAM calculations are shown in the left column, with present DFT work in the right column. Plots on the top row are for pure titanium and plots at the bottom represent a transition from a bcc  $L6_0$  structure to the  $\alpha''$  structure proposed by Sun *et al.* [136]. The bcc  $\beta$  structures are located at  $\eta = \xi = 0$

and the  $\alpha$  and  $\alpha''$  structures are located at  $\eta = \xi = 1$ . Energies are measured relative to the minimum in each plot.

Shear ( $\xi$ ) represents simultaneous elongation along  $[011]_\beta$  and  $[0\bar{1}1]_\beta$ , which maps in a linear fashion both the  $b/a$  and  $c/a$  ratios of the orthorhombic cell from  $\sqrt{2}$  to their optimal values in the martensite. Varying the axial ratios with the same parameter is an approximation. EMTO-CPA results of Li *et al.* [156], who examine the optimal relationship between  $b/a$  and  $c/a$ , indicate that the induced error of the present assumption is on the order of 1 meV/atom for pure Ti. Their results also suggest that the optimal relationship between  $c/a$  and  $b/a$  becomes more linear with increased niobium content, so this error should decrease.

Shuffle ( $\eta$ ) represents a shift of alternating  $(011)_\beta$  planes in a  $[0\bar{1}1]_\beta$  direction, described by changing  $y$  from  $1/4$  in the bcc lattice ( $\eta = 0$ ) to  $y = 1/6$  ( $\eta = 1$ ) in the hcp lattice. In  $\alpha''$ , the value of  $y$  corresponding to  $\eta = 1$  is taken from Sun *et al.* to be  $y = 0.2$ , but present DFT calculations find an optimal value of  $y = 0.204$ . Axial ratios corresponding to  $\xi = 1$  are the optimal values in the present DFT work. The overall lattice constant  $a$  is an average of the appropriate values of the  $\beta$  and martensite lattices.

GMEAM and DFT are in good agreement for the burgers transition in pure titanium, and are consistent with the LDA-DFT and EAM results of Masuda-Jindo *et al.* [52].

GMEAM underestimates the difference in energy between  $\beta$ - $L6_0$  and  $\alpha''$  as it assigns  $L6_0$  an energy about 15 meV/atom lower than DFT. Furthermore, GMEAM predicts a  $\alpha''$  phase with incomplete shuffle and shear compared to the DFT structure, indicating a difference in lattice constants and parameter  $y$ . Fully relaxed DFT cell parameters of  $\alpha''$  are  $a = 3.33$  Å,  $b = 4.77$  Å,  $c = 4.41$  Å and  $y = 0.204$  while GMEAM predicts  $a = 3.24$  Å,  $b = 4.78$  Å,  $c = 4.48$  Å and  $y = 0.208$ . Despite

this fitting error, the discussion of Figure 6.9 shows that the lattice constants of solid-solution  $\alpha''$  predicted by the fitted potential agree well with experiment.

The evolution of martensite phases in  $\beta$  or near- $\beta$  titanium alloys is important to their morphology and mechanical behavior. The hcp-Ti  $\alpha$  phase becomes distorted when alloying with  $\beta$ -stabilizing elements, eventually leading to the  $\alpha''$  orthorhombic phase. This distortion follows the same shuffle mechanism employed in Figure 6.8, and the position of the minimum-energy state changes with niobium content. We now investigate this deformation in solid-solution Ti-Nb.

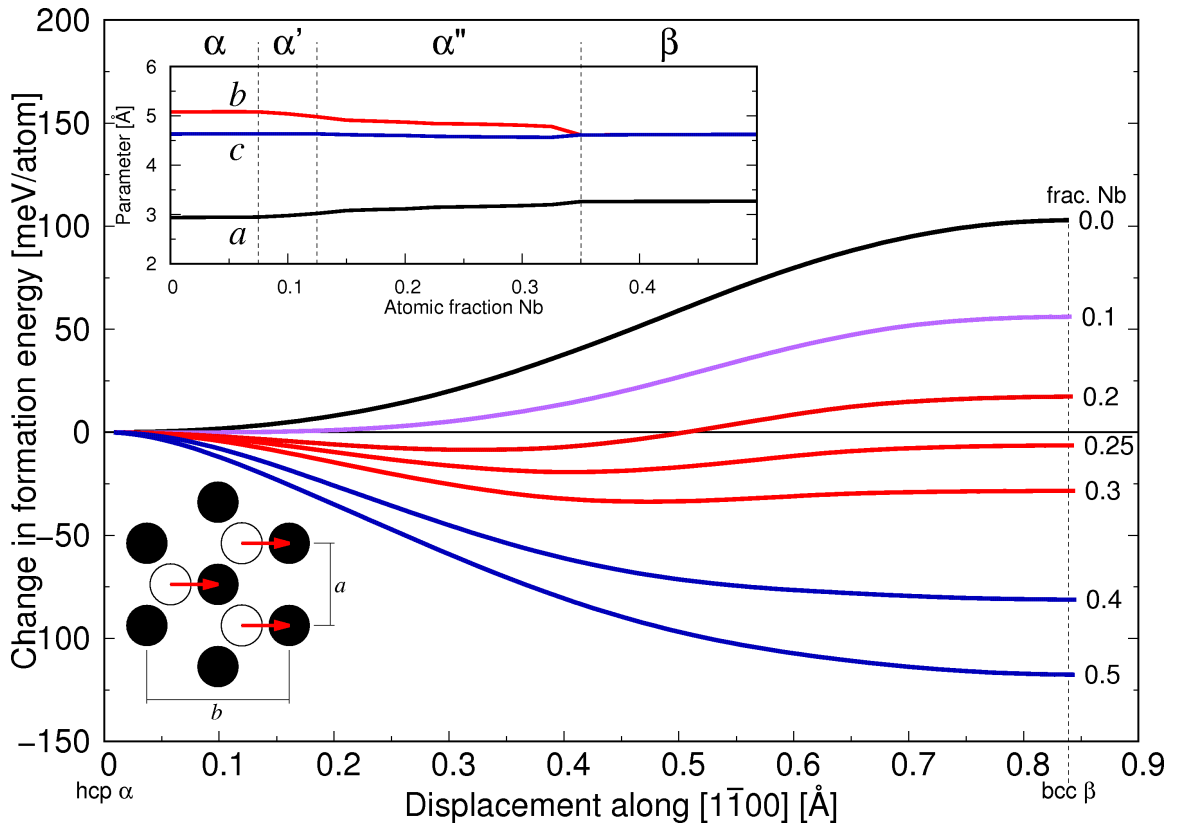


Figure 6.9: Evolution of the 0 K equilibrium structure with niobium in solid solution as calculated with GMEAM. The four-atom orthorhombic hcp unit cell is repeated  $10 \times 10 \times 5$  (2,000 total atoms) and atomic decoration is randomly assigned to match the niobium concentration shown on the right-hand side of the curves. The horizontal axis represents displacement in angstroms as alternating basal planes are shifted along  $[1\bar{1}00]_\alpha$ . The displacement for the completed transformation to bcc is labeled on the right for pure Ti; because the lattice parameter  $b$  increases with Nb content, other curves slightly exceed this value. At each point the simulation cell parameters are relaxed to zero pressure. Curves are colored according to the lowest energy structure along the transition path where black is  $\alpha$  (hcp), purple is  $\alpha'$ , red is  $\alpha''$  and blue is  $\beta$  (bcc). Cell dimensions from this structure at 18 concentrations are plotted in the inset with phase boundaries. Only select stoichiometries are plotted in the main figure for clarity. Niobium induces a strain in the hexagonal structure, destabilizing it in favor of  $\alpha'$  by  $\sim 7.5$  at.% Nb,  $\alpha''$  between  $\sim 12.5$  and  $\sim 35$  at.% Nb, and bcc beyond 35 at.% Nb.

Figure 6.9 reports the GMEAM  $\alpha \leftrightarrow \beta$  transition energy as a function of displacement in the  $[1\bar{1}00]_\alpha$  direction of alternating basal planes  $(0002)_\alpha$  for various niobium

concentrations (labeled on the curves) at 0 K. At each displacement, the cell is relaxed to zero pressure. The equivalent four-atom orthorhombic cell (bottom left) lattice constants of the lowest-energy structure for 18 concentrations are plotted in the inset. For clarity, only select concentrations are plotted in the main figure. At 10 at.% Nb, no significant minimum develops with respect to the shifting of atomic planes but a slight change in lattice constants  $a$  and  $b$  indicates a breaking of the perfect hexagonal symmetry, consistent with the formation of an  $\alpha'$  martensite phase [51]. With a concentration 20 at.% niobium, a partial displacement of  $(0002)_\alpha$  planes is energetically favorable by about 12 meV/atom. This local minimum represents the orthorhombic  $\alpha''$  phase, which is the equilibrium structure up to 35 at.% Nb. Lattice constants of this solid solution  $\alpha''$  structure at 25 at.% Nb are  $a = 3.15 \text{ \AA}$ ,  $b = 4.84 \text{ \AA}$  and  $c = 4.58 \text{ \AA}$ , very close the experimental values of  $a = 3.19 \text{ \AA}$ ,  $b = 4.80 \text{ \AA}$  and  $c = 4.64 \text{ \AA}$  reported by Sun *et al.* [136]. Beyond 35 at.%, bcc is the lowest energy structure. At this point niobium has completely stabilized the bcc phase as can be seen by the lattice parameters where  $c = b = a\sqrt{2}$ .

The shape-memory effect (SME) is known to exist in binary Ti-Nb alloys [157, 158], gum metals [26, 23] and other titanium and Ti-Nb alloys [51, 159, 36]. The SME is characterized by a recovery of initial geometric shape after deformation at a low temperature and subsequent heating. The physical processes that underly this effect are stress- and temperature-induced martensitic phase transitions. Upon straining, a stress-induced transition grows the martensite domains. Subsequent heating of the material induces a reverse transition wherein martensite domains are destroyed and the accumulated stress and strain are recovered. Below, we demonstrate the ability of the fitted GMEAM potential to model the stress- and temperature-induced martensitic transitions that underly the SME in Ti-25 at.%Nb.

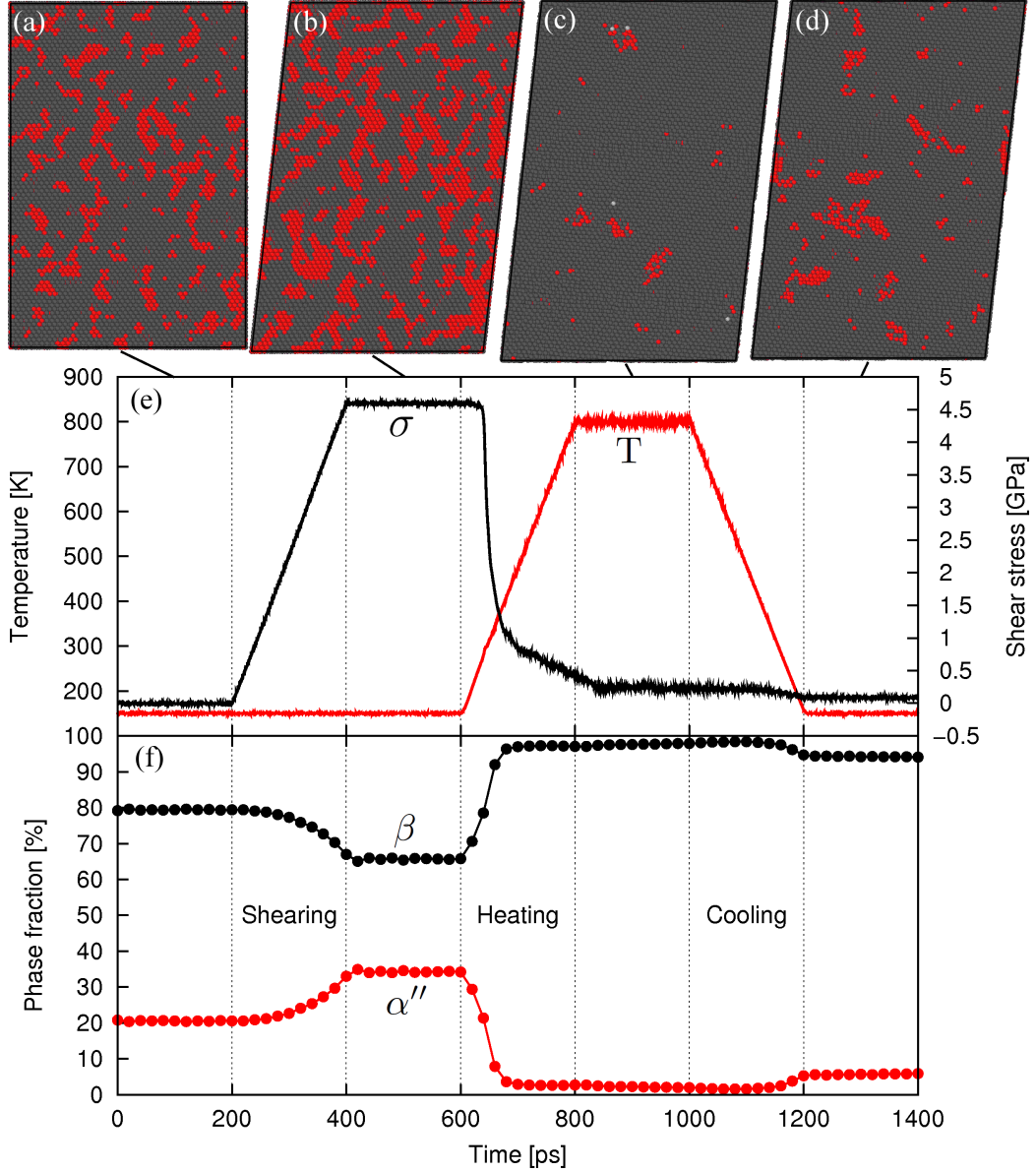


Figure 6.10: 364,500-atom NPT simulation of stress- and temperature-induced martensitic transitions in Ti-25 at.%Nb using the fitted GMEAM potential with a timestep of 1 fs. (a) shows the cell microstructure at 150 K and 0 GPa with atoms colored by local crystal structure. Grey atoms are identified as bcc and red atoms as  $\alpha''$ . (b) shows an increase in  $\alpha''$  martensite upon shearing. (c) shows that a subsequent heating of the cell to 800 K destroys the martensite domains, releasing most of the accumulated shear stress as shown in (e). Martensite domains grow upon cooling (d), but account only for 5.8% of atoms, compared to 20.9% in the pre-cycle structure (f). Structure identification is done by polyhedral template-matching [160] as implemented in the current version of OVITO [43, 44].

Figure 6.10 displays results of a 364,500-atom constant-NPT simulation of stress- and temperature-induced martensitic transitions in Ti-25 at%Nb using the fitted GMEAM potential with a timestep of 1 fs. The simulation cell is a  $45 \times 45 \times 45$  supercell of the four-atom orthorhombic hcp cell. Atoms are assigned chemical species randomly, and the cell is first equilibrated at 150 K and 1 atm pressure. At the top of the figure, cross-sections of the cell are shown at significant points in the simulation. The plane of the page corresponds to  $(001)_{\alpha''}$  or  $(110)_{\beta}$ . Atoms are assigned a color based on local crystal structure as determined by polyhedral template-matching (PTM) [160] as implemented in OVITO [43, 44]. Grey atoms are austenite ( $\beta$ ) and red atoms are martensite ( $\alpha''$ ). Note that the PTM method does not distinguish between  $\alpha$ ,  $\alpha'$  or  $\alpha''$ , but the martensite structure is referred to as  $\alpha''$  consistent with the stoichiometry used here and the results presented in Figure 6.9. The middle panel (e) plots shear stress and simulation temperature as functions of time and the bottom panel (f) shows the fraction of atoms identified as martensite and austenite as functions of time.

Between 200 and 400 ps, a shear strain of 5% is applied to the  $[100]_{\beta}(0\bar{1}1)_{\beta}$  shear system. As a result, the fraction of atoms in  $\alpha''$  domains increases by 15%. A total of 4.5 GPa of shear stress is accumulated by the cell, and this holds constant between 400 and 600 ps. The simulation cell is heated from 150 K to 800 K between 600 and 800 ps. As can be seen in the bottom panel, martensite domains begin transforming to austenite (bcc) immediately upon heating. By 640 ps, when the temperature is roughly 410 K, the  $\beta$  phase has been saturated at about 95% coinciding with a nearly-complete release of the accumulated shear stress. This gives us an estimate of 410 K for the austenite finish temperature predicted by GMEAM, consistent with the experimental value of 390 K reported by Al-Zain *et al.* [158]. Cooling the cell does not cause austenite to revert to martensite until the temperature reaches about

300 K, and the recovered volume fraction of martensite is only 5.8%. This is not a complete cycle of the shape-memory effect but nonetheless demonstrates the ability of the fitted potential to model stress- and temperature-induced martensitic transitions in Ti-25 at.%Nb.

In summary, the  $\omega \leftrightarrow \beta$  and  $\alpha \leftrightarrow \beta$  transitions in Ti-Nb alloys have been examined using the fitted GMEAM potential. The potential was shown to be consistent with present and past DFT calculations, and was used to investigate the effect of alloying on these transitions. The  $\omega \leftrightarrow \beta$  transition in solid solution was found to lack the 5 meV/atom barrier present in Figure 6.6. The  $\alpha$  phase was found to distort when alloyed with niobium, first breaking perfect hexagonal symmetry to form  $\alpha'$  at ~7.5 at.%, then becoming the orthorhombic  $\alpha''$  phase between ~12.5 and ~35 at.%. The stress- and temperature-induced martensitic transitions between  $\alpha''$  and  $\beta$  that underly the SME in Ti-Nb alloys were demonstrated by NPT simulation.

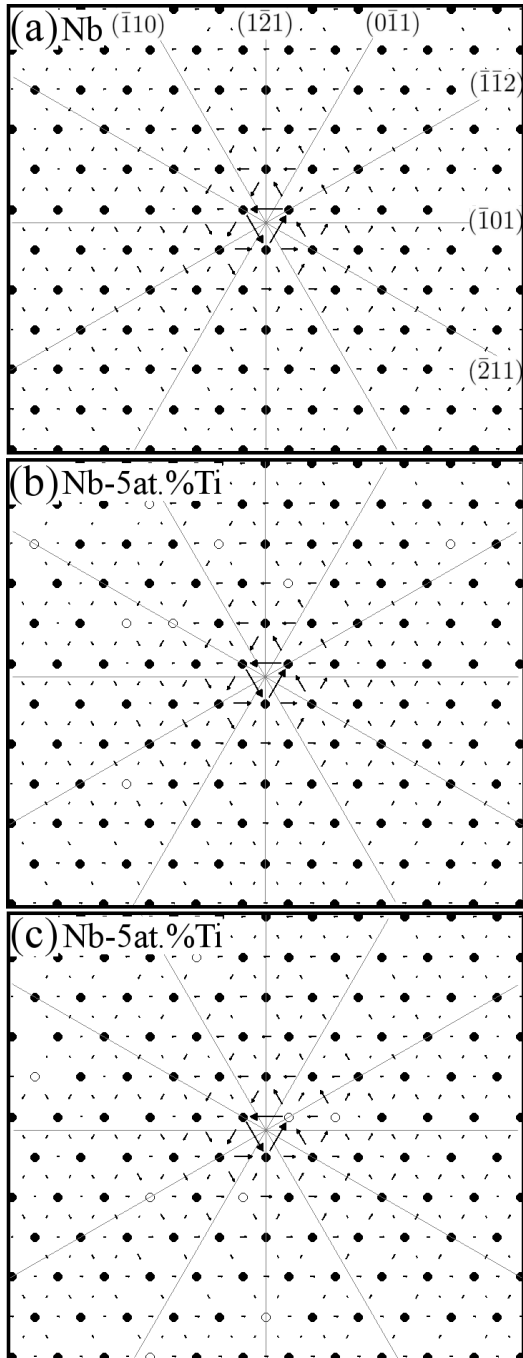


Figure 6.11: Core structure of a  $1/2[111]$  screw dislocation in (a) pure niobium and (b) and (c) two configurations of  $\text{Nb}_{95}\text{Ti}_5$ . Traces of planes, which are labeled in (a), cross at the origin of the elastic solution. Only screw components (displacements parallel to the burgers vector) are plotted. Niobium atoms are shown in black and titanium atoms are shown in white. GMEAM predicts a symmetric core in pure niobium, with little effect on the structure from the presence of titanium solute atoms.

## 6.4 Dislocation Core Structures

We consider screw dislocations in bcc Nb and hcp Ti and analyze the effect of alloying on the core structure. In both cases a large supercell with periodicity along the dislocation line and fixed boundary conditions in the other two directions is employed. Atoms are displaced in this direction according to the strain field solution from linear elasticity,  $u_z = (b/2\pi)\tan^{-1}y/x$ , as described in Hirth and Lothe [161]. Fixing atoms at the boundary ensures that the relaxed cell satisfies the long-range boundary conditions imposed by the dislocation. We have employed this method in our previous work on niobium [86], molybdenum [88] and tungsten [98], where more information is available.

Figure 6.11 contains differential displacement maps of a  $1/2[111]$  screw dislocation in (a) bcc Nb, (b) and (c) two configurations of a bcc Nb-5 at.%Ti alloy. Traces of atomic planes, labeled in part (a), cross at the origin of the elastic solution. The simulation cell has directions  $[1\bar{2}1]$ ,  $[\bar{1}01]$ , and  $[111]$  along  $x$ ,  $y$ , and  $z$  repeated  $114 \times 190 \times 8$  for a total of 1,042,109 atoms with 5 at.% Ti in solid solution. A cylindrical region containing 435,168 atoms, concentric with the dislocation, is relaxed to obtain the core structure. In pure Nb, only a single periodic unit is used along the  $z$  direction. GMEAM predicts a symmetric core for pure niobium (a), which is found to be very resilient to alloying with Ti in (b) and (c). Even when the titanium solute atom lies on the central triad around the dislocation, as in (c), only slight distortion of the symmetric core is observed. While the six-fold symmetry around the core is broken, the core does not become a three-fold “degenerate” core such as that found for niobium in Fellinger *et al.* [86]. The fitted potential thus predicts titanium solute atoms to have little effect on the slip behavior of bcc niobium.

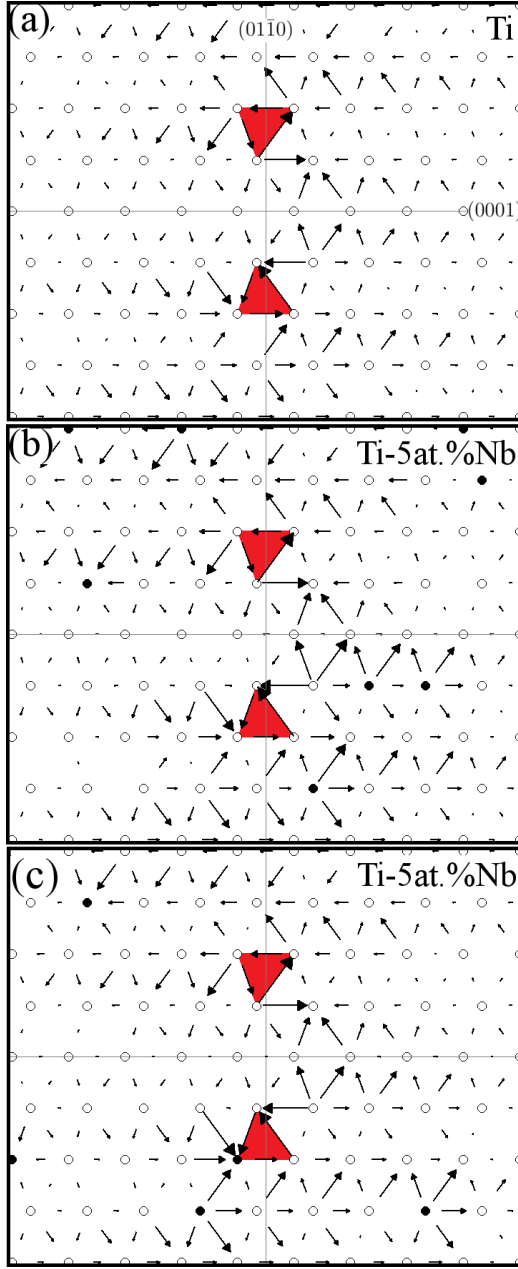


Figure 6.12: Core structure of a  $1/3[1\bar{1}20]$  screw dislocation in (a) pure titanium and (b) and (c) two configurations of  $\text{Ti}_{95}\text{Nb}_5$ . Traces of planes, which are labeled in (a), cross at the origin of the elastic solution. Only screw components (displacements parallel to the burgers vector) are plotted. Partial dislocations are represented by closed triads of atoms, shaded in red to guide the eye. Niobium atoms are shown in black and titanium atoms are shown in white. The structure of this symmetric core is consistent with previous DFT and MEAM calculations by Ghazisaeidi and Trinkle as well as Tarrat *et al.* [152, 153]. The presence of Nb near the core breaks the mirror symmetry and causes spreading, primarily into basal planes, but preserves the dissociated structure.

Figure 6.12 shows differential displacement maps of a  $1/3[1\bar{2}10]$  prismatic dislocation in (a) hcp Ti and (b) and (c) two configurations of an hcp Ti-5 at.%Nb alloy. In these maps, a closed triad of atoms represents a displacement of  $b/2$ , i.e. a partial dislocation. These triads are shaded in red to guide the eye. Traces of atomic planes, labeled in (a), cross at the origin of the elastic solution. The simulation cell has directions  $[1\bar{1}00]$ ,  $[0001]$  and  $[1\bar{2}10]$  along  $x$ ,  $y$  and  $z$ , repeated  $155 \times 144 \times 8$  for a total of 714,240 atoms with 5 at.% Nb in solid solution. For the dislocation in pure Ti (a), only a single periodic unit is used in the  $z$  direction. Of the possible locations for the elastic origin, it is placed in the lower energy “mirror” configuration as determined by previous *ab initio* studies [152, 153]. A cylindrical region containing 366,912 atoms, concentric with the dislocation, is relaxed to obtain the core structure.

GMEAM predicts the dislocation to dissociate in the prismatic plane, separated by an (easy)  $\{01\bar{1}0\}\langle 11\bar{2}0\rangle$  stacking fault with symmetry across the basal, consistent with DFT and MEAM results from Ghazisaeidi and Trinkle [152] and DFT results of Tarrat *et al.* [153]. Sub-plots (b) and (c) are different  $(1\bar{2}10)$  cross-sections of the same cell, and show significant distortion of the dissociated core structure relative to that in pure titanium. In (b), the presence of Nb atoms near the elastic core causes a spreading into the basal plane. The atoms causing this distortion are the closest solute atoms to the elastic origin, but do not lie on either of the partial dislocation triads. In (c), where niobium atoms are on and near the bottom partial in a pyramidal plane, spreading is less pronounced. Solute atoms appear to have the most significant effect when located near the elastic core on basal planes between the partial dislocations.

The fitted GMEAM potential predicts niobium solutes to have a more significant effect on dislocation core structure in titanium than the converse. This is sensible given that hcp Nb is roughly four times higher in formation energy than bcc Ti. The fundamental structure of the dislocations is not affected at 5 at.% solute content in

either alloy.

## 6.5 Summary

We present a GMEAM-like empirical potential for Ti-Nb alloys, fitted to data across the range of concentrations but focused on martensitic transformations and multi-phase properties of gum metal approximants near 25 at.% Nb. The fitted potential is shown to be consistent with previous calculations and measurements of elastic constants, thermal expansion, point defects, stacking faults and martensitic transitions.

We study the impact of alloying on the energetics of martensitic phase transition pathways at 0 K. For the  $\beta$  to  $\omega$ -Ti transition (Fig. 6.7), a lack of transition barrier in contrast to the DFT results of Lai *et al.* [135] and the present work (Fig. 6.6), both of which employed a G1 supercell, is found. The fitted GMEAM potential predicts a distortion of the  $\alpha$  martensite with niobium content, estimated by calculations along the Burgers transformation pathway (Fig. 6.9), consistent with experiment. The  $\alpha''$  structure is found to persist in solid solution until 40 at.% Nb at 0 K. Stress- and temperature-induced transitions between  $\beta$  and  $\alpha''$  which underly the shape-memory effect in Ti-25 at.%Nb are demonstrated by NPT simulation (Fig. 6.10) in a cell with a single  $\beta$  grain.

The effect of solute atoms, with concentrations of 5 at.%, on dislocation cores in hcp-Ti and bcc-Nb is also examined. Symmetric cores of the  $\frac{1}{2}\langle 111 \rangle$  screw dislocation in bcc-Nb (Fig. 6.11) are found to be mostly unaffected by titanium solutes, with small amounts of distortion but no significant spreading or change of core structure. The  $\frac{1}{3}\langle 1\bar{1}20 \rangle$  dislocation in hcp-Ti (Fig. 6.12), which dissociates in the prismatic plane, is seen to spread primarily into basal planes depending on the location of niobium solutes, but the dissociated structure is preserved.

The fitted potential is suitable for the study of plastic deformation, martensitic transitions,  $\omega$ -phase formation, defect structures and their interplay in Ti-Nb alloys.

## Chapter 7:

# Conclusions and Future Directions

This work has presented two robust empirical extensions of the modified embedded atom formalism, parameterized by spline functions and force-matched to large density-functional theory databases. The potentials have demonstrated accuracy in a variety of static and dynamic material conditions including phase transitions and plastic deformation. Such robust interatomic potentials are desirable to have for all material systems but require a great deal of effort to develop.

Future development of MEAM-like empirical potentials will necessarily involve large fitting databases and highly flexible models as employed in the present work. The choice of model should be based on the complexity of the material under study, but results presented here suggest that large databases produce highly transferable potentials, even for a single-phase system such as tungsten.

The SW+MEAM model presented in Chapter 5 could be applied to other transition metals at high pressure, or possibly to lanthanide and actinide materials whose many-phase nature requires great flexibility to model accurately. As was described by Nicklas[94], additional Stillinger-Weber type terms can be added to the total energy, without redundancy, to achieve greater model flexibility with the same formalism.

The choice of model form for an alloy potential depends similarly on the complexity of the material’s phase diagram. The GMEAM model presented in Chapter 6 was chosen for its flexibility. High flexibility was needed because of the number of energetically-similar phases, but this form is unlikely to transfer easily to ternary or quaternary alloy systems. The number of functions in GMEAM scales *cubically* with the number of atomic species  $N$  as  $N[(N + 1)(N + 2)/2 + 2]$ . Thus for a ternary system 36 functions would need to be fit. For a quaternary alloy, the number would be 68. One needs to generate enough *consistent* DFT data to properly saturate the domains of all of these functions before development can even begin!

In principle one could limit the number of spline knots in each function in order to reduce the data necessary to saturate their domains, but an easier starting point would be a different formulation of MEAM for alloys. Zhang and Trinkle [162] developed a MEAM potential for the binary Ti-O species in which the triplet term does not depend on the central atom as in the present GMEAM formulation. This is most consistent with the original inspiration of the Stott-Zaremba corollary. Another option is to have the angular function depend only on the central atom and not all three species in a triplet. Both of these forms only scale quadratically with  $N$ , and thus offer a simpler starting point for the development of ternary or quaternary alloy potentials.

Roughly 2 million CPU-hours were spent developing the Ti-Nb potential of the present work. Given a similar number of spline knots per function, a commensurate database size and comparable parallelization speedups, the necessary CPU-hours for developing spline-based potentials can be estimated as a function of constituent species. Figure 7 plots these development times for up to five-species alloys.

In summary, the state-of-the-art empirical potentials developed in this work provide more accurate descriptions of two technologically important metals. Interatomic potentials will remain an important tool in materials development for the foreseeable

future, and an approximate roadmap for the development of similarly complex models has been presented.

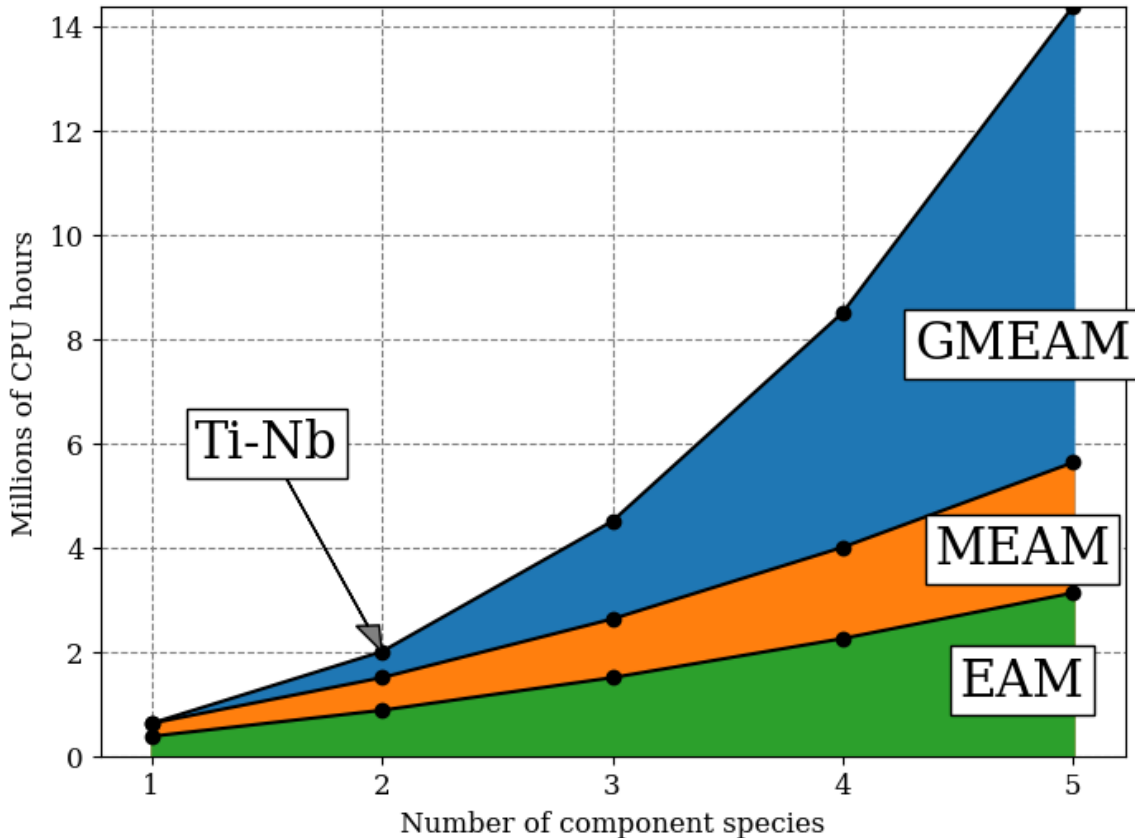


Figure 7.1: Estimated number of CPU hours for developing embedded-atom type potentials for alloys. MEAM here is taken to be the form proposed by Zhang and Trinkle [162]. Estimation is done assuming equivalent computational efficiency and commensurate databases and spline parameterizations. Values are computed based on the number of functions in each model. Trends are quadratic for EAM and MEAM but cubic for GMEAM, emphasizing the need to use simpler model formulations for ternary and higher compounds.

# Bibliography

- [1] Furio Ercolessi and James B. Adams. Interatomic potentials from first-principles calculations: the force-matching method. *Europhys. Lett.*, 26:583, 1994.
- [2] T. J. Lenosky, B. Sadigh, E. Alonso, V. V. Bulatov, T. D. de la Rubia, J. Kim, A. F. Voter, and J. D. Kress. Highly optimized empirical potential model of silicon. *Modelling Simul. Mater. Sci. Eng.*, 8:825, 2000.
- [3] T. Karabacak, A. Mallikarjunan, J. P. Singh, D. Ye, G. Wang, and T. Lu.  $\beta$ -phase tungsten nanorod formation by oblique-angle sputter deposition. *Appl. Phys. Lett.*, 83(15):3096–3098, 2003.
- [4] T. Karabacak, P. Wang, G. Wang, and T. Lu. Phase transformation of single crystal  $\beta$ -tungsten nanorods at elevated temperatures. *Thin Solid Films*, 493:293–296, 2005.
- [5] J. Wang, Z. Zeng, C. R. Weinberger, Z. Zhang, T. Zhu, and S. X. Mao. *In situ* atomic-scale observation of twinning-dominated deformation in nanoscale body-centered cubic tungsten. *Nat. Mat.*, 14:594–600, 2015.
- [6] E. Ozawa, Y. Kawakami, and T. Seto. Formation and size control of tungsten nanoparticles produced by Nd:YAG laser irradiation. *Scr. Mater.*, 44:2279–2283, 2001.

- [7] H. Lei, Y. J. Tang, J. J. Wei, J. Li, X. B. Li, and H. L. Shi. Synthesis of tungsten nanoparticles by sonoelectrochemistry. *Ultrason. Sonochem.*, 14:81–83, 2007.
- [8] Y. Shibuta and T. Suzuki. A molecular dynamics study of the phase transition in bcc metal nanoparticles. *J. Chem. Phys.*, 129:144102, 2008.
- [9] S. S. Harilal, N. Farid, A. Hassanein, and V. M. Kozhevnikov. Dynamics of femtosecond laser produced tungsten nanoparticle plumes. *J. Appl. Phys.*, 114:203302, 2013.
- [10] K. L. Chopra, M. R. Randlett, and R. H. Duff. Face-centered cubic modification in sputtered films of tantalum, molybdenum, tungsten, rhenium, hafnium and zirconium. *Phil. Mag.*, 16:261, 1967.
- [11] A. M. Haghiri-Gosnet, F. R. Ladan, C. Mayeux, H. Launois, and M. C. Joncour. Stress and microstructure in tungsten sputtered thin films. *J. Vac. Sci. Technol. A*, 6:2663, 1989.
- [12] I. A. Weerasekera, S. I. Shah, D. V. Baxter, and K. M. Unruh. Structure and stability of sputter deposited beta-tungsten thin films. *Appl. Phys. Lett.*, 64:3231, 1994.
- [13] G. J. Ackland and R. Thetford. An improved n-body semi-empirical model for body-centered cubic transition metals. *Phil. Mag. A*, 56:15, 1987.
- [14] M. I. Baskes. Modified embedded-atom potentials for cubic materials and impurities. *Phys. Rev. B*, 46:2727, 1992.
- [15] B. J. Lee, M. I. Baskes, H. Kim, and Y. K. Cho. Second nearest-neighbor modified embedded atom method potentials for bcc transition metals. *Phys. Rev. B*, 64:184102, 2001.

- [16] X. W. Zhou, R. A. Johnson, and H. N. G. Wadley. Misfit-energy-increasing dislocations in vapor-deposited cofe/nife multilayers. *Phys. Rev. B*, 69:144113, 2004.
- [17] P. M. Derlet, D. Nguyen-Manh, and S. L. Dudarev. Multiscale modeling of crowdion and vacancy defects in body-centered-cubic transition metals. *Phys. Rev. B*, 76:054107, 2007.
- [18] M. Mrovec, R. Gröger, A. G. Bailey, D. Nguyen-Manh, C. Elsässer, and V. Vitek. Bond-order potential for simulations of extended defects in tungsten. *Phys. Rev. B*, 75:104119, 2007.
- [19] J. Wang, Y. L. Zhou, M. Li, and Q. Hou. A modified W-W interatomic potential based on ab initio calculations. *Modell. Simul. Mater. Sci. Eng.*, 22:015004, 2014.
- [20] S. T. Murphy, S. L. Daraszewicz, Y. Giret, M. Watkins, A. L. Shluger, K. Tanimura, and D. M. Duffy. Dynamical simulations of an electronically induced solid-solid phase transformation in tungsten. *Phys. Rev. B*, 92:134110, 2015.
- [21] T. Saito, T. Furuta, J.-H. Hwang, S. Kuramoto, K. Nishino, N. Suzuki, R. Chen, A. Yamada, K. Ito, Y. Seno, T. Nokana, H. Ikehata, N. Nagasako, C. Iwamoto, Y. Ikuhara, and T. Sakuma. Multifunctional alloys obtained via a dislocation-free plastic deformation mechanism. *Science*, 18:464–467, 2003.
- [22] Y. L. Hao, S. J. Li, S. Y. Sun, and R. Yang. Effect of zr and sn on young's modulus and superelasticity of Ti-Nb-based alloys. *Mat. Sci. Eng. A*, 441:112–118, 2006.

- [23] H. Y. Kim, Y. Ikehara, J. I. Kim, H. Hosoda, and S. Miyazaki. Martensitic transformation, shape memory effect and superelasticity of Ti-Nb binary alloys. *Acta Mater.*, 54:2419–2429, 2006.
- [24] S. Kuramoto, T. Furauta, J. Hwang, K. Nishino, and T. Saito. Elastic properties of gum metal. *Mat. Sci. Eng. A*, 442:454–457, 2006.
- [25] R. J. Talling, R. J. Dashwood, M. Jackson, and D. Dye. On the mechanism of superelasticity in gum metal. *Acta Mater.*, 57:1188–1198, 2009.
- [26] H. Y. Kim, H. Satoru, J. H. Kim, H. Hosoda, and S. Miyazaki. Mechanical properties of shape memory behavior of Ti-Nb alloys. *Mater. Trans.*, 45:2443–2448, 2004.
- [27] X. Tang, T. Ahmed, and H. J. Rack. Phase transformations in ti-nb-ta and ti-nb-ta-zr alloys. *J. Mater. Sci.*, 33:1805–1811, 2000.
- [28] J.-P. Liu, Y.-D. Wang, Y.-L. Hao, Y. Wang, Z.-H. Nie, D. Wang, Y. Ren, Z.-P. Lu, J. Wang, H. Wang, X. Hui an dN. Lu, M. J. Kim, and R. Yang. New intrinsic mechanism on gum-like superelasticity of multifunctional alloys. *Sci. Rep.*, 3:2156, 2013.
- [29] M. Uy. Gutkin, T. Ishizaki, S. Kuramoto, I. A. Ovid'ko, and N. V. Skiba. Giant faults in deformed gum metal. *Int. J. Plast.*, 24:1333–1359, 2008.
- [30] Y. Hang, G. P. Li, G. M. Cheng, H. Wang, M. Zhang, F. Xu, and K. Yang. Stress-induced  $\alpha''$  martensite and twinning in a multifunctional titanium alloy. *Scripta Mater.*, 58:9–12, 2008.

- [31] Y. Yang, G. P. Li, G. M. Cheng, Y. L. Li, and K. Yang. Multiple deformation mechanisms of Ti-22.4Nb-0.73Ta-2.0Zr-1.34O alloy. *Appl. Phys. Lett.*, 94:061901, 2009.
- [32] H. Xing, J. Sun, Q. Yao, W. Y. Guo, and R. Chen. Origin of substantial plastic deformation in gum metals. *Appl. Phys. Lett.*, 92:151905, 2008.
- [33] E. Plancher, C. C. Tasan, S. Sandlöbes, and D. Raabe. On dislocation involvement in ti-nb gum metal plasticity. *Scripta Mater.*, 68:805–808, 2013.
- [34] D. Raabe, B. Sander, M. Friák, D. Ma, and J. Neugebauer. Theory-guided bottom-up design of  $\beta$ -titanium alloys as biomaterials based on first principles calculations: Theory and experiments. *Acta Mater.*, 55:4475–4487, 2007.
- [35] M. Friák, W. A. Counts, D. Ma, B. Sander, D. Holec, D. Raabe, and J. Neugebauer. Theory-guided materials design of multi-phase ti-nb alloys with bone-matching elastic properties. *Materials*, 5:1853–1872, 2012.
- [36] S. Prokoshkin, V. Brailovski, S. Dubinskiy, Y. Zhukova, V. Sheremetev, A. Konopatsky, and K. Inaekyan. Manufacturing, structure control, and functional testing of Ti-Nb-based SMA for medical application. *Shap. Mem. Superelasticity*, 2:130–144, 2016.
- [37] M. Dalstra, G. Denes, and B. Melsen. Titanium-niobium, a new finishing wire alloy. *Orthod. and Craniofac. Res.*, 3:6–14, 2000.
- [38] O. Madelung. *Introduction to Solid-State Theory*. Springer-Verlag, Berlin Heidelberg New York, 1978.
- [39] W. Setyawan and S. Curtarolo. High-throughput electronic band structure calculations: challenges and tools. *Comp. Mat. Sci.*, 49:299, 2010.

- [40] D. Trinkle. Lattice and elastic constants of titanium-niobium monoborides containing aluminum and vanadium. *Scripta Mater.*, 56(273-276), 2006.
- [41] D. Alf  , G. D   Price, and M. J. Gillan. Thermodynamics of hexagonal-close-packed iron under earth's core conditions. *Phys. Rev. B*, 64:045123, 2001.
- [42] S. R. Bahn and K. W. Jacobsen. An object-oriented scripting interface to a legacy electronic structure code. *Comput. Sci. Eng.*, 4:56, 2002.
- [43] A. Stukowski. Visualization and analysis of atomistic simulation data with OVITO - the open visualization tool. *Modell. Simul. Mater. Sci. Eng.*, 18:015012, 2010.
- [44] A. Stukowski. Structure identification methods for atomistic simulations of crystalline materials. *Modell. Simul. Mater. Sci. Eng.*, 20(4):045021, 2012.
- [45] C. W. Passchier and R. A. J. Trouw. *Microtectonics*. Springer-Verlag, Berlin, Germany, 2005.
- [46] V. Vitek, R. C. Perrin, and D. K. Bowen. The core structure of  $\frac{1}{2}(111)$  screw dislocations in b.c.c. crystals. *Phil. Mag.*, 21(173):1049–1073, 1970.
- [47] R. Gr  ger, A. G. Bailey, and V. Vitek. Multiscale modeling of plastic deformation of molybdenum and tungsten: 1. atomistic studies of the core structure and glide of  $1/2|111\bar{c}$  screw dislocations at 0 K. *Acta Mater.*, 56:5401, 2008.
- [48] E. B. Tadmor and R. Miller. *Modeling Materials: Continuum, Atomistic and Multiscale Techniques*. Cambridge University Press, 2011.
- [49] O. Penrose. *Foundations of Statistical Mechanics: A Deductive Treatment*. Dover Publications, Mineola, New York, USA, 2005.

- [50] S. R. Nishitani, H. Kawabe, and M. Aoki. First-principles calculations on bcc-hcp transition of titanium. *Mater. Sci. Eng. A*, 312:77, 2001.
- [51] G. Lütjering and J. C. Williams. *Titanium*. Springer-Verlag, Berlin Heidelberg New York, 2003.
- [52] K. Masuda-Jindo, S. R. Nishitani, and V. VanHung. hcp-bcc structural phase transformation of titanium: Analytic model calculations. *Phys. Rev. B*, 70:184122, 2004.
- [53] D. R. Trinkle III. *A theoretical study of the HCP to omega martensitic phase transition in titanium*. PhD thesis, The Ohio State University, 2003. [https://etd.ohiolink.edu/pg\\_10?0::NO:10:P10\\_ACCESSION\\_NUM:osu1070481734](https://etd.ohiolink.edu/pg_10?0::NO:10:P10_ACCESSION_NUM:osu1070481734).
- [54] R. G. Hennig, D. R. Trinkle, J. Bouchet, S. G. Srinivasan, R. C. Albers, and J. W. Wilkins. Impurities block the  $\alpha$  to  $\omega$  martensitic transformation in titanium. *Nat. Mater.*, 4:129, 2005.
- [55] R. G. Hennig, T. J. Lenosky, D. R. Trinkle, S. P. Rudin, and J. W. Wilkins. Classical potential describes martensitic phase transformations between the  $\alpha$ ,  $\beta$ , and  $\omega$  titanium phases. *Phys. Rev. B*, 78:054121, 2008.
- [56] W. Petry, A. Heiming, J. Trampenau, M. Alba, C. Herzig, H. R. Schober, and G. Vogl. Phonon dispersion of the bcc phase of group-IV metals. I. bcc titanium. *Phys. Rev. B*, 43:10933, 1991.
- [57] K. Einarsson, B. Sadigh, G. Grimvall, and V. Ozolinu. Phonon instabilities in fcc and bcc tungsten. *Phys. Rev. B*, 79(11):2073, 1997.

- [58] Y. Giret, S. L. Daraszewicz, D. M. Duffy, A. L. Shluger, and K. Tanimura. Non-thermal solid-to-solid phase transitions in tungsten. *Phys. Rev. B*, 90:094103, 2014.
- [59] W. G. Burgers. On the mechanism of the cubic-body-centered modification into the hexagonal-close-packed modification of zirconium. *Physica*, 1:561, 1934.
- [60] E. C. Bain and N. Y. Dunkirk. The nature of martensite. *Trans. AIME*, 70:25, 1924.
- [61] D. De Fontaine. Mechanical instabilities in the bcc lattice and the beta to omega phase transformation. *Acta Metallurgica*, 18:275, 1970.
- [62] N. W. Ashcroft and N. D. Mermin. *Solid State Physics*. Brooks/Cole, Belmont, California, USA, 1976.
- [63] M. Finnis. *Interatomic Forces in Condensed Matter*. Oxford University Press, New York, New York, USA, 2003.
- [64] W. Kohn and L. J. Sham. Self-consistent equations including exchange and correlation effects. *Physical Review*, 140:A1133–A1138, 1965.
- [65] J. Paier, M. Marsman, K. Hummer, and G. Kresse. Screened hybrid density functionals applied to solids. *J. Chem. Phys.*, 124:154709, 2006.
- [66] G. Kresse and J. Hafner. Ab-initio molecular dynamics for liquid metals. *Phys. Rev. B*, 47:558, 1993.
- [67] G. Kresse and J. Hafner. Ab-initio molecular simulation of the liquid-metal-amorphous-semiconductor transition in germanium. *Phys. Rev. B*, 49:14251, 1994.

- [68] G. Kresse and J. Furthmüller. Efficiency of ab-initio total energy calculations for metals and semiconductors using a plane-wave basis set. *Comput. Mater. Sci.*, 6:15–50, 1996.
- [69] G. Kresse and J. Furthmüller. Efficient iterative schemes for ab-initio total-energy calculations using a plane-wave basis set. *Phys. Rev. B*, 54:11169, 1996.
- [70] H. J. Monkhorst and J. D. Pack. Special points for brillouin-zone integrations. *Phys. Rev. B*, 13:5188, 1976.
- [71] M. Methfessel and A. T. Paxton. High-precision sampling for brillouin-zone integration in metals. *Phys. Rev. B*, 40:3616, 1989.
- [72] T. Schneider and E. Stoll. Molecular-dynamics study of a three-dimensional one-component model for distortive phase transitions. *Phys. Rev. B*, 17:1302, 1978.
- [73] H. J. C. Berendsen, J. P. M. Postma, W. F. van Gunsteren, A. DiNola, and J. R. Haak. Molecular dynamics with coupling to an external bath. *J. Chem. Phys.*, 81:3684, 1984.
- [74] S. Nosé. A unified formulation of the constant temperature molecular-dynamics methods. *J. Chem. Phys.*, 81:511–519, 1984.
- [75] W. G. Hoover. Canonical dynamics: Equilibrium phase-space distributions. *Phys. Rev. A.*, 31:1695, 1985.
- [76] S. Melchionna, G. Ciccotti, and B. L. Holian. Hoover npt dynamics for systems varying in shape and size. *Molec. Phys.*, 78:533, 1993.
- [77] J. E. Lennard-Jones. On the determination of molecular fields. *Proc. R. Soc. Lond. A*, 106:738, 1924.

- [78] M. I. Baskes. Application of the embedded-atom method to covalent materials: a semiempirical potential for silicon. *Phys. Rev. Lett.*, 59:2666, 1987.
- [79] M. J. Stott and E. Zaremba. Quasiatoms: An approach to atoms in nonuniform electronic systems. *Phys. Rev. B.*, 22:1564, 1980.
- [80] J. K. Nørskov and N. D. Lang. Effective medium theory of chemical binding: Application to chemisorption. *Phys. Rev. B*, 21:2131, 1980.
- [81] J. A. Moriarty. Zero-order pseudoatoms and the generalized pseudopotential theory. *Phys. Rev. B*, 10:3075, 1974.
- [82] J. A. Moriarty. Density-functional formulation of the generalized pseudopotential theory. *Phys. Rev. B*, 26:1754, 1982.
- [83] A. Bere, P. Vermaut, A. Hairie, E. Paumier, P. Ruterana, and G. Nouet. Modified stillinger-weber potential for planader defects modeling in gan. *Mater. Sci. Forum*, 294-296:223, 1999.
- [84] H. Lei, J. Chen, and P. Ruterana. Role of *c*-screw dislocations on indium segregation in ingan and inaln alloys. *Appl. Phys. Lett.*, 96:161901, 2010.
- [85] M. I. Baskes, J. S. Nelson, and A. F. Wright. Semiempirical modified embedded-atom potentials for silicon and germanium. *Phys. Rev. B*, 40:6085, 1989.
- [86] M. R. Fellinger, H. Park, and J. W. Wilkins. Force-matched embedded-atom method potential for niobium. *Phys. Rev. B*, 81:144119, 2010.
- [87] R. F. Zhang, J. Wang, I. J. Beyerlein, and T. C. Germann. Twinning in bcc metals under shock loading: a challenge to empirical potentials. *Phil. Mag.*, 91:731–740, 2011.

- [88] H. Park, M. R. Fellinger, T. J. Lenosky, W. W. Tipton, D. R. Trinkle, S. P. Rudin, C. Woodward, J. W. Wilkins, and R. G. Hennig. Ab-initio based empirical potential used to study the mechanical properties of molybdenum. *Phys. Rev. B*, 85:214121, 2012.
- [89] W. Ko, B. Grabowski, and J. Neugebauer. Development and application of a Ni-Ti interatomic potential with high predictive accuracy of the martensitic phase transition. *Phys. Rev. B*, 92:134107, 2015.
- [90] K. W. Jacobsen, J. K. Nørskov, and M. J. Puska. Interatomic interactions in the effective-medium theory. *Phys. Rev. B*, 35:7423, 1987.
- [91] J. D. Kress and A. E. DePristo. Corrected effective medium method. i. one-body formulation with applications to atomic chemisorption and diatomic molecular potentials. *J. Chem. Phys.*, 88:2596, 1988.
- [92] J. D. Kress and A. E. DePristo. Corrected effective medium method. ii. n-body formulation. *J. Chem. Phys.*, 88:2596, 1988.
- [93] M. S. Daw. Model of metallic cohesion: The embedded-atom method. *Phys. Rev. B*, 39:7441, 1989.
- [94] J. W. C. Nicklas. *Accurately modelling complex materials*. PhD thesis, The Ohio State University, 2013. Chapter 5, pages 70-104, [https://etd.ohiolink.edu/pg\\_10?0::NO:10:P10\\_ACCESSION\\_NUM:osu1366210034](https://etd.ohiolink.edu/pg_10?0::NO:10:P10_ACCESSION_NUM:osu1366210034).
- [95] M. J. D. Powell. An efficient method for finding the minimum of a function of several variables without calculating derivatives. *Computer Journal*, 7(2):155–162, 1964.

- [96] F. H. Stillinger and T. A. Weber. Computer simulation of local order in condensed phases of silicon. *Phys. Rev. B*, 31:5262, 1985.
- [97] M. S. Daw and M. I. Baskes. Embedded-atom method: Derivation and application to impurities, surfaces, and other defects in metals. *Phys. Rev. B*, 29:6443, 1984.
- [98] R. C. Ehemann, J. Nicklas, H. Park, and J. W. Wilkins. Ab initio based empirical potential applied to tungsten at high pressure. *Phys. Rev. B*, 95:184101, 2017.
- [99] G. Kresse, J. Furthmüller, and J. Hafner. *Ab initio* force constant approach to phonon dispersion relations of diamond and graphite. *Europhys. Lett.*, 39(9):729, 1995.
- [100] S. Plimpton. Fast parallel algorithms for short-range molecular dynamics. *J. Comp. Phys.*, 117:1–19, 1995.
- [101] R. Kinslow. *High-velocity impact phenomena*. Academic Press, New York, New York, USA, 1970.
- [102] Y. S. Touloukian, R. K. Kirby, R. E., and P. D. Desai. *Thermophysical properties of matter: thermal expansion–metallic elements and alloys*, volume 12. Plenum Press, New York, New York, USA, 1975.
- [103] W. P. Davey. Precision measurements of the lattice constants of twelve common metals. *Phys. Rev.*, 25:753, 1925.
- [104] H. Hartmann, F. Ebert, and O. Bretschneider. Elektrolysen in phosphatschmelzen. i. die elektrolytische gewinnung von - und -wolfram. *Zeitschrift fr Anorganische und Allgemeine Chemie*, 198:116, 1931.

- [105] A. D. Taylor and N. J. Doyle. The solid solubility of nitrogen in Nb and Nb-rich Nb-Hf, Nb-Mo and Nb-W alloys. part ii: The ternary systems Nb-Hf-N, Nb-Mo-N, and Nb-W-N. *J. Less-Common Met.*, 13:413–430, 1967.
- [106] Y. Wang, S. Curtarolo, C. Jiang, R. Arroyave, T. Wang, G. Ceder, L. Q. Chen, and Z. K. Liu. Ab initio lattice stability in comparison with CALPHAD lattice stability. *Computer Coupling of Phase Diagrams and Thermochemistry*, 28:79, 2004.
- [107] F. Favot and A. DalCorso. Phonon dispersions: performance of the generalized gradient approximation. *Phys. Rev. B*, 60(16):11427–11431, 1999.
- [108] D. I. Bolef and J. de Klerk. Elastic constants of single-crystal Mo and W between 77 and 500 k. *J. Appl. Phys.*, 33:2311, 1962.
- [109] S. H. Chen and B. N. Brockhouse. Lattice vibrations of tungsten. *Solid State Commun.*, 2:73–77, 1964.
- [110] C. S. Becquart and C. Domain. Ab initio calculations about intrinsic point defects and he in w. *Nucl. Instrum. Meth. B*, 225:23, 2007.
- [111] D. Nguyen-Manh, A. P. Horsfield, and S. L. Dudarev. Self-interstitial atom defects in bcc transition metals: Group-specific trends. *Phys. Rev. B*, 73:020101(R), 2006.
- [112] W. Xu and J. A. Moriarty. Atomistic simulation of ideal shear strength, point defects, and screw dislocations in bcc transition metals: Mo as a prototype. *Phys. Rev. B*, 54(10):6941, 1996.
- [113] J. A. DiCarlo, C. L. Snead, and A. N. Goland. Stage-I interstitials in electron-irradiated tungsten. *Phys. Rev.*, 178:1059, 1969.

- [114] S. Okuda and H. Mizubayashi. Free migration of interstitials in tungsten. *Phys. Rev. Lett.*, 34:815, 1975.
- [115] T. Amino, K. Arakawa, and H. Mori. Detection of one-dimensional migration of self-interstitial atoms in tungsten using high-voltage electron microscopy. *Sci. Rep.*, 6:26099, 2016.
- [116] J. S. Hirschhorn. Stacking faults in the refractory metals and alloys — a review. *J. Less-Common Met.*, 5:493, 1963.
- [117] L. Vitos, A. V. Ruban, H. L. Skriver, and J. Kollár. The surface energy of metals. *Surf. Sci.*, 411:186, 1998.
- [118] A. Moitra, S. Kim, J. Houze, B. Jelinek, S. Kim and S. Park, R. M. German, and M. F. Horstemeyer. Melting tungsten nanoparticles: a molecular dynamics study. *J. Phys. D: Appl. Phys.*, 41:185406, 2008.
- [119] W. R. Tyson and W. A. Miller. Surface free energies of solid metals: Estimation from liquid surface tension experiments. *Surf. Sci.*, 62:267–276, 1976.
- [120] L. Z. Mezey and J. Giber. The surface free energies of solid chemical elements: calculation from internal free enthalpies of atomization. *Jpn. J. Appl. Phys. Part 1*, 21:1569, 1982.
- [121] A. T. Paxton, P. Gumbsch, and M. Methfessel. A quantum mechanical calculation of the theoretical strength of metals. *Philos. Mag. Lett.*, 63(5):267–274, 1991.
- [122] L. Romaner, C. Ambrosch-Draxl, and R. Pippal. Effect of rhenium on the dislocation core structure in tungsten. *Phys. Rev. Lett.*, 104:195503, 2010.

- [123] X. Tian and C. Woo. The movement of screw dislocations in tungsten. *Mat. Sci. Eng. A*, 369:210–214, 2004.
- [124] M. S. Duesbery and V. Vitek. Plastic anisotropy in b.c.c. metals. *Acta Mater.*, 46(5):1481–1492, 1998.
- [125] Y. T. Zhu, X. Z. Liao, and X. L. Wu. Deformation twinning in nanocrystalline materials. *Prog. Mat. Sci*, 57:1–62, 2012.
- [126] W. C. Swope, H. C. Andersen, P. H. Berens, and K. R. Wilson. A computer simulation method for the calculation of equilibrium constants for the formation of physical clusters of molecules: application to small water clusters. *J. Chem. Phys.*, 76:637, 1982.
- [127] X. J. Zhang and C. L. Chen. Pressure dependence of phonon dispersion in bcc tungsten. *Chin. J. Phys.*, 51(2):359–367, 2013.
- [128] M. S. Daw, S. M. Foiles, and M. I. Baskes. Embedded-atom method: a review of theory and applications. *Mater. Sci. Rep.*, 9:7–8, 1993.
- [129] P. E. Blöchl. Projector augmented-wave method. *Phys. Rev. B*, 50:17953, 1994.
- [130] J. P. Perdew, K. Burke, and M. Ernzerhof. Generalized gradient approximation made simple. *Phys. Rev. Lett.*, 77:3865, 1996.
- [131] John P. Perdew, K. Burke, and Matthias Ernzerhof. Erratum: Generalized gradient approximation made simple. *Phys. Rev. Lett.*, 78:1396, 1997.
- [132] M. R. Fellinger. *First Principles-Based Interatomic Potentials for Modeling the Body-Centered Cubic Metals V, Nb, Ta, Mo, and W*. PhD thesis, The Ohio State University, 2013. Chapter 4, page 142, [https://etd.ohiolink.edu/pg-107115612085608190::NO:10:P10\\_ETD\\_SUBID:3564](https://etd.ohiolink.edu/pg-107115612085608190::NO:10:P10_ETD_SUBID:3564).

- [133] P. Lazar, M. Jahnátek, J. Hafner, N. Nagasako, R. Asahi, C. Blaas-Schenner, M. Stöhr, and R. Podloucky. Temperature-induced martensitic phase transitions in gum-metal approximants: First-principles investigations for  $Ti_3Nb$ . *Phys. Rev. B*, 84:054202, 2011.
- [134] C. Jiang, C. Wolverton, J. Sofo, L.Q. Chen, and Z.K. Liu. First-principles study of binary bcc alloys using special quasirandom structures. *Phys. Rev. B*, 69:214202, 2004.
- [135] M. J. Lai, C. C. Tasan, J. Zhang, B. Grabowski, L. F. Huang, and D. Raabe. Origin of shear induced  $\beta$  to  $\omega$  transition in ti-nb-based alloys. *Acta Mater.*, 92:55–63, 2015.
- [136] J. Sun, Q. Yao, H. Xing, and W. Y. Guo. Elastic properties of  $\beta$ ,  $\alpha''$  and  $\omega$  metastable phases in Ti-Nb alloy from first-principles. *J. Phys. Condens. Matter*, 19:486215, 2007.
- [137] M.-K. Han, J.-Y. Kim, M.-J. Hwang, H.-J. Song, and Y.-J. Park. Effect of nb on the microstructure, mechanical properties, corrosion behavior and cytotoxicity of ti-nb alloys. *Materials*, 8:5986–6003, 2015.
- [138] S. Zinelis, A. Tsetsekou, and T. Papadopoulos. Thermal expansion and microstructural analysis of experimental metal-ceramic titanium alloys. *J. Prosthet. Dent.*, 90:332, 2003.
- [139] B. Bi Argent and G.J.C. Milne. The physical properties of niobium, tantalum, molybdenum and tungsten. *J. Less-Common Met.*, 2:154–162, 1960.
- [140] A. Yu. Nikonov, A. M. Zharmukhametova, and A. I. Dmitriev. Ab initio calculations for search optimization of multicomponent alloy configurations. *AIP Conf. Proc.*, 1783:020165, 2016.

- [141] R. J. Talling, R. J. Dashwood, M. Jackson, S. Kuramoto, and D. Dye. Determination of  $C_{11} - C_{12}$  in Ti-36Nb-2Ta-3Zr-0.3O (wt.%) (gum metal). *Acta Mater.*, 59:669–672, 2008.
- [142] H. Ledbetter, H. Ogi, S. Kai, S. Kim, and M. Hirao. Elastic constants of body-centered cubic titanium monocrystals. *J. Appl. Phys.*, 95:4642–4644, 2004.
- [143] R. Hermann, H. Hermann, M. Calin, B. Büchner, and J. Eckert. Elastic constants of single-crystalline  $\beta$ -Ti<sub>70</sub>Nb<sub>30</sub>. *Scripta Mater.*, 66:198–201, 2012.
- [144] C. N. Reid, J. L. Routbort, and R. A. Maynard. Elastic constants of Ti-40 at.% Nb at 298 k. *J. Appl. Phys.*, 44:1398, 1973.
- [145] K. J. Carroll. Elastic constants of niobium from 4.2 to 300 k. *J. Appl. Phys.*, 36:3689, 1965.
- [146] H. W. Jeong, Y. S. Yoo, Y. T. Lee, and J. K. Park. Elastic softening behavior of Ti-Nb single crystal near martensitic transformation temperature. *J. Appl. Phys.*, 108:063515, 2010.
- [147] D. Farkas and C. Jones. Interatomic potentials for ternary Nb-Ti-Al alloys. *Modelling Simul. Mater. Sci. Eng.*, 4:23–32, 1996.
- [148] A. T. Raji, S. Scandolo, R. Mazzarello, S. Nsengiyumva, M. Härtig, and D. T. Britton. Ab initio pseudopotential study of vacancies and self-interstitials in hcp titanium. *Phil. Mag.*, 89:1629–1645, 2009.
- [149] M. A. Cerdeira, S. L. Palacios, C. González, D. Fernández-Pello, and R. Iglesias. Ab initio simulations of the structure, energetics and mobility of radiation-induced point defects in bcc nb. *J. Nucl. Mater.*, 478:185–196, 2016.

- [150] F. Dausinger, J. Fuss, J. Schweikhardt, and H. Shultz. Free migration of self-interstitials in bcc refractory metals. *J. Nucl. Mater.*, 69:689–692, 1978.
- [151] H. Shultz. Defect parameters of b.c.c. metals: group-specific trends. *Mater. Sci. Eng. A*, 141:149, 1991.
- [152] M. Ghazisaeidi and D. R. Trinkle. Core structure of a screw dislocation in ti from density functional theory and classical potentials. *Acta Mater.*, 60:1287–1292, 2012.
- [153] N. Tarrat, M. Benoit, D. Caillard, L. Ventelon, N. Combe, and J. Morillo. Screw dislocation in hcp ti: Dft dislocation excess energies and metastable core structures. *Modell. Simul. Mater. Sci. Eng.*, 22:055016, 2014.
- [154] A. Devaraj, S. Nag, R. Srinivasan, R. E. A. Williams, S. Banerjee, R. Banerjee, and H. L. Fraser. Experimental evidence of concurrent compositional and structural instabilities leading to  $\omega$  precipitation in titanium-molybdenum alloys. *Acta Mater.*, 60:596–609, 2012.
- [155] Y. Zheng, T. Alam, R. E. A. Williams, S. Nag, R. Bangerjee, and H. L. Fraser. Structural and compositional characteristics of isothermal omega phase in beta titanium alloys. pages 59–71, 2016.
- [156] C.-X. Li, H.-B. Luo, Q.-M. Hu, R. Yang, F.-X. Yin, O. Umezawa, and L. Vitos. Lattice parameters and relative stability of  $\alpha''$  phase in binary titanium alloys from first-principles calculations. *Solid State Commun.*, 159:70, 2013.
- [157] Y. W. Chai, H. Y. Kim, H. Hosoda, and S. Miyazaki. Self-accommodation in Ti-Nb shape memory alloys. *Acta Mater.*, 57:4054–4064, 2009.

- [158] Y. Al-Zain, H. Y. Kim, H. Hosoda, T. H. Nam, and S. Miyazaki. Shape memory properties of Ti-Nb-Mo biomedical alloys. *Acta Mater.*, 58:4212–4223, 2010.
- [159] K. Inaekyan, V. Brailovski, S. Prokoshkin, V. Pushin, S. Dubinskiy, and V. Sheremetev. Comparative study of structure formation and mechanical behavior of age-hardened Ti-Nb-Zr and Ti-Nb-Ta shape memory alloys. *Mater. Charact.*, 103:65–74, 2015.
- [160] P. M. Larsen, S. Schmidt, and J. Schiøtz. Robust structural identification via polyhedral template matching. *Modell. Simul. Mat. Sci. Eng.*, 24:055007, 2016.
- [161] J. P. Hirth and J. Lothe. *Theory of Dislocations*. Krieger, Malabar, Florida, USA, 1982.
- [162] P. Zhang and D. R. Trinkle. A modified embedded atom method potential for interstitial oxygen in titanium. *Comp. Mater. Sci.*, 124:204, 2016.